THÈSE
DE L'UNIVERSITÉ DU LITTORAL COTE D'OPALE

Laboratoire d'Océanologie et de Géosciences

Présentée par

Griet NEUKERMANS

Pour obtenir le grade de Docteur en Sciences
de la Matière, du Rayonnement et de l'Environnement
Spécialité
Océanographie

Sujet de thèse

Les particules en suspension dans les eaux côtières turbides: estimation par mesures optiques in situ et depuis l'espace

Soutenue le 18 avril 2012

devant le jury composé de

Directeur de thèse	Hubert LOISEL (LOG, France)
Co-Directeur de thèse	Kevin RUDDICK (MUMM, Belgique)
Rapporteurs	David ANTOINE (LOV, France)
	Michael TWARDOWSKI (WET Labs, USA)
Membres de jury	Jean-François BERTHON (JRC, Italy)
	Emmanuel BOSS (UMaine, USA)
	François SCHMITT (LOG, France)

DISSERTATION

UNIVERSITÉ DU LITTORAL COTE D'OPALE

Laboratoire d'Océanologie et de Géosciences

By

Griet NEUKERMANS

Submitted in partial fulfillment of the requirements for the degree of Doctor in Science (Oceanography)

Subject

Optical in situ and geostationary satellite-borne observations of suspended particles in coastal waters

Defended on 18 April 2012

for the dissertation committee composed of

Promoter	Hubert LOISEL (LOG, France)
Co-Promoter	Kevin RUDDICK (MUMM, Belgium)
Reporters	David ANTOINE (LOV, France)
	Michael TWARDOWSKI (WET Labs, USA)
Committee members	Jean-François BERTHON (JRC, Italy)
	Emmanuel BOSS (UMaine, USA)
	François SCHMITT (LOG, France)

Print: Silhouet, Maldegem

2012 ASP nv (Academic and Scientific Publishers nv)
Ravensteingalerij 28
B-1000 Brussel
Tel. + 32 (0)2 289 26 50
Fax + 32 (0)2 289 26 59
info@aspeditions.be
www.aspeditions.be

ISBN 978 90 7028 949 2
NUR 912
Legal deposit D/2012/11.161/015

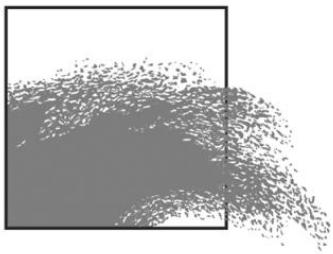

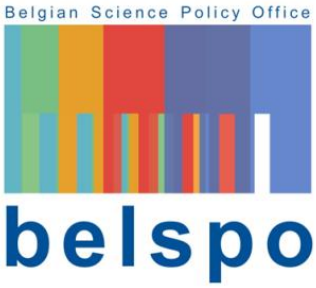

This thesis work was funded by the Belgian Science Policy Office (BELSPO) STEREO Programme in the framework of the BELCOLOUR-2 (SR/00/104) and GEOCOLOUR (SR/00/139) projects. This work was also supported by Centre National d'Etude Spatiale (CNES) in the frame of the COULCOT project (TOSCA program).

Keywords: diurnal variability, tidal variability, resuspension, PAR attenuation, particulate scattering coefficient, bio-optics, particle size distribution, mass-specific scattering coefficient, light attenuation, turbidity, suspended particulate matter concentration measurement protocol, ocean colour, remote sensing, atmospheric correction, meteorological satellite, SEVIRI, MODIS.

To those who inspired me

CONTENT

ACKNOWLEDGEMENTS

This dissertation is the result of collaboration between the Laboratoire d'Océanographie et de Géosciences (LOG) and the Management Unit of the North Sea Mathematical Models (MUMM). I am very grateful to the numerous people who contributed to this work.

My foremost gratitude to my promoter and co-promoter, Hubert Loisel and Kevin Ruddick, for their guidance, mentoring, and support. I was a lucky pupil to have learned from the masters in marine optics and atmospheric correction!

I thank the reporters of my dissertation, David Antoine and Mike Twardowski, and members of the dissertation committee, Jean-François Berthon, Emmanuel Boss, and François Schmitt for evaluating and reviewing this work.

Many thanks to my colleagues of the Remote Sensing and Ecosytem Modeling team of MUMM and of the Physical Oceanography, Transport, and Remote Sensing team of LOG. I received a great deal of support and assistance of a few people in particular: Xavier Mériaux for data processing and lab analysis, Lucie Courcot for Electron Microscopy analysis, Clémence Goyens for translating the abstract, Michel Laréal for technical support, Quinten Vanhellemont for providing ocean colour data, Geneviève Lacroix for hydrodynamic modeling, and Bouchra Nechad for suspended matter retrieval algorithms.

The crews of research vessels *Belgica*, *Alliance*, *Papy Jo*, and *Zeeleeuw* are thanked for their kind help during many sea campaigns. Thanks to the Chemistry Laboratory of MUMM for their analysis of hundreds of suspended matter and phytoplankton pigment samples. I also thank Flanders Marine Institute (VLIZ) for providing a LISST instrument during several campaigns.

I am very grateful to Nicolas Clerbaux of the Royal Meteorological Institute of Belgium for providing SEVIRI data and kind support. Thanks to Naomi Greenwood of the Centre for Environment, Fisheries & Aquaculture Science, for providing SmartBuoy data and kind help.

Thanks to the BELCOLOUR-2 and GEOCOLOUR project scientists and steering committee members for scientific discussions and data sharing.

Finally, a special thanks to my parents, Peter and Jelle, for giving me the chance to study, develop, and grow, and for their trust, love, and support. Many thanks to my family and friends for their love and understanding.

Griet

ABSTRACT

Particles suspended in seawater include sediments, phytoplankton, zooplankton, bacteria, viruses, and detritus, and are collectively referred to as suspended particulate matter, SPM. In coastal waters, SPM is transported over long distances and in the water column by biological, tide or wind-driven advection and resuspension processes, thus varying strongly in time and space. These strong dynamics challenge the traditional measurement of the concentration of SPM, [SPM], through filtration of seawater sampled from ships. Estimation of [SPM] from sensors recording optical scattering allows to cover larger temporal or spatial scales. So called ocean colour satellites, for example, have been used for the mapping of [SPM] on a global scale since the late 1970s. These polar-orbiting satellites typically provide one image per day for the North Sea area. However, the sampling frequency of these satellites is a serious limitation in coastal waters where [SPM] changes rapidly during the day due to tides and winds. Optical instruments installed on moored platforms or on under-water vehicles can be operated continuously, but their spatial coverage is limited. This work aims to advance in situ and space-based optical techniques for [SPM] retrieval by investigating the natural variability in the relationship between [SPM] and light scattering by particles and by investigating whether the European geostationary meteorological SEVIRI sensor, which provides imagery every 15 minutes, can be used for the mapping of [SPM] in the southern North Sea.

Based on an extensive in situ dataset, we show that [SPM] is best estimated from red light scattered in the back directions (backscattering). Moreover, the relationship between [SPM] and particulate backscattering is driven by the organic/inorganic composition of suspended particles, offering opportunities to improve [SPM] retrieval algorithms. We also show that SEVIRI successfully retrieves [SPM] and related parameters such as turbidity and the vertical light attenuation coefficient in turbid waters. Even though uncertainties are considerable in clear waters, this is a remarkable result for a meteorological sensor designed to monitor clouds and ice, much brighter targets than the sea! On cloud free days, tidal variability of [SPM] can now be resolved by remote sensing for the first time, offering new opportunities for monitoring of turbidity and ecosystem modelling. In June 2010 the first geostationary ocean colour sensor was launched into space which provides hourly multispectral imagery of Korean waters. Other geostationary ocean colour sensors are likely to become operational in the (near?) future over the rest of the world's seas. This work allows us to maximally prepare for the coming of geostationary ocean colour satellites, which are expected to revolutionize optical oceanography.

RÉSUMÉ

Les particules en suspension dans l'eau de mer incluent les sédiments, le phytoplancton, le zooplancton, les bactéries, les virus, et des détritus. Ces particules sont communément appelés matière en suspension (MES). Dans les eaux côtières, la MES peut parcourir de longues distances et être transportée verticalement à travers la colonne d'eau sous l'effet des vents et des marées favorisant les processus d'advection et de resuspension. Ceci implique une large variabilité spatio-temporelle de MES et quasiment impossible à reconstituer à travers les mesures traditionnelles des concentrations de MES, [MES], par filtration de l'eau de mer à bord de bateaux. La [MES] peut être obtenue à partir de capteurs optiques enregistrant la diffusion et déployés soit de manière in-situ, soit à partir d'un satellite dans l'espace. Depuis la fin des années 70, par exemple, les satellites « couleur de l'eau » permettent d'établir des cartes de [MES] globales. La fréquence d'une image par jour pour la mer du Nord de ces capteurs polaires représente un obstacle non-négligeable pour l'étude de variabilité de la [MES] dans les eaux côtières où la marée et les vents engendrent des variations rapides au cours de la journée. Cette limitation est d'autant plus importante pour les régions avec une couverture nuageuse fréquente. Les méthodes in-situ à partir d'un navire autonome ou d'une plateforme amarrée permettent d'enregistrer des données en continu mais leur couverture spatiale reste néanmoins limitée. Ce travail a pour objectif de mettre en avant les techniques de mesures in-situ et satellites de la [MES] en se concentrant principalement sur deux points. Premièrement, d'acquérir une meilleure connaissance de la variabilité de la relation entre la [MES] et la lumière diffuse, et deuxièmement, d'établir des cartes de [MES] dans la mer du Nord avec le capteur géostationnaire météorologique Européen (SEVIRI), qui donne des images chaque 15 minutes.

La variabilité de la relation entre la [MES] et la lumière diffuse est étudiée à l'aide d'une banque de données in-situ. Nous démontrons que la [MES] est le mieux estimée à partir des mesures dans l'intervalle rouge du spectre de lumière rétro-diffuse. Par ailleurs, la relation entre la [MES] et la rétrodiffusion est gouvernée par la composition organique/inorganique des particules, ce qui représente des possibilités d'amélioration pour les algorithmes d'estimation de [MES] à partir de la couleur de l'eau. Nous démontrons aussi qu'avec SEVIRI il est possible d'estimer la [MES], la turbidité et le coefficient d'atténuation, deux variables étroitement liées à la [MES], avec généralement une bonne précision. Bien qu'il y ait d'importantes incertitudes dans les eaux claires, cette réussite est remarquable pour un capteur météorologique initialement conçu pour le suivi des nuages et des masses glacières, cibles beaucoup plus brillantes que la mer! Ce travail démontre pour la première fois que la variabilité de la [MES] à l'échelle temporelle des marées dans les eaux côtières au sud de la Mer du Nord peut être capturée et mesurée par le biais de la télédétection de la couleur de l'eau ; ce qui ouvre des opportunités pour le monitoring de la

turbidité et pour la modélisation des écosystèmes. Le premier capteur géostationnaire couleur de l'eau à été lancé en juin 2012, donnant des images multispectrale des eaux coréennes chaque heure. D'autres capteurs vont probablement suivre dans l'avenir (proche ?), couvrant le reste des eaux du globe. Ce travail nous permet de préparer, de façon optimale, l'arrivée de ces capteurs qui vont révolutionner l'océanographie optique.

SAMENVATTING

De in zeewater aanwezige zwevende materie zoals sedimenten, fytoplankton, zooplankton, bacteriën, virussen en detritus, worden collectief “suspended particulate matter” (SPM) genoemd. In kustwateren worden deze deeltjes over lange afstanden en in de waterkolom getransporteerd door biologische processen of wind- of getijdenwerking, waardoor SPM sterk varieert in ruimte en tijd. Door deze sterke dynamiek wordt de traditionele bemonstering van de concentratie van SPM, [SPM], door middel van filtratie van zeewaterstalen aan boord van schepen ontoereikend. Optische technieken die gebruik maken van de lichtverstrooiingseigenschappen van SPM bieden een gebieds- of tijdsdekkend alternatief. Zogenaamde “ocean colour” satellieten bijvoorbeeld leveren beelden van o.a. [SPM] aan het zeeoppervlak op globale schaal sinds eind 1970, met een frequentie van één beeld per dag voor de Noordzee. Deze frequentie is echter onvoldoende in onze kustwateren waar [SPM] drastisch kan veranderen in enkele uren tijd. Optische instrumenten aan boord van schepen of op onderwatervoertuigen kunnen continu meten, maar de gebiedsdekking is beperkt. Dit werk heeft tot doel de lichtverstrooiingseigenschappen van SPM te karakterizeren en te onderzoeken of de Europese geostationaire weersatelliet, die elk kwartier een beeld geeft, kan worden gebruikt voor de kartering van [SPM] in de zuidelijke Noordzee.

Op basis van een grote dataset van in situ metingen tonen wij aan dat [SPM] het nauwkeurigst kan worden bepaald door de meting van de verstrooiing van rood licht in achterwaartse richtingen (terugverstrooiing). Bovendien blijkt de relatie tussen [SPM] en terugverstrooiing afhankelijk van de organische-anorganische samenstelling van zwevende stof, wat mogelijkheden biedt tot het verfijnen van teledetectiealgoritmen voor [SPM]. Voorts tonen wij aan dat de Europese weersatelliet, SEVIRI, successvol kan worden aangewend voor de kartering van [SPM] en gerelateerde parameters zoals troebelheid en lichtdemping in de waterkolom. Hoewel met grote meetonzekerheid in klaar water toch een opmerkelijk resultaat voor een sensor die ontworpen werd voor detectie van wolken en ijs! Op wolkenvrije dagen wordt hierdoor de getijdendynamiek van [SPM] in de zuidelijke Noordzee voor het eerst detecteerbaar vanuit de ruimte, wat nieuwe mogelijkheden biedt voor de monitoring van waterkwaliteit en verbetering van ecosysteemmodellen. Sinds juni 2010 is de eerste geostationaire ocean colour satelliet een feit: elk uur een multispectraal beeld van Koreaanse wateren. Vermoedelijk zullen er in de (nabije?) toekomst meer volgen over Europa en Amerika. Dit werk laat toe ons maximaal voor te bereiden op de komst van zo’n satellieten, waarvan verwacht wordt dat zij een nieuwe revolutie in optische oceanografie zullen ontketenen.

LIST OF ABBREVIATIONS AND ACRONYMS

AAOT	Acqua Alta Oceanographic Tower
ac-9	Nine-channel Absorption and Attenuation Meter
AERONET	Aerosol Robotic Network
AERONET-OC	Aerosol Robotic Network-Ocean Colour
AGRI	Advanced Geosynchronous Radiation Imager
ANOVA	Analysis Of Variance
AOP	Apparent Optical Property
AU	Astronomical Units
AVHRR	Advanced Very High Resolution Radiometer
C-star	WET Labs transmissometer
CDOM	Colored Dissolved Organic Matter
COHERENS	COupled Hydrodynamical Ecological model for REgioNal Shelf seas
CTD	Conductivity, Temperature, Depth
c.v.	Coefficient of variation
CZCS	Coastal Zone Color Scanner
d.f.	Degrees of freedom
DL	Detection Limit
DM	Dissolved Matter
DOM	Dissolved Organic Matter
ECO-BB9	Nine-channel backscattering meter
ESA	European Space Agency
EUMETSAT	European Organisation for the Exploitation of Meteorological Satellites
FCI	Flexible Combined Imager
FNU	Formazine Nephelometric Units
GF/F	Glass Fiber Filter
GOCI	Geostationary Ocean Colour Imager
HICO	Hyperspectral Imager for the Coastal Ocean
HPLC	High Performance Liquid Chromatography
HRV	High Resolution Visual broadband of SEVIRI
IOCCG	International Ocean Color Coordinating Group
IOP	Inherent Optical Property

IQR	Interquartile range, difference between 75^{th} and 25^{th} percentile value
ISO	International Standards Organization
LED	Light Emitting Diode
LISST	Laser In Situ Scattering and Transmissometry device
LOWTRAN	Low Resolution Spectral Transmission
MASCOT	Multi-Angle Scattering Optical Tool
MERIS	Medium Resolution Imaging Spectrometer
MODIS	Moderate Resolution Imaging Spectroradiometer
MPE	Median relative prediction error
MSG	METEOSAT Second Generation
MSU	Multichannel Scanning Unit
MTG	METEOSAT Third Generation
NASA	National Aeronautics and Space Administration
NB	Normalized Bias
NAE	Normalized Absolute Error
NCEP	National Center for Environmental Prediction
NIR	Near-infrared wavelength range
NOAA	National Oceanic and Atmospheric Administration
OBS	Optical Backscatter
PAR	Photosynthetically Available Radiation
PPE	Prediction percentile error
PSD	Particle Size Distribution
PSU	Practical Salinity Units
PWC	Precipitable water content
RMSE	Root mean square error
RSS	Rapid Scan Service
SeaWiFS	Sea-viewing Wide Field-of-view Sensor
SBE	SeaBird Electronics
SEVIRI	Spinning Enhanced Visible and Infrared Imager
SNR	Signal-to-Noise Ratio
SPM	Suspended Particulate Matter
SSW	Synthetic Seawater
SWIR	Short wave infrared wavelength range
TOA	Top of atmosphere

UTC	Universal Time Coordinated
VIS	Visible wavelength range
VSF	Volume Scattering Function
WET Labs	Western Environmental Technology Laboratories

LIST OF SYMBOLS

Symbol	Parameter definition, units
α	Angström exponent, dimensionless
A_0	SEVIRI solar channel calibration correction factor, dimensionless
A_S, A_T	[SPM] and turbidity retrieval algorithm calibration constants, mg L^{-1} or FNU
[AC]	Total particle projected area concentration, m^{-1}
$[AC]_i$	Particle projected area concentration in the *i*-th size bin of the LISST, m^{-1}
a, a_p, a_{DOM}	Total, particulate, and dissolved matter absorption coefficient, m^{-1}
B_S, B_T	[SPM] and turbidity retrieval algorithm offsets, mg L^{-1} or FNU
β, β_p, β_w	Total, particulate, and pure water volume scattering function, m^{-1} sr^{-1}
$\tilde{\beta}$	Scattering phase function, sr^{-1}
b, b_p, b_w	Total, particulate, and pure water scattering coefficient, m^{-1}
b_p^m	b_p:[SPM], mass-specific scattering coefficient, m^2 g^{-1}
b_b , b_{bp}, b_{bw}	Total, particulate, and pure water backscattering coefficient, m^{-1}
$\tilde{b}_{bp}$	Backscattering ratio, b_{bp}:b_p, dimensionless
b_{bp}^m	b_{bp}:[SPM], mass-specific backscattering coefficient, m^2 g^{-1}
b_s	Side scattering coefficient, relative to a formazine particle suspension, FNU
b_s^m	b_s:[SPM], mass-specific side scattering coefficient, FNU m^3 g^{-1}
[Chl *a*]	Chlorophyll *a* pigment concentration, μg L^{-1}
c_f	Calibration gain factor for SEVIRI bands, mWm^{-2} sr^{-1} cm
c_p	Particulate beam attenuation coefficient, m^{-1}
c_p^m	c_p:[SPM], mass-specific beam attenuation coefficient, m^2 g^{-1}
Δ	Uncertainty of a measurement
Δ_a	Aerosol correction uncertainty, dimensionless
Δ_d	Digitization uncertainty, dimensionless
Δ_w	Turbid water uncertainty, dimensionless
D_A	Mean particle diameter, weighted by area, μm
D_i	Mean diameter of the *i*-th LISST size bin, μm

ε	VIS06:VIS08 band ratio of aerosol reflectances, dimensionless
E_d	Downwelling spectral irradiance, W m^{-2} nm^{-1}
E_0	Total spectral scalar irradiance, W m^{-2} nm^{-1}
E_0^{TOA}	Extraterrestrial solar irradiance at TOA, $Wm^{-2}\mu m^{-1}$
f'	Reflectance model factor, dimensionless
F	F-statistic
ϕ, ϕ_v, ϕ_0	Azimuth angle, sensor and sun azimuth angle
Φ_0	Incident flux, W nm^{-1}
Φ_a	Absorbed flux, W nm^{-1}
Φ_b	Scattered flux, W nm^{-1}
Φ_t	Transmitted flux, W nm^{-1}
γ	Hyperbolic slope of particle number concentration size distribution, dimensionless
γ	VIS06:VIS08 ratio of two-way aerosol transmittances, dimensionless
K_d	Spectral diffuse attenuation coefficient for downwelling irradiance, m^{-1}
K_{PAR}^{SB}	Vertical attenuation of photosynthetically active radiation derived from SmartBuoy PAR data, m^{-1}
$K_{PAR,\otimes}$	Vertical attenuation of photosynthetically active radiation derived from SEVIRI on the HRV grid, m^{-1}
K_{PAR}	Diffuse attenuation coefficient of PAR, m^{-1}
$\overline{K}_{\mathrm{PAR}}$	Vertically averaged diffuse attenuation coefficient of PAR, m^{-1}
λ	Wavelength of light, nm or μm
λ_0	Waveband central wavelength, nm or μm
L_a^{TOA}	Aerosol radiance at TOA, W m^{-2} sr^{-1} μm^{-1}
L_g^{TOA}	Sunglint radiance at TOA, W m^{-2} sr^{-1} μm^{-1}
L_r^{TOA}	Rayleigh (air molecule) radiance at TOA, W m^{-2} sr^{-1} μm^{-1}
L_{ra}^{TOA}	Aerosol-Rayleigh multiple scattering radiance at TOA, W m^{-2} sr^{-1} μm^{-1}
L_{sea}^{0+}	Total upwelling radiance, W m^{-2} sr^{-1} μm^{-1}
L_{sky}^{0+}	Sky radiance, W m^{-2} sr^{-1} μm^{-1}

L_{tot}^{TOA}	Total radiance and reflectance at TOA, W m^{-2} sr^{-1} μm^{-1}
L_w^{TOA}, L_w^{0+}	Water-leaving radiance at TOA and above-water, W m^{-2} sr^{-1} μm^{-1}
L_{wc}^{TOA}	White-cap radiance at TOA, W m^{-2} sr^{-1} μm^{-1}
m	Two-way airmass, dimensionless
$N(D)dD$	Number of particles in the size range D to dD, dimensionless
$N(D_i)$	Number of particles in the i-th LISST size bin per unit volume and per unit diameter increment, μL L^{-1} μm^{-1}
N	Real part of the refractive index, relative to water, dimensionless
n_o	Total number of observations
n_x	Number of outliers
$\omega(\lambda)$	Sensor spectral response function, dimensionless
Ω	Solid angle, sr
p	Statistical significance, dimensionless
PAR	Photosynthetically active radiation, photons s^{-1} m^{-2}
[PIC]	Particulate inorganic carbon concentration, μg L^{-1}
[PIM]	Particulate inorganic matter concentration, g m^{-3}
[POC]	Particulate organic carbon concentration, μg L^{-1}
[POM]	Particulate organic matter concentration, g m^{-3}
Q	Ratio of subsurface upwelling irradiance to the subsurface upwelling radiance, sr
Q_{bb}	Backscattering efficiency, dimensionless
Q_{bbe}	Mean backscattering efficiency, weighted by area, dimensionless
Q_{bse}	Mean side scattering efficiency, weighted by area, FNU m^{-1}
Q_c	Attenuation efficiency, dimensionless
Q_{ce}	Mean attenuation efficiency, weighted by area, dimensionless
r	Correlation coefficient, dimensionless
$\Re$	Air-water interface reflection and refraction factor, dimensionless
R	Irradiance reflectance, dimensionless
r_0	Calibration offset factor for SEVIRI bands, mWm^{-2} sr^{-1} cm
r_{rs}	Subsurface remote sensing reflectance, sr^{-1}
R_{rs}	Remote sensing reflectance, sr^{-1}
ρ_a	Particle population mean apparent density (dry weight:wet volume), kg L^{-1}

ρ_a^{TOA}	Aerosol reflectance at TOA, dimensionless
ρ_{ag}	Aggregate apparent density (dry weight:aggregate interstitial volume), kg L^{-1}
ρ_{ap}	Solid particle apparent density (dry weight: particle internal fluid volume), kg L^{-1}
ρ_c	Rayleigh and gas corrected reflectance at TOA, dimensionless
ρ_g^{TOA}	Sun glint reflectance at TOA, dimensionless
ρ_{ra}^{TOA}	Rayleigh-aerosol interaction reflectance at TOA, dimensionless
ρ_{sky}	Reflectance factor for sky radiance at air-sea interface, dimensionless
ρ_{tot}^{TOA}	Total reflectance at TOA, dimensionless
ρ_w^{TOA}	Marine reflectance at TOA, dimensionless
ρ_w^{0+}	Above-water marine reflectance, dimensionless
$\rho_{w,\otimes}^{0+}$	Above-water marine reflectance on HRV grid, dimensionless
ρ_{wc}^{TOA}	White cap reflectance at TOA, dimensionless
σ	VIS06:VIS08 band ratio of marine reflectance (dimensionless), or standard deviation, depending on the context
[SPM]	Suspended particulate matter concentration, g m^{-3}
$t_o^a, t_v^a, t_{o,v}^a$	Sun-sea, sea-sensor, and two-way aerosol transmittance, dimensionless
$t_o^g, t_v^g, t_{o,v}^g$	Sun-sea, sea-sensor, and two-way atmospheric gas transmittance, dimensionless
$t_o^r, t_v^r, t_{o,v}^r$	Sun-sea, sea-sensor, and two-way Rayleigh transmittance, dimensionless
T, T_b, T_a	Turbidity, Turbidity before, and after SPM filtration, FNU
$T_0, T_v, T_{o,v}$	Total sun-sea, sea-sensor, and two-way atmospheric transmittance, dimensionless
T^{SB}	T recorded by SmartBuoy, m^{-1}
$T_\otimes$	Turbidity retrieved by SEVIRI on the HRV grid, FNU
τ_a	Aerosol optical thickness, dimensionless
θ_m	Centroid angle of a backscattering instrument, °
θ_v	Viewing zenith angle, °
θ_0	Solar zenith angle, °
V	Filtration volume, L

V_{opt}	Optimal Filtration volume, L
[VC]	Total volume concentration of particles, μL L^{-1}
$[VC]_i$	Volume concentration of particles in the i-th LISST size class, μL L^{-1}
w_b, w_a	Weight of a GF/F filter before filtration and after filtration and drying in the lab, g
χ , χ_p	Proportionality factor between $\beta(\theta_m,\lambda)$ and $b_b(\lambda)$ and between $\beta_p(\theta_m,\lambda)$ and $b_{bp}(\lambda)$, dimensionless
χ	hyperbolic c_p spectral slope

LIST OF FIGURES

LIST OF TABLES

GENERAL INTRODUCTION

Coastal waters are important ecological systems and among the most productive natural systems on Earth. These waters are a complex mixture of constituents, which can be broadly classified into dissolved substances and suspended particulate matter, SPM. Suspended particles include microscopic algae, bacteria, viruses, zooplankton, detritus, and mineral particles brought to the sea by rivers or dust winds. Coastal waters are highly dynamic environments, where physical, biological, and geological processes contribute to rapid changes in seawater constituents, resulting in a high variability in space and time. This high spatio-temporal variability poses challenges for the adequate measurement of seawater constituents. Optical techniques can be used to retrieve quantitative information of certain seawater constituents, whose nature and quantity directly affect the optical properties of the water, resulting for example in colour upon interaction with sunlight. Traditional ship-based sampling of seawater constituents is costly, time consuming, and limited in space and time whereas optical measurements can be acquired remotely (from satellites or aircrafts) or in situ (on ships, moored platforms, or autonomous underwater vehicles), allowing to sample at much higher spatial and temporal scales. To the extent that reliable relationships between constituents and optical properties can be determined, information on constituent characteristics may be available at the same set of scales.

Suspended particles scatter light in all directions, with an intensity that is, to first order, determined by their concentration. Second order effects are caused by variations in particle size, shape, composition and internal structure. Of particular interest to remote sensing studies is the light scattered in the backward direction, which can be detected by a satellite sensor. In situ relationships between total light scattering and the dry weight concentration of SPM, [SPM], have been examined in open ocean and coastal waters since the early 1970s, when the first instrumentation became commercially available (Gibbs 1974; Carder et al. 1975; Pak and Zaneveld 1977). Good relationships are generally found, but reported values of mass-specific particulate scattering, i.e. scattering per unit [SPM], vary strongly (Hill et al. 2011). In situ instrumentation to record backscattering became commercially available only since the mid 1990's and few studies (Snyder et al. 2008; Boss et al. 2009c; Deyong et al. 2009; Martinez-Vicente et al. 2010) have investigated relationships between backscattering and [SPM] in natural waters. Our present understanding of the effect of particle characteristics on scattering and backscattering is mainly based on laboratory measurements (Morel and Bricaud 1986; Volten et al. 1998; Stramski et al. 2002) and/or theoretical calculations (Morel and Ahn 1991; Kitchen and Zaneveld 1992; Babin et al. 2003; Clavano et al. 2007). To advance our understanding of optical variability in natural waters, studies combining measurements of scattering properties of SPM with investigations of the fundamental causes

driving their variability are needed. The first major objective of this work is to investigate the in situ relationships between (back)scattering properties and [SPM] and to investigate the natural variability of mass-specific (back)scattering properties with respect to particle density, composition, and size, based on an intensive sampling program in optically complex coastal and more offshore waters around Europe and French Guyana.

Space-based remote sensing of optical properties of seawater is achieved from so called 'ocean colour' satellite sensors. The goal of ocean colour remote sensing is to derive quantitative information on seawater constituents from variations in the spectral form and magnitude of light leaving the water. This requires effective removal of the atmospheric signal that is sensed by ocean colour sensors at the top of the atmosphere, the so called 'atmospheric correction'. Ocean colour remote sensing began in 1978 with the launch of NASA's polar-orbiting Coastal Zone Color Scanner (CZCS, Hovis et al. 1980) satellite sensor. This proof-of-concept mission provided unprecedented imagery of phytoplankton biomass (chlorophyll *a*, Chl *a*) for the global open ocean until 1986, which revolutionized the field of biological oceanography. After a gap of 10 years, new polar-orbiting ocean colour sensors with improved radiometric, spectral, and spatial resolution were launched, including the Sea-viewing Wide Field-of-view Sensor (SeaWiFS, Hooker et al. 1993) in 1997, and the Moderate Resolution Imaging Spectroradiometer (MODIS, Salomonson et al. 1987) and Medium Resolution Imaging Spectrometer (MERIS, Rast et al. 1999) in 2002. These sensors have now become well-established sources of Chl *a* and [SPM] in open ocean and in coastal waters (McClain 2009), where new atmospheric corrections were developed (Moore et al. 1999; Ruddick et al. 2000; Stumpf et al. 2003a). Imagery of [SPM] from ocean colour satellites have been assimilated in modelling studies of sediment transport (Van Raaphorst et al. 1998; Fettweis and Van den Eynde 2003; Vos et al. 2000), coastal erosion, and ecosystems (Lacroix et al. 2007). There has also been considerable progress towards many new products including particulate and dissolved organic and inorganic carbon (Stramski et al. 1999; Vantrepotte et al. 2011), particle size distribution (Loisel et al. 2006; Kostadinov et al. 2009), phytoplankton species composition (Alvain et al. 2008), vertical light attenuation (Stumpf et al. 1999), turbidity (Stumpf et al. 1999; Woodruff et al. 1999; Nechad et al. 2009) etc.

However, the typical sampling frequency of these satellites of one image per cloud-free day at a given location is a serious limitation in coastal waters where seawater constituents change rapidly during the day due to tides and winds. This frequency is further reduced for regions of frequent cloud cover. Satellites in geostationary orbit can sample at frequencies of minutes to hours. The Geostationary Ocean Colour Imager (GOCI, Faure et al. 2008), launched by the Korean Space Agency in June 2010, is the first ocean colour sensor in geostationary orbit, providing hourly images of waters surrounding the Korean peninsula at a spatial resolution of 500 m. European and American space agencies also have plans to

launch geostationary ocean colour sensors covering the rest of the world's seas. While we eagerly await the coming of these sensors, the potential of the readily available geostationary meteorological sensors for marine applications can be tested. The European geostationary meteorological SEVIRI sensor, for example, has a few broad spectral bands in the visible (VIS) and near-infrared (NIR), which may be all that is needed to detect [SPM] in turbid waters, as shown by Stumpf and Pennock 1989 for the Advanced Very High Resolution Radiometer (AVHRR). The second major objective of this work is to investigate whether the high spatio-temporal dynamics of [SPM] in the southern North Sea can be resolved by SEVIRI.

This dissertation is organized as follows: Chapter 1 describes the constituents of seawater and their interaction with light, defines optical properties, and describes in situ optical instrumentation to familiarize the beginner with terms used throughout this work. In the second chapter, we focus on the measurement procedure for the dry weight concentration of suspended particulate material, [SPM], which is determined via filtration of seawater on glass-fiber filters. More specifically, we investigate procedural uncertainties related to salt retention, filter preparation, weighing, and handling in the laboratory, and filtration volume. We also investigate how turbidity measurements, which are simple and fast, can be used to optimize [SPM] measurement. In Chapter 3 we investigate the natural variability in the relationship between [SPM] and light scattering based on an extensive dataset of in situ measurements of optical properties, [SPM], particle density, and composition. This relationship is poorly characterized at present and directly affects the retrieval accuracy of [SPM] from optical measurements. In Chapter 4 we develop and validate the atmospheric correction for SEVIRI, to derive marine reflectance in SEVIRI's red waveband, using the NIR band to correct for aerosol scattering. We further quantify uncertainties on the derived marine reflectance due to atmospheric correction and sensor digitization. The temporal dynamics of [SPM] and covarying parameters resolved by SEVIRI are then validated with in situ data in Chapter 5. The overall conclusions of this work are summarized in Chapter 6.

This work resulted in three peer-reviewed publications, which are available in open access (use the web address to download the publications):

- Neukermans, G., K. Ruddick, E. Bernard, D. Ramon, B. Nechad, and P.-Y. Deschamps. 2009. Mapping total suspended matter from geostationary satellites: a feasibility study with SEVIRI in the Southern North Sea. Opt. Express **17:** 14029-14052. Open access: http://www.opticsinfobase.org/oe/viewmedia.cfm?URI=oe-17-16-14029&seq=0
- Neukermans, G., H. Loisel, X. Meriaux, R. Astoreca, and D. McKee. 2012. In situ variability of mass-specific beam attenuation and backscattering of marine particles with respect to particle size, density, and composition. Limnol. Oceanogr. **57:** 124–144, doi:110.4319/lo.2011.4357.4311.0124.

Open access: http://aslo.org/lo/toc/vol_57/issue_1/0124.pdf and web appendix: http://www.aslo.org/lo/toc/vol_57/issue_1/0124a.pdf

- Neukermans, G., K. Ruddick, and N. Greenwood. accepted. Diurnal variability of turbidity and light attenuation in the southern North Sea from the SEVIRI geostationary sensor. Remote Sens. Environ. (web address not available at the time of printing of this book)

Chapter 1 OPTICAL PROPERTIES AND SEAWATER CONSTITUENTS: DEFINITIONS AND MEASUREMENT

This introductory chapter describes the constituents of seawater and their interaction with light. We further define optical properties and describe how they are measured in situ. This chapter is mainly based on textbooks in marine optics, including Mobley 1994; Kirk 1996; Jonasz and Fournier 2007; Babin et al. 2008 and review papers such as Stramski et al. 2004.

1.1 Seawater constituents

Natural seawater is composed of water with inorganic salts and gasses dissolved in it, as well as particulate and dissolved materials of inorganic or organic origin, living or non-living. These constituents cover a broad size range, spanning several orders of magnitude from water molecules of size ~0.1nm to large particles and gas bubbles of several mm in size (see Figure 1.1). In optical oceanography, the constituents of natural seawater are traditionally divided into broad categories including pure seawater, dissolved matter (DM), and suspended particulate matter (SPM). The separation between SPM and DM is determined operationally based on filtration of seawater through a certain type of filter with a certain pore size. SPM is commonly defined as all matter retained on a GF/F glass fiber filter which effectively retain particles larger than about 0.4 μm to 0.7 μm, although it is noted that retention size may depend on filtration volume (Sheldon 1972; Sheldon and Sutcliffe 1969). We further note that this size cut-off is quite arbitrary and is to be appropriately chosen depending on the optical application.

Living biological particles include viruses, bacteria, phytoplankton, and zooplankton, whereas non-living particulate matter includes organic detritus (bodies or fragments of dead organisms as well as fecal material) and inorganic particles (minerals such as clay, feldspars, sand, quartz, and calcite). Inorganic particles in marine waters may originate from atmospheric dust, transported to the sea by winds, eroded soil transported by rivers, or bottom sediments suspended in the water column by currents and tides. Mixed organic–inorganic types also occur and may exists as single cells such as coccolithophores (phytoplankton with calcium carbonate plates), but also as amorphous agglomerations of many organic and inorganic particles held together by a sugar-based mucus. These aggregates are also called flocs or ‘marine snow’. Suspended particles thus exhibit an enormous diversity in terms of particle size, shape (see Figure 1.2), internal structure, and composition (i.e., refractive index), which all influence their optical properties.

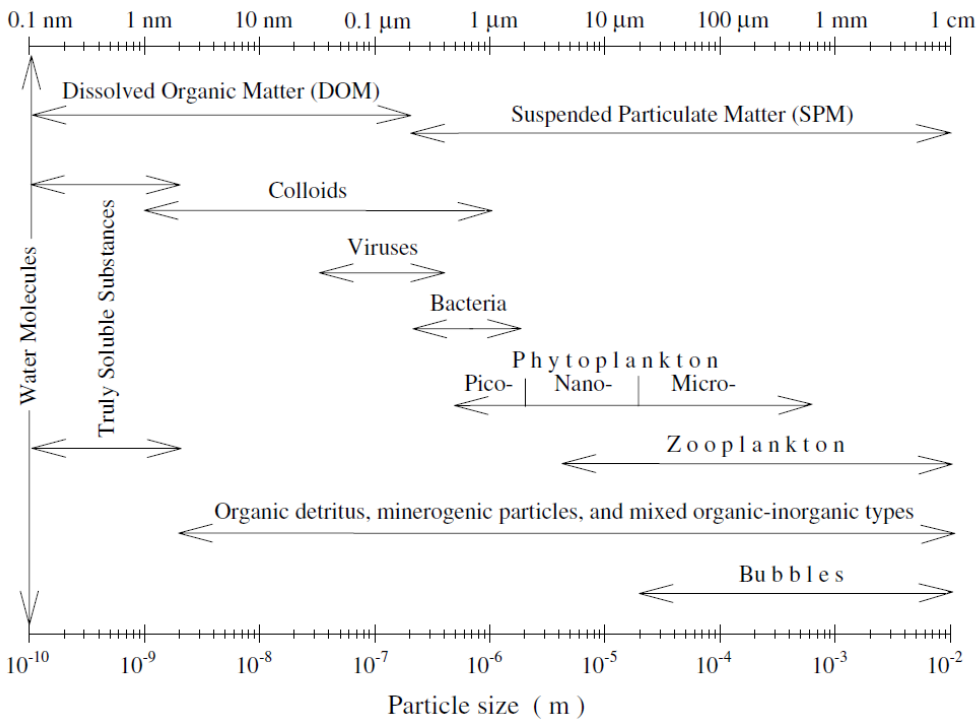

Figure 1.1. Size spectrum of seawater constituents between 0.1 nm and 1cm. Arrow ends indicate approximate boundaries for different constituent categories (source: Stramski et al. 2004).

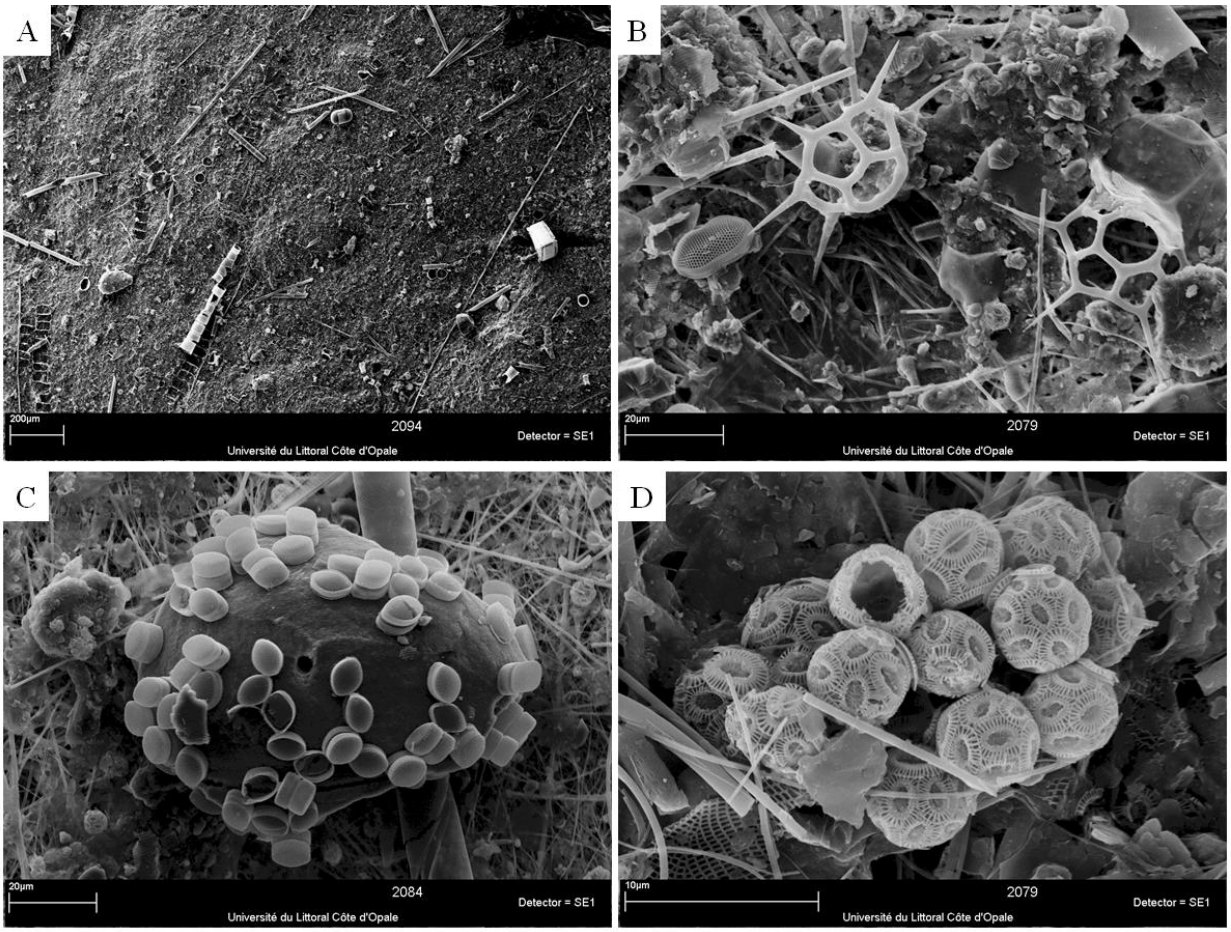

Figure 1.2. Scanning Electron Microscopy images of particles retained on a GF/F glass fiber filter for a sample collected in the southern North Sea in September 2011, showing the enormous diversity in particle shapes and sizes. (A) Large diatom chains (microphytoplankton), large diatoms, and mineral particles. (B, C, D) Smaller particles: nanophytoplankton, and small minerogenic particles. (C) diatoms attached to a mineral particle. (D) coccolithophores.

1.2 Optical properties

Seawater constituents interact with light through the wavelength dependent processes of scattering and absorption, giving the water its colour upon interaction with visible sunlight. Quantitative information on seawater constituents can be obtained from optical techniques, which may be operated in situ (optical instruments deployed on ships, moored platforms, or autonomous underwater vehicles) or remotely (sensors operated from aircrafts or satellites). Both techniques have different spatial, spectral, temporal, and technical capabilities and limitations, some of which are discussed here.

A distinction is traditionally made (Preisendorfer 1961) between inherent optical properties (IOPs), which depend only on the properties of the medium and its constituents, and apparent optical properties (AOPs), which depend both on the IOPs and on the way the medium is illuminated. In this

section we define the fundamental IOPs and AOPs, give their inter-relationships, discuss measurement techniques and give an overview of how IOPs and AOPs relate to seawater constituents.

1.2.1 Inherent optical properties (IOPs)

1.2.1.1 DEFINITION OF IOPS

When light propagates through ocean water, it interacts with molecules and particles of the medium mainly through elastic scattering and absorption of photons. While the former involves the redirection of energy with respect to its initial direction of propagation without a change in photon energy, the latter involves the conversion of photon energy into other forms such as heat or biomass. Other secondary interactions include inelastic processes such as fluorescence by dissolved organic matter and phytoplankton pigments, and Raman scattering by the water molecules.

Consider a infinitely narrow collimated beam of monochromatic radiation (wavelength λ) of spectral radiant power or flux $\Phi_0(\lambda)$ (W nm^{-1}) incident on a layer of water of thickness dx as schematically illustrated in Figure 1.3(A). A part $\Phi_a(\lambda)$ of the incident power $\Phi_0(\lambda)$ is absorbed within the layer of water, another part $\Phi_b(\lambda)$ is scattered out from it in all directions. The remaining power $\Phi_t(\lambda)$ is transmitted through the layer with no change in direction. In the case of elastic scattering, energy is conserved so that:

$$\Phi_0(\lambda) = \Phi_a(\lambda) + \Phi_b(\lambda) + \Phi_t(\lambda) \tag{1.1}$$

The spectral absorption and scattering coefficients, $a(\lambda)$ and $b(\lambda)$, respectively, relate the absorbed and scattered power to the incident power when travelling through an infinitely thin layer of water of thickness dx (units: m^{-1}):

$$d\Phi_a(\lambda) = a(\lambda)\Phi_0(\lambda)dx \tag{1.2}$$

$$d\Phi_b(\lambda) = b(\lambda)\Phi_0(\lambda)dx \tag{1.3}$$

The sum of these coefficients gives the beam attenuation coefficient $c(\lambda)$ (units: m^{-1}):

$$c(\lambda) = a(\lambda) + b(\lambda) \tag{1.4}$$

Let $d\Phi_c(\lambda) = d\Phi_a(\lambda) + d\Phi_b(\lambda)$ represent the loss of power by absorption and scattering when the beam passes through the thin layer, then:

$$d\Phi_c(\lambda) = c(\lambda)\Phi_0(\lambda)dx \tag{1.5}$$

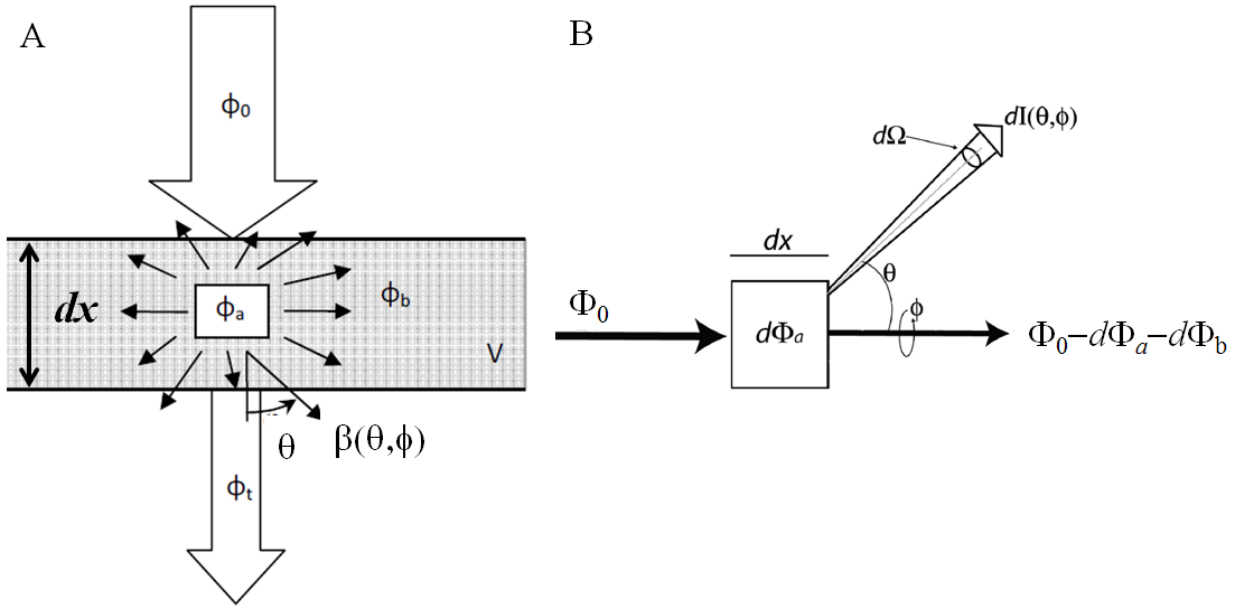

Figure 1.3. Schematical geometrical configurations used to define absorption, scattering, and attenuation coefficients. (A) Fluxes of light when passing through a volume of seawater (after Morel 2008), (B) The elementary volume of thickness d*x*, seen as a point source from which originates the scattered radiation in all directions (after Morel 2008 and Mobley 1994)

Consider the power $\Phi_b(\theta,\phi,\lambda)$ scattered out of the beam into a solid angle Ω in direction (θ,ϕ) represented by its nadir and azimuthal scattering angles θ and ϕ with respect to the direction of the incident beam (*see* Figure 1.3(B)). The intensity of light scattered by an infinitesimal volume in an infinitesimal solid angle $d\Omega$ containing (θ,ϕ), $dI(\theta,\phi,\lambda)$ (units: W sr^{-1} nm^{-1}), is $d\Phi_b(\theta,\phi,\lambda)/d\Omega$. Analogous to the definitions of $a(\lambda)$ and $b(\lambda)$, the scattered intensity is proportional to the incident power and the elementary thickness via the angular volume scattering function (VSF), $\beta(\theta,\phi,\lambda)$ (units: m^{-1} sr^{-1}):

$$dI(\theta,\varphi,\lambda) = \beta(\theta,\varphi,\lambda)\Phi_0(\lambda)dx \tag{1.6}$$

or

$$d^2\Phi_b(\theta,\varphi,\lambda) = \beta(\theta,\varphi,\lambda)\Phi_0(\lambda)dx\,d\Omega \tag{1.7}$$

The total power lost from the beam by elastic scattering is gained over all other directions and is thus obtained by integrating Eq. (1.7) over all solid angles:

$$d\Phi_b(\lambda) = \Phi_0(\lambda)dx\int_0^{4\pi}\beta(\theta,\varphi,\lambda)\,d\Omega \tag{1.8}$$

Combining with Eq. (1.3) gives the relationship between $b(\lambda)$ and $\beta(\theta,\phi,\lambda)$:

$$b(\lambda) = \int_0^{4\pi} \beta(\theta,\phi,\lambda)\, d\Omega = \int_0^{2\pi}\int_0^{\pi} \beta(\theta,\phi,\lambda) \sin\theta\, d\theta\, d\phi \qquad (1.9)$$

In natural waters, particles are assumed to be randomly oriented, so that:

$$b(\lambda) = 2\pi \int_0^{\pi} \beta(\theta,\lambda) \sin\theta\, d\theta \qquad (1.10)$$

Eq. (1.9) and (1.10) show that $b(\lambda)$ is an IOP obtained by integration of $\beta(\theta,\phi,\lambda)$ over all scattering directions θ and ϕ. Integration over the back directions, gives the backscattering coefficient:

$$b_b(\lambda) = 2\pi \int_{\pi/2}^{\pi} \beta(\theta,\lambda) \sin\theta\, d\theta \qquad (1.11)$$

This coefficient is of particular importance to remote sensing, as remote sensing reflectance is approximately proportional to $b_b/(a+b_b)$ (Gordon et al. 1988, *see* Eq. (1.27)). The ratio $\tilde{b}_b(\lambda) = b_b(\lambda)/b(\lambda)$ is referred to as the backscattering ratio or backscattering fraction. The quantity $\tilde{\beta}(\theta,\lambda) = \beta(\theta,\lambda)/b(\lambda)$ is the scattering phase function (units: sr^{-1}), which provides a convenient measure of the angular distribution of scattered intensity regardless of the overall magnitude of scattering. Note that integration of $\tilde{\beta}(\theta,\lambda)$ over back directions yields $\tilde{b}_b(\lambda)$.

1.2.1.2 PARTITIONING OF IOPS

IOPs are additive, meaning that for a seawater sample containing a mixture of constituents, the absorption and scattering coefficients of the various constituents are independent, and the total coefficient is obtained from summation of all constituents. Bulk IOPs are the sum of the IOPs for pure seawater itself and all its individual constituents. In practice, components are grouped based on operational or functional criteria. As described previously, two general categories of seawater constituents have been considered, DOM and SPM, giving the following partitioning of a and b_b:

$$a(\lambda) = a_w(\lambda) + a_{DOM}(\lambda) + a_p(\lambda) \qquad (1.12)$$

$$b_b(\lambda) = b_{bw}(\lambda) + b_{bp}(\lambda) \qquad (1.13)$$

where the *w*, *DOM*, and *p* subscripts denote the contributions from pure seawater, DOM, and SPM, respectively. Eq. (1.13) can be written analogously for b. The absorption by particulate material is commonly separated further into phytoplankton (ph subscript) and non-algal particles (NAP subscript) because these are spectrally very different. An illustration of spectral variability of absorption and backscattering for each component is shown in Figure 1.4 and the resulting above-water remote sensing reflectance (after Eq.(1.21)) is also shown. Input concentrations typical for southern North Sea coastal

waters were taken: [NAP]=10 g m^{-3} , a_{DOM}(443nm)=0.01 m^{-1} , and Chl a=1 mg m^{-3} . The IOPs of pure seawater are considered known at visible wavelengths (Morel 1974; Pope and Fry 1997, *see* Figure 1.4), where the backscattering coefficient is half of the total scattering coefficient.

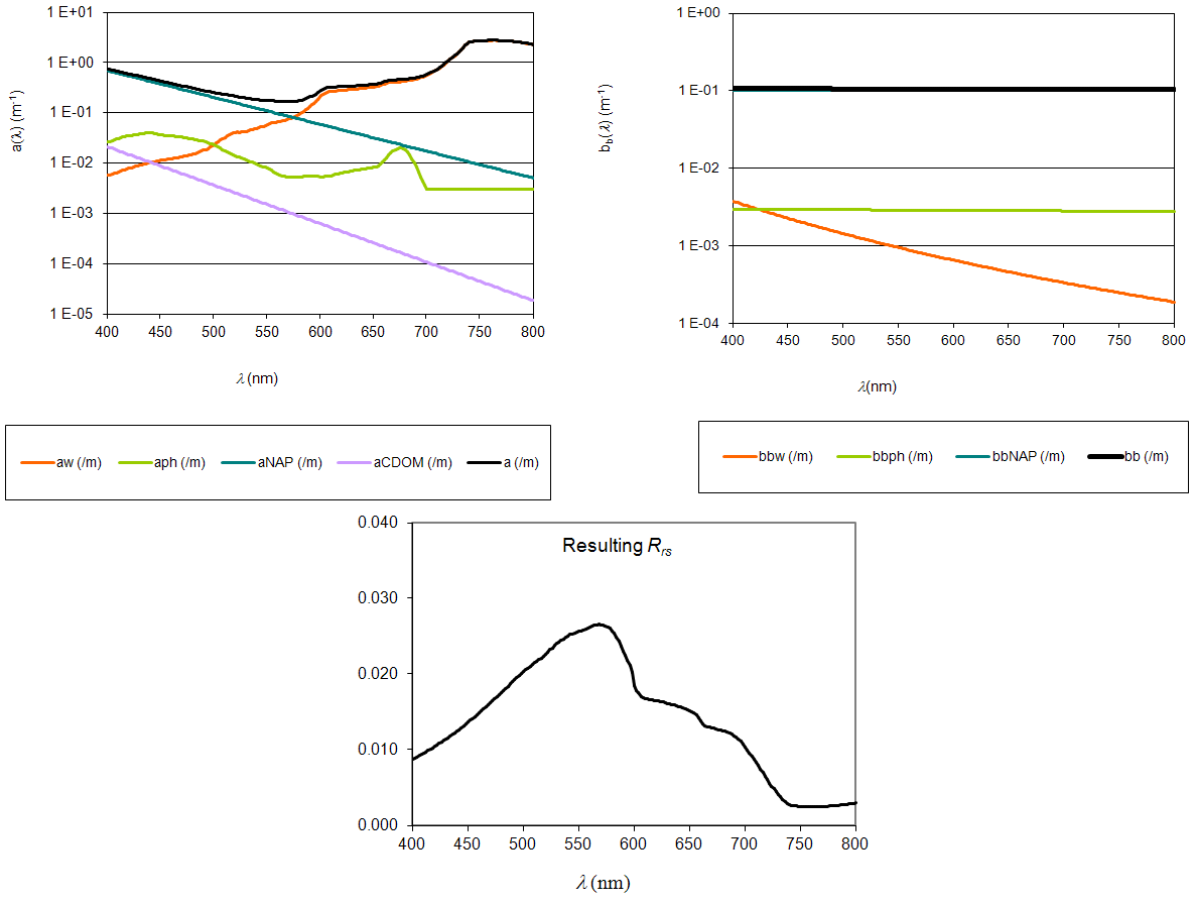

Figure 1.4. (top) Spectral absorption and backscattering coefficients of pure seawater, phytoplankton, non-algal particles, and DOM (denoted by 'w', 'ph', 'NAP' and 'CDOM', respectively). Pure water absorption and scattering after Morel 1974; Pope and Fry 1997, respectively. (bottom) the resulting remote sensing reflectance computed from Eq. (1.21).

1.2.1.3 CONCENTRATION-SPECIFIC IOPS

To first order, IOPs vary with the concentration of seawater constituents. In the case of particles, the most widely used parameter for concentration is the dry weight concentration, [SPM], expressed in mg L^{-1} or g m^{-3}. Concentration-specific IOPs, i.e. IOPs normalized by the constituent concentration, typically are less variable than absolute IOPs, responding to changes in the characteristics of the material in a given category. IOPs may be decomposed into concentration-specific IOPs as follows:

$$a(\lambda) = a_w(\lambda) + C_{DOM} a^*_{DOM}(\lambda) + C_p a^m_p(\lambda) \tag{1.14}$$

$$b_b(\lambda) = b_{bw}(\lambda) + C_p b^m_{bp}(\lambda) \tag{1.15}$$

where *C* denotes the concentration of the constituents, and the *m* superscript denotes the mass-specific particulate IOPs. Note that Eq. (1.15) assumes that dissolved substances do not contribute significantly to the bulk scattering and backscattering coefficients. Pure seawater absorbs and scatters light, but is not an important source of IOP variability in natural waters, although there is some small variability at certain wavelengths associated with temperature and salinity variations (Pegau et al. 1997; Zhang et al. 2009).

1.2.2 Apparent optical properties (AOPs)

AOPs, such as the variously defined reflectances, depend strongly enough on the IOPs that they can be characteristic of a water body and its constituents, but light field geometry must also be taken into account to completely explain their variability. AOPs are determined from measurements of radiometric quantities such as downwelling or upwelling plane irradiance, and upwelling radiance.

When describing the radiant field inside a scattering and absorbing medium, radiance is the fundamental radiometric quantity. The geometry of the light field is shown in Figure 1.5A. Spectral radiance is defined as the power or flux in a specified direction (θ,ϕ) per unit solid angle, Ω, per unit area, *A*, and per wavelength interval, $d\lambda$, or intensity per unit area, per unit wavelength interval (units: W m^{-2} sr^{-1} nm^{-1}):

$$L(\theta,\phi,\lambda) = \frac{d^2\Phi(\lambda)}{dA d\Omega d\lambda} = \frac{dI(\lambda)}{dA d\lambda} \tag{1.16}$$

The downwelling spectral irradiance on a horizontal plane at depth *z*, $E_d(\lambda, z)$, is the integral of all spectral radiances $L(\theta,\phi,\lambda)$ at depth *z* headed downward from the upper hemisphere weighted by the cosine of the incidence angle (*see* Figure 1.5B) (units: W m^{-2} nm^{-1}):

$$E_d(\lambda, z) = \int_0^{2\pi} \int_0^{\pi/2} L(\theta,\phi,\lambda,z) \cos\theta \sin\theta \, d\theta \, d\phi \tag{1.17}$$

Similarly, an upward spectral irradiance can be defined, $E_u(\lambda, z)$, involving an integration over the lower hemisphere:

$$E_u(\lambda, z) = \int_0^{2\pi} \int_{\pi/2}^{\pi} L(\theta,\phi,\lambda,z) \left|\cos\theta\right| \sin\theta \, d\theta \, d\phi \tag{1.18}$$

The total spectral scalar irradiance, $E_0(\lambda, z)$ defined as (units: W m^{-2} nm^{-1}):

$$E_0(\lambda,z)=\int_0^{2\pi}\int_0^{\pi} L(\theta,\phi,\lambda,z)\sin\theta\, d\theta\, d\phi \tag{1.19}$$

expresses the total radiant power incident from all directions on a infinitesimal sphere (it is also called 'flux density'). It is important to note the different angular weightings applied to the planar (downward/upward) irradiances, $E_d(\lambda,z)$ and $E_u(\lambda,z)$, and the spherical (scalar) irradiance, $E_0(\lambda,z)$. These definitions imply the use of different measurement geometries for instruments, respectively flat "cosine" collectors for $E_d(\lambda,z)$ and $E_u(\lambda,z)$, and spherical collectors for $E_0(\lambda,z)$.

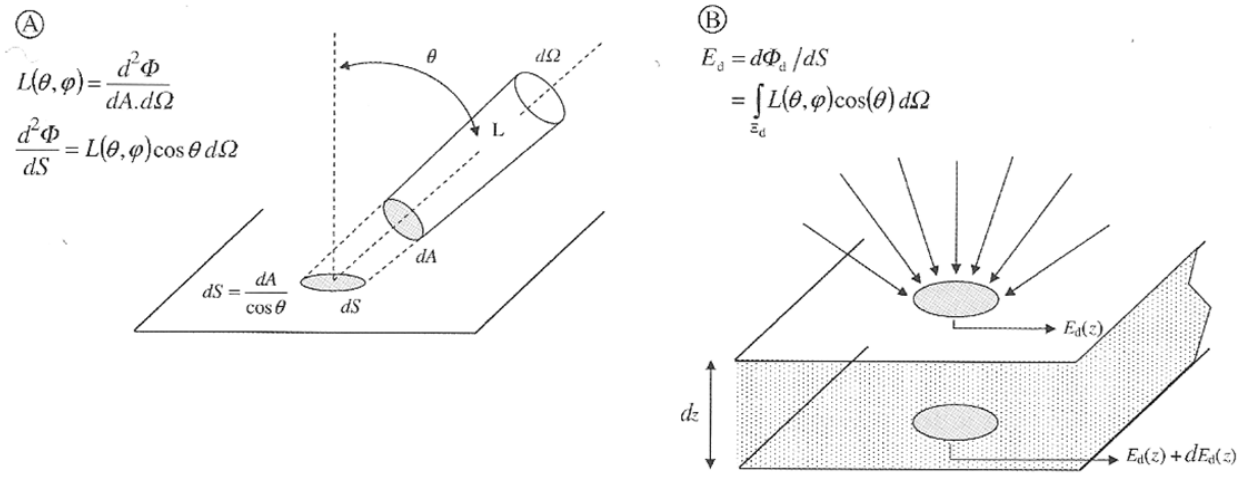

Figure 1.5. Geometrical configuration used for defining radiance (A), plane irradiance (B), and the coefficient for downwelling irradiance, K_d (B) (source: Morel 2008).

1.2.2.1 REFLECTANCES

The irradiance reflectance is a dimensionless quantity defined as the ratio of the upward to the downward spectral irradiance at depth *z*:

$$R(\lambda,z)=\frac{E_u(\lambda,z)}{E_d(\lambda,z)} \tag{1.20}$$

Ocean colour is defined by spectral variations in irradiance reflectance just below the sea surface, *z*='0-'. $R(\lambda,0-)$ describes the capacity of seawater to return radiation towards the atmosphere. In the context of remote sensing, it is common to deal with remote sensing reflectance, R_{rs} (units: sr^{-1}), which is closely related to $R(\lambda)$, but makes use of upwelling radiance rather than irradiance, and is defined just above the air-sea interface (*z*='0+') as:

$$R_{rs}(\theta,\phi,\lambda,0+) = \frac{L_w(\theta,\phi,\lambda,0+)}{E_d(\lambda,0+)} \tag{1.21}$$

where $L_w(\theta,\phi,\lambda,0+)$ is a radiance scattered from the ocean interior and leaving the ocean in a direction (θ,ϕ) and $E_d(\lambda,0+)$ is the downward irradiance just above the surface. In other words, R_{rs} decomposes R into its component radiances as a function of the viewing angles θ and ϕ. R_{rs} is a measure of how much of the downwelling light that is incident onto the water surface is eventually returned through the surface in direction (θ,ϕ), so that it can be detected by a radiometer pointed in the opposite direction. Superscripts 0+ or 0- are commonly used to indicate above-water or subsurface, respectively.

The marine reflectance or water-leaving reflectance, $\rho_w^{0+}(\lambda) = \pi R_{rs}(\lambda)$, is also frequently used. In turbid water remote-sensing applications, the angular dependence of R_{rs} is often ignored.

1.2.2.2 DIFFUSE ATTENUATION COEFFICIENTS

The vertical attenuation of irradiance in the water column is typically approximately exponential:

$$E_d(\lambda,z) = E_d(\lambda,0-)\exp\left(-\int_0^z K_d(\lambda,z')dz'\right) \tag{1.22}$$

The spectral diffuse attenuation coefficient for downwelling irradiance at depth z, $K_d(\lambda,z)$, defines the rate of decrease of downwelling irradiance at a given depth z. See Figure 1.5B for light field geometry. Solving Eq. (1.22) for $K_d(\lambda,z)$ gives:

$$K_d(\lambda,z)dz = -\frac{dE_d(\lambda,z)}{E_d(\lambda,z)} = -d\ln E_d(\lambda,z) \tag{1.23}$$

This coefficient is used in models of light penetration, for example to compute primary production as a function of light availability at depth (Behrenfeld and Falkowski 1997) and is also often used as an index of water clarity (Stumpf et al. 1999; Woodruff et al. 1999).

The most commonly used parameter in ecological studies is the diffuse attenuation coefficient of photosynthetically available radiation (PAR) at depth z, $K_{\mathrm{PAR}}(z)$. PAR is a broad band (350-700 nm), spectrally integrated flux of quanta per unit time at depth z (units: photons s^{-1} m^{-2}):

$$\mathrm{PAR}(z) = \int_{350nm}^{700nm} \frac{\lambda}{hc} E_0(\lambda,z)d\lambda \tag{1.24}$$

where *h* is Plank's constant , *c* is the speed of light in vacuum, and E_0 is the spectral scalar irradiance defined in (1.19). Defining $\overline{K}_{\mathrm{PAR}}(z)$ as the vertically averaged $K_{\mathrm{PAR}}(z)$ between the surface and depth z:

$$\overline{K}_{\mathrm{PAR}}(z) = \frac{1}{z}\int_0^z K_{PAR}(z')dz' = -\frac{\ln \mathrm{PAR}(z) - \ln \mathrm{PAR}(0-)}{z} \tag{1.25}$$

Eq. (1.22) can be rewritten:

$$\mathrm{PAR}(z) = \mathrm{PAR}(0-)\exp\left(-\overline{K}_{\mathrm{PAR}}(z)z\right) \tag{1.26}$$

In vertically well-mixed waters $\overline{K}_{\mathrm{PAR}}(z)$ is commonly assumed to be only weakly depth dependent (Rochford et al. 2001; Rasmus et al. 2004; Carter et al. 2005) and the $\overline{K}_{\mathrm{PAR}}(z)$ is usually calculated within the euphotic zone, where $\mathrm{PAR}(z)$ falls down to 1% of its subsurface value. Several studies have, however, demonstrated significant depth dependence of $K_{\mathrm{PAR}}(z)$ (Morel 1988; Lee et al. 2005; Lee 2009) even in well-mixed water columns because of vertical variation in the angular and/or spectral distribution of radiance.

1.2.3 Link between IOPs and AOPs

The radiative transfer equation describes the propagation of light (radiance) through seawater characterized by its IOPs. This equation has no analytical solutions, but approximate numerical solutions can be computed, for example with the commercial Hydrolight software package (Mobley 1994).

Simplified analytical models link IOPs to AOPs, such as the simplified reflectance model based on a first order version of the model of Gordon et al. 1988:

$$r_{rs}(\lambda) = \frac{f'}{Q}\frac{b_b(\lambda)}{a(\lambda)+b_b(\lambda)} \tag{1.27}$$

where r_{rs} is the subsurface remote sensing reflectance:

$$r_{rs}(\lambda) = \frac{L_w(\theta,\phi,\lambda,0-)}{E_d(\lambda,0-)} \tag{1.28}$$

f' is a varying dimensionless factor (Morel and Gentili 1991) and Q is the ratio of subsurface upwelling irradiance to the subsurface upwelling radiance in the viewing direction. The subsurface reflectance can be related to the marine reflectance and to the remote sensing reflectance by:

$$\rho_w^{0+}(\lambda) = \pi\Re r_{rs}(\lambda) = \pi R_{rs}(\lambda) \tag{1.29}$$

where $\Re$ represents reflection and refraction effects at the sea surface (Morel and Gentili 1996). A typical value of $f'/Q = 0.13$ for sediment-dominated waters (Loisel and Morel 2001) and $\Re$ =0.529 (Morel and Gentili 1996).

An approximation of subsurface K_d to IOPs based on empirical work and Monte Carlo simulations (Gordon 1989) gives:

$$K_d(\lambda,0-) = 1.04\frac{a(\lambda)+b_b(\lambda)}{\mu_d} \tag{1.30}$$

where μ_d is the average cosine of the downwelling light just beneath the surface. Morel and Loisel 1998 empirically modeled K_d of the euphotic zone as function of *a* and *b*:

$$\overline{K}_d(\lambda) = \frac{a(\lambda)}{\mu_d}\left(1+G(\mu_d)\frac{b(\lambda)}{a(\lambda)}\right)^{1/2} \tag{1.31}$$

Where $G(\mu_d)$ is a model parameter which varies with μ_d and the VSF of the water medium.

1.3 Measuring optical properties

1.3.1 IOPs

1.3.1.1 BEAM ATTENUATION

Beam attenuation, $c(\lambda)$, can be obtained by measuring the loss of power of an unpolarized collimated monochromatic light beam with incident power $\Phi_0(\lambda)$ over a finite distance *l* within a homogeneous medium. The remaining (transmitted) flux at distance *l*, $\Phi_l(\lambda)$, relates to $c(\lambda)$ via integration of Eq. (1.5) between 0 and *l*:

$$\Phi_l(\lambda) = \Phi_0(\lambda)\exp\left(-c(\lambda)l\right) \tag{1.32}$$

and thus:

$$c(\lambda) = \frac{-1}{l}\ln\left(\frac{\Phi_l(\lambda)}{\Phi_0(\lambda)}\right) \tag{1.33}$$

This is the principle by which *c* meters, also called beam attenuation meters or transmissometers, function. Transmissometers have been routinely used since the 1970's, although with different characterisations, such as wavelength of the source beam, beam width, instrument path length, *l*, detector design etc. The path length should be such that multiple scattering in the measuring volume is negligible, but large enough so that attenuation is detectable (e.g., a 5 cm path length in turbid coastal waters and a 25 cm path length in clear oceanic waters).

The measurement of the transmitted flux $\Phi_t(\lambda)$ requires the use of collimating optics to exclude light scattered in the near-forward direction, which is significant since the VSF of particles is strongly forward peaked. Ideally, the transmissometer should have an acceptance angle for scattered light of 0°, but this cannot be achieved in practice while allowing transmitted light to be detected. Consequently, all transmissometers accept some near-forward scattered light with measured attenuation $c_m(\lambda)$, related to the true $c(\lambda)$:

$$c_m(\lambda) = c(\lambda) - 2\pi \int_0^{\theta_a} \beta(\theta, \lambda) \sin\theta \, d\theta \tag{1.34}$$

where the error term is dependent on the acceptance angle of the instrument θ_a and on the VSF (Boss et al. 2009b). Most transmissometers have in-water θ_a between 0.01° and 1.2°. Since the VSF is strongly forward peaked for larger particles, the error term increases with increasing particle size for a given θ_a , as shown by Figure 1.7 from Boss et al. 2009b.

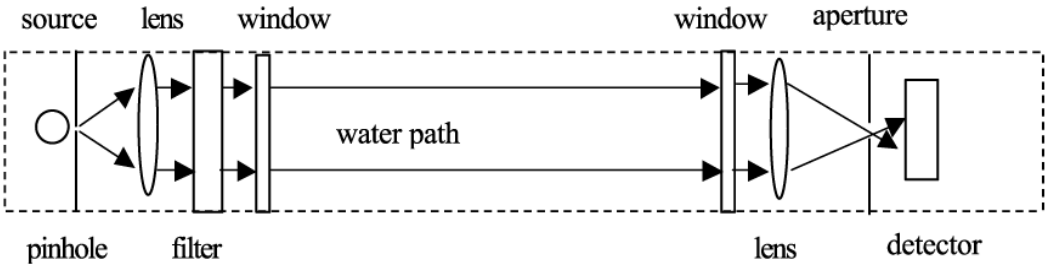

Figure 1.6. Typical transmissometer design (source: Pegau et al. 2003).

Transmissometers are usually operated near λ=660nm where absorption by dissolved substances a_{DOM} is negligible so that after Eqs. (1.12) and (1.13):

$$c(660) = c_w(660) + c_p(660) \tag{1.35}$$

Transmissometers are blanked with ultrapure Milli-Q water so that the particulate beam attenuation coefficient, c_p, can be directly measured.

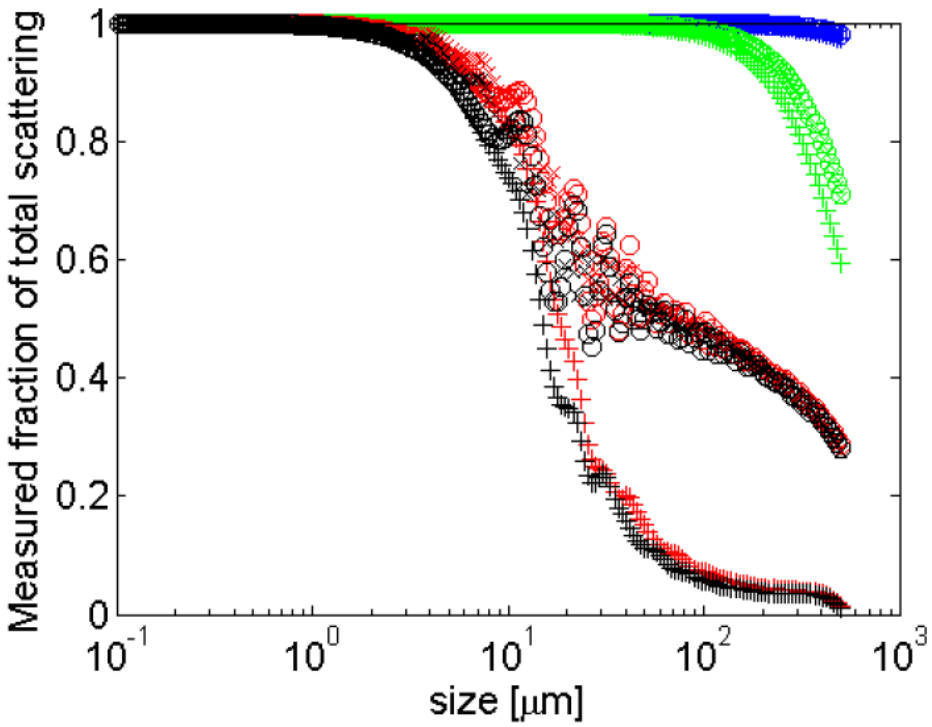

Fig. 2. Ratio of scattering coefficients based on integrating the VSF (β) from π to the acceptance angle to the total scattering coefficient for homogeneous spheres with three different indices of refraction (n=1.05+i0.005 (+), n=1.05+i0.0001 (o), 1.15+i0.0001 (x)) and four different acceptance angles matching those of the instruments we compare in this paper (1.2°-black, 0.93°-red, 0.026°-green, and 0.006°- blue, Table 1) as function of size.

Figure 1.7. Source: Boss et al. 2009b (instruments compared in his paper are the WET Labs C-Star, WET Labs ac-9, LISST 100-B, and LISST-100X-FLOC)

1.3.1.2 COMBINED MEASUREMENTS OF ABSORPTION AND ATTENUATION

The development of multi-wavelength and hyperspectral combination *a* and *c* meters in the mid 1990s (Moore et al. 1992; Pegau et al. 1995) led to significant advancements in the measurement of IOPs. The most widely used instruments are the WET Labs ac-9 (9 wavelengths) and ac-s (hyperspectral), where $a(\lambda)$ is determined based on the reflective tube principle (Zaneveld et al. 1990; Kirk 1992). Instrument design is similar to transmissometer design, except that the configuration is optimized to collect as much scattered light as possible, allowing measurement of $\Phi_0(\lambda)$-$\Phi_a(\lambda)$. The optical path is surrounded by a quartz reflective tube, reflecting forward scattered light back into the sampling path. For natural particle suspensions the majority of light is scattered forward, but a small amount of light will be lost by backscattering or imperfect reflection at the walls, and needs to be accounted for (Sullivan et al. 2006) in order not to overestimate $a(\lambda)$. Additional corrections for the dependency of $a(\lambda)$ on temperature and

salinity are needed (Pegau et al. 1997). Measurement uncertainties of optical properties using the ac-9 instrument have been reported by Leymarie et al. 2010.

The simultaneous $c(\lambda)$ and $a(\lambda)$ measurements are blanked to ultrapure Milli-Q water so that the combined attenuation and absorption due to dissolved and particulate matter are measured directly. The particulate scattering coefficient, $b_p(\lambda)$, can be derived from these by difference.

1.3.1.3 VOLUME SCATTERING FUNCTION AND BACKSCATTERING COEFFICIENTS

Measurement of the VSF over the full angular range (between 0° and 180°) involves making a large number of measurements at discrete angles, each covering a large dynamic range especially in the near-forward angles. Instruments satisfying these complex requirements have been developed (Petzold 1972; Lee and Lewis 2003; Sullivan and Twardowski 2009; Twardowski et al. 2012), but none are commercially available at present. Since the late 1990s, $b_b(\lambda)$ has been routinely determined from one or a couple of measurements of the VSF in the backward direction. Measurement of $\beta(\theta,\lambda)$ at a single angle θ_m>90° has been found to be significantly correlated to $b_b(\lambda)$ (Oishi 1990; Boss and Pegau 2001Oishi 1990; Maffione and Dana 1997) via a proportionality factor χ:

$$b_b(\lambda) = 2\pi\chi\beta(\theta_m,\lambda) \tag{1.36}$$

Errors are minimized to a few percent at θ_m between 117° en 120° (Oishi 1990; Boss and Pegau 2001) where χ is independent of the contribution of $\beta_w(\lambda)$ to $\beta(\lambda)$ (Boss and Pegau 2001). Removal of the variable contribution of $\beta_w(\lambda)$ to $\beta(\lambda)$ prior to conversion leads to more accurate results, especially in clear waters (Boss and Pegau 2001), hence:

$$b_b(\lambda) = 2\pi\chi_p\left(\beta(\theta_m,\lambda) - \beta_w(\theta_m,\lambda)\right) + b_{bw}(\lambda) \tag{1.37}$$

where χ_p is the proportionality factor between $\beta_p(\theta_m,\lambda)$ and $b_{bp}(\lambda)$ defined analogously to χ in Eq. (1.36). Values of $\beta_w(\theta_m,\lambda)$ and $b_{bw}(\lambda)$ for pure seawater from Zhang et al. (2009) are thought to be accurate within 2%. Empirically determined χ_p factors as a function of θ_m are reported by Sullivan and Twardowski 2009 and have lowest uncertainty of maximally 2% in the range 110°-120°. The WET Labs BB-9 and the HOBI Labs Hydroscat instruments are widely used multi-wavelength backscattering instruments based on a single angle measurement of $\beta(\theta,\lambda)$. In practice, the measured $\beta(\theta_m,\lambda)$ is the result of a weighted portion of $\beta(\theta,\lambda)$ in the vicinity of θ_m, described by an instrument geometry dependent angular weighting function W(θ):

$$\beta(\theta_m,\lambda) = \int_0^\pi \beta(\theta,\lambda)W(\theta)d\theta \tag{1.38}$$

The configuration of the WET Labs ECO BB-9 instrument, used in this study, and its angular weighting function is shown in Figure 1.8.

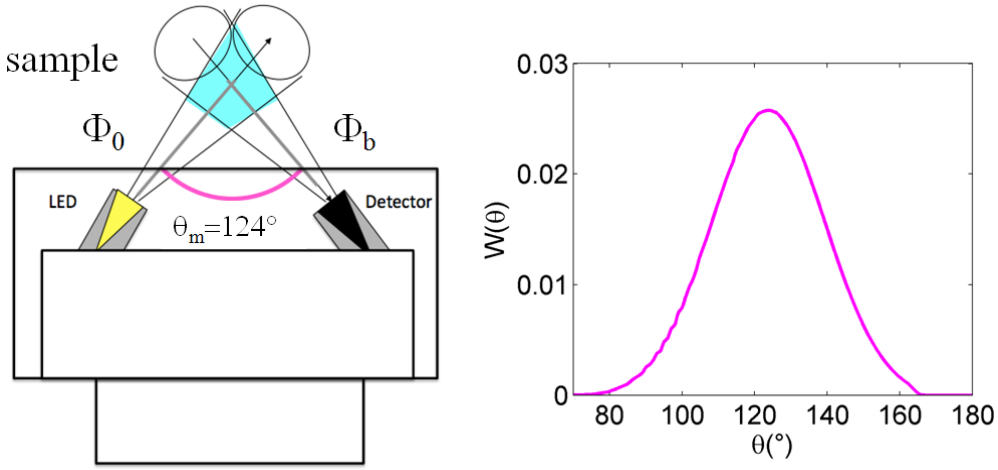

Figure 1.8. Schematic of a volume scattering measurement for the WET Labs ECO BB-9 instrument and its angular weighting function (centroid angle θ_m=124°).

1.3.1.4 TURBIDITY

Turbidity, defined by ISO 7027 (1999) as 'the reduction of transparency of a liquid caused by the presence of undissolved matter', can be determined either semi-quantitatively (e.g., Secchi disk, turbidity tube) or quantitatively using optical instrumentation (light attenuation and side scatter). Measurements of turbidity with Secchi disks or turbidity tubes have been registered for over a century and constitute a valuable historic archive. They are simple, but somewhat subjective and not very precise. Further analytical test methods for turbidity are given by EPA 1993 and APHA 1998.

Many instruments for quantitative measurement of turbidity (turbidimeters) compliant with the ISO 7027 requirements are commercially available in a variety of designs: portable (Orbeco-Hellige TB200, HF Scientific Micro 100, LaMotte 2020wi, Thermo Scientific Orion AQ4500), laboratory (Hanna HI 88713, HI 83414, HI 88703, Hach 2100AN), or submersible (Hydrolab 4-Beam turbidity sensor, Forest Technology Systems DTS-12, Greenspan sensors, ...). A complete overview of turbidity sensors and specifications is given by Andrews (USGS National Field Manual for the Collection of Water-Quality Data, Techniques of Water-Resources Investigations, Book 9) and can be found at http://water.usgs.gov/owq/turbidity_codes.xls.

Turbidity sensors have the advantage of being relatively inexpensive, compared to the instruments measuring IOPs in SI units. Measurements of turbidity may be expressed in Formazine Nephelometric Units (FNU), Nephelometric Turbidity Units (NTU), Formazin Turbidity Units (FTU), or

Nephelometric Turbidity Ratio Units (NTRU) etc., depending on the measurement method and the spectral characteristics of the incident light.

Even if two turbidity instruments of different design are calibrated with the same suspension of formazine, they will not give the same output in natural seawater because of their different configurations. Because turbidity measurements should always be interpreted with reference to the measurement (instrumentation) method and because some methods, particularly the EPA method based on a lamp with peak spectral response "between 400nm and 600nm", are imprecisely defined, the optics community has not been so enthusiastic about them. However, many scientists involved in water quality monitoring, particularly of inland waters, but also, more recently of marine waters (Nechad et al. 2009), consider turbidity as a key parameter, one that is explicitly required by the EU Marine Strategy Framework Directive.

The Hach 2100P portable turbidity instrument used in this work is an ISO compliant turbidity instrument. It measures the ratio of LED light scattered at an angle of 90° ±2.5° at a wavelength of 860 nm ±60 nm to forward transmitted light, as compared to the same ratio for a standard suspension of Formazine, which is supplied in sealed vials with long-term stability as a calibration reference. Turbidity recorded in this way (by nephelometry) is expressed in Formazine Nephelometric Units (FNU).

1.3.2 AOPs

AOPs are recorded by optical radiometers which collect a spectral radiant flux, either a radiance, *L*, or an irradiance, *E*. Methods for marine optical radiometry can be roughly separated in above-water and in-water systems. In-water systems can provide a characterization of the radiometric properties of the water column through radiance and irradiance measurements from a variety of configurations and deployment gears, such as profilers or buoys. Vertical irradiance profiles allow the derivation of $K_d(\lambda, z)$ after Eq. (1.23). Derivation of $L_w^{0+}(\lambda)$, however, requires the extrapolation of in-water radiometric measurements from below the sea surface to above the sea surface, which is a significant source of uncertainty, particularly in high attenuation, turbid waters and for red and NIR wavelengths. In this work, above-water radiometry was used to determine above-water reflectance.

1.3.2.1 ABOVE-WATER RADIOMETRY

Above-water radiometry allows to determine $\rho_w^{0+}(\lambda)$ from simultaneous above-water measurements of downwelling irradiance, $E_d^{0+}(\lambda)$, total upwelling radiance (i.e., from the water and from the air-sea

interface) at a zenith angle of 40°, $L_{sea}^{0+}(\lambda)$, and sky radiance, $L_{sky}^{0+}(\lambda)$, in the direction of the region of sky that reflects into the sea-viewing sensor as follows:

$$\rho_w^{0+}(\lambda) = \pi \frac{L_{sea}^{0+}(\lambda) - \rho_{sky} L_{sky}^{0+}(\lambda)}{E_d^{0+}(\lambda)} \tag{1.39}$$

where ρ_{sky} is the air-water interface reflection coefficient for radiance equal to the Fresnel reflection coefficient in the case of a flat sea surface (Mueller et al. 2000). The ρ_{sky} coefficient is expected to vary strongly with wind speed for clear sky conditions because of reflection of brighter parts of the sky in the case of higher waves (Mobley 1999), but is approximately independent of wind speed for cloudy conditions, giving (Ruddick et al. 2006):

$$\rho_{sky} = \begin{cases} 0.0256 + 0.00039W + 0.000034W^2 & \text{for } \dfrac{L_{sky}^{0+}(750)}{E_d^{0+}(750)} < 0.05 \\ 0.0256 \text{ for } \dfrac{L_{sky}^{0+}(750)}{E_d^{0+}(750)} \geq 0.05 \end{cases} \tag{1.40}$$

The accuracy of the $\rho_w^{0+}(\lambda)$ measurement depends heavily on the capability of correcting for air-sea interface reflections.

In this work, three TriOS-RAMSES hyperspectral radiometers were simultaneously deployed to record $E_d^{0+}(\lambda)$, $L_{sea}^{0+}(\lambda)$, and $L_{sky}^{0+}(\lambda)$ over the wavelength range of 350–950 nm at 2.5 nm resolution. The radiometers were mounted on a steel frame as shown in Figure 1.9. Zenith angles of the sea- and sky-viewing radiance sensors were 40°. The frame was fixed to the prow of the ship, facing forward to minimize ship shadow and reflection (Hooker and Morel 2003). The ship was maneuvered on station to point the radiance sensors at a relative azimuth angle of 135° away from the sun, as shown in Figure 1.9. The reader is referred to Ruddick et al. 2006, including the Web Appendices, for details on measurement protocol and data treatment.

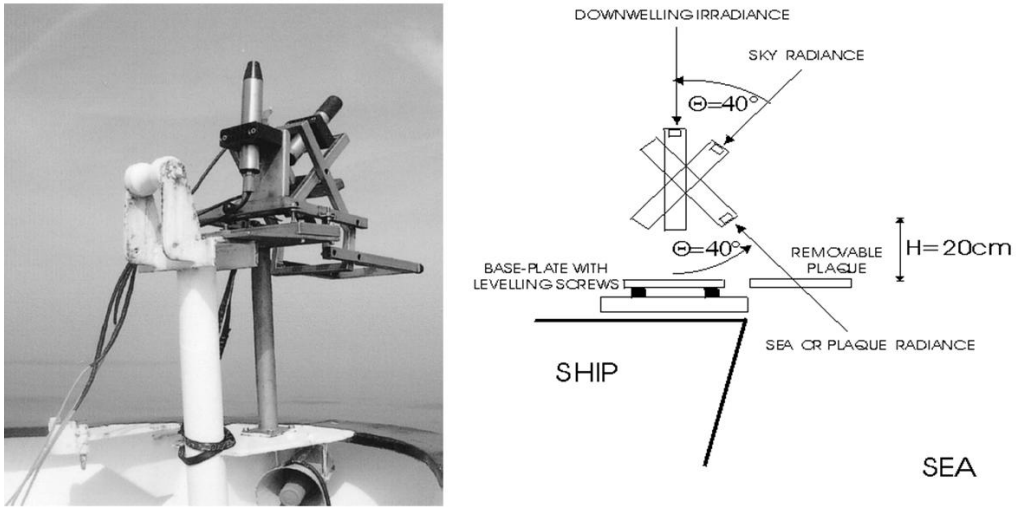

Figure 1.9. (left) Frame with three Trios-RAMSES hyperspectral radiometers, installed on the prow of a research vessel. (right) Details of measurement configuration.

Chapter 2 TURBIDITY MEASUREMENTS TO OPTIMIZE MEASUREMENTS OF SUSPENDED PARTICULATE MATTER CONCENTRATION

This chapter is in preparation for submission to Limnology and Oceanography Methods

Abstract

The dry weight concentration of suspended particulate material, [SPM] (units: mg L^{-1}), is measured by passing a known volume of seawater through a pre-weighed filter and re-weighing the filter after drying. This is apparently a simple procedure, but accuracy and precision of [SPM] measurements vary widely depending on the measurement protocol and the experience and skills of the person filtering. We show that measurements of turbidity, *T* (units: FNU), which are low cost, simple, and fast, can be used to (i) optimally set the filtration volume, (ii) to detect problems with the mixing of the sample during subsampling for filtration, and (iii) to quality control [SPM] data. A relationship between *T* and 'optimal filtration volume', V_{opt}, the volume at which enough matter is retained by the filter for precise measurement, but not so much that the filter clogs, is set-up. This relationship is based on an assessment of procedural uncertainties in the [SPM] measurement, including salt retention, filter preparation, weighing, and handling in the laboratory and at sea and on a value for minimum relative precision between replicates. The role of filtration volume on the precision of [SPM] measurement is investigated by filtering volumes of seawater ranging between one fifth and twice the optimal volume. It is shown that [SPM] measurements are most precise (with increases by up to 20%) and cost effective when the optimal volume is filtered. The 90% prediction bounds of the *T* vs. [SPM] regression allow to quality control [SPM].

2.1 Introduction

Suspended particulate matter (SPM) is operationally defined via filtration of seawater as the material retained on a certain type of filter with certain pore size, while the matter that passes through a small pore size filter is defined as dissolved matter (DM). For DM, typically a polycarbonate membrane filter with a 0.2 μm nominal pore size is used, while for SPM GF/F glass fiber filters with a nominal pore size of 0.7 μm are commonly used (ISO 1997; van der Linde 1998; Tilstone et al. 2003), although 0.4 μm pore size

polycarbonate filters may also be used (Strickland and Parsons 1968; Mueller et al. 2003). SPM may also be referred to as total suspended solids (TSS), total suspended matter (TSM), or total particulate matter (TPM) and includes both organic (autotrophic organisms, heterotrophic bacteria, and detritus) and mineral particles. The term 'total' may be misleading, however, since very small particles pass through the filter and their dry weight is not included. We therefore adopted the symbol SPM. The dry weight concentration of SPM, [SPM] in units of mg L^{-1} or g m^{-3}, is determined gravimetrically by passing a known volume of seawater through a pre-weighed filter. The filter is then reweighed after drying and [SPM] is calculated from the ratio of the difference in filter weight by the volume of the filtrate. Protocols for [SPM] measurement vary widely in procedures for filter preparation and treatment, including washing, drying, and ashing, and washing of sea salt after filtration. Also, while the measurement of [SPM] is apparently a simple procedure, accuracy and precision of the measurements vary widely depending on the measurement protocol (materials used, filter preparation and treatment, laboratory conditions etc.) and the experience and skills of the person filtering.

Because [SPM] is defined by operation, many measurement protocol specifications have been evaluated previously. The retention of salts by glass fiber filters leading to overestimation of [SPM] has gained considerable attention, and washing of filters and filter edges with deionized water (or milliQ water) after filtration have been proposed to remove sea salt (Strickland and Parsons 1968; van der Linde 1998). Different wash volumes have been recommended, varying between 30 mL (Pearlman et al. 1995) and 250 mL (Sheldon 1972). Despite a milliQ wash of 300 mL, Stavn et al. 2009 found salt retention by GF/F filters to vary between 0.6 mg and 1.1 mg with increasing salinity from 15 to 34 PSU (Practical Salinity Units, *see* their Figure 1) and irrespective of filtration volume. The loss of organic cellular material through cell-wall rupture by osmotic gradient after rinsing with milliQ is considered to be less important (van der Linde 1998), especially when SPM is mainly inorganic, although some protocols state that the rinsing should be done with 10-20 mL of isotonic ammonium formate solution instead (ICES 2004; PML and ICES 2004). The vacuum pressure under which filtration takes place was not found to affect the mass retention by the filters (Sheldon 1972), even though delicate particles might break when the pressure is too high. A pressure of 300-400 mm Hg is recommended (Stavn et al. 2009). The effective pore diameter of glass fiber or polycarbonate filters is known to decrease from the nominal value with increasing filtration volume until the filter is clogged (Sheldon 1972; Sheldon and Sutcliffe 1969). For example, GF/F glass fiber filters with a nominal pore size of 0.7 μm can effectively retain particles as small as 0.4 μm in diameter.

The filtration volume should be such that the mass retained by the filter is sufficient to be precisely measured, but not so much that the filter clogs. Despite its importance, the estimation of filtration volume is somewhat arbitrary and depends on the experience of the person carrying out the

filtration. In this study we investigate how low cost, simple, and fast measurements of turbidity, which is a good proxy for [SPM] (Boss et al. 2009c; Neukermans et al. 2012), can be used to estimate filtration volume. We further investigate [SPM] measurement uncertainties associated with filter preparation and treatment, salt retention, and filtration volume.

2.2 Materials and methods

2.2.1 Measurement of [SPM]

2.2.1.1 MEASUREMENT PROTOCOL

[SPM] is determined gravimetrically following the protocol of Tilstone et al. 2003, based on van der Linde 1998, by filtration of a known volume of sea water onto 47 mm Whatman GFF glass fiber filters with a nominal pore size of 0.7 μm. The filters were pre-ashed at 450 °C for 1 h (see step 1 in the flowchart in Figure 2.1), gently washed in 0.5 L of MilliQ water (2) to remove friable fractions that can be dislodged during filtration, dried at 75 °C for 1 h (3), pre-weighed on a Sartorius LE 2445 analytical balance with an accuracy of 0.1 mg (4), stored in a desiccator for use within two weeks (5), and transferred to clean 50 mm diameter petri plates for transport.

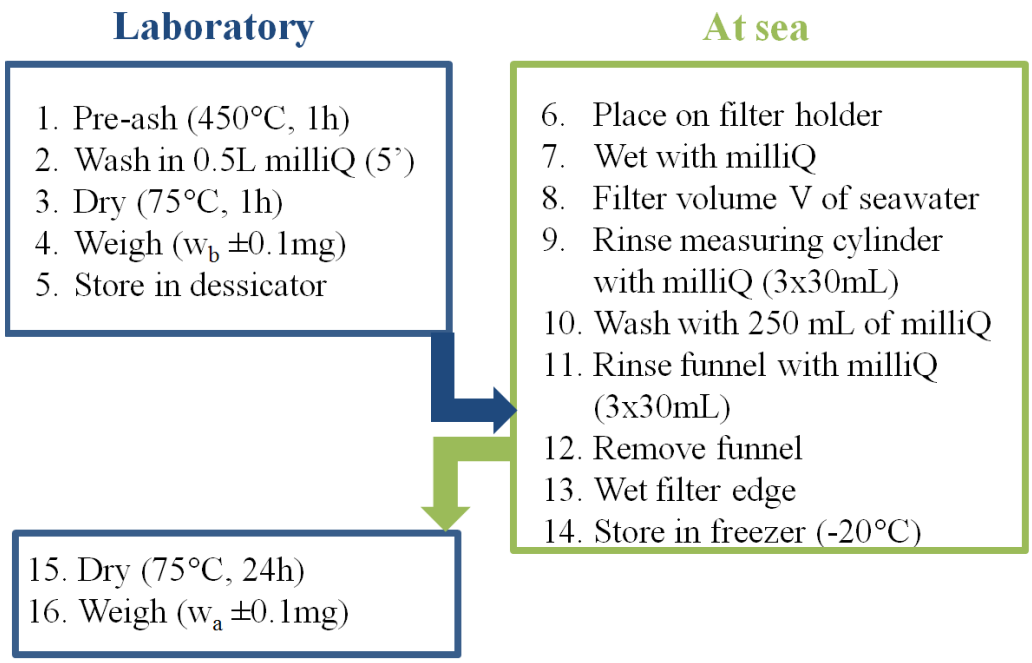

Figure 2.1. Procedural flow for the measurement of [SPM] of seawater.

Seawater samples were filtered immediately after collection on triplicate ashed and pre-weighed filters using a 250 mL Millipore apparatus with an applied vacuum of 300-400 mm Hg. Filter supports were washed before filtration with milliQ to remove any particles that had adhered to the glass. After placement on the fritted glass filter supports (6), filters were wetted with milliQ (7) and a known volume of seawater, *V*, was passed through the filter (8). The measuring cylinder was rinsed with 3 x 30 mL aliquots of milliQ water to flush any remaining particles (9). To remove salt, filters were washed with 250 mL of milliQ water after filtration (10). The filter funnel was also rinsed with 3 x 30 mL aliquots of milliQ water (11). After removal of the funnel, the filter edge was carefully washed with milliQ to flush possible diffused salt (13, Strickland and Parsons 1968). The total milliQ wash volume per filter is 400-450 mL, much larger than recommended by Sheldon 1972, 300 mL, Trees 1978, 50 mL, and Pearlman et al. 1995, 30 mL. The samples were stored at -20°C until further analysis in MUMM's Marine Chemistry Laboratory (14), usually within a few months after sampling. Filters were dried for 24 h at 75 °C (15) and re-weighed on the same balance (16) to obtain [SPM] (=$(w_a - w_b)$: *V*).

2.2.1.2 FILTER BLANKS

At the start and the end of each sampling campaign, a series of filter blanks or procedural control filters were included, to assess uncertainties associated with filter operations in the laboratory and during filtrations. For blank measurements, either synthetic seawater (SSW), prepared by dissolving 34 g of NaCl in 10 L of milliQ water, or milliQ water were used. An overview of various types of filter blanks and their operations is given in Table 2.1. The milliQ and SSW filter blanks were treated exactly as the sample filters (steps 1-16 in Figure 2.1) except that 250 mL of milliQ or 500 mL of SSW was passed through the filter instead of a volume *V* of sampled seawater (step 8). No liquid was passed through the dry filter blanks, which were subjected only to freezing (step 14) before further analysis in the lab. A one-way analysis of variance (ANOVA) was carried out to test for differences between blanks (*see* section 2.2.5 for details).

Table 2.1. Overview of types of [SPM] procedural control filters and treatments.

filter	**filter operations (numbers as in** Figure 2.1**)**	**volume filtered**	**n**	**sampled**
dry blank	1-5, 14, 15-16	NA*	87	2008-2010
milliQ blank	1-16, replacing samples with milliQ water in step 8	250 mL	96	2008-2010
SSW blank	1-16, replacing samples with SSW water in step 8	500 mL	126	2007-2010
sample	1-16	variable	366	2007-2010

*: not applicable

2.2.1.3 SALT RETENTION TESTS

A laboratory experiment was carried out to test whether salts diffused onto the rim of the filter were properly flushed by the rim rinsing procedure (step 13 in Figure 2.1). First, all steps of the procedure in Figure 2.1 were carried out filtering a volume of 250 mL SSW onto 10 replicate filters. Next, all steps except the rim rinsing (step 13) were carried out filtering a volume of 250 mL SSW onto another set of 10 filters. Differences between groups were then tested statistically as described in section 2.2.5.

To test whether a wash volume of 400-450 mL was sufficient to flush salts irrespective of sample volume, different volumes of SSW ranging between 150 and 2000 mL were filtered according to the procedure in Figure 2.1. Differences in $w_a - w_b$ between SSW volume groups were tested statistically as described in section 2.2.5.

2.2.2 Turbidity measurements

Turbidity, *T*, defined by ISO 1999 as 'the reduction of transparency of a liquid caused by the presence of undissolved matter', can be quantified in various ways (e.g., Secchi disk, light attenuation, side scatter). The Hach 2100P portable turbidity instrument measures the ratio of LED light scattered at an angle of 90°±2.5° at a wavelength of 860 nm ±60 nm to forward transmitted light, as compared to the same ratio for a standard suspension of Formazine. This optical measurement technique of *T* from the side scattering coefficient is in accordance with ISO 1999. *T* is expressed in Formazine Nephelometric Units (FNU) and instruments are calibrated using a set of Formazin Turbidity Standards. At the start of each sea campaign, instrument stability is ensured by recording turbidity of Hach STABLCAL Formanzin standards of 0.1, 20, 100, and 800 FNU and instrument recalibration is done if necessary. Side scattering signals are averaged over 10 measurements at 1.2 second intervals. Glass sample cells of 10 mL are used to record seawater *T*. The glass cell is rinsed with sampled seawater before filling. The exterior of the sample cell is rinsed with milliQ water, dried with paper tissue, swiped with a soft microfiber lint-free cloth treated with silicon oil, and swiped again with a dry cloth. Prior to turbidity measurement, the sample cell is visually inspected for dust particles or air bubbles. *T* was recorded in triplicate, gently tumbling the sample cell between each measurement.

T is recorded before and after [SPM] filtrations to check adequate mixing of the water sample during subsampling for filtration. Each *T* measurement typically takes about four minutes to complete and portable turbidity meters can be purchased for less than 1000 US dollars.

2.2.3 Optimal filtration volume

2.2.3.1 *T* AS PROXY FOR [SPM]

T and [SPM] measurements were carried out in surface waters in coastal and offshore waters around Europe and French Guyana between 2007 and 2010. Sampling sites are described in Neukermans et al. 2012. A 'least squares cubic' type II regression (York 1966) is applied to the log transformed *T* and [SPM] data. The least squares cubic regression, which takes into account measurement uncertainties, is applied after removal of outliers identified by the MATLAB robustfit.m routine. Correlation coefficients are given with their 95% confidence intervals, obtained from bootstrapping. Details of these statistical procedures are described in section 3.5.1.3 on page 82.

Based on the [SPM]-*T* regression, an estimate of [SPM] can be derived from measurements of *T* prior to filtration. From this estimate of [SPM], the volume of seawater to be filtered so that an optimal mass is retained by the filter can then be estimated as described in section 2.2.3.

2.2.3.2 DETERMINING OPTIMAL FILTRATION VOLUME

The filtration volume, *V*, should be high enough so that the dry mass of the particles retained by the filter, $w_a - w_b$, is sufficient to be precisely measured, but not so much that the filter clogs. Its estimation requires a quantification of minimum measurement uncertainty on $w_a - w_b$, assessed from procedural control filters, and a maximum value for the relative uncertainty on [SPM]. The approach is described below.

For measurements of weight, the detection limit (DL) of the balance gives the minimum measurement uncertainty. The minimum uncertainty on the difference between filter weights before and after filtration, $w_a - w_b$, is then given by (ISO 1995):

$$\Delta w_{bal} = \sqrt{2}\mathrm{DL} \tag{2.1}$$

In this study, DL=0.1 mg so that Δw_{bal} =0.14 mg. Let Δw_p denote the combined uncertainties on the dry mass of retained particles resulting from filter preparation and handling (including weighing) in the laboratory and at sea, then $\Delta w_p \geq \Delta w_{bal}$. This estimate of combined uncertainties, Δw_p, is protocol dependent and can be assessed from procedural control filters. It follows that the uncertainty on [SPM] from replicate measurements, Δ[SPM], is at best equal to $\Delta w_p \times V(\mathrm{L})^{-1}$ (in mg L^{-1}). Further uncertainties on [SPM] include uncertainties due to sample mixing and uncertainties in measurement of sample volume. For the relative uncertainty on [SPM], Δ[SPM]:[SPM], we can write:

$$\frac{\Delta w_p}{V[\mathrm{SPM}]} \leq \frac{\Delta[\mathrm{SPM}]}{[\mathrm{SPM}]} \tag{2.2}$$

Let u_s be the maximum allowable relative uncertainty on [SPM] from replicate measurements. Then

$$V \geq \frac{\Delta w_p}{u_s[\mathrm{SPM}]} \tag{2.3}$$

The optimal filtration volume, V_{opt}, is the smallest volume that satisfies Eq. (2.3) with a certain level of confidence, where [SPM] is estimated from T prior to filtration:

$$V_{opt} = \frac{\Delta w_p}{u_s[\mathrm{SPM}]} \tag{2.4}$$

2.2.4 Effect of filtration volume on precision of [SPM] measurements

To investigate the effect of filtration volume on the precision of [SPM] measurements, six experiments were carried out in the southern North Sea in September 2009 and 2011 for clear (T < 5 FNU), moderately turbid (5 FNU<T<20 FNU), and turbid waters (T>20 FNU). For each water sample listed in Table 2.2, [SPM] measurements were performed with filtration volumes of 0.2, 0.5, 1, and 2 times V_{opt} and every filtration was done on five replicate filters. T was continuously monitored during the course of each filtration experiment, to ensure good mixing of the sampled seawater. Table 2.2 lists the sampling time and location, salinity, temperature, depth, [Chl *a*], and the mean and standard deviation of T for each sample.

Table 2.2. Overview of water samples collected in the southern North Sea for filtration experiments with salinity, temperature, chlorophyll *a* concentration, and turbidity, T , with standard deviation ΔT.

sample	date	time (h UTC)	latitude	longitude	salinity (PSU)	temp (°C)	depth (m)	chl a (mg m^{-3})	T (FNU)	ΔT (FNU)
Cl	14-Sep-11	12:12	51° 29.259' N	2° 50.490' E	34.67	17.15	28.81	*	2.98	0.32
WGAB	17-Sep-09	19:48	51° 57.630' N	2° 05.510' E	34.89	17.63	?	0.9	6.83	0.14
O924A	16-Sep-09	13:59	51° 26.012' N	3° 28.474'E	32.70	17.39	16.12	4.5	10.93	0.18
Mod	15-Sep-11	11:25	51° 20.781' N	2° 57.254' E	34.63	16.86	12.64	*	12.18	0.42
T	14-Sep-11	7:05	51° 22.663' N	3° 02.194' E	34.69	16.95	10.77	*	25.53	0.31
MH5	17-Sep-09	14:16	51° 50.954' N	1° 38.965' E	34.73	17.30	22.65	<0.06	53.30	1.59

*: Not available yet

2.2.5 Between group statistical analysis

Between group differences are investigated by one-way analysis of variance (ANOVA), comparing the means of several groups to test the hypothesis that they are all the same, against the alternative that they are not all the same. To test which pairs of means are significantly different, paired-sample *t*-tests were

done at the 5% significance level. Analyses were carried out using the statistics toolbox of MATLAB, version R2011b.

Graphical illustrations of the distribution of observations are done with boxplots. The edges of the box indicate the 25th and 75th percentiles, while the red line represents the sample median. The length of the box is called the interquartile range (IQR). Observations further than 1.5 IQR from the 25th and 75th percentiles are marked as outliers and indicated by red crosses. This range corresponds to ±2.7 standard deviations and 99.3% data coverage if normally distributed. The whiskers extend to minimum and maximum observations that are not marked as outliers.

2.3 Results and discussion

2.3.1 Uncertainties in [SPM] measurement

2.3.1.1 SALT RETENTION TESTS

Results from lab experiments with SSW show significantly higher residual weight (p=0.003, F=11.76, d.f.=17, ANOVA) when the rim is not rinsed (see Figure 2.2), compared to when the filter rim is rinsed. This is in accordance with previous works that stressed the importance of rinsing of the filter rim to flush out diffused salts (Strickland and Parsons 1968; van der Linde 1998).

The volume of SSW filtered was not found to affect SSW blank residual weights (p=0.72, F=0.57, ANOVA, see Figure 2.3), which were not significantly different from zero. This suggests that salts are washed out using a wash volume of 400-450 mL of milliQ, independent of the volume of SSW filtered. This is partially in accordance with Stavn et al. 2009 who found salt retention of 1.1 mg, independent of volume of seawater filtered for a salinity of 34 PSU and a wash volume of 300 mL (see their Table 1).

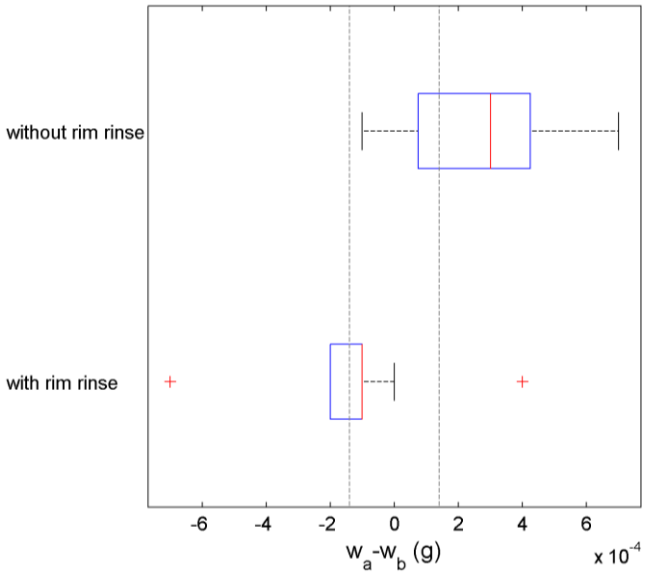

Figure 2.2. Difference in filter weight before and after filtration of 250 mL of SSW of 34 PSU, with and without rinsing of the filter rim (step 13 in protocol in Figure 2.1). Grey dashed lines represent uncertainty on $w_a - w_b$ due to the detection limit of the balance, Δw_{bal} =0.14 mg.

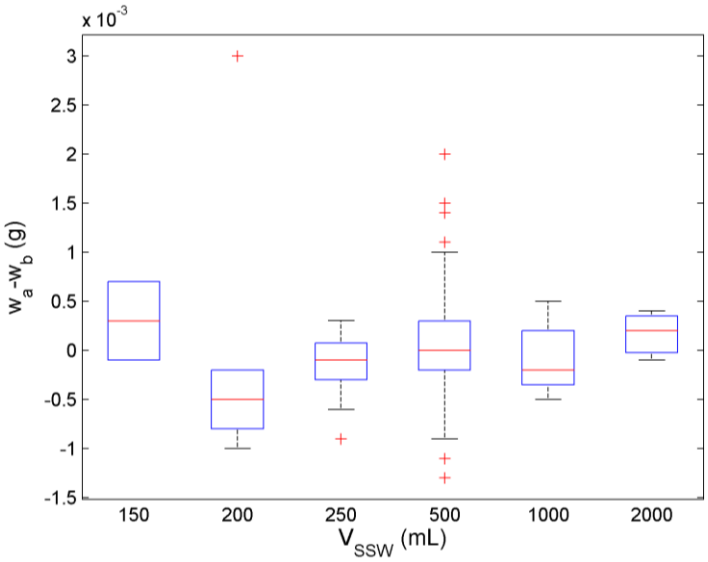

Figure 2.3. Difference in filter weight before and after filtration vs. filtered volume of SSW of 34 PSU. Number of observations for each volume are 2, 6, 15, 95, 5, and 3, respectively.

2.3.1.2 FILTER BLANKS

Figure 2.4 shows the differences in filter weight before and after filtration, WD $= w_a - w_b$, for dry, milliQ, and SSW blanks. About 46% of the blank weight differences were found within the uncertainty

on WD due to the detection limit of the balance, Δw_{bal} =0.14 mg (see Figure 2.4). The median absolute value of WDs for all blanks is 0.2 mg, with 90% of the values below 0.6 mg. WDs were not significantly different between blank types (p=0.21, F=1.55, d.f.=2, ANOVA), suggesting that salt is properly washed out.

WDs for dry blanks are significantly positive (t-test, p<0.001), while the mean WDs for milliQ and SSW blanks are not significantly different from zero (t-test, p=0.8 and p=0.5, respectively) with WD<0 in 50% of the cases. This suggests that friable fractions of glass fiber filters may have dislodged during filtration, while these should have been washed out before filtration (step 2 in Figure 2.1).This process may be mitigated by repeating the pre-ashing, washing, and drying of the filters in the preparation phase (steps 1-4 in Figure 2.1) several times until a constant weight is achieved. Stavn et al. (2009) recommend 3-4 repeat cycles to better control loss of filter mass, but does not eliminate it (Feely et al. 1991).

No significant differences in WDs of SSW blanks were found between campaigns in 2007-2010 (p=0.11, F=1.41, d.f.=27, ANOVA), indicating stability of humidity and temperature conditions in the laboratory and of sample treatment.

SSW blank WDs are thought to best reflect procedural uncertainties associated with filtration of saline waters. Therefore, estimates of Δw_p at the 50% and 90% confidence level are obtained from the 50th and 90th percentiles of absolute WDs for SSW, equal to 0.2 mg and 0.9 mg, respectively. These are further used in the calculation of the optimal filtration volume from Eq. (2.4) in section 2.3.2.1.

2.3.1.3 SAMPLE MIXING

Figure 2.5(a) shows the comparison between T recorded before and after filtration. The mean bias (=(T_a-T_b):T_b) is close to zero (-2%) and symmetrically distributed with 90% of the values between -28% and 23%. Prediction error, PE=|T_a-T_b|:T_b, is generally between 1% and 39% with a median of 6%. In clear waters (T_b<5 FNU) both bias and prediction error, denoted with 'c' subscript, show higher variability, due to higher measurement uncertainties. Also shown in Figure 2.5(a) are observations recorded before June 2008 when seawater samples were stirred up with a measuring cylinder and then subsampled using a 1L container (see Figure 2.6(a)). Comparison of T_a and T_b for this dataset is especially poor in clear water (T_b < 5 FNU) where the distribution of the bias is strongly positive (90% of the observations between -12% and 144% with a median of 9%). This suggests contamination of the water sample during the mixing procedure, possibly by contact with the glove worn by the person filtering. From June 2008 onwards, seawater samples were mixed by gently tumbling a closed 10 L container around several times before subsampling (see Figure 2.6(b)). This illustrates the use of T measurements to detect problems with sample mixing.

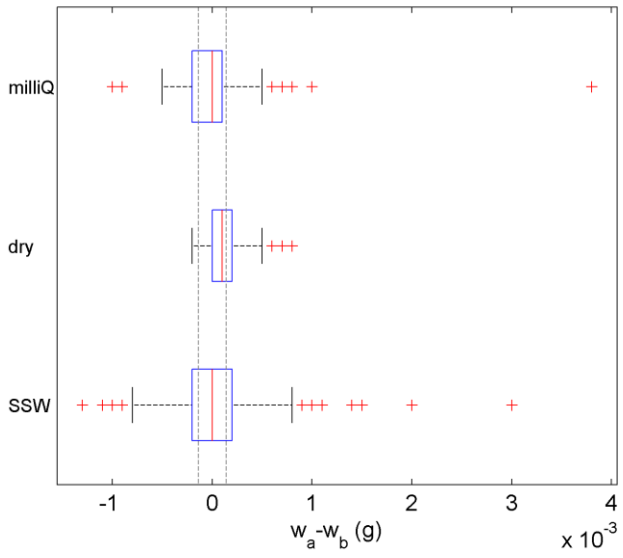

Figure 2.4. Difference in filter weight before and after filtration, WD=$w_a - w_b$, for different blanks collected at the start and the end of each campaign between 2007 and 2010. Grey dashed lines represent uncertainties on WD due to the detection limit of the balance (Δw_{bal} =0.14 mg).

2.3.2 Uncertainties in [SPM] measurement from filtration volume

2.3.2.1 DETERMINING OPTIMAL FILTRATION VOLUME

A total of 366 simultaneous measurements of *T* (=mean of *T* measurements before and after filtration) and [SPM] were done. Observations where only one [SPM] replicate remained were rejected (n=9). Least squares cubic regression gives:

$$\log_{10}[\mathrm{SPM}] = 0.97(\pm 0.01)\log_{10} T - 0.01(\pm 0.01) \qquad (2.5)$$

The regression statistics and its 90% prediction bounds are shown in Figure 2.5(b). The offset of the regression line is not significantly different from zero for the tumble mixing dataset, whereas a significantly positive offset (0.14±0.02) was found for the hand mixing dataset, suggesting sample contamination by hand mixing. The model for [SPM] in Eq. (2.5) performs well with a median prediction error (MPE) of 11% and with prediction errors below 40% in 95% of the cases. The 90% prediction bounds of the regression line, shown in Figure 2.5, can be used to quality control [SPM] by flagging data outside these boundaries as suspect.

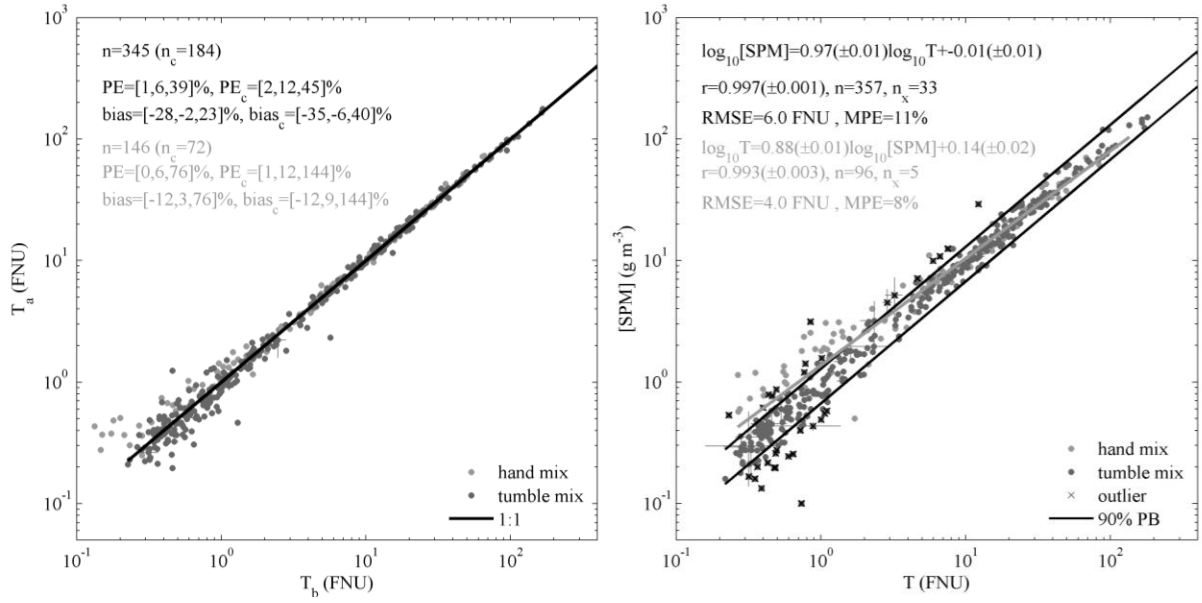

Figure 2.5. (a) Comparison of *T* before and after filtration, with statistics given using hand mixing and tumble mixing for all observations and in clear waters (T_b<5 FNU) and (b) relationship between *T* and [SPM] with type II regression and statistics using hand mixing and tumble mixing. The 90% prediction bounds of the regression are also shown. Errorbars in (a) and (b) represent the standard deviation from replicate measurements of *T* and [SPM].

Figure 2.6. Mixing methods for subsampling of seawater for filtration: (a) seawater is stirred up with a measuring cylinder and then subsampled using a 1L container, (b) seawater is mixed by gently tumbling a closed 10 L container mounted on a rotating frame attached to the wall in the wet lab of the ship.

For our purposes, a maximum uncertainty of u_s=15% on [SPM] is desired. The filtration volume is optimally set by measuring T before filtration and using the regression model in Eq. (2.5) to predict [SPM]. From Eq. (2.4) it follows that Δ[SPM] is expected to be below 15% in 50% (90%) of the cases for a filtration volume V_{50} (V_{90}) of:

$$V_{50} = \frac{\Delta w_{p,50}}{0.15[\mathrm{SPM}]} \quad \text{and} \quad V_{90} = \frac{\Delta w_{p,90}}{0.15[\mathrm{SPM}]} \tag{2.6}$$

where $\Delta w_{p,50}$ and $\Delta w_{p,90}$ are the 50th and 90th percentiles of weight differences for SSW blanks, i.e. 0.2 mg and 0.9 mg, respectively. Table 2.3 lists V_{50} and V_{90} for T between 0.5 FNU and 140 FNU. For practical use, volumes are rounded to give R(V_{50}) and R(V_{90}), respectively.

Table 2.3. Lookup table for recommended filtration volume as function of turbidity so that relative uncertainty on [SPM] replicates is within 15% in 50% of the cases ($R(V_{50})$) and in 90% of the cases ($R(V_{90})$).

T (FNU)	$[SPM]_{50}$ (mg/L)	V_{50} (mL)	V_{90} (mL)	$V_{90,u}$ (mL)	$R(V_{50})$ (mL)	$R(V_{90})$ (mL)
0.5	0.50	2673	12027	18032	3000	12000
1	0.98	1364	6140	8990	1000	6000
2	1.91	697	3134	4482	500	3000
3	2.84	470	2115	2984	500	2000
4	3.75	356	1600	2235	350	1500
5	4.66	286	1289	1787	250	1250
6	5.56	240	1080	1488	250	1000
7	6.45	207	930	1275	200	1000
8	7.35	182	817	1115	200	800
9	8.23	162	729	991	150	750
10	9.12	146	658	891	150	600
11	10.00	133	600	810	150	600
13	11.76	113	510	685	100	500
14	12.64	105	475	636	100	500
15	13.51	99	444	593	100	400
16	14.39	93	417	556	100	400
18	16.13	83	372	494	100	400
19	17.00	78	353	468	75	375
21	18.73	71	320	423	75	300
22	19.60	68	306	404	75	300
26	23.04	58	260	342	50	250
27	23.90	56	251	329	50	250
32	28.18	47	213	277	50	200
33	29.04	46	207	269	50	200
37	32.45	41	185	240	50	200
38	33.30	40	180	234	50	200
40	34.99	38	171	222	50	175
45	39.23	34	153	197	25	150
50	43.45	31	138	177	25	150
55	47.66	28	126	161	25	125
65	56.04	24	107	136	20	110
70	60.22	22	100	127	20	100
75	64.39	21	93	118	20	90
80	68.55	19	88	111	20	90
85	72.70	18	83	104	20	80
95	80.98	16	74	93	20	70
100	85.11	16	70	89	20	70
110	93.36	14	64	80	10	60
115	97.47	14	62	77	10	60
140	117.96	11	51	63	10	50

2.3.2.2 EFFECT OF FILTRATION VOLUME ON PRECISION OF [SPM] MEASUREMENT

The filtration volume was optimally set based on *T* measurements before each filtration experiment using $R(V_{90})$ in Table 2.3. An overview is given in Table 2.4, which also shows the time required to pass a given volume of sample through five replicate filters. No significant changes in *T* were found before and after each filtration experiment ($p>0.05$, ANOVA), indicating good sample mixing throughout the experiments.

Table 2.4. Overview of turbidity, *T* , with standard deviation ΔT, optimal filtration volume obtained from $R(V_{90})$ in Table 2.3, and time required to pass seawater through five replicate filters.

				Filtration time (minutes)			
sample	T (FNU)	ΔT (FNU)	V_{opt} (mL)	0.2 V_{opt}	0.5 V_{opt}	V_{opt}	2 V_{opt}
Cl	2.98	0.32	1500	17	20	29	94
WGAB	6.83	0.14	1000	13	10	24	64
O924A	10.93	0.18	500	19	12	15	78
Mod	12.18	0.42	500	10	11	16	48
T	25.53	0.31	250	20	12	30	25
MH5	53.30	1.59	150	6	8	21	18

The coefficient of variation, c.v. (=standard deviation: mean from five [SPM] replicates), is plotted as function of filtration volume normalized by V_{opt} in Figure 2.7. Results suggest that filtering more or less than the optimal volume gives a lower precision in the [SPM] measurement, except for the most turbid water sample, MH5, where c.v. is lowest at twice V_{opt}. It can be seen from filtration times in Table 2.4 that passing twice V_{opt} was not problematic for the most turbid samples, MH5 and T, while for other samples filtration time at least tripled, to exceeding 1 h. It is thought that filter clogging may be more likely in the presence of biological particles, but this remains uncertain at this time.

Differences between c.v.'s for different filtration volumes were tested for significance by computing c.v.'s for a random selection of three out of five replicates without replacement and repeating this procedure 100 times. The median, 10^{th} , and 90^{th} percentiles of each c.v. dataset are also shown in Figure 2.7. ANOVA tests show that the c.v. is significantly higher, and often higher than the desired precision of 15%, when one fifth of the optimal volume is filtered than when larger volumes are filtered. C.v. decreases significantly when filtration volume is increased to half V_{opt}, except for sample CL. Further decrease of c.v. when filtration volume is increased to V_{opt} is significant at stations CL, WGAB, 0924A, and T. A significant increase in c.v. is observed when filtering more than V_{opt} for samples WGAB, 0924A, MOD, and T. These slight increases in inter-replicate variability may be caused by the higher likelihood

of spraying off particles during rim rinsing (step 13 in Figure 2.1) when filters are saturated with particles, as shown for MOD at filtration volumes of V_{opt} in Figure 2.8(a,b) and 2 V_{opt} in Figure 2.8(c,d).

[SPM] means were independent of filtration volume, as shown in Figure 2.9, with the exception of significantly lower [SPM] for the smallest filtration volume for samples 0924A and MH5. This could be an effect of the reduction of the effective pore size with increasing volume. This phenomenon is known to be somewhat unpredictable and to depend on the particle size distribution and the shape of the particles in suspension (Sheldon and Sutcliffe 1969; Sheldon 1972).

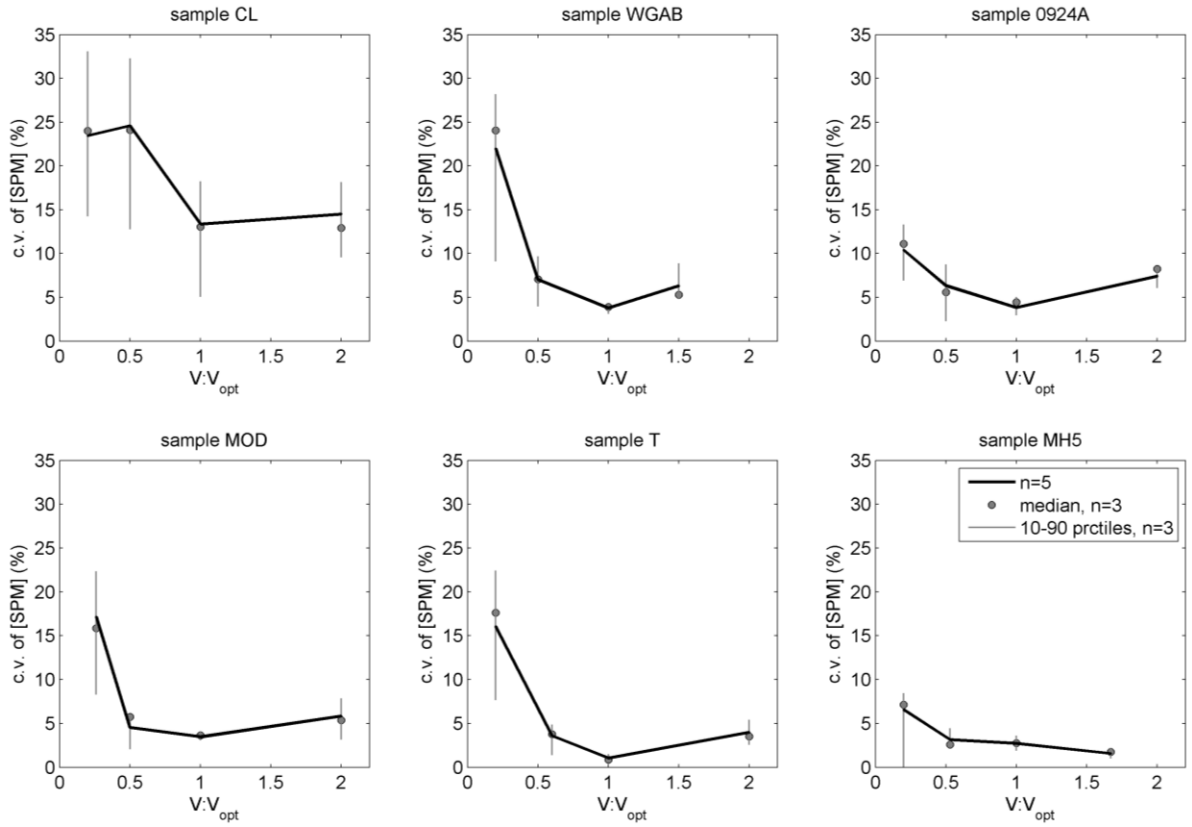

Figure 2.7. Coefficient of variation, c.v. (in %) of [SPM], obtained from five replicates vs. filtration volume, normalized to the optimal filtration volume, V_{opt}. Shown in grey are the median, 10th, and 90th percentiles of c.v. obtained from 100 resamplings without replacement of 3 [SPM] replicates out of 5.

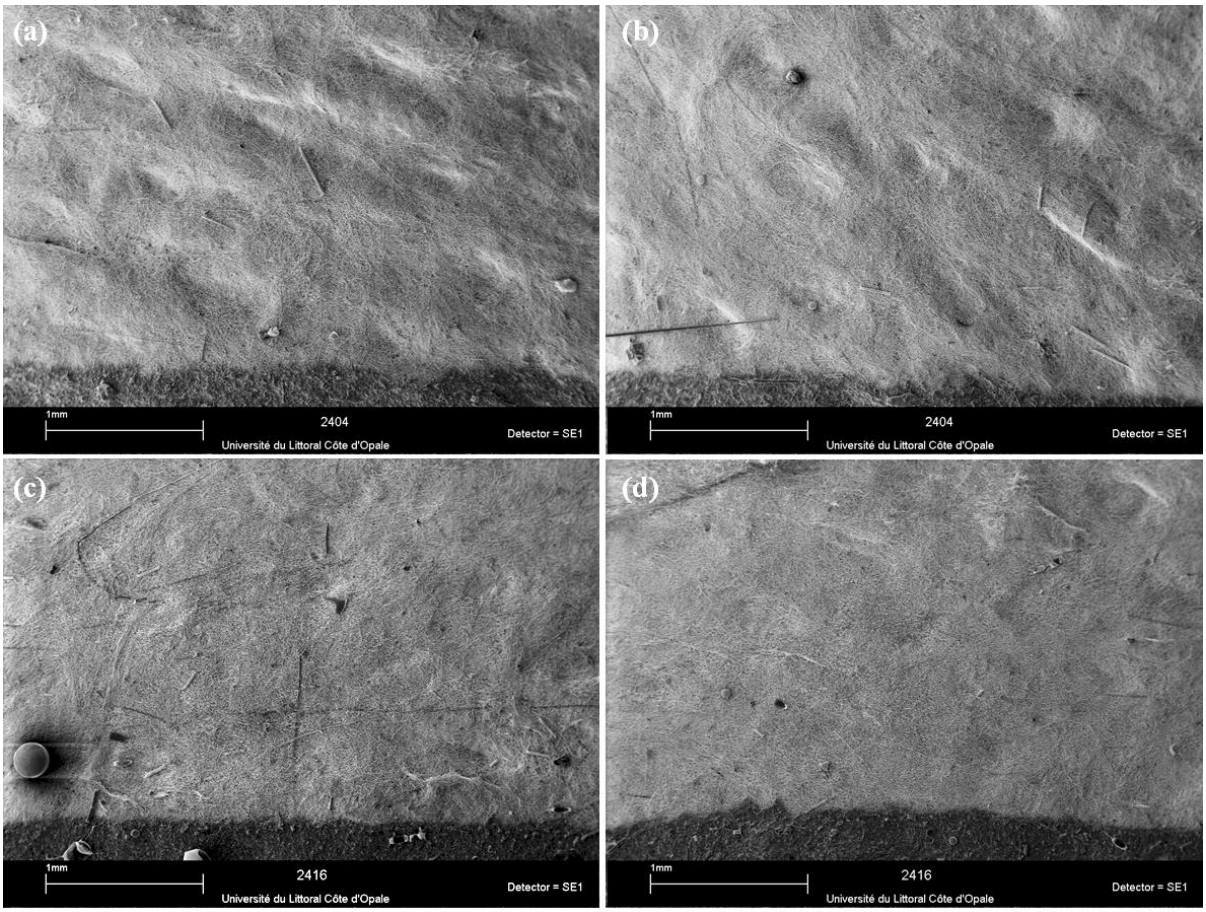

Figure 2.8. Scanning Electron Microscopy images of two selected zones on the GF/F filter rim of sample MOD with filtration volume V_{opt} (a,b) or $2xV_{opt}$ (c, d), showing particles that got displaced onto the filter rim during the rinsing of the rim.

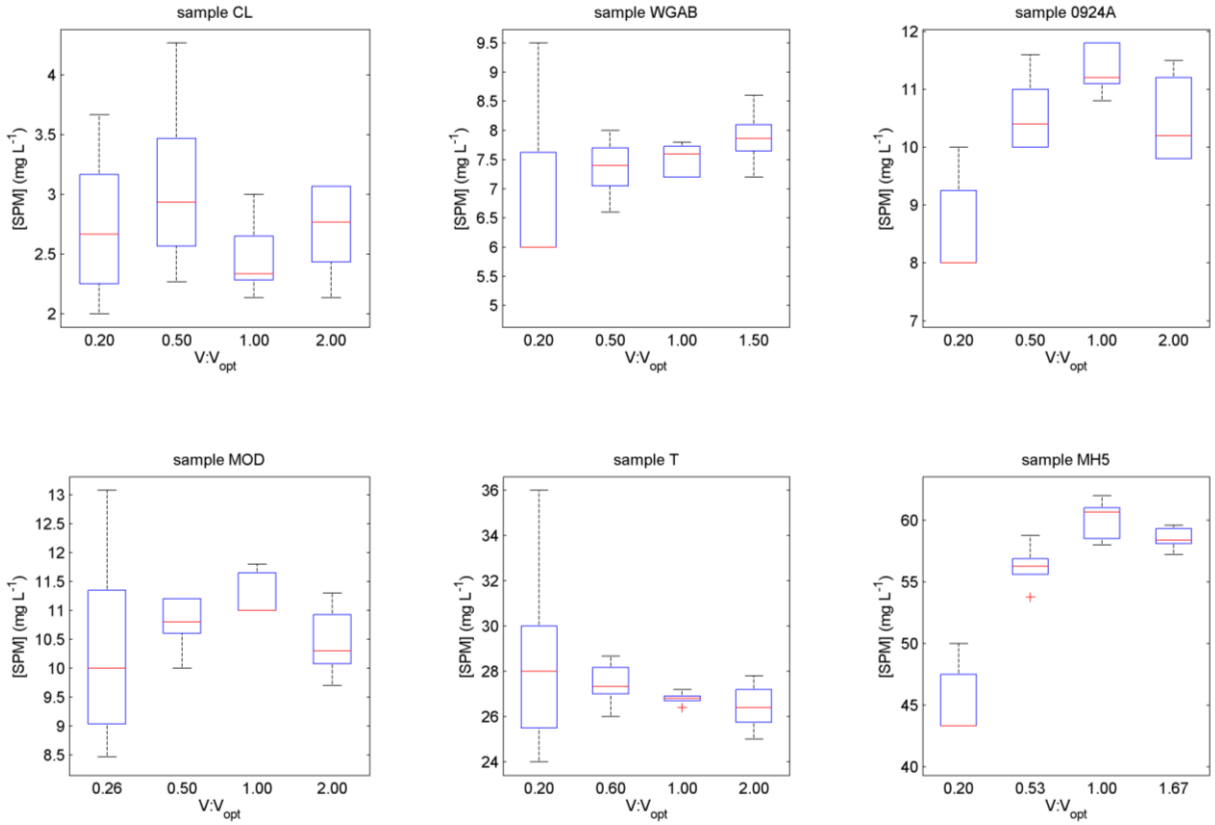

Figure 2.9. Boxplot of [SPM] obtained through filtration of different volumes of sampled seawater at six different stations.

Least-squares regressions of WD vs. filtered volume of seawater are shown in Figure 2.10. The offsets of the regression lines for all samples are not significantly different from zero, again indicating that salts are properly washed from the filters. It has been noted by Trees 1978 that the relationship between filtration volume and retained mass is linear only when salts are properly washed out.

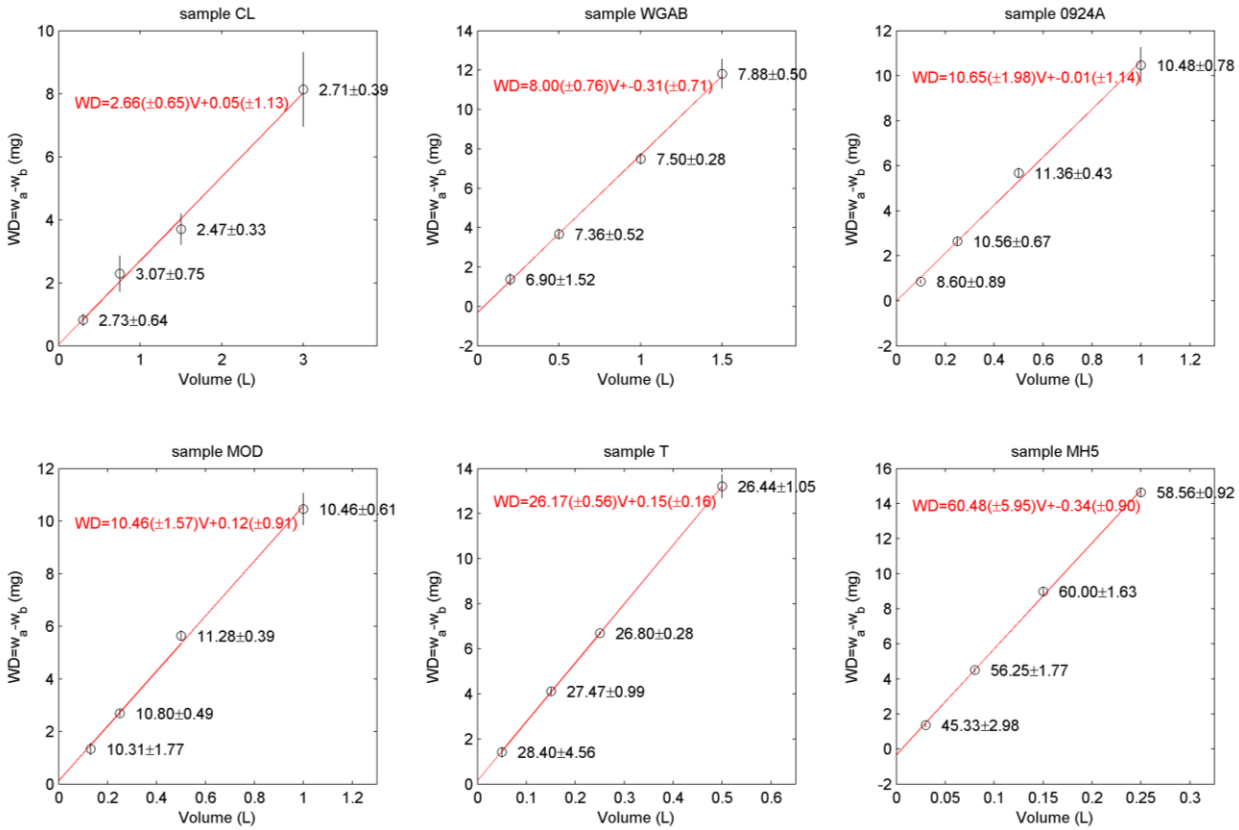

Figure 2.10. Scatterplots of particulate dry mass ($w_a - w_b$,) vs. filtrate volume. The errorbars denote the standard error on particulate dry mass obtained from 5 replicates. The mean and standard error of [SPM] are also shown for each filtration volume. Shown in red are the regression line and its equation with 95% confidence intervals of the coefficient estimates.

2.4 Conclusion

This study shows that simple, fast, and low cost measurements of turbidity, T , can be used to optimize [SPM] measurements. More specifically, turbidity measurements can be used to optimally set the filtration volume , to detect problems with the mixing of the sample during subsampling for filtration, and for the quality control of [SPM]. The relationship between T and optimal filtration volume is set-up using estimates of [SPM] measurement procedural uncertainties from blank measurements and a value for maximum allowable uncertainty on [SPM]. Procedural uncertainties were assessed from filter blanks where synthetic seawater of a typical salinity is passed through, representing uncertainties due to filter preparation, handling, and rinsing of sea salt. The use of various types of filter blanks subjected to different steps in the measurement procedure may help reveal sources of uncertainty. In this study, for example, differences in weights of dry and wet filter blanks suggest that friable fractions of glass fiber filters may have dislodged during filtration. This fiber loss may be mitigated in the future by repeating the

pre-ashing, washing, and drying steps of filters in the preparation phase until constant weight is achieved. Blank filters and regressions of residual weight vs. filtration volume suggest that salts are properly flushed using a wash volume of 400-450 mL of milliQ for water samples with salinities of 33-35 PSU, while a wash volume of 300 mL has been shown to be insufficient (Stavn et al. 2009).

We further investigated the role of filtration volume on the precision of [SPM] measurement by filtering volumes of seawater ranging between one fifth and twice the optimal filtration volume. It is shown that if the optimal volume is filtered, [SPM] measurements are most precise and cost effective. In most cases filtering twice the optimal volume caused clogging and tripled filtration times to over 1 hour, which is impractical and problematic in limited ship time.

It is recommended that each research group establishes their own relationship between turbidity and optimal filtration volume, which is specific to the type of turbidity instrument, the uncertainties of the [SPM] measurement procedure which can be assessed from procedural control filters, and the desired maximum relative variability between replicates.

Chapter 3 IN SITU VARIABILITY OF MASS-SPECIFIC BEAM ATTENUATION AND BACKSCATTERING OF MARINE PARTICLES WITH RESPECT TO PARTICLE SIZE, DENSITY, AND COMPOSITION

This chapter was published as Neukermans et al. 2012 in open access available from http://aslo.org/lo/toc/vol_57/issue_1/0124.pdf.

Abstract

This study analyzes relationships between concentration of suspended particles represented by dry mass, [SPM], or area, [AC], and optical properties including particulate beam attenuation (c_p), side scattering (b_s), and backscattering (b_{bp}), obtained from an intensive sampling program in coastal and offshore waters around Europe and French Guyana. To first order optical properties are driven by particle concentration with best predictions of [SPM] by b_{bp} and b_s, and of [AC] by c_p. Second order variability is investigated with respect to particle size, apparent density (dry weight to wet volume ratio), and composition. Overall, the mass-specific particulate backscattering coefficient, b_{bp}^m (=b_{bp}:[SPM]), is relatively well constrained, with variability of a factor 3-4. This coefficient is well correlated with particle composition with inorganic particles having values about 3 times greater (b_{bp}^m=0.012 m² g^{-1}) than organic particles (b_{bp}^m =0.005 m² g^{-1}). The mass-specific particulate attenuation coefficient, c_p^m (=c_p:[SPM]), on the other hand, varies over one order of magnitude and is strongly driven (77% of the variability explained) by particle apparent density. In this dataset particle size does not affect c_p^m and affects b_{bp}^m only weakly in clear (case 1) waters, despite size variations over one order of magnitude. A significant fraction (40-60%) of the variability in b_{bp}^m remains unexplained. Possible causes are the limitation of the measured size distributions to the 2-302 μm range and effects of particle shape and internal structure which affect b_{bp} more than c_p and were not accounted for.

3.1 Introduction

The inherent optical properties (IOPs) of particles suspended in seawater (e.g., phytoplankton, detritus, heterotrophic bacteria, viruses, and mineral particles) are driven to first order by their concentration.

Second order effects are caused by variations in particle size, material composition (i.e., refractive index), shape, and internal structure. Strong relationships are generally found between IOPs and suspended particulate matter concentration, [SPM] (Babin et al. 2003; Boss et al. 2009c), or chlorophyll *a* concentration, [Chl *a*], widely used as an index of phytoplankton biomass (Bricaud et al. 1998; Loisel and Morel 1998). Such relationships were derived from in situ measurements, whereas our present understanding of the effect of particle characteristics on IOPs is mainly based on laboratory measurements and theoretical calculations. For instance, studies investigating optical variability of phytoplankton cells with cell size and refractive index (Morel and Bricaud 1986;Ahn et al. 1992;Vaillancourt et al. 2004) or induced by environmental factors (Stramski and Morel 1990; Stramski et al. 2002) were performed in laboratories. Other laboratory studies focused on optical variability of mineral particles (Volten et al. 1998; Stramski et al. 2007). Studies of optical variability with respect to particle size and refractive index (Morel and Bricaud 1981; Morel and Ahn 1991;) as well as shape and structure (Kitchen and Zaneveld 1992; Gordon and Du 2001; Clavano et al. 2007) were based on theoretical calculations. Assessment of IOP variability in optically complex waters with respect to particle concentration and bulk particle characteristics (e.g., size and composition) has started only recently with the availability of appropriate in situ instrumentation (Babin et al. 2003; Peng and Effler 2007; Woźniak et al. 2010). In this paper, we focus on in situ variability of particulate scattering properties.

It is generally observed that particulate attenuation (c_p), scattering (b_p), and backscattering (b_{bp}) coefficients (units: m^{-1}) increase with concentration of suspended particles. The mass-specific attenuation (c_p^m), scattering (b_p^m), and backscattering (b_{bp}^m) coefficients are expected to vary with the nature of the particles (size, refractive index, structure, shape, and composition). These mass-specific optical coefficients represent an optical cross section per unit mass in units of $m^2\ g^{-1}$. Understanding their variability is of fundamental importance for radiative transfer studies in marine waters, studies coupling optics with ecosystem and biogeochemical models, in situ monitoring of suspended particle dynamics, as well as for ocean color remote sensing. For instance, b_{bp} normalized by [SPM] or [Chl *a*] strongly influences the remote sensing retrieval accuracy of [SPM] or [Chl *a*], respectively (Brown et al. 2008; Nechad et al. 2010; Loisel et al. 2010). Suspended particles affect the propagation of light in the ocean and light availability to marine organisms. Direct laboratory measurements of biogeochemical components are not practically feasible at the spatial and temporal scales required to validate ecosystem and biogeochemical models. Optical measurements can be used to accommodate this need.

Since the early 1970s, when the first commercial transmissometers became available, relationships between [SPM] (in $g\ m^{-3}$) and c_p or b_p have been examined in open ocean and coastal waters (Gibbs 1974; Carder et al. 1975; Pak and Zaneveld 1977). Values of c_p^m or b_p^m reported in the literature

vary over one order of magnitude, from 0.05 $m^2 g^{-1}$ to 1.5 $m^2 g^{-1}$ (Baker and Lavelle 1984;Wells and Kim 1991; Gardner et al. 2001, but *see* Hill et al. 2011 for a comprehensive overview). Theoretical and experimental work focused on the effect of particle size on c_p^m and b_p^m (Pak et al. 1970; Spinrad et al. 1983; Baker and Lavelle 1984). However, despite large variability in particle size, in situ measurements of c_p^m vary much less (Bunt et al. 1999; Mikkelsen and Pejrup 2000). The recent modeling work of Boss et al. 2009a) suggests that the process of particulate aggregation, the formation of flocs composed of mineral and organic particles with water trapped in between, constrains the sensitivity of c_p^m to particle size. This hypothesis is supported by in situ measurements of Hill et al. 2011). Inverse relationships between b_p^m and particle diameter may however be found when particles are less aggregated (Woźniak et al. 2010).

An explanation of the observation that b_p^m is significantly lower in coastal waters (≈0.5 $m^2 g^{-1}$) than in open ocean waters (≈1 $m^2 g^{-1}$) was given by Babin et al. 2003) on the basis of Mie scattering calculations, modeling marine particles as homogeneous, solid spheres. In coastal waters, where mineral material is more common than organic material, the larger apparent density, ρ_{ap} (particle dry weight: wet volume), of the former counterbalances the effect of its higher refractive index. This explanation has, however, been challenged by several studies (Martinez-Vicente et al. 2010; Woźniak et al. 2010). Seasonal changes of b_p^m in a low turbidity station in the western English Channel have been related to the composition of particulate organic matter, POM (Martinez-Vicente et al. 2010). Bowers et al. 2009) show that the variability of b_p^m in a shallow shelf sea dominated by mineral aggregates is mainly explained by changes in the aggregate apparent density, ρ_{ag} (dry weight: wet volume ratio of material in the aggregate), while particle size has only little effect on b_p^m. Note that there is a difference between ρ_{ap} and ρ_{ag}. Whereas wet volume in ρ_{ap} refers to the particle internal fluid volume, it refers to the aggregate interstitial fluid volume in ρ_{ag}. Hill et al. 2011 suggest that the large range of c_p^m and b_p^m values are caused by variability in particle composition, size, and the finite acceptance angle of the optical instruments. Also, [SPM] has been measured using various protocols with varying filter pore sizes, filter types, and corrections for residual salts. The choice of statistical approach (e.g., simple descriptive statistics vs. regression analysis) may also influence the apparent range of variability of normalized IOPs (*see* McKee et al. 2009 for similar effects on the particulate backscattering to scattering ratio, $\tilde{b}_{bp}$).

Much less is known about the relationship between b_{bp} and [SPM], the variability of b_{bp}^{m}, and even about the sources of b_{bp} itself. This is due to a lack of an appropriate theoretical framework for modeling b_{bp} and of commercial in situ sensors for determination of b_{bp} which became available only since the mid 1990s. Our understanding of the major contributors to b_{bp} in natural waters is uncertain and it is unknown which particles backscatter light most efficiently (Stramski et al. 2004). Mie scattering theory suggests substantial contributions to b_{bp} from submicron particles (Stramski and Kiefer 1991), but there is strong evidence that application of this model is inappropriate for computations of b_{bp} for natural particle assemblages (Bohren and Singham 1991;Kitchen and Zaneveld 1992; Clavano et al. 2007). In situ measurements of bulk and size fractionated measurements of b_{bp} in the open ocean showed strong contributions to b_{bp} from particles larger than 3 μm and negligible contributions from particles below 0.2 μm (Dall'Olmo et al. 2009).

Studies of the relationship between b_{bp} and [SPM] are not always consistent. Some studies show good correlations between b_{bp} and [SPM] (Boss et al. 2009c), while others find better correlations with particulate inorganic matter concentration, [PIM], than with [SPM] (Deyong et al. 2009; Martinez-Vicente et al. 2010). McKee and Cunningham 2006 observed good correlations between b_{bp} and both [SPM] and [PIM] in mineral-dominated turbid waters in the Irish Sea, while much weaker correlations were found in clear, more organic-dominated waters. Snyder et al. 2008 show evidence of spatial variability of b_{bp}^{m} along the U.S. coast and found significant differences between the mass-specific coefficients b_{bp}: [PIM] and b_{bp}:[POM], where [POM] is the particulate organic matter concentration, and [SPM]=[PIM]+[POM]. Several studies in U.S. coastal waters showed that [SPM] correlates better with b_{bp} than with c_p or b_p (Snyder et al. 2008; Boss et al. 2009c). The projected surface area concentration of suspended particles, [AC], is also known to correlate well with b_{bp}. Based on a laboratory experiment, Hatcher et al. 2001 found b_{bp} to increase with [AC] of phytoplankton-mud aggregates larger than 10 μm, despite a drop in [SPM]. Flory et al. 2004 found b_{bp} to linearly increase in situ with [AC] of aggregates larger than 100 μm.

Various types of instruments are available to obtain the particle size distribution (PSD), such as electrical impedance particle sizers (Coulter Counter), laser diffractometers (Laser In Situ Scattering and Transmissometry device, Sequoia Scientific, LISST-100X), and particle imaging systems (FlowCAM), but none of these instruments operate over the full optically significant size range from submicron particles to large millimeter-sized flocs. Electron microscopy could cover a broader range (including submicron particles), but is hampered by complex sample preparation, treatment, and analysis (Wells and Goldberg 1994; Peng and Effler 2007; 2010). The LISST-100X instrument series offer several advantages including rapid in situ measurements over relatively large volumes of water and coverage of a broad size

range (1.25-250 μm for type B and 2.5-500 μm for type C). Also, unlike the Coulter Counter and the FlowCAM, there is no need for discrete water sampling or sample handling, which may disrupt fragile aggregates. LISST instruments have been shown to provide PSDs that are comparable to other sizing instruments over a wide range of environmental particle types (Agrawal et al. 2008; Andrews et al. 2010; Reynolds et al. 2010). However, in order to obtain particle size information, an optical model needs to be assumed for inversion of the angular pattern of near-forward scattered light recorded by the LISST. Assumptions on the refractive index of the particles significantly affect the retrieved PSD (Andrews et al. 2010), especially for particles below 20 μm. Other disadvantages of the LISST are its lower size resolution and hence, its inability to detect narrow features in the PSD (Reynolds et al. 2010).

Despite recent availability of the required optical instrumentation, studies combining measurements of optical properties of marine particles with investigations of the fundamental causes driving their variability (particle size, apparent density, refractive index, and composition) are rare. Particularly, investigations of optical variability with respect to particle size are limited by the lack of measurements of the PSD over the full optically significant size range. Coverage of submicron particles is of special concern, given that under typical conditions in the open ocean and at 550 nm Mie theory predicts dominant contributions (70-90%) to b_{bp} and significant contributions (up to 50%) to c_p (Stramski and Kiefer 1991). Fractionation experiments in open ocean and coastal waters, however, suggest contributions from submicron particles to b_{bp} of only 10-30% and a much greater importance of particles larger than 3 μm of 53±7% (at 470 nm, Dall'Olmo et al. 2009) and about 70% (at 440 nm, Roesler and Boss 2008), respectively.

In the present study, we present and analyze combined measurements of in situ optical properties, particle concentration, apparent density, composition, and size distribution (obtained with a LISST, covering the size range 2.4-302 μm). An intensive sampling program (366 stations) in optically complex coastal and more offshore waters around Europe and French Guyana was carried out. Optical properties (c_p, b_s, and b_{bp}), [SPM], and the PSD were determined by the same people using the same instruments and protocols. The objectives are to re-investigate the relationships between optical properties (c_p, b_s, and b_{bp}) and proxies of particle concentration, such as [SPM] and [AC]. We also investigate the feasibility of assessing variability of b_{bp}^m and c_p^m with respect to bulk particle composition, apparent density, and size.

3.2 Methods

3.2.1 Description of the study areas

Fourteen sampling campaigns in coastal and offshore waters were conducted between April 2008 and July 2010, covering a wide variety of suspended particles in terms of concentration, composition, and size. A

total of 366 stations were visited: 213 in the southern North Sea and the English Channel (April, June, July 2008, 2009, and 2010; September 2008 and 2009; January 2010), 59 in the northeast Atlantic Ocean (June 2008, 2009 and 2010), 60 in the Ligurian Sea (March 2009) and 34 in French Guyana waters (October 2009). A map of the sampling locations is shown in Figure 3.1.

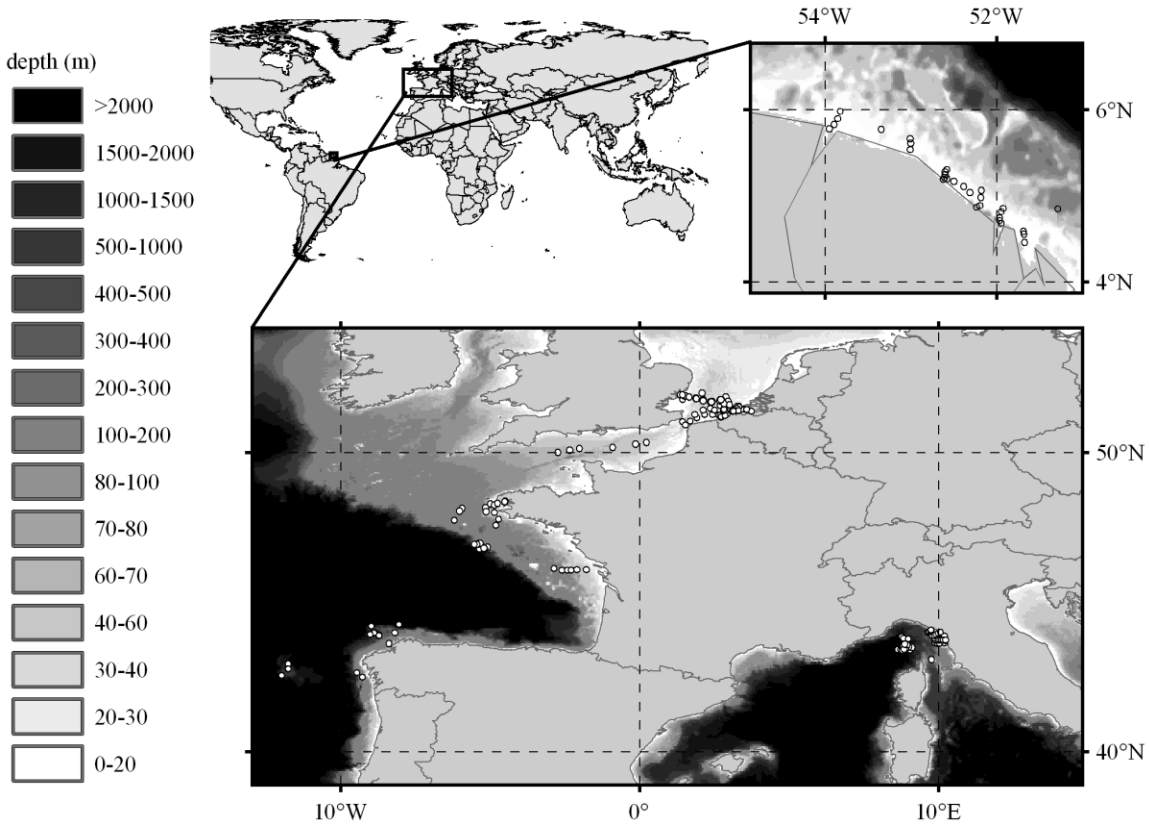

Figure 3.1. Location of stations sampled during 14 campaigns between April 2008 and July 2010. Bathymetry is also shown (source: General Bathymetric Chart of the Oceans, GEBCO_08 30' Grid, version 20100927, http://www.gebco.net)

The southern North Sea and the English Channel are shallow sea regions, rarely deeper than 50 m, subject to strong semi-diurnal tidal currents with a typical amplitude of 1 m s^{-1}. Particles in suspension originate from various sources, including coastal and sea bottom erosion, river discharges, inflow from the Atlantic Ocean, atmospheric dust, and dredging operations. A decrease of [SPM] with distance from the coast is generally observed, from above 100 g m^{-3} in the near shore waters to below 0.5 g m^{-3} in the deepest offshore waters. The cruise periods in the southern North Sea cover the bloom onset, development, and collapse of the prymnesiophyte *Phaeocystis globosa* and the dinoflagellate *Noctiluca scintillans*, as well as periods of lower biological activity. Particle composition shows high seasonal variability (Loisel et al. 2007; Astoreca et al. 2009; Martinez-Vicente et al. 2010).

The northeastern Atlantic waters between the Bay of Biscay and the Galicia Bank are typically case 1 waters with IOPs driven by phytoplankton and associated materials. Water samples were taken on and off the continental shelf with water depths varying between 20 and 300 m and [SPM] usually below 2 g m^{-3}. In June 2010, a bloom of an as yet unidentified *heliozoan* spp. occurred (F. Gomez pers. comm.). The Ligurian Sea between Corsica and northwest Italy is typically case 1, though a number of case 2 stations were sampled close to the Italian coast near the Arno river outflow. Samples were taken on and off the continental shelf with water depths varying between 30 and 500 m.

The French Guyana coastal waters are turbid and their IOPs are mainly driven by mineral particles of terrestrial origin (Loisel et al. 2009). These waters are strongly influenced by the Amazon river and affected by local features such as mud banks (Froidefond et al. 2002; Froidefond et al. 2004; Vantrepotte et al. in press).

3.2.2 Optical measurements

At each station, an optical profiling package (*see* Figure 3.2) was deployed in surface waters for several minutes, followed by a vertical profile from the surface to 2-3 m above the bottom. The package included a conductivity-temperature-depth (CTD) profiler (Sea Bird), a Western Environmental Technology Laboratory (WET Labs) ECO BB-9 backscattering instrument, a WET Labs ECO-Fl chlorophyll fluorometer, a WET Labs C-Star transmissometer for beam attenuation, a WET Labs ac-s for hyperspectral attenuation and absorption measurements, and a Laser In Situ Scattering and Transmissometry device (LISST-100X, Sequoia Scientific) for PSD and beam attenuation measurements. The ac-s was equipped with a SeaBird 3K pump with a coarse mesh steel screen for water flow into the 10 cm path-length tubes. Data from the WET Labs instruments were collected and recorded with a WET Labs Data Handler (DH-4) as a function of time for each of the instruments, enabling simultaneous collection, time stamping, storage, and merging of data from different instruments. The sampling frequency of all instruments was 1 Hz. At each station and for each instrument, about 100-200 surface waters scans were collected and median averaged. The difference between the 75^{th} and 25^{th} percentile value, known as the interquartile range (IQR), was taken as a measure of dispersion. These statistics are more robust to outliers than the mean and the standard deviation.

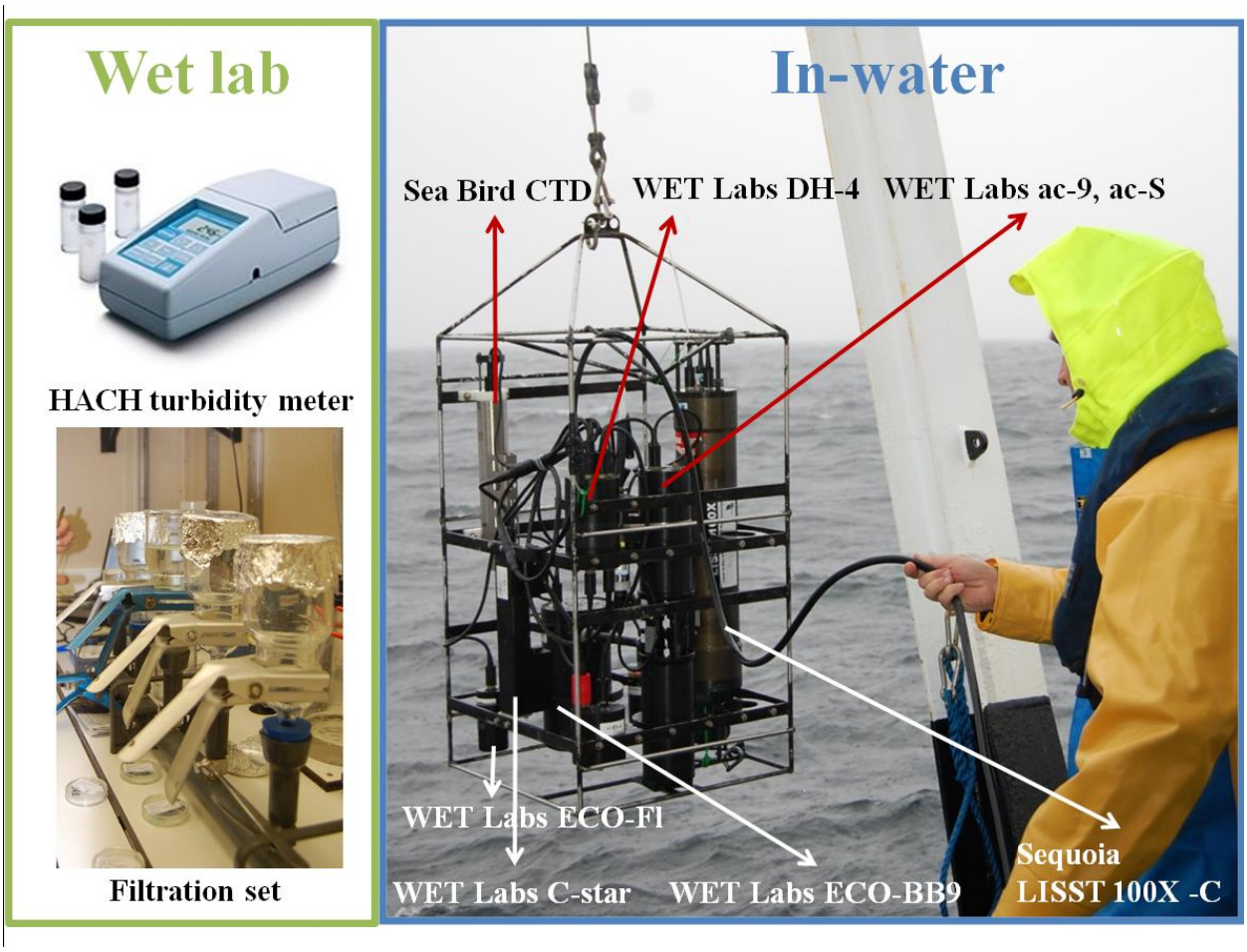

Figure 3.2. Instruments used in the wet lab of the ship (turbidity meter and filtration set) and instruments used for in-water measurements of optical properties (optical profiling package).

Beam attenuation (c) is calculated from light transmission (T), which is the light intensity reaching a detector through a sample relative to a blank. Let l be the path length of the instrument, then $c = -l^{-1}\ln(T)$. The C-Star measures c at 660 nm (±20 nm) over a 10 cm path length and has an in-water acceptance angle of 1.2°. The C-Star instrument was calibrated by WET Labs on a yearly basis and additional calibrations with MilliQ water were carried out three times per campaign. After calibration, the C-Star measurement directly gives c_p (units: m^{-1}), assuming that colored dissolved organic matter (CDOM) does not absorb at 660 nm. In addition to near-forward scattering (which is inverted to provide particle size information as described in the next section), the LISST records c at 670 nm (±0.1 nm) over a 5 cm path length with an in-water acceptance angle of 0.0135°. The LISST gives c_p after calibration with MilliQ water performed before and after each campaign assuming that CDOM does not absorb at 670 nm.

The ac-s records the absorption and attenuation spectrum at 4 nm resolution between 400 and 730 nm with 15 nm bandwidth, has a 10 cm path length and an in-water acceptance angle of 0.93°. A MilliQ water calibration was performed before and after each campaign. Temperature and salinity corrections were performed on the raw data (Pegau et al. 1997), and absorption measurements were corrected for residual scattering following Sullivan et al. 2006.

During two selected campaigns, a WET Labs ac-9 instrument was deployed vertically on a bench in the wet lab of the ship. Surface water sampled simultaneously with the optical package was passed through the measuring tubes manually. The instrument measures absorption and attenuation in 9 bands: 412, 440, 488, 510, 555, 630, 650, 676, and 715 nm, has a 25 cm path length and an in-water acceptance angle of 0.93°. A water calibration using MilliQ water was performed on a daily basis. Data were recorded for 2 minutes, and then median-averaged over 0.5 minutes of noise-free data. Temperature and salinity were recorded together with the data using a Hanna digital thermometer and a Seabird Thermosalinometer SBE-21, respectively. Temperature and salinity corrections, as well as a residual scattering correction were performed similarly to the ac-s measurements.

Backscattering coefficients $b_b(\lambda)$ at nominal wavelengths of 488, 510, 532, 595, 650, 676, 765, and 865 nm were collected with the ECO BB-9. The instrument records the volume scattering function, β, at a centroid angle of 124° (revised from 117° as reported in Sullivan et al. submitted). Data conversion from raw β to calibrated β was performed using the WAP software provided by WET Labs. Data were corrected for temperature and absorption effects and the contribution by pure water (Zhang et al. 2009) to β was subtracted to obtain particulate volume scattering function, β_p. Particulate backscattering coefficients, b_{bp}, were obtained from β_p by multiplying by $2\pi\chi$, with χ =1.1 (Sullivan and Twardowski 2009). The BB-9 instrument was calibrated by WET Labs on a yearly basis. An additional correction of b_{bp} by a factor 0.82 (=0.9:1.1) was applied following Sullivan et al. 2005.

Turbidity, defined by ISO 1999 as 'the reduction of transparency of a liquid caused by the presence of undissolved matter', can be quantified in various ways (e.g., Secchi disk, light attenuation, side scatter). The Hach 2100P portable turbidity instrument measures the ratio of light scattered at an angle of 90°±2.5° at a wavelength of 860±60 nm to forward transmitted light, as compared to the same ratio for a standard suspension of Formazine. This optical measurement technique of turbidity from the side scattering coefficient, b_s, is in accordance with ISO 1999. In this chapter, turbidity will be denoted b_s, referring to the measurement method of side scattering. b_s, expressed in Formazine Nephelometric Units (FNU), was recorded on 10 mL subsamples in triplicates before and after filtration. These replicates were median-averaged and the IQR was computed.

The spectral dependency of c_p or b_{bp} is beyond the scope of this paper and has been investigated by other authors (Snyder et al. 2008). Instead, we focus on c_p and b_{bp} at a wavelength of 650 nm, where

the attenuation by particles ($c_p = a_p + b_p$) is essentially determined by their scattering properties because a_p, the absorption by living and non-living particles, only makes a very small contribution (Loisel and Morel 1998). For example, in this dataset (272 observations) the median contribution of a_p to c_p is 1.5%, with a maximum of 6%.

3.2.3 Water sampling

At each station, water samples were collected just below the sea surface with 10 L Niskin bottles simultaneously with in situ optical measurements. [SPM] was determined gravimetrically (van der Linde 1998) by filtration of a known volume of sea water onto 47 mm Whatman GFF glass fiber filters with a nominal pore size of 0.7 μm, which effectively retain particles larger than about 0.4 μm in size. The filters were pre-ashed at 450°C for 1 h, gently washed in 0.5 L of MilliQ water, dried at 75°C for 1 h, pre-weighed on a Sartorius LE 2445 analytical balance with an accuracy of 0.1 mg, and stored in a desiccator for use within two weeks. Seawater samples were filtered immediately after collection on triplicate filters. To remove salt, filters were washed with 250 mL of MilliQ water after filtration. The samples were stored at -20°C until further analysis in MUMM's Marine Chemistry Laboratory, usually within a few months after sampling. Filters were dried for 24 h at 50°C and re-weighed to obtain [SPM]. All SPM filtrations were carried out by the lead author in triplicate using the same protocol. From these, the median and IQR were computed for each sample. Observations where the IQR exceeded 45% of the median [SPM] value were rejected. Concentration of Chl *a* and other pigments was determined by high-performance liquid chromatography (HPLC) analysis. Water samples were filtered in duplicate through 0.7 μm Whatman 47 mm GFF glass fiber filters, which were stored in liquid nitrogen until analysis in the laboratory. Pigment data were then averaged.

During some selected campaigns (92 stations) the SPM sample filters were burned for 5 h at 450 °C and then re-weighed to obtain [PIM] and [POM] by difference. From April 2010 onwards, seawater samples were analyzed for concentration of particulate organic ([POC]) and inorganic ([PIC]) carbon concentration determined with a Thermo scientific Carbon/Hydrogen/Nitrogen (CHN) elemental analyzer. Note that [SPM] includes all organic and mineral material above approximately 0.5-0.7 μm and [POC] and [POM] include autotrophic organisms, heterotrophic bacteria, and detritus. Observations were classified into clear (case 1) and turbid (case 2) waters using the relationship between b_{bp} (532 nm) and [Chl *a*] established by Loisel et al. 2010: $b_{bp} = 0.00299 \times [\text{Chl } a]^{0.704}$. Based on their in situ dataset, the threshold between case 1 and case 2 water was set at $b_{bp} = 3 \times 0.00299 \times [\text{Chl } a]^{0.704}$.

3.2.4 Particle size and mean apparent density

The scattering pattern at a wavelength of 670 nm in 32 logarithmically spaced scattering angles in the near-forward direction is recorded with a Sequoia Scientific LISST-100X type C described by Agrawal and Pottsmith 2000. The volume concentration for each of its 32 particle size classes is obtained through inversion of the angular forward scattering pattern based on the principles of light diffraction. This inversion has traditionally been done using Sequoia Scientific's inversion matrix based on a combination of Mie theory calculations (applicable strictly to homogeneous spherical particles) for several refractive indices.

Recently, empirically based inversion techniques for random shaped particles became available (Agrawal et al. 2008). The term 'random shaped' refers to the particles not having a preferred axis, excluding platy or elongated particles, and can be thought of as 'spherical surfaces with random bumps, scratches, and digs superimposed' (Agrawal et al. 2008). This inversion mitigates the problem of an artificial rising tail at the fine particle end of the number concentration PSD. This artifact was first attributed to particle shape effects by Agrawal et al. 2008, but Andrews et al. 2010 attributed it to a mismatch between the refractive index of small particles and the refractive index of the inversion matrix.

While all aforementioned LISST inversions assume that particles are solid, the LISST has been found to size aggregates as well, if sufficiently opaque (Hill et al. 2011; Slade et al. 2011). This is consistent with Latimer 1985) modeling of an aggregate as a combination of a particle with lower index of refraction and a coated particle.

The random shape inversion matrix (Agrawal et al. 2008) was used in this study, giving volume concentration, $[VC]_i$ (in μL L^{-1}), in each size class i with geometric mean diameter D_i in the range 2-350 μm. Note that Mie inversion shifts the size range to 2.5-500 μm for a type C LISST 100X operating at a wavelength of 670 nm. Basic MATLAB scripts for data processing, provided by Sequoia Scientific were adapted by the authors for adequate data quality control, custom data processing, and visualization purposes. LISST data have been reported to show considerable instability in the smallest and largest size range (Traykovski et al. 1999; Jouon et al. 2008), likely due to the presence of particles smaller and coarser than the measured size range. Hence, data from the outer and inner ring were excluded from further analysis. Instability in the smallest size ranges has also been related to effects of stray light (Reynolds et al. 2010; Andrews et al. 2011a).

Assuming spherical particles, the cross sectional area concentration of particles in size bin i, $[AC]_i$ (in m^{-1}), can be obtained from $[VC]_i$:

$$[AC]_i = \frac{3}{2D_i}[VC]_i \qquad (3.1)$$

where $2 \le i \le 31$ and 2.4 μm $\le D_i \le$ 302.1 μm. The total cross sectional area and volume concentrations, [AC] and [VC], are obtained by summation over size classes 2 to 31. Andrews et al. 2010) compared [AC] and [VC] derived from a LISST 100X (type B) using various inversion matrices against microscopy data for phytoplankton and mixed field samples. They report ratios of LISST-derived [AC] and [VC] obtained with the random shape matrix inversion to microscopy-derived [AC] and [VC] within the ranges of 0.56-0.98 and 0.34-1.08, respectively.

The mean apparent density of the suspended particle population, ρ_a (in kg L^{-1}), is the dry weight to wet volume ratio:

$$\rho_a = \frac{[\mathrm{SPM}]}{[\mathrm{VC}]} \tag{3.2}$$

The wet volume concentration, [VC], can refer to both the particle internal fluid volume, as well as the aggregate interstitial volume. Note that particles with diameter above approximately 0.4 μm are retained on a GFF glass fiber filter (effective pore size of 0.7μm), while [VC] only accounts for particles in the 2.4-302 μm range.

Marine particles are comprised of water and solid material. Let V_s and V_w be the volumes of solid and watery material of which a particle is comprised and ρ_s be the density of the solid material. Then, ρ_a can be written as:

$$\rho_a = \frac{V_s}{V_s + V_w}\rho_s \tag{3.3}$$

When the particle contains any water, ρ_a will be less than ρ_s and can be less than the density of seawater. For phytoplankton ρ_s varies between 1.24 and 1.53 kg L^{-1} and V_w between 40% and 80% (Aas 1996), giving ρ_a between 0.25 and 0.92 kg L^{-1}. For aggregated particles consisting of organic and/or inorganic compounds, V_w is mostly interstitial and size dependent (Boss et al. 2009a) and can approach 100% for the largest aggregates. This results in ρ_a as low as 0.01 kg L^{-1}.

A Junge power law distribution was fitted to the LISST data:

$$N(D_i) = KD_i^{-\gamma} \tag{3.4}$$

with $2 \le i \le 31$, where $N(D_i)$ is the number of particles in size class i per unit sampling volume and per unit width of diameter interval (units: L^{-1} μm^{-1}) and γ is called the Junge parameter. The size distribution of marine particles is influenced by various physical and biological processes, so it is unlikely that its full complexity can be completely described by a relatively simple mathematical model, such as the Junge model. This model, however, remains the most frequently used in optical studies. Its goodness of fit is evaluated by the R^2 statistic, the relative deviation of the model from the observations, and the 95%

confidence interval on the least-square estimation of γ. Typical values of γ range between 3 and 5 (Jonasz 1983; Buonassissi and Dierssen 2010; Reynolds et al. 2010). The PSD and its shape are investigated in more detail in the appendix in section 3.5.2.2.

For a given particle population we define the mean diameter weighted by area, D_A (in μm), as follows:

$$D_A = \frac{\sum_{i=2}^{31} [AC]_i D_i}{[AC]} \tag{3.5}$$

In sedimentology, this is termed the Sauter diameter.

3.2.5 Mass-specific attenuation and backscattering coefficients

For a population of spherical particles of identical ρ_a, the mass-specific beam attenuation coefficient, c_p^m (or analogously, the mass-specific particulate backscattering coefficient, b_{bp}^m) can be written as:

$$c_p^m = \frac{c_p}{\rho_a [\mathrm{VC}]} = \frac{\frac{\pi}{4}\int N(D) Q_c(D,n,\lambda) D^2 dD}{\rho_a \frac{\pi}{6}\int N(D) D^3 dD} \tag{3.6}$$

where $N(D)dD$ is the number of particles per unit volume in the size range from D to $D+dD$ and Q_c (dimensionless) is the attenuation efficiency factor, which varies with size (D), wavelength (λ), and refractive index (n) of the particles (Van De Hulst 1957). This efficiency factor is dimensionless and represents the ratio of the attenuation (backscattering) cross section to the geometric cross section.

The refractive index, n, can be estimated from the particulate backscattering ratio $\tilde{b}_{bp}$ using the Mie theory-based model of Twardowski et al. 2001):

$$n = 1 + 1.671 \tilde{b}_{bp}^{0.582} \tag{3.7}$$

This model performs reasonably well for γ<4 with differences of only a few percent between Eq. (3.7) and the more complex model for n based on $\tilde{b}_{bp}$ and γ (Twardowski et al. 2001). Eq. (3.7) is preferred here for the sake of simplicity and presentation purposes and because γ exceeds 4 in only 5% of the cases in our dataset. The particulate backscattering ratio, $\tilde{b}_{bp}$, represents the fraction of light scattered in the backward direction and has been related to the biogeochemical composition ([POC]: [Chl *a*]) of the particles (Loisel et al. 2007) and to the PSD (Ulloa et al. 1994; Loisel et al. 2006).

Consider a particle population composed of spheres of a single diameter D, then Eq. (3.6) simplifies to:

$$c_p^m = \frac{3}{2}\frac{Q_c}{\rho_a D} \tag{3.8}$$

For particle populations consisting of spheres of identical composition and density it follows that c_p^m is inversely proportional to particle diameter. For particles large compared to the wavelength of light, smaller particles attenuate more light per unit mass than large particles because their surface to volume ratio is larger (e.g., Hill et al. 2011)We can rewrite Eq. (3.6) in the form of Eq. (3.8) by defining the effective attenuation efficiency, Q_{ce}, the mean attenuation efficiency of all particles weighted by area (Eq. 3.2 in Morel 1973; Bowers et al. 2009):

$$Q_{ce} = \frac{\int N(D)Q_c(D)D^2 dD}{\int N(D)D^2 dD} \tag{3.9}$$

and $D_A = \frac{\int N(D)D^3 dD}{\int N(D)D^2 dD}$, the mean particle diameter weighted by area, which is equivalent to Eq. (3.5). Eq. (3.6) then becomes:

$$c_p^m = \frac{3}{2}\frac{Q_{ce}}{\rho_a D_A} \tag{3.10}$$

The coefficient c_p^m (in m^2 g^{-1}) is also the attenuation cross section per unit mass of particles in suspension. Eq. (3.6) and Eqs. (3.8)-(3.10) can be written for backscattering in the same way. Q_{ce} can be assessed either directly from its definition, i.e., Q_{ce}=c_p:[AC] (*see* Eq. (3.6)), or indirectly, from linear regression between c_p^m and the inverse of the product of ρ_a and D_A (*see* Eq. (3.10)). Computations of Q_{bbe} can be done by analogy.

The experimental value of Q_{ce} (=c_p:[AC]) can be used to check whether the bulk of the particles contributing to c_p are sized by the LISST, through a comparison with its theoretical value (Behrenfeld and Boss 2006). According to optical theory, the value of Q_c for a single spherical particle large compared to the wavelength of the light should be around 2 and not exceed 3.2 (Van De Hulst 1957). Underestimation of [AC] will lead to higher Q_{ce} values. The first cause of underestimation of [AC] is the limited size range of the PSD (2.4 – 302 μm in this study). Oubelkheir et al. 2005 reported c_p:[AC] ratios up to 14 due to particles outside their PSD range (1.6-50 μm). The second cause is the underestimation of [AC] of particles that are sized by the LISST. Andrews et al. 2010 report underestimates of LISST-derived [AC] values obtained from an inversion for random shape particles compared to microscopy-derived [AC] values by a factor of 1.02 to 1.79. Therefore, a maximum value for c_p:[AC] of 5.7 (=3.2×1.79) is expected

if the bulk of the particles are sized by the LISST. Observations exceeding this maximum value are rejected.

From Eq. (3.10) it follows that particle size, density, and composition affect c_p^m (b_{bp}^m) directly through D_A and ρ_a, and indirectly through Q_{ce} (Q_{bbe}). The effect of size, density, and composition on mass and area-specific c_p and b_{bp} is investigated in this paper. Correlation analysis and 'least squares cubic' regressions (York 1966), which take into account measurement uncertainties in the data, are used throughout the paper. The derivation of uncertainties on optical and biogeochemical variables is given in the Appendix, section 3.5.1.2. The least squares cubic regression is applied after removal of outliers identified by the MATLAB robustfit.m routine (*see* Appendix, section 3.5.1.3). Correlation coefficients obtained from bootstrapping are given with their 95% confidence intervals, which is also described in the Appendix, section 3.5.1.4.

3.3 Results

3.3.1 Instrument intercomparison for particulate beam attenuation

$c_{p,}$ measured by the LISST, C-Star, ac-9, and ac-s instruments are compared. The first three instruments measure c_p at slightly different wavelengths (670, 660, and 650 nm, respectively). Based on 158 spectra of c_p recorded by the ac-s, a median $c_p(650):c_p(670)$ ratio of 1.01 was found, with 90% of the ratios in the interval [0.99 , 1.03], indicating that the spectral variation of c_p between 650 and 670 nm is negligible. Good linearity in log-log space (r=0.87±0.04) was found for 188 simultaneous observations of c_p(LISST) and c_p(C-Star). Results are shown in Figure 3.3A. As expected, c_p(LISST) values are larger than c_p(C-Star) values in most cases due to the smaller acceptance angle of the LISST. Occasionally, however, the C-Star reported higher c_p values than the LISST, possibly due to slight differences in sampling time between the two instruments, high temporal variability of IOPs, and other measurement uncertainties. The median measurement uncertainty on c_p(LISST) was used as a tolerance distance from the 1:1 line (represented by the dotted line in Figure 3.3A), below which observations were removed from further analysis (n_o=16, with n_o denoting the number of observations). The correlation coefficient for the remaining 172 observations is 0.91±0.03. The median c_p(LISST):c_p (C-Star) ratio is 1.6 with 90% of the ratios in the interval [0.9,3.3], and increases with increasing particle size as shown in Figure 3.3B (r=0.88±0.08, n_o=158 after removal of observations with Q_{ce}>5.7, *see* next subsection for explanation). Similar results were found by Boss et al. 2009b who reported a mean LISST-B (acceptance angle of 0.0269°) to C-Star c_p ratio of 1.4 (90% in the interval [1.1, 1.8]) at a coastal station in the Northeast of the USA.

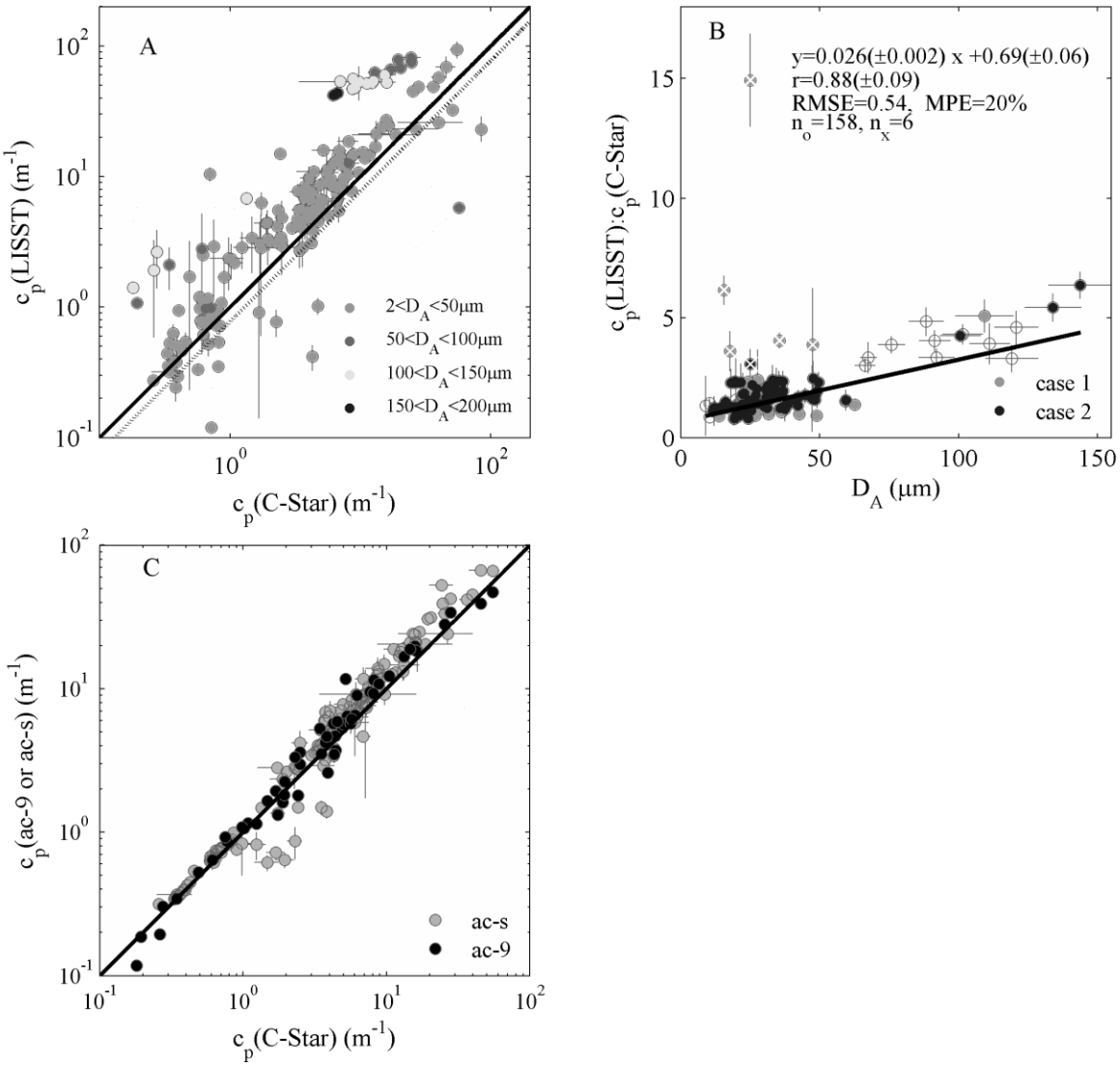

Figure 3.3. (A) Scatter plot of particulate beam attenuation (c_p) measured simultaneously with LISST and C-Star instruments, coded according to particle size (D_A). The 1:1 line (solid) and the rejection threshold line ($\log_{10}(c_p(\text{LISST}))=\log_{10}(c_p\ (\text{C-Star})-0.1124$, dotted) are shown. (B) Scatter plot of c_p(LISST): c_p(C-Star) vs. D_A. The type-II regression line (*see* section 3.5.1.3 for details) is shown, with its equation and statistics. Error bars corresponding to uncertainties above 100% are not shown for clarity. (C) Scatter plot of c_p measured simultaneously by the C-Star and the ac-s or ac-9. The 1:1 line is also shown. On each panel, error bars denote uncertainty estimates as derived in the section 3.5.1.2.

Both c_p(ac-s) and c_p(ac-9) are in good agreement with c_p(C-Star), with correlation coefficients of 0.97±0.01 (n_o=149) and 0.98±0.02 (n_o=57), respectively (*see* Figure 3.3C). Because of the smaller acceptance angles of the ac-9 and ac-s instruments, data generally lie above the 1:1 line. Some

observations, however, are found below the 1:1 line. Recall that the ac-9 measurements were carried out in the wet lab of the ship on seawater sampled simultaneously with the optical profiling package. Small differences in sampling time or depth between the sample bottle and the profiling package may result in ac-9 observations below the 1:1 line. All ac-s observations below the 1:1 line were recorded in April 2010 during a bloom of *Phaeocystis globosa* colonies. It is hypothesized that these did not entirely pass through the ac-s steel mesh screen on the intakes to the sample chambers of the ac-s, or the pump got clogged by mucilage present in high concentrations during blooms. This analysis suggests that pumping seawater through the chambers of the ac-s can reduce c_p if particles larger than the steel mesh screen size are present or the pump is clogged by mucilage. Boss et al. 2009b showed that in a coastal environment dominated by aggregates, pumped c_p(LISST-B) was about 30% higher than undisturbed c_p(LISST-B), possibly caused by disruption of aggregates.

3.3.2 Relationships between scattering properties and particle concentration by area or dry weight

Relationships and correlations between various IOPs and area ([AC]) and mass ([SPM]) concentration are investigated. Observations are retained where all optical properties (c_p, b_s, and b_{bp}), [SPM] and [AC] were recorded (n_o=119) and where the bulk of the particles were sized by the LISST (Q_{ce} < 5.7). A total of 107 data points remain, of which 35 are classified as case 1 and 72 as case 2 waters. The ac-s c_p measurements are not included due to uncertainties on the effect of the steel mesh screen as described above.

Scatter plots of c_p, b_s, and b_{bp} as a function of [SPM] and [AC] in log-log space are shown in Figure 3.4. Each parameter covers about 2 orders of magnitude. All scattering properties correlate well with both area and mass concentration, with correlation coefficients above 0.93 (*see* Table 3.1). For c_p, no significant differences between correlations with [AC] (r_{LISST} =0.98±0.01, $r_{\text{C-Star}}$ = 0.95±0.04) or with [SPM] (r_{LISST}=0.94±0.04, $r_{\text{C-Star}}$=0.95±0.02) were found. The coefficients b_s and b_{bp} are significantly better correlated with [SPM] (r_{bs}=0.988±0.007, r_{bbp}=0.986±0.007) than with [AC] (r_{bs}=0.93±0.05, r_{bbp} =0.92±0.05). In the case of b_s, this could be attributed to the fact that the exact same volume of seawater on which b_s was recorded, was passed through the filter for determination of [SPM]. Recall that while [AC] includes particles between 2.4 and 302 μm, [SPM] is the mass concentration of particles larger than approximately 0.4 μm. The lower correlation of b_{bp} with [AC] than with [SPM] might be attributed to differences in particle size ranges covered by each parameter. These include particles smaller than 2.4 μm, which are thought to be important contributors to b_{bp} assuming particles are homogeneous spheres (Stramski et al. 2004), and particles larger than 302 μm, which may contribute substantially to b_{bp} (Hatcher et al. 2001; Flory et al. 2004).

Table 3.1. Correlation coefficients (*r* with 95% confidence interval, *see* section 3.5.1.4 for computation) between an optical property and either area concentration, [AC], or mass concentration, [SPM] (in log log space) for 107 observations (35 case 1 and 72 case 2). The median, 5th, and 95th percentile values of mass- and area-specific optical properties are shown. Correlations and mass-specific coefficients for all simultaneous observations of an optical property and [SPM] are also shown between brackets (database size, n_t, is indicated in italic).

			Population percentile values		
parameter	case (n_t)	*r*	5	50	95
c_p^m (LISST)	1	0.85±0.10	0.57	1.40	3.46
	(*44*)	(0.75±0.16)	(0.46)	(1.29)	(3.73)
	2	0.78±0.08	0.36	0.71	1.14
	(*96*)	(0.68±0.12)	(0.28)	(0.72)	(2.99)
	1+2	0.94±0.04	0.38	0.79	2.22
	(*180*)	(0.88±0.04)	(0.31)	(0.80)	(3.19)
Q_{ce}(LISST)	1	0.98±0.02	1.86	2.50	4.20
	2	0.92±0.05	2.24	3.35	4.54
	1+2	0.98±0.01	2.03	3.08	4.47
c_p^m (C-Star)	1	0.89±0.09	0.33	0.97	2.01
	(*65*)	(0.86±0.08)	(0.44)	(0.81)	(1.79)
	2	0.78±0.08	0.25	0.45	0.71
	(*105*)	(0.92±0.03)	(0.25)	(0.45)	(0.78)
	1+2	0.95±0.02	0.26	0.54	1.39
	(*206*)	(0.94±0.02)	(0.25)	(0.53)	(1.36)
Q_{ce} (C-Star)	1	0.85±0.18	0.84	1.84	3.04
	2	0.83±0.06	1.31	2.14	3.32
	1+2	0.95±0.04	1.18	2.00	3.30
b_s^m	1	0.95±0.05	0.50	0.84	1.34
	(*80*)	(0.89±0.06)	(0.57)	(0.96)	(1.82)
	2	0.95±0.04	0.75	1.04	1.30
	(*145*)	(0.990±0.004)	(0.79)	(1.08)	(1.50)
	1+2	0.988±0.007	0.63	0.99	1.32
	(*333*)	(0.987±0.003)	(0.66)	(1.08)	(1.82)
Q_{bse}	1	0.86±0.11	0.77	1.55	4.62
	2	0.83±0.07	2.52	5.30	7.81
	1+2	0.93±0.05	0.98	4.47	7.54
b_{bp}^m	1	0.96±0.03	0.0038	0.0054	0.0097
	(*80*)	(0.86±0.06)	(0.0038)	(0.0069)	(0.0127)
	2	0.92±0.04	0.0067	0.0100	0.0141
	(*137*)	(0.97±0.01)	(0.0065)	(0.0104)	(0.0152)
	1+2	0.986±0.007	0.0043	0.0091	0.0133
	(*229*)	(0.97±0.01)	(0.0043)	(0.0094)	(0.0149)
Q_{bbe}	1	0.83±0.16	0.0041	0.0103	0.0340
	2	0.81±0.12	0.0256	0.0489	0.0828
	1+2	0.92±0.05	0.0067	0.0424	0.0797

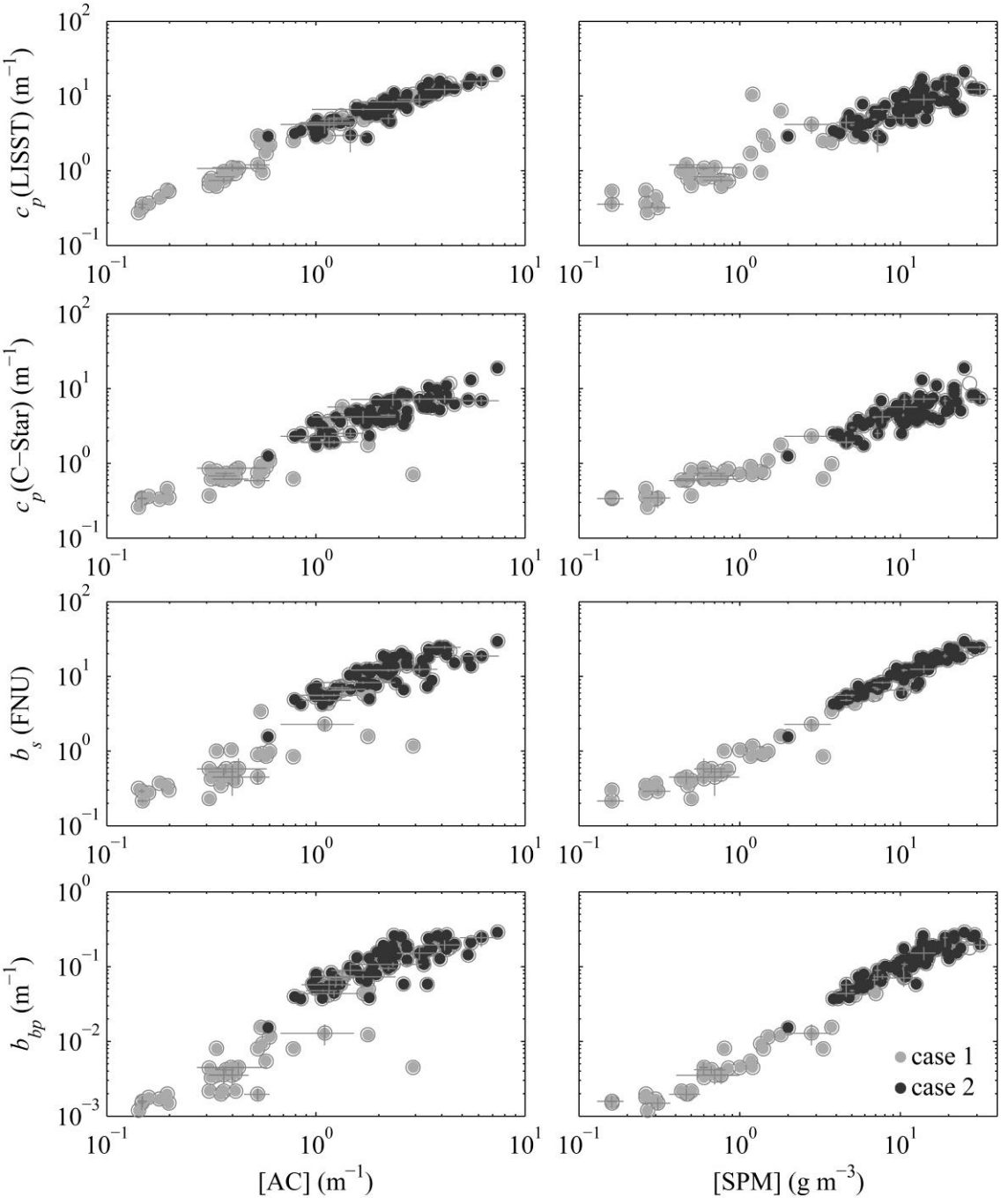

Figure 3.4. Log-log scatter plots of c_p(LISST), c_p(C-Star), b_s, and b_{bp} vs. area concentration, [AC] (left column) and mass concentration, [SPM] (right column) for 35 case 1 and 72 case 2 waters. Error bars denote uncertainty estimates as derived in section 3.5.1, shown only for 20 random observations for the sake of clarity.

Flory et al. 2004 studied the relationship between b_{bp} and [AC] for flocs larger than 100 μm during the onset, development, and collapse of a spring phytoplankton bloom in Nova Scotia. Their b_{bp} and [AC] data ranges were comparable to this study. They report b_{bp}(589nm):[AC] values as the slope of a b_{bp} vs. [AC] regression with a value of 0.012±0.001 before the bloom when particles were mainly inorganic, and 0.0029±0.0001 during and after the bloom when the suspended particulate matter was dominated by larger organic particles and aggregates. In this study we find higher values of 0.041±0.003 for case 2 waters (with median n of 1.15, 90% in the interval [1.10, 1.20], n_o=72) and 0.012±0.002 for case 1 waters (with median n of 1.07, 90% in the interval [1.04, 1.13], n_o=35).

The 5, 50, and 95th percentile values of the ratios of optical properties to area and mass concentration are shown in Table 3.1. Rejecting the 10% most extreme values, Q_{ce}(LISST), that is c_p(LISST):[AC], varies by about a factor 2 between 1.86 and 4.54, while c_p^m(LISST) covers almost one order of magnitude ranging between 0.36 and 3.46. Comparable results are observed for c_p(C-Star). For b_{bp} and b_s, however, Q_{bbe} (Q_{bse}) spans more than one order of magnitude, while b_{bp}^m and b_s^m vary by factors of 3 to 4.

Carder et al. 1975 argued that in the case of solid spherical particles b_p^m would vary less than b_p:[AC] because of the more or less concomitant variations in n and ρ_a. While b_{bp}^m varies less than b_{bp}:[AC], the opposite is observed for c_p^m (which is comparable to b_p^m at 650 nm) and c_p:[AC]. In what follows, the sensitivity of mass-specific (back) scattering to each of the components in Eq. (3.10) (i.e., particle size, density, efficiency, and composition) is examined. Next, a similar sensitivity analysis is done for efficiency factors of attenuation (Q_{ce}) and backscattering (Q_{bbe}).

3.3.3 Investigation of the variability of mass-specific scattering properties

Correlation coefficients, regression equations, and goodness of fit statistics for c_p^m(LISST) and b_{bp}^m vs. D_A, ρ_a, efficiency factors, and composition are shown in Table 3.2. A selection of corresponding scatter plots and best fit lines are shown in Figure 3.6A-G. A large portion of the variability in c_p^m(LISST) is explained by $(\rho_a D_A)^{-1}$ (r=0.95±0.03, Figure 3.6A). Attenuation efficiency factors, $Q_{ce,}$ were obtained from a linear regression of c_p^m and $(\rho_a D_A)^{-1}$ by multiplication of the slope of the regression line in Table 3.2 by 2:3 (*see* Eq. (3.10)). Median Q_{ce}(LISST) values of 2.13±0.07 (r=0.96±0.04) and 3.07±0.02 (r=0.84±0.06) are obtained for case 1 and case 2 waters, respectively. Bowers et al. (2009) find Q_{ce}=1.27±0.05 for

mainly mineral particles along the South and West coast of Britain where b_p^m(670 nm) varied between 0.06 and 1.01 m^2 g^{-1}. Differences in Q_{ce} could be due to acceptance angle effects.

When the effects of ρ_a^{-1} and D_A^{-1} are considered separately, we find that changes in ρ_a almost entirely control changes in c_p^m(LISST) (r=0.88±0.06), with denser particles having lower c_p^m, while changes in particle size have little influence (*see* Table 3.2 and Figure 3.6B). Bowers et al. (2009) also find that most of the variability in b_p^m is explained by ρ_a (59%) with little contribution from D_A (15%). In case 2 waters, c_p^m(C-Star) increased with decreasing D_A (r=0.54±0.15 with D_A^{-1}, n_o=72, p<0.001, *see* Figure 3.5). This size effect could be caused by the large acceptance angle of the C-Star instrument: the fraction of c_p that is actually detected decreases rapidly with D_A (Boss et al. 2009b, *see* Figure 1.7), whereas a large fraction of the particle mass might be contained in larger particles that the C-Star is relatively insensitive to.

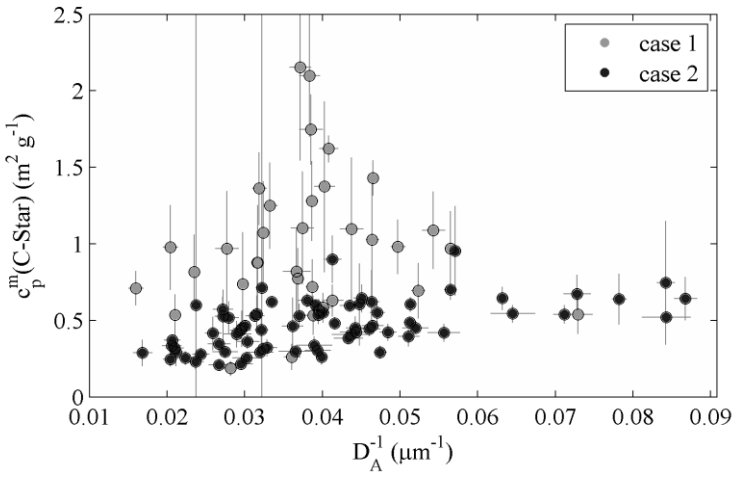

Figure 3.5. c_p^m(C-Star) versus D_A^{-1} in case 1 and case 2 waters.

Table 3.2. Correlations and regression analysis of mass-specific attenuation (c_p^m) and backscattering (b_{bp}^m) vs. mean particle diameter (D_A), mean apparent density (ρ_a), mean optical efficiency factors (Q_{ce}, Q_{bbe}), and particle composition. ns: not significant (i.e., p>0.05), *: p<0.001, n_o is the number of observations, n_x is the number of outliers removed as described in section 3.5.1.3.

			c_p^m (LISST)			b_{bp}^m		
x	case	n_o	n_x	r	equation, RMSE, MPE(%)	n_x	r	equation, RMSE, MPE(%)
$(\rho_a D_A)^{-1}$	1	35	3	0.96±0.04*	3.2(±0.1) x+0.17(±0.04),0.23,12	0	ns	-
	2	72	1	0.84±0.06*	4.6(±0.3) x +0.04(±0.05),0.13,15	1	0.28±0.23	-
	1+2	107	4	0.95±0.03*	3.5(±0.1) x +0.18(±0.03),0.16,13	2	-0.43±0.14*	-0.014(±0.001) x +0.0117(±0.0004),0.0030,18
ρ_a^{-1}	1	35	5	0.92±0.07*	0.113(±0.007) x +0.29(±0.05),0.30,12	0	ns	-
	2	72	1	0.53±0.19*	0.12(±0.01) x +0.21(±0.06),0.22,22	2	0.36±0.23	-
	1+2	107	5	0.88±0.06*	0.123(±0.006) x +0.21(±0.04),0.25,19	2	-0.46±0.12*	-0.0005(±0.0001) x +0.0118 (±0.0004),0.0029,19
D_A^{-1}	1	35	1	ns	-	1	0.37±0.21*	0.09(±0.03) x +0.002(±0.001),0.0017,20
	2	72	0	ns	-	2	ns	-
	1+2	107	11	ns	-	1	ns	-
Q_{ce} or Q_{bbe}	1	35	2	ns	-	0	0.35±0.28	-
	2	72	3	0.37±0.22	-	4	0.43±0.21*	0.11(±0.01) x +0.004(±0.001),0.0019,11
	1+2	107	11	ns	-	2	0.76±0.10*	0.12(±0.01) x +0.0040(±0.0004),0.0020,12
$\frac{[POC]}{[POC]+[PIC]}$	1	17	1	ns	-	0	ns	-
	2	30	1	ns	-	0	-0.56±0.21*	-0.008(±0.002) x +0.014(±0.001),0.0018,11
	1+2	47	1	0.51±0.26*	0.95(±0.25) x +0.35(±0.15),0.35,31	0	-0.64±0.14*	-0.009(±0.002) x +0.014(±0.001),0.0023,19

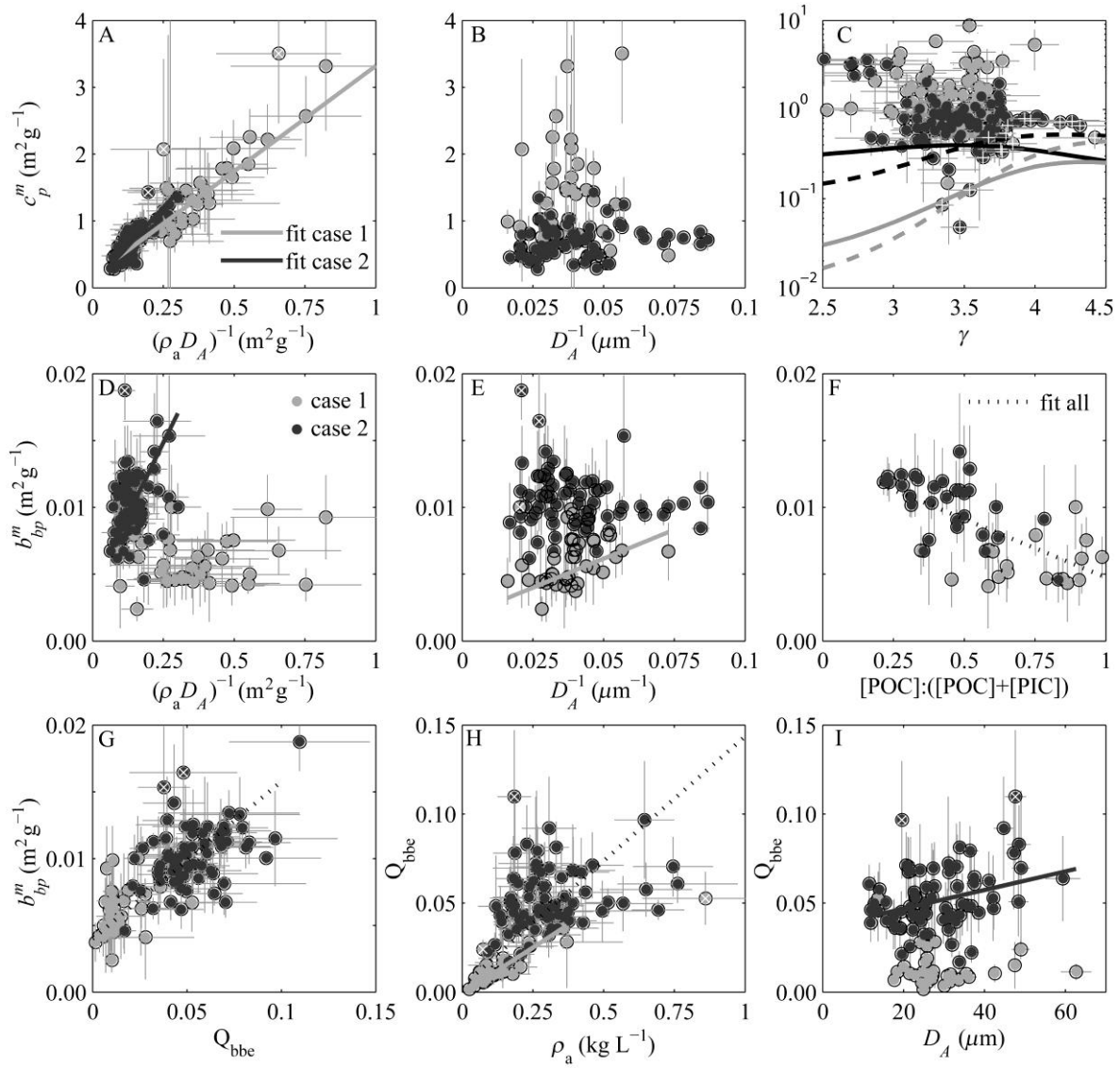

Figure 3.6. Scatter plots of mass-specific beam attenuation, $c_p^m(\mathrm{LISST})$ vs. (A) the scattering cross section (inverse of the product of apparent density and diameter, $(\rho_a D_A)^{-1}$), (B) the inverse of particle diameter weighted by area, D_A^{-1}, and (C) hyperbolic slope of the PSD. Modeling results of Boss et al. 2009a are shown for solid spherical particles (black lines) and for aggregates (grey lines) with refractive indices of 1.05+0.0001*i* (solid) and 1.15+0.0001*i* (dashed). Scatter plots of mass-specific backscatter, b_{bp}^m vs. (D) $(\rho_a D_A)^{-1}$, (E) D_A^{-1}, (F) [POC]:([POC]+[PIC]), and (G) backscattering efficiency, Q_{bbe} (=b_{bp}:[AC]). Scatter plots of Q_{bbe} vs. ρ_a (H) and D_A (I). Error bars on all panels denote uncertainties as derived in section 3.5.1.2. Equations and statistics of the fitted lines can be found in Table 3.2 and Table 3.3.

The relative size independency of c_p^m has been explained by the process of particle aggregation (Boss et al. 2009a; Hill et al. 2011). When particles aggregate and grow in size, they incorporate water in their structure and their density decreases. When ρ_a is inversely proportional to diameter ($\rho_a \propto D_A^{-1}$), it

follows from Eq. (3.10) that c_p^m is independent of size, as pointed out previously by several authors (Hill et al. 1994; Ganju et al. 2006; Curran et al. 2007). The relationship between ρ_a and D_A is shown in Figure 3.7. Overall, ρ_a and D_A are inversely related (r=-0.78±0.12, $\rho_a \propto D_A^{-1.24(\pm 0.05)}$, n_o=140). The relationship is tighter in case 2 waters (r=-0.83±0.12, $\rho_a \propto D_A^{-1.31(\pm 0.05)}$, n_o=81) than in case 1 waters (r=0.49±0.29, $\rho_a \propto D_A^{-1.30(\pm 0.32)}$, n_o=35).

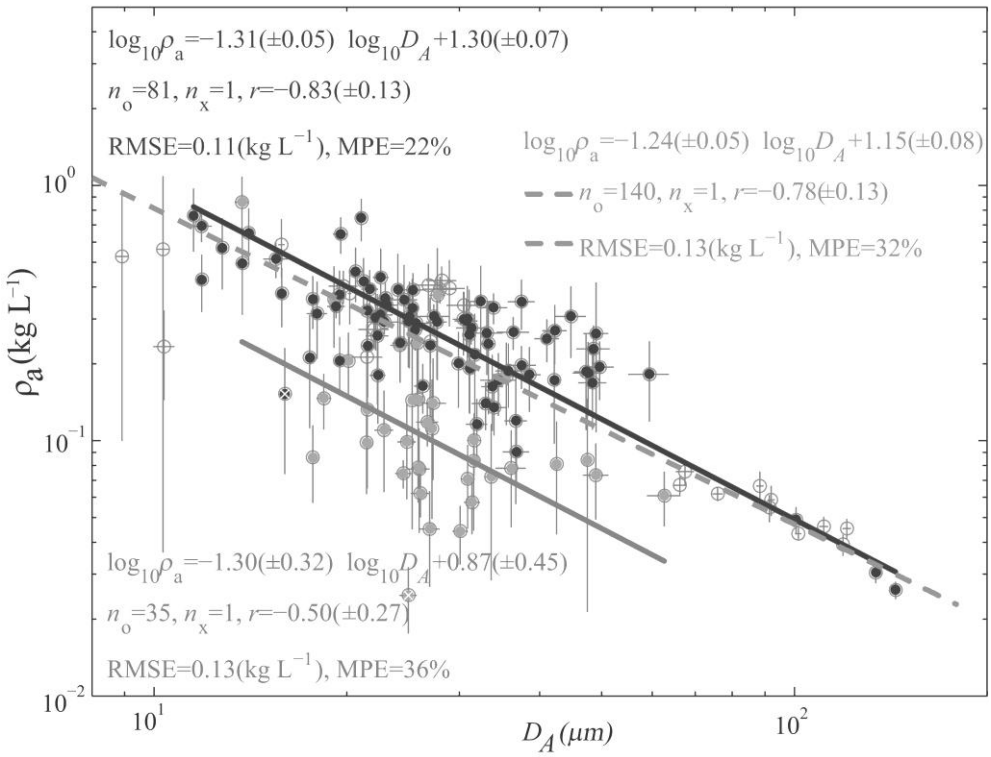

Figure 3.7. Mean particle apparent density (ρ_a) vs. mean particle diameter weighted by area (D_A). The relationship is shown for all data (black circles), for case 1 (grey dots) and case 2 waters (black dots). Statistics and equations of the type-II regression lines (see section 3.5.1.3 for details) fitted to each dataset are also shown. Error bars denote uncertainty estimates as derived in section 3.5.1.2.

Significant deviations from the Junge PSD model given in Eq. (3.4) were observed (*see* Appendix, section 3.5.2). The Junge PSD model generally overestimated number concentrations by up to a factor 3 at the fine (< 4 μm) and large (> 60 μm) particle end of the PSD and underestimated in between. Even though the Junge model provided a relatively poor fit to the measured PSDs, the Junge parameter, γ, can be used as a rough indicator of the relative proportion between the number of small and large particles. No significant correlations are found between c_p^m or b_{bp}^m and γ (*see* Figure 3.6C). According to Mie theory, c_p^m should increase over one order of magnitude with increasing γ,

and the increase is steeper with increasing real part of the refractive index (*see* grey lines in Figure 3.6C from Boss et al. 2009a for a wavelength of 660 nm). If, however, particles are modeled as aggregates rather than solid spheres, c_p^m is rather insensitive to γ (*see* black lines in Figure 3.6C from Boss et al. 2009a). Also shown in Figure 3.6C are the 10% highest density observations (n_o=16, ρ_a > 0.45 kg L^{-1}), which are thought to be least aggregated. These observations show a sharp increase in c_p^m with γ increasing from 3 to 4 and then a plateau between 4 and 4.5. This is in accordance with Mie theory, although there is an offset in absolute values of c_p^m possibly due to differences in densities between the model and the in situ measurements. A mean γ of 3.4±0.3 and 3.5±0.4 is observed in case 1 and case 2 waters, respectively, which is in close agreement with the mean value of 3.5 found by Reynolds et al. 2010 from many PSDs measured in coastal waters.

Whereas 90% of the variability in c_p^m could be attributed to $(\rho_a D_A)^{-1}$, variability in b_{bp}^m was more difficult to discern and correlation coefficients for the parameters tested are lower (*see* Table 3.2). In contrast to c_p^m, variability in b_{bp}^m is not explained well by $(\rho_a D_A)^{-1}$, though there is a clear separation between case 1 and case 2 waters as shown in Figure 3.6D. Higher correlations are found between b_{bp}^m and particle composition, as quantified by the ratio of [POC] to the sum of [POC] and [PIC] (r=-0.64±0.14, Table 3.2). The robust regression line fitted to the pooled dataset (case 1 and case 2 waters) is shown in Figure 3.6F with equation (*see* also Table 3.2):

$$b_{bp}^m = -0.009(\pm 0.002)\frac{[\mathrm{POC}]}{[\mathrm{POC}]+[\mathrm{PIC}]} + 0.014(\pm 0.001) \qquad (3.11)$$

Waters dominated by inorganic particles backscatter up to 2.4 times more per unit dry mass (b_{bp}^m =0.0121±0.0023 $m^2\ g^{-1}$) than waters dominated by organic particles (b_{bp}^m =0.0051±0.0023 $m^2\ g^{-1}$). The [POC] dataset comprises 47 observations in southern North Sea and northeastern Atlantic waters, with D_A ranging between 14 and 49 μm and ρ_a ranging between 0.07 and 0.86 kg L^{-1}. A similar, but weaker, relationship (r=-0.43±0.30) is found for 22 [POM]:[SPM] observations in the southern North Sea, giving the following robust fit:

$$b_{bp}^m = -0.009(\pm 0.003)\frac{[\mathrm{POM}]}{[\mathrm{SPM}]} + 0.010(\pm 0.001) \qquad (3.12)$$

Here, D_A varied between 23 and 135 μm, ρ_a between 0.04 and 0.39 kg L^{-1}, and [POM] :[SPM] between 20% and 90%. [POM] and [PIM]-specific b_{bp} varies between 0.001 and 0.05 $m^2\ g^{-1}$, which is in good agreement with the 0.001-0.025 $m^2\ g^{-1}$ range reported by Snyder et al. 2008 where [POM]:[SPM] varied between 34% and 70%. Martinez-Vicente et al. 2010 report a b_{bp}(532nm):[PIM] of 0.0055±0.0012 $m^2\ g^{-1}$ (n_o=16), at the lower limit of our observations.

In case 1 waters, none of the variables correlated significantly with b_{bp}^{m} at the p<0.001 level, except particle size (*see* Table 3.2). Smaller particles with D_A around 15 μm have b_{bp}^{m} values of 0.0080±0.0017 m² g^{-1} and backscatter about twice as much per unit mass than larger particles with D_A around 50 μm. However, this relationship is weak (*see* Figure 3.6E), explaining only 14% of the variability. In case 2 waters no correlation with size is found, which is in accordance with the clay particle aggregation experiment by Slade et al. 2011. Possible causes for lower correlations in case 1 waters are higher contributions to b_{bp} from submicron particles which are not included in the PSD and/or higher measurement uncertainties compared to case 2 waters.

Whereas no sensitivity of c_p^m to Q_{ce} is found (*see* Table 3.2), significant positive correlations are found between b_{bp}^{m} and Q_{bbe} for case 2 waters and pooled case 1+case 2 waters with correlation coefficients of 0.43±0.21 and 0.76±0.10 respectively. The relationship between b_{bp}^{m} and Q_{bbe} is shown in Figure 3.6G. In what follows we investigate the effect of D_A, ρ_a, and composition on the optical efficiency factors, Q_{ce} and Q_{bbe}.

3.3.4 Investigation of the variability of attenuation and backscattering efficiency

Correlation coefficients, regression equations, and goodness of fit statistics between the optical efficiency factors (Q_{ce} and Q_{bbe}) and potential drivers of optical variability (D_A, ρ_a, and composition) are shown in Table 3.3. Both Q_{ce} and Q_{bbe} are mostly driven by particle composition, with correlation coefficients of -0.65±0.14 and -0.69±0.12, respectively. Inorganic-dominated waters with 80% [PIC] have mean Q_{ce} values of 3.6±0.42 which is about twice as high as the mean Q_{ce} value of 2.29±0.42 for organic-dominated waters with 5% [PIC]. Variability of Q_{bbe} covers about one order of magnitude, from 0.007 for organic-dominated waters to 0.067±0.018 for inorganic-dominated waters. No further drivers of Q_{ce} were identified. This efficiency factor did not correlate with particle size and only 15% of its variability could be attributed to ρ_a.

Besides particle composition, other drivers of Q_{bbe} were identified depending on the water type. In case 1 waters, 90% of the Q_{bbe} values range between 0.004 and 0.034 with a median value of 0.010 (*see* Table 3.1). Vaillancourt et al. 2004) report Q_{bbe} factors at λ=620 nm between 0.001 and 0.068, with a mean of 0.011, for 28 phytoplankton cultures with diameters from 1.4 to 35 μm. This is in good agreement with our case 1 observations. About 85% of the variability is attributed to ρ_a (*see* Table 3.3and Figure 3.6H). The densest particle suspensions (ρ_a=0.37 kg L^{-1}) have mean Q_{bbe} values of 0.036, and backscatter light 20 times more efficiently than porous particle suspensions (ρ_a=0.02 kg L^{-1}). In case 2 waters we find higher Q_{bbe} factors, with 90% of the values ranging between 0.026 and 0.083 and a median value of 0.049. These values correspond well with the Q_{bbe} range of 0.046 to 0.062 and mean value of 0.051 at λ=650 nm as reported by Peng and Effler 2010 for mineral particle

populations. A small fraction (21%) of the variability in Q_{bbe} is attributed to particle size (*see* Table 3.3). Since only particles between 2.4 and 302 μm were sized and included in [AC], these results should be interpreted cautiously.

Table 3.3. Correlations and regression analysis of optical efficiency factors (Q_{ce}, Q_{bbe}) vs. mean particle diameter (D_A), mean apparent density (ρ_a), and particle composition. ns: not significant (i.e., p>0.05), *: p<0.001, n_o is the number of observations, n_x is the number of outliers removed as described in section 3.5.1.3.

			Q_{ce}			Q_{bbe}		
x	case	n_o	n_x	r	equation, RMSE, MPE(%)	n_x	r	equation, RMSE, MPE(%)
ρ_a	1	35	1	0.44±0.35	-	2	0.92±0.11*	0.10(±0.01) x -0.0007(±0.0007),0.0037,19
	2	72	0	ns	-	1	0.32±0.19	-
	1+2	107	1	0.39±0.13*	4.4(±0.5) x +2.0(±0.1),0.82,16	1	0.63±0.11*	0.14 (±0.01) x +0.004(±0.004),0.0203,42
D_A	1	35	1	ns	-	6	ns	-
	2	72	0	ns	-	2	0.46±0.18*	0.0001 (±0.0002) x +0.04(±0.01),0.0182,21
	1+2	107	0	ns	-	0	ns	-
$\frac{[POC]}{[POC]+[PIC]}$	1	17	0	-0.63±0.23*	-2.5(±0.8) x +4.5(±0.6),0.59,18	4	ns	-
	2	30	1	ns	-	0	-0.59±0.19*	-0.08(±0.02) x +0.09(±0.01),0.016,21
	1+2	47	2	-0.65±0.14*	-1.7(±0.3) x +3.9(±0.2),0.42,10	0	-0.69±0.12*	-0.08(±0.01) x +0.083(±0.007),0.018,29

3.3.5 Scattering measurements as proxies for [SPM]

When all observations are considered (n_o=366), regardless of whether information on size or composition is available, optical and [SPM] data each span over 3 orders of magnitude. The data range is slightly lower for b_{bp} due to saturation of the instrument at high levels of [SPM]. Correlation coefficients and 5, 50, and 95th percentile values of mass-specific scattering properties are shown in Table 3.1. Correlations are similar to the values found for the more limited dataset presented in Table 3.1: b_s correlates best with [SPM], followed by b_{bp} and c_p.

The median c_p^m (C-Star) values are close to the mean b_p^m (555 nm) values of 1 and 0.5 m^2 g^{-1} reported by Babin et al. 2003) for case 1 and case 2 waters, respectively, whereas the c_p^m (LISST) values are about 60% higher due to acceptance angle effects. McKee and Cunningham 2006) best-fit value of c_p^m (650 nm, ac-9)=0.34±0.01 m^{2}g^{-1} for mineral-rich case 2 waters in the Irish Sea is at the lower end of our C-Star observations. Values of b_{bp}^m by Martinez-Vicente et al. 2010 and Loisel et al. 2009 at λ=532 nm are 0.0034±0.0008 m^{2}g^{-1} (n_o=19) and 0.0065±0.0025 m^{2}g^{-1} (n_o=13) respectively, and are at the lower end of our observations.

Scatter plots of c_p(LISST), c_p(C-Star), b_{bp}, and b_s as a function of [SPM] for all available data are shown in Figure 3.8. On each plot, the least squares regression line, its 90% prediction bounds, equation, and statistics are also shown. For comparison, the 90% prediction bounds of the c_p(676 nm, ac-9) vs. [SPM] data from Babin et al. 2003 are also indicated in Figure 3.8A,B, as well as the c_p(650 nm, ac-9) vs. [SPM] data from McKee and Cunningham 2006. The effect of the smaller acceptance angle of the ac-9 instrument used by Babin et al. 2003 is clearly visible in Figure 3.8A.

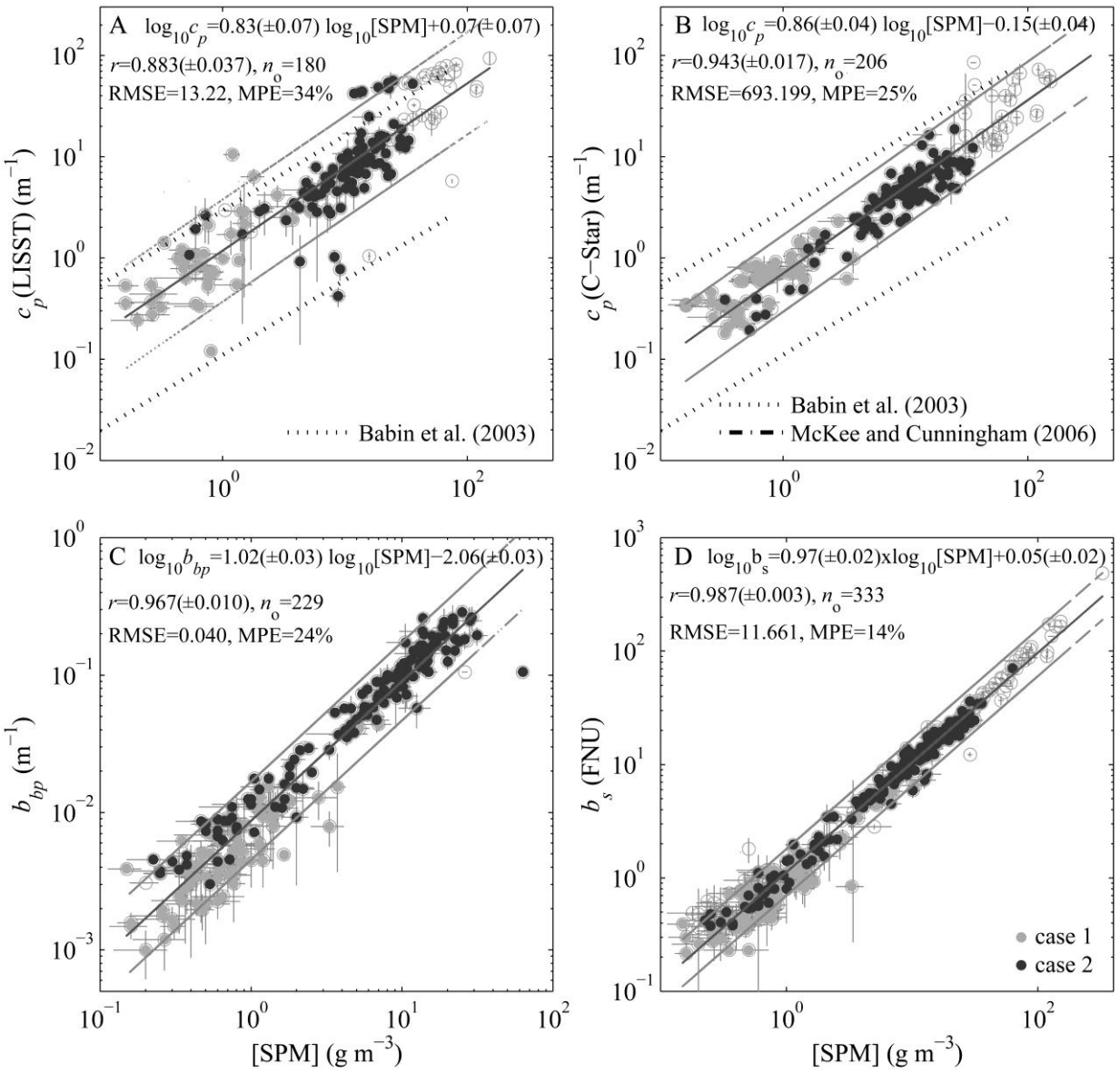

Figure 3.8. Scatter plots of (A) c_p(LISST), (B) c_p(C-Star), (C) b_{bp}, and (D) b_s vs. [SPM]. Robust regression lines are shown in black, together with their 90% prediction bounds, equations and statistics. (A, B) For comparison, the 90% prediction bounds of the c_p(676 nm)-[SPM] data of Babin et al. 2003 and the c_p(650 nm)-[SPM] data of McKee and Cunningham 2006.

To compare the performance of c_p, b_s, and b_{bp} as proxies for [SPM], data points where all optical properties and [SPM] were recorded were retained (n_o=126). Linear regression prediction models for [SPM] were established. All scattering properties are relatively good predictors of [SPM], with correlation coefficients above 0.90. Model performances were evaluated through comparison of the ratio of the absolute difference between [SPM] from regression and its observed value to its observed value,

the prediction percentile error (PPE). Results are shown in Table 3.4. In 50% and 95% of the cases, a b_{bp} -based [SPM] model agrees with the observed [SPM] within 18% and 47%, respectively. The b_s-based [SPM] model performs best, predicting [SPM] within 41% of its true value in 95% of the cases. Boss et al. 2009c found b_{bp} to be the best proxy for [SPM], followed by b_s and c_p. Their comparison was based on 85 samples from the eastern and western coasts of North America with [SPM] ranging between 1.2 and 82.4 g m^{-3}. For comparison with Boss et al. 2009c, prediction percentile errors obtained from our observations covering the same [SPM] range are shown between brackets in Table 3.4 (n_o=98), as well as the PPE's and correlation coefficients found by those authors. In the present study, b_s was recorded on a subsample of the Niskin seawater sample, which might explain the better performance of the b_s-based model compared to models based on optical properties recorded in-water.

Table 3.4. Optical properties as proxies for [SPM]. Prediction percentile error, PPE, i.e., the ratio of the absolute value of the difference between a type-II regression model derived [SPM] and its observed value to its observed value. Values between brackets for an optical model with 1.2<[SPM]<82.4 g m-3 for our dataset and for the dataset of Boss et al. 2009c in italic. r is the correlation coefficient with its 95% confidence interval (see section 3.5.1.4 for details).

		Population percentiles (%)		
PPE	*r*	5	50	95
c_p (LISST)	0.90±0.05	4	37	283
c_p (C-Star)	0.95±0.01 (0.89±0.04, *0.970±0.005*)	4 (3, *2*)	32 (29, *16*)	107 (59, *54*)
b_s	0.990±0.006 (0.97±0.02, *0.962±0.008*)	1 (1, *2*)	11 (10, *21*)	41 (37, *51*)
b_{bp}	0.987±0.006 (0.96±0.02, *0.982±0.005*)	1 (1, *1*)	18 (17, *9*)	47 (44, *36*)

3.4 Discussion and conclusion

In this study, we show that first order variability of c_p, b_{bp}, and b_s is driven by particle concentration with best predictions of dry mass concentration, [SPM], by b_{bp} and b_s and of surface area concentration, [AC], by c_p. Second order variability of c_p and b_{bp} was investigated with respect to the nature of the particles in suspension through analysis of variability in mass-specific (c_p^m and b_{bp}^m) and area-specific coefficients in response to changes in particle composition, size, and density. PSDs were derived from a LISST particle sizer, covering the size range 2.4-302 μm. We have shown that the variability of c_p^m (LISST) covers

more than 1 order of magnitude from 0.28 to 3.45 m² g^{-1}. About 90% of its variability is due to the direct combined effect of particle apparent density and size, $(\rho_a \times D_A)^{-1}$, with the strongest contribution coming from ρ_a which explains 77% of the variability. The coefficient b_{bp}^m shows less variability with 90% of the observations varying by a factor 3-4 between 0.004 and 0.014 m² g^{-1}. Factors driving variability in b_{bp}^m are more difficult to discern although particle composition, which acts indirectly on b_{bp}^m via Q_{bbe}, explains about 40% of the variability. Inorganic particles are, on average, about 2-3 times more efficient per unit mass (b_{bp}^m =0.012 m² g^{-1}) than organic particles (b_{bp}^m =0.005 m² g^{-1}).

Carder et al. 1975 reasoned that for solid spherical particles b_p^m would vary less than b_p:[AC] because of the more or less concomitant variations in n and ρ_a. Figure 3.9 shows the variability of $\tilde{b}_{bp}$ (related to n via Eq. (3.7)) with ρ_a and particle composition. Significant correlations are found between $\tilde{b}_{bp}$ (and n) and particle composition, as quantified by (i) [POC]:([POC]+[PIC]), with r=-0.62±0.15 and n_o=48 (*see* Figure 3.9A), (ii) [POM]:[SPM], with r=-0.65±0.19 and n_o=23 (*see* Figure 3.9B), and (iii) [POC]:[SPM], with r=-0.75±0.09 in log-log scale and n_o=48 (*see* Figure 3.9D). These relationships agree with expectations of low n (1.02-1.10) for particles dominated by organic material (Aas 1996) and higher n (1.15-1.22) for inorganic particles (Woźniak and Stramski 2004). Both $\tilde{b}_{bp}$ and n are positively correlated with ρ_a with correlation coefficients (in log log scale) of 0.75±0.09 for 111 observations (*see* Figure 3.9C).

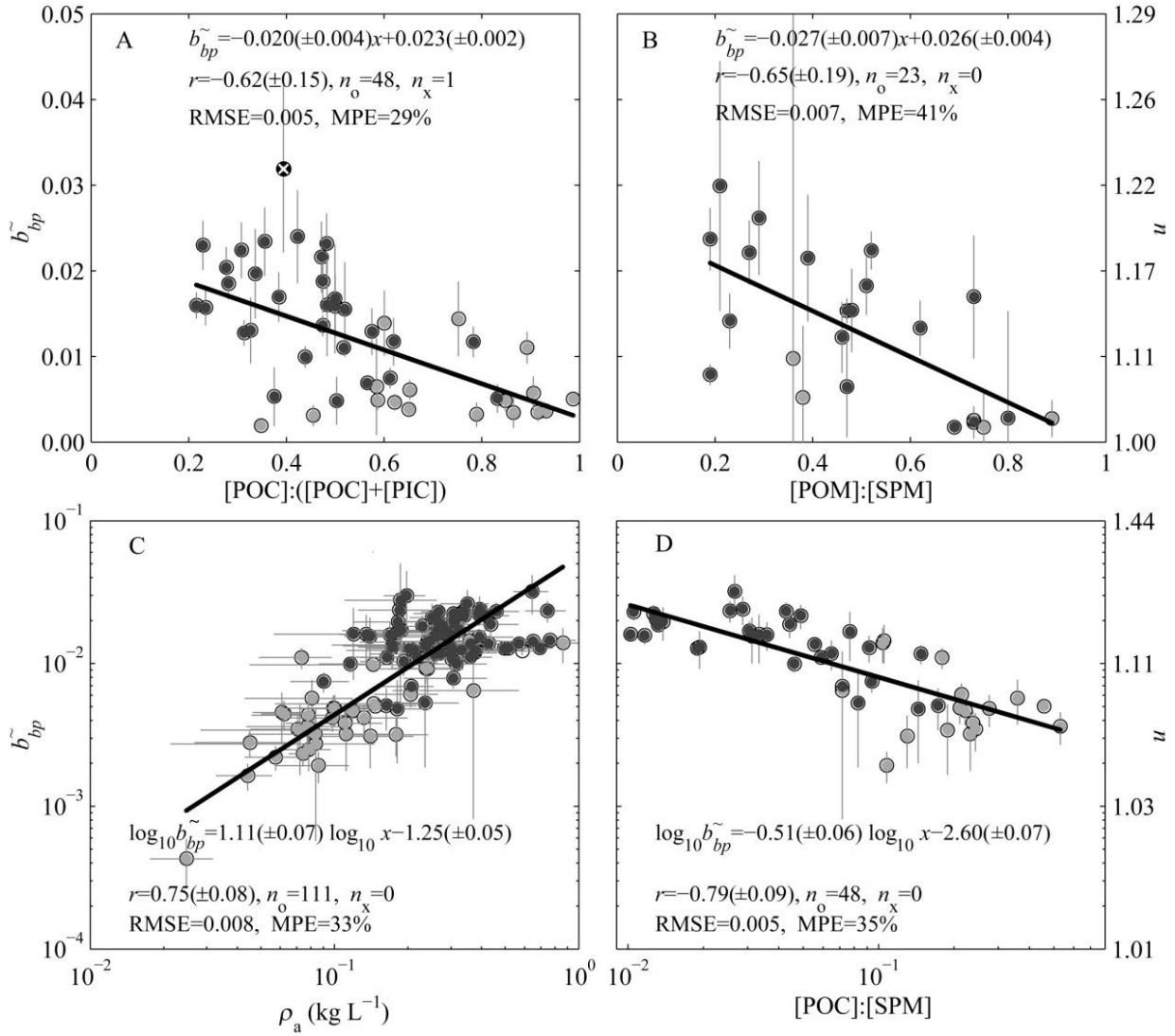

Figure 3.9. Scatter plots of the backscattering ratio, $\tilde{b}_{bp}$ (=bbp:cp(LISST)) vs. (A) [POC]:([POC]+[PIC]), (B) [POM]:[SPM], (C) mean apparent density (ρ_a), and (D) [POC]:[SPM]. Regression lines, with equations and statistics are shown on each panel (see section3.5.1 for details). Case 1 waters are shown in grey and case 2 waters in black. Error bars denote uncertainty estimates as derived in section 3.5.1.2.

Since n increases with ρ_a, optical efficiency factors (Q_{bbe} ,Q_{ce}) and ρ_a will compensate each other in Eq. (3.10) if they are sufficiently sensitive to n (particle composition) and if the mass-normalized optical property shows sufficient sensitivity to optical efficiency. The coefficient c_p^m shows no sensitivity to Q_{ce} , hence variability in c_p^m is almost entirely controlled by $\rho_a \times D_A$. This explains the order of

magnitude variability in c_p^m observed in this study. In the case of b_{bp}^m, Q_{bbe}, and ρ_a compensate each other (*see* Figure 3.6H, Table 3.2, and Table 3.3), which explains why b_{bp}^m shows less variability.

Potential drivers of mass-specific optical properties were identified via Eq. (3.10). These are particle composition (via optical efficiency), ρ_a, and D_A. While 90% of the variability in c_p^m is explained by variations in the denominator, $\rho_a \times D_A$, this approach was not so successful in explaining variability in b_{bp}^m. Only 40-60% of the variability in b_{bp}^m could be explained, and even less in case 1 waters. Possible causes are uncertainties in the assessment of $Q_{bbe} \times (\rho_a \times D_A)^{-1}$ due to the limited size range covered by the LISST PSD, and the potential inappropriateness of Eq. (3.10) for b_{bp}^m due to sensitivity to particle shape and internal structure.

We recall that ρ_a and D_A are derived from a PSD between 2.4 and 302 μm (Eqs. 2 and 5). Mie theory predicts that the contribution of submicron particles, which are not included in the PSD, to b_{bp} is significant and higher than for c_p (Stramski and Kiefer 1991). Experimental results, on the other hand, show that their significance for b_{bp} may be overstated (Roesler and Boss 2008;Dall'Olmo et al. 2009) and that the homogeneous spherical model is inappropriate for modeling b_{bp} (Kitchen and Zaneveld 1992; Clavano et al. 2007).

We further note that Eq. (3.10) is based on sphericity of the particles, material homogeneity across the PSD, and the assumption that IOPs can be related to bulk particle properties. It is known that nonsphericity and a heterogeneous interior of particles affect light scattered in the backward direction more than when integrated over all directions (Kitchen and Zaneveld 1992;Clavano et al. 2007). Hence, Eq. (3.10) may be inappropriate in the case of b_{bp}.

PSDs obtained with a LISST are affected by the assumed optical model, particularly by the assumed index of refraction of the particles. A priori knowledge of particle composition, however, does not necessarily improve the accuracy of LISST' derived PSDs (Andrews et al. 2010). Overall, Mie-based models with low indices of refraction, such as Sequoia's Mie composite model, lead to artificially high concentrations of small particles, whereas models assuming a high index of refraction, such as Sequoia's random shape inversion model used here, do not have this artifact (Agrawal et al. 2008; Andrews et al. 2010). A Mie model with inorganic refractive index was found to produce the most accurate results for PSD shape, [AC], and [VC] (Andrews et al. 2010). Theoretical models allowing for more realistic particle shapes and structures than homogeneous spheres are expected to help improve the accuracy of LISST PSDs, but concerns remain about small out-of-range particles (Andrews et al. 2010) and effects of stray light, particularly for surface water deployments (Reynolds et al. 2010; Andrews et al. 2011a).

Efforts to explain the in situ variability of b_{bp}^{m}, or optical variability in general, may be more successful with acquisition of PSDs over the full range of optically significant particles, from sub-micron sized particles to large aggregates several mm in diameter, and inclusion of particle shape and internal structure information. Underwater digital holographic particle imaging sensors, such as Sequoia's LISST-HOLO operating over the 25-2500 μm size range, have become available recently and research is ongoing for extension of these systems into the sub-micron range (A. Nimmo-Smith and M. Twardowski pers. comm.). These sensors may offer new capabilities for obtaining PSDs, including information on complex particle shapes and structures that will facilitate development of new models relating IOPs to PSDs.

3.5 Appendices

3.5.1 Dealing with measurement uncertainties: propagation of uncertainties and linear regression methods

(published as Web Appendix to Neukermans et al. 2012, available in open access from http://www.aslo.org/lo/toc/vol_57/issue_1/0124a.pdf)

All measurements are subject to measurement uncertainties, which propagate into quantities derived from measurements with uncertainties and which require proper treatment in regression analysis. Type-II linear regression methods, such as 'least square cubic' regression (York 1966), are designed to take into account these measurement uncertainties. Uncertainty estimates from repeat measurements of optical properties and particle concentration are given first. Next, uncertainties of derived quantities, such as mass and area-specific IOPs, are computed via standard error propagation. These uncertainties are shown as error bars on scatter plots in the main text and used as input to the type-II least-squares cubic regression. The treatment of outliers and calculation of the correlation coefficient and its uncertainty are also described.

3.5.1.1 REPEAT MEASUREMENTS OF IOPS AND PARTICLE CONCENTRATION

IOPs were recorded in surface waters during several minutes resulting in about 100-200 scans for each IOP. Spikes in optical data are common and have been associated with rare large particles and aggregates (Townsend et al. 1992; Costello et al. 1995a; Slade et al. 2011). Central tendency was quantified by the median of all scans, which is more robust to outliers than the mean. The difference between the 75th and 25th percentile value, known as the interquartile range, IQR, was taken as a measure of dispersion. The 25th and 75th percentiles from n observations are obtained through interpolation of the sorted observations which are taken to be the $\frac{0.5\times100}{n}, \frac{1.5\times100}{n}, ..., \frac{(n-0.5)\times100}{n}$ percentiles. If there are outliers in the

data, the IQR is more representative than the more commonly used standard deviation (σ) as an estimate of the spread of the data. Optical data are presented as median values±IQR. For normally distributed data this interval corresponds to mean±1.35×σ and encompasses about 80% of the data.

Note that other sources of uncertainty, such as those associated with instrument calibration and design (Boss et al. 2004 for backscattering (b_{bp}); Leymarie et al. 2010 for attenuation (c_p) and absorption) are not included.

Uncertainties on area concentration, [AC], and volume concentration, [VC], were derived from the dispersion of raw scattering recorded by an in situ Laser Scattering and Transmissometry device (LISST) during a surface deployment (*see* Table 1). Uncertainties on dry mass concentration (i.e., suspended particulate matter concentration, [SPM]) and side scattering (b_s) are derived from replicate measurements. These measurements were also median-averaged. An overview of uncertainty estimates of optical and concentration measurements is given in Table 3.5.

3.5.1.2 PROPAGATION OF UNCERTAINTY

To estimate the standard uncertainty on a function f of several variables (x_1,x_2,…x_n) with standard uncertainties $\sigma(x_1)$, $\sigma(x_2)$, … $\sigma(x_n)$, the formula for first order error propagation is used (ISO 1995):

$$\sigma(f)=\left(\sum_{i=1}^{n}\sum_{j=1}^{n}\frac{\partial f}{\partial x_i}\frac{\partial f}{\partial x_j}\mathrm{cov}(x_i,x_j)\right)^{1/2} \tag{3.13}$$

where $\mathrm{cov}(x_i,x_j)$ denotes the covariance between x_i and x_j and $\mathrm{cov}(x_i,x_i)=\sigma^2(x_i)$, the variance of x_i. Note that $\mathrm{cov}(x_i,x_i)$ is zero when x_i and x_j are independent variables and that $\mathrm{cov}(x_i,x_j)=r(x_i,x_j)\sigma(x_i)\sigma(x_j)$, where $r(x_i,x_j)$ denotes the correlation between x_i and x_j.

Many of the derived quantities in the main text are of the form: $f=\frac{x_1}{x_2}$. Application of Eq. (3.13) then gives:

$$\sigma\left(\frac{x_1}{x_2}\right)=\frac{x_1}{x_2}\left(\left(\frac{\sigma(x_1)}{x_1}\right)^2+\left(\frac{\sigma(x_2)}{x_2}\right)^2-2\frac{\sigma(x_1)\sigma(x_2)}{x_1x_2}r(x_1,x_2)\right)^{1/2} \tag{3.14}$$

When x_1 and x_2 are positively correlated, an upper bound on Eq.(3.14) is given by:

$$\sigma\left(\frac{x_1}{x_2}\right)=\frac{x_1}{x_2}\left(\left(\frac{\sigma(x_1)}{x_1}\right)^2+\left(\frac{\sigma(x_2)}{x_2}\right)^2\right)^{1/2} \tag{3.15}$$

An upper bound on uncertainty of apparent density, ρ_a ([SPM]:[VC]), mass-specific IOPs (c_p^m, b_s^m, and b_{bp}^m), and area-specific IOPs (Q_{ce}, Q_{bse}, and Q_{bbe}) is then given by Eq. (3.15) because [VC] is positively correlated with [SPM] and IOPs are positively correlated with [SPM] and [AC]. The standard uncertainties (σ) of [SPM], [VC], [AC], and IOPs are given by their uncertainty estimate, Δ, shown in Table 3.5.

Application of Eq. (3.13) to $f = (\rho_a D_A)^{-1} = \dfrac{[\mathrm{VC}]}{D_A[\mathrm{SPM}]}$, where D_A is the mean diameter weighted by area, gives the following upper bound on the uncertainty:

$$\Delta(\rho_a D_A)^{-1} = \frac{[\mathrm{VC}]}{D_A[\mathrm{SPM}]}\left(\left(\frac{\Delta[\mathrm{SPM}]}{[\mathrm{SPM}]}\right)^2 + \left(\frac{\Delta[\mathrm{VC}]}{[\mathrm{VC}]}\right)^2 + \left(\frac{\Delta D_A}{D_A}\right)^2\right)^{1/2} \qquad (3.16)$$

because $\mathrm{cov}([\mathrm{SPM}], D_A) = 0$, $\mathrm{cov}([\mathrm{SPM}],[\mathrm{VC}]) > 0$, and $\mathrm{cov}(D_A,[\mathrm{VC}]) > 0$.

Table 3.5. Uncertainty estimates on optical and particle concentration measurements, and their derived quantities.

Parameter	Uncertainty
[AC]	$\Delta[\mathrm{AC}] = [\mathrm{AC}]\dfrac{\Delta[\mathrm{VC}]}{[\mathrm{VC}]}$
b_{bp}	Δb_{bp}=IQR obtained from a surface water deployment (100-200 scans)
$\tilde{b}_{bp}$	$\Delta\tilde{b}_{bp} = \tilde{b}_{bp}\left(\left(\dfrac{\Delta b_{bp}}{b_{bp}}\right)^2 + \left(\dfrac{\Delta b_p}{b_p}\right)^2\right)^{1/2}$
b_{bp}^m	$\Delta b_{bp}^m = b_{bp}^m\left(\left(\dfrac{\Delta[\mathrm{SPM}]}{[\mathrm{SPM}]}\right)^2 + \left(\dfrac{\Delta b_{bp}}{b_{bp}}\right)^2\right)^{1/2}$
b_s	Δb_s=IQR obtained from 6 replicates
b_s^m	$\Delta b_s^m = b_s^m\left(\left(\dfrac{\Delta[\mathrm{SPM}]}{[\mathrm{SPM}]}\right)^2 + \left(\dfrac{\Delta b_s}{b_s}\right)^2\right)^{1/2}$
c_p	Δc_p=IQR obtained from a surface water deployment (100-200 scans)

c_p^m	$\Delta c_p^m = c_p^m \left(\left(\frac{\Delta[\mathrm{SPM}]}{[\mathrm{SPM}]} \right)^2 + \left(\frac{\Delta c_p}{c_p} \right)^2 \right)^{1/2}$
D_A	$\Delta D_A = \mathrm{IQR}\left(\frac{[\mathrm{AC}]_i D_i}{[\mathrm{AC}]} \right)$ with $2 \le i \le 31$
Q_{bbe}	$\Delta Q_{bbe} = Q_{bbe} \left(\left(\frac{\Delta[\mathrm{AC}]}{[\mathrm{AC}]} \right)^2 + \left(\frac{\Delta b_{bp}}{b_{bp}} \right)^2 \right)^{1/2}$
Q_{bse}	$\Delta Q_{bse} = Q_{bse} \left(\left(\frac{\Delta[\mathrm{AC}]}{[\mathrm{AC}]} \right)^2 + \left(\frac{\Delta b_s}{b_s} \right)^2 \right)^{1/2}$
Q_{ce}	$\Delta Q_{ce} = Q_{ce} \left(\left(\frac{\Delta[\mathrm{AC}]}{[\mathrm{AC}]} \right)^2 + \left(\frac{\Delta c_p}{c_p} \right)^2 \right)^{1/2}$
ρ_a	$\Delta \rho_a = \rho_a \left(\left(\frac{\Delta[\mathrm{SPM}]}{[\mathrm{SPM}]} \right)^2 + \left(\frac{\Delta[\mathrm{VC}]}{[\mathrm{VC}]} \right)^2 \right)^{1/2}$
[SPM]	Δ[SPM] =IQR obtained from 3 replicates
[VC]	$\Delta[\mathrm{VC}] = 0.5\left(\sum_{i=2}^{31} inv(\mathrm{median}(scat_i) + \mathrm{IQR}(scat_i)) - \sum_{i=2}^{31} inv(\mathrm{median}(scat_i) - \mathrm{IQR}(scat_i) \right.$, where *inv* denotes the LISST scattering inversion of Agrawal et al. 2008 and $scat_i$ is the raw scattering on the i^{th} ring detector of the LISST obtained during surface water deployment

3.5.1.3 LEAST SQUARES REGRESSION FOR MEASUREMENTS WITH UNCERTAINTIES

As in situ data is subject to measurement uncertainty, type-II linear regressions are applied. The 'least squares cubic' regression developed by York 1966, as implemented in the MATLAB routine lsqcubic.m by E.T. Peltzer (*see* the excellent web page http://www.mbari.org/staff/etp3/regress/index.htm for details) is used. x and y data are weighted by the inverse-square of their measurement uncertainties, $(\Delta x)^{-2}$ and $(\Delta y)^{-2}$, respectively. The line is then fit by minimizing the weighted residuals in both x and y simultaneously.

The least squares cubic regression, like the ordinary least squares method, is strongly influenced by outliers. To identify outliers, the MATLAB robustfit.m routine was used, which implements an iterative reweighted least squares procedure. In the first iteration, each point is assigned equal weight and regression coefficients are estimated using ordinary least squares. At subsequent iterations, weights are recomputed so that points farther from model predictions, $\hat{y}$, in the previous iteration are given lower weight. Model coefficients are then recomputed using weighted least squares. The process continues until the values of the coefficient estimates converge within a specified tolerance. The Talwar weighting function was used, assigning zero weight in the i^{th} iteration to observations satisfying:

$$\left|\frac{y-\hat{y}}{s\sqrt{1-h}}\right| \geq t \tag{3.17}$$

and a weight of 1 elsewhere. The default tuning constant t=2.795 was used. The nominator in Eq. (3.17) is the residual in the i-1th iteration and h are the leverage values from that least-squares fit. The robust variance, s, is given by the median absolute deviation of the residuals from their median, normalized by 0.6745 to make the estimate unbiased for the normal distribution. Each leverage value, h_k, determines the influence of the observed response y_k on the predicted response $\hat{y}_k$. For leverage values near 1 ($\frac{1}{n} \leq h_k \leq 1$), the predicted response approximates the observed response. Observations satisfying Eq. (3.17) are outliers and were removed prior to least-squares cubic regression. The lsqcubic.m routine provides the slope and y-intercept of the regression line, with their standard deviation and the correlation coefficient weighted by $(\Delta x)^{-2}$ and $(\Delta y)^{-2}$.

Uncertainties on particulate organic and inorganic carbon concentration, [POC] and [PIC], and on particulate organic and inorganic matter concentration, [POM] and [PIM], could not be assessed due to a lack of replicate measurements. These are thought to be small though (*see* for example Stramski et al. 2008 for uncertainties on [POC]). For regressions involving these quantities, the MATLAB robustfit.m routine with Talwar weighting function, described previously, was applied. Note that this corresponds to an ordinary least squares regression applied to an outlier-free dataset.

To assess goodness-of-fit of the regression line to the data, the well known root-mean-square-error, RMSE, and the median relative prediction error, MPE, were computed:

$$\mathrm{RMSE} = \sqrt{\frac{1}{n-2}\sum_{k=1}^{n}(y_k-\hat{y}_k)^2} \tag{3.18}$$

$$\mathrm{MPE} = \mathrm{median}\left|\frac{y_k-\hat{y}_k}{y_k}\right| \tag{3.19}$$

where n is the number of observations.

3.5.1.4 CORRELATION COEFFICIENT UNCERTAINTY ESTIMATION

Since there is no simple statistical formula to calculate the uncertainties in the correlation coefficient, r, between two variables having disparate uncertainties or experimental precision, a bootstrap procedure is used to obtain the statistics of r (Boss et al. 2009c). This procedure involves choosing random samples with replacement from the dataset and their uncertainties and calculating the weighted correlation coefficient r using the lsqcubic.m routine. The number of elements in each bootstrap sample equals the number of elements in the original data set. A hundred bootstrap samples of r were taken in this way. The distribution of r appeared normal, so the mean and the standard deviation of r (σ_r) are reported. The 95% (99.9%) confidence interval of r is $r \pm 1.96 \times \sigma_r$ ($r \pm 3.29 \times \sigma_r$), from which the statistical significance (p-value) was derived.

When data uncertainties are unknown (e.g., for [POC] or [POM]), the Pearson's product-moment correlation coefficient, r, obtained by dividing the covariance of two variables of size n by the product of their standard deviations, is reported. The uncertainty on r represents a 95% confidence interval, based on the Fisher r-to-z transformation ($z=0.5\times[\log_e(1+r)\times(1-r)^{-1}]$) with approximate variance $(n-3)^{-1}$.

3.5.2 IOPs and particle size distributions

Supplemental data and analysis from the study presented in this chapter are provided here. Attention is given to particle size distributions obtained with a LISST-C instrument and how deviations from the commonly assumed Junge power law distribution in Eq. (3.4) may affect theoretical relationships between IOPs and PSDs. First we attempt to investigate which particle size classes contribute most to variability in IOPs.

3.5.2.1 SCATTERING PROPERTIES VS. AREA CONCENTRATION BY SIZE CLASS

Correlations between IOPs (c_p, b_s, and b_{bp}) and [AC] in each individual LISST size bin are investigated. As explained previously, the inner and outer ring data corresponding to the largest and smallest particles, respectively, were excluded. Observations are retained where all IOPs and [SPM] were recorded (n_o=119) and where the bulk of the particles were sized by the LISST ($Q_{ce} < 5.7$). A total of 107 data points remain, of which 35 are classified as case 1 and 72 as case 2 waters. Note that c_p from the ac-s instrument is not included due to uncertainties on the effect of the steel mesh screen. Correlation coefficients between IOPs and $[AC]_i$, $r([AC]_i)$, for case 1 and case 2 waters are shown in Figure 3.10A,C, while correlations with cumulative $[AC]_i$, $r([AC]_i^{cum})$, are shown in Figure 3.10B,D.

For case 1 waters, all correlations are significant (p<0.05), except in the last 3 size bins (D_i=216 μm to 302 μm) and all IOPs show similar correlation size patterns. The highest correlations are found at two size intervals, extending from 4-10 μm and from 50-130 μm. A similar bimodal correlation size pattern for c_p(LISST) has been observed previously in a New Caledonian coral reef lagoon with correlation peaks of 0.6 for c_p(LISST) at 3-5 μm and at 40-100 μm and was explained by particle aggregation processes (Jouon et al. 2008). The observed bimodality in our study may partly be explained by covariation of $[AC]_i$ for particles in the size range 7 to 10 μm and particles between 50 and 70 μm, possibly caused by biological and/or aggregation processes. An example of such a covariation is shown in Figure 3.10A for particles of size 7.8 μm (size bin 9, grey lines). Covariation of $[AC]_i$ between all size bins is shown in Figure 3.11 for case 1 and case 2 waters. The bimodality of $[AC]_i$ and the dependency of $[AC]_i$ for 4-5 adjacent size bins are clearly visible.

The cumulative [AC] of all particles smaller than 6.6 μm explains about 56% of the variability in the c_p(C-Star), b_s, and b_{bp} and about 80% of the variability in c_p(LISST), as shown in Figure 3.10B. Accounting for particles larger than 10 μm only slightly increases the correlation between the cumulative $[AC]_i$ and IOPs, which is in accordance with Mie theory.

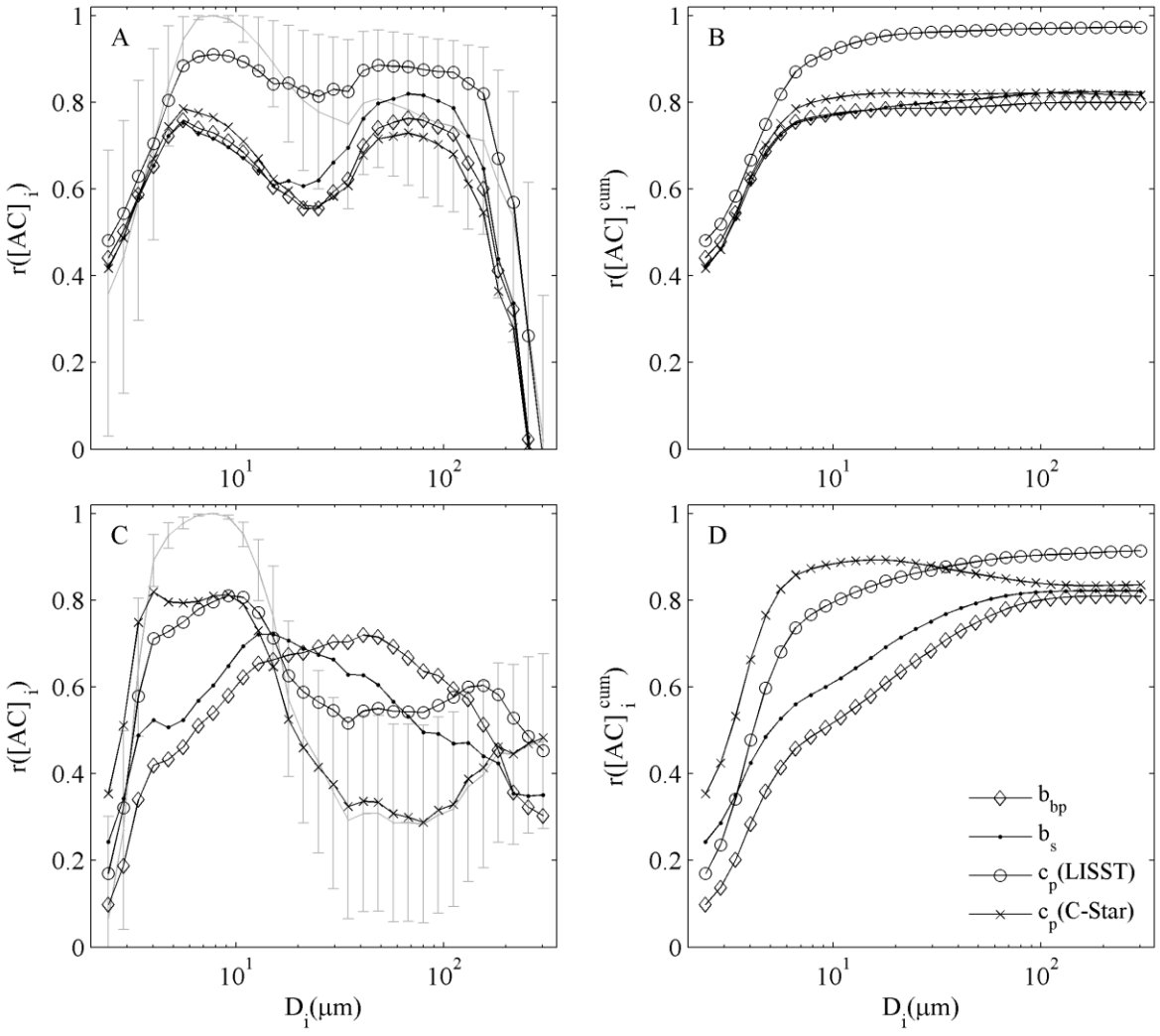

Figure 3.10. Correlation coefficients of various scattering properties *vs.* area concentration, $[AC]_i$, per LISST size class in log log space for case 1 (A) and case 2 waters (C). Correlation coefficients of various scattering properties *vs.* the cumulative $[AC]_i$, $r([\mathrm{AC}]_i^{cum})$, in log log space for case 1(B) and case 2 waters (D). Correlation coefficients between $[AC]_9$ (D_i = 7.8 μm) and all other $[AC]_i$ in log log space with 95% confidence intervals are shown in grey.

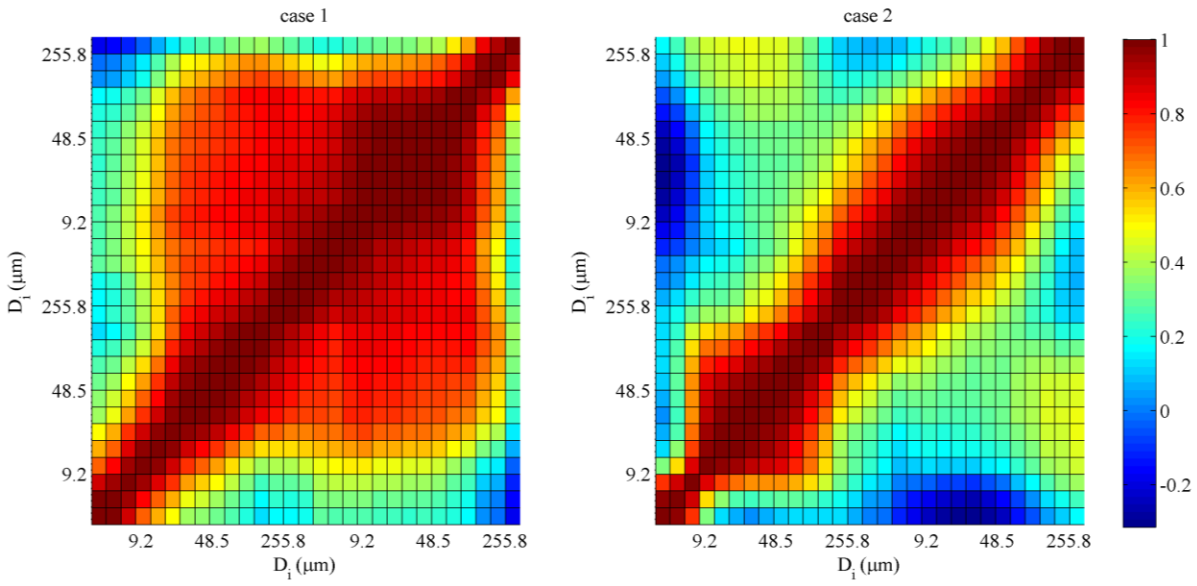

Figure 3.11. Correlation coefficients between area concentration recorded in each LISST size bin in case 1 (left) and case 2 (right) waters.

In case 2 waters all correlations are significant (p<0.05). Contrary to case 1 waters, the correlation pattern for c_p is different from the b_s and b_{bp} correlation patterns. A bimodal correlation pattern is observed for c_p(C-Star) covarying with the covariation pattern of $[AC]_9$ for particles of size 7.8 μm (*see* Figure 3.10C). The highest correlation is observed with particles of size 4-10 μm and a second correlation peak is observed for the largest particles (200-300 μm). A similar behaviour is found for c_p(LISST), but with a secondary correlation maximum at 100-200 μm. The correlation patterns for b_s and b_{bp} are unimodal with peaks at 15 μm and 50 μm, respectively.

The cumulative [AC] of all particles smaller than 6.6 μm explains about 72% and 55% of the variability in c_p recorded by the C-Star and LISST instruments, respectively. An additional 30% of the variability in c_p(LISST) is explained by accounting for the larger particles, while including larger particles decreases the correlation between the cumulative $[AC]_i$ and c_p(C-Star) as shown in Figure 3.10D. Particles smaller than 6.6 μm explain less than 30% of the variability in b_s and b_{bp}. Accounting for particles up to 100 μm further increases the correlation coefficients for b_s and b_{bp} up to 0.83.

In both case 1 and case 2 waters c_p(C-Star) correlates best with concentration of particles between 4 and 10 μm with a correlation size spectrum parallel to the covariation size spectrum of $[AC]_9$ with D_9=7.8 μm (*see* grey lines in Figure 3.10A,C), while c_p(LISST) correlates better with larger particles than c_p(C-Star). This is consistent with the study of Boss et al. 2009b) on the effect of the acceptance angle on c_p (*see* his Figure 2). They show that for particles of 150 μm a LISST-C instrument captures b_p (similar to

c_p at 670 nm) almost entirely, while a C-Star instrument can only detect between 2 and 45% of b_p, depending mostly on particle absorption. For particles smaller than 10 μm, the effect of the C-Star acceptance angle on c_p(670 nm) is small, with over 80% of the true c_p being measured by the instrument.

In general, the weakest correlations are found at the extreme scattering angels. Care should be taken in the interpretation of these patterns because LISST measurements are affected by straylight (Reynolds et al. 2010; Andrews et al. 2011a) causing errors in the largest angles (smallest particles), and by turbulent refractive index discontinuities (Andrews et al. 2011b) causing instabilities in the smallest angles (largest particles). We observe the weakest correlations in the first 6 size bins in case 1waters, and in the first 4 size bins in the more turbid case 2 waters. Straylight contamination is indeed expected to be stronger in clearer waters. Reynolds et al. 2010) reported a straylight effect in the first 7 size bins of their LISST instrument operating at 532 nm. At this wavelength, pure water absorption is a factor 10 smaller than at 670 nm, so straylight is expected to be less of an issue with the LISST instrument used here. Further uncertainties are caused by a mismatch in the refractive index assumed for inversion and the refractive index of the particles in suspension, which is especially important for particles smaller than 20 μm (Andrews et al. 2010).

Rare, large particles or aggregates cause spikes in the optical signal (Costello et al. 1995b; Briggs et al. 2011; Slade et al. 2011), which may be removed through median-filtering. The IQR can be used as an indicator for spikiness of IOP measurements. Significant (p<0.01) positive log-log correlations between the relative uncertainty on IOPs (=IQR(IOP):median(IOP)) and D_A are observed, with correlation coefficients of 0.45±0.16 and 0.35±0.18 for b_{bp} and c_p(LISST), respectively (*see* Figure 3.12). This agrees with the study of Briggs et al. 2011) who found spike height in b_{bp} signals to be affected mainly by particle cross sectional area. No such correlations (p>0.05) were found for c_p(C-Star) or c_p(ac-s), possibly because of their large acceptance angle and hence low sensitivity to large particles. Spikiness of IOP signals is also affected by sampling volume, which varies widely between instruments as shown in Table 3.6. A WET Labs BB-9 instrument samples a volume of water 2 times smaller than that sampled by the LISST, so its signal is expected to fluctuate more strongly in the presence of large, rare particles.

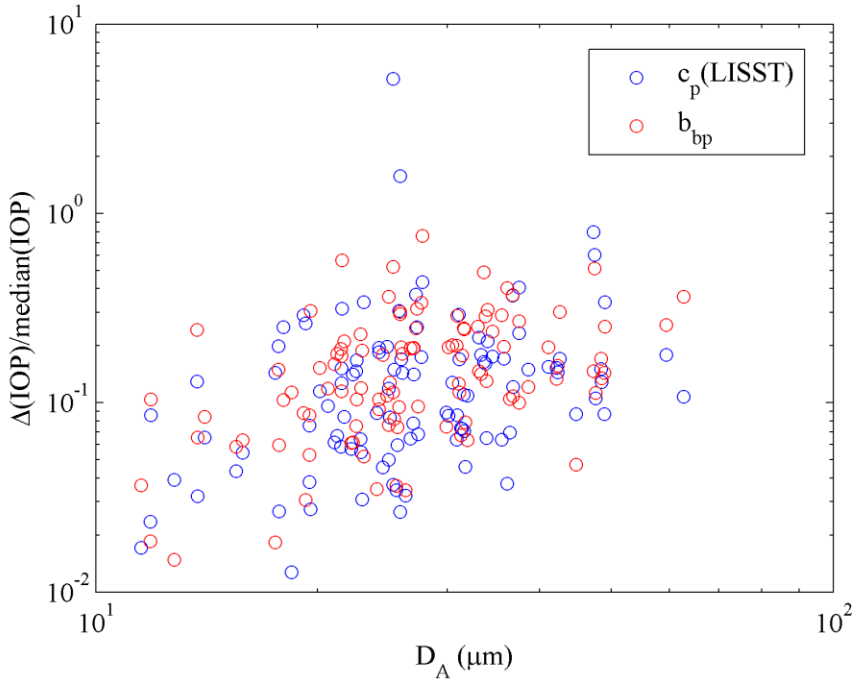

Figure 3.12. Coefficient of variation of c_p(LISST) and b_{bp} as function of mean particle size, D_A.

Table 3.6. Volume of seawater sampled per scan of the beam transmissometers and the backscattering instrument used in this study. Path length and beam width of beam transmissometers are also given.

Instrument	Path length (cm)	Beam width (cm)	Volume sampled per scan (ml)
LISST-C	5	1	3.9
WET Labs ac-s	10	0.8	5.0
WET Labs ac-9	25	0.8	12.6
WET Labs C-Star	10	1.5	17.7
WET Labs BB-9			~2

3.5.2.2 PARTICLE SIZE DISTRIBUTIONS

The particle size distribution (PSD) gives the relationship between particle size and particle concentration. Particle concentration may be represented by particle number, cross sectional area, or volume. The particle number size distribution, $N(D)$, expressed as number of particles per unit particle size per unit sampling volume, is defined as follows (Jonasz and Fournier 2007):

$$dN = N(D)dD \tag{3.20}$$

where *dN* is the mean number concentration of particles in a given size interval [*D*, *D*+*dD*). Particle area and volume size distributions, AC(*D*) and VC(*D*), are defined analogously.

The Junge PSD model, $N_j(D)$, in Eq. (3.4) is the most frequently used theoretical model for the particle number size distribution. For such distributions and assuming spherical geometry, the PSDs by volume and area concentration satisfy

$$\mathrm{VC}(D) \propto D^{-\gamma+3} \text{ and } \mathrm{AC}(D) \propto D^{-\gamma+2} \tag{3.21}$$

Figure 3.13A, B, C shows in situ PSDs recorded with a LISST instrument by particle number, area, and volume concentration. Clearly, the shape of the PSDs by area and volume concentration is not well described by the Junge model. This has been reported before (e.g., Reynolds et al. 2010) and is not surprising given the diverse physical and biological interactions influencing PSDs and the diversity in particle shapes.

Figure 3.13D shows the median, 5th, and 95th percentile values of the normalized bias, *NB*, of *N*(*D*) from the Junge particle number PSD calculated as:

$$NB(D_i) = \frac{N_j(D_i) - N(D_i)}{N(D_i)} \tag{3.22}$$

for case 1 (n_0=105) and case 2 (n_0=149) waters. In case 2 waters, the Junge model performed reasonably well with *NB* generally below 40%, except at the fine (<4-7 μm) and large (>100 μm) particle ends of the PSD where particle number concentrations are overestimated up to a factor 5. In case 1 waters, the overall Junge model performance was poor, especially at the fine particle end of the PSD and in the range 50-150 μm. Overestimation at the fine particle end could be caused by aggregation of smaller particles into larger flocs, but may also be LISST measurement artefacts caused by straylight or sensitivity of the inversion of forward scattered light to particle composition outlined above. We note that measurements of the PSD using Coulter counters have also suggested a decrease in the hyperbolic PSD slope around particles of size 3-8 μm (Kitchen et al. 1982; Jonasz 1983), but there is no consensus on whether this change in slope is real or due to instrumental artifacts.

Even if the Junge model provides a relatively poor fit to the measured PSDs, the Junge parameter γ in Eq. (3.4) can be used as a rough indicator of the relative proportion between the number of small and large particles. For an extensive literature review of Junge PSD slopes, the reader is referred to Jonasz and Fournier 2007.

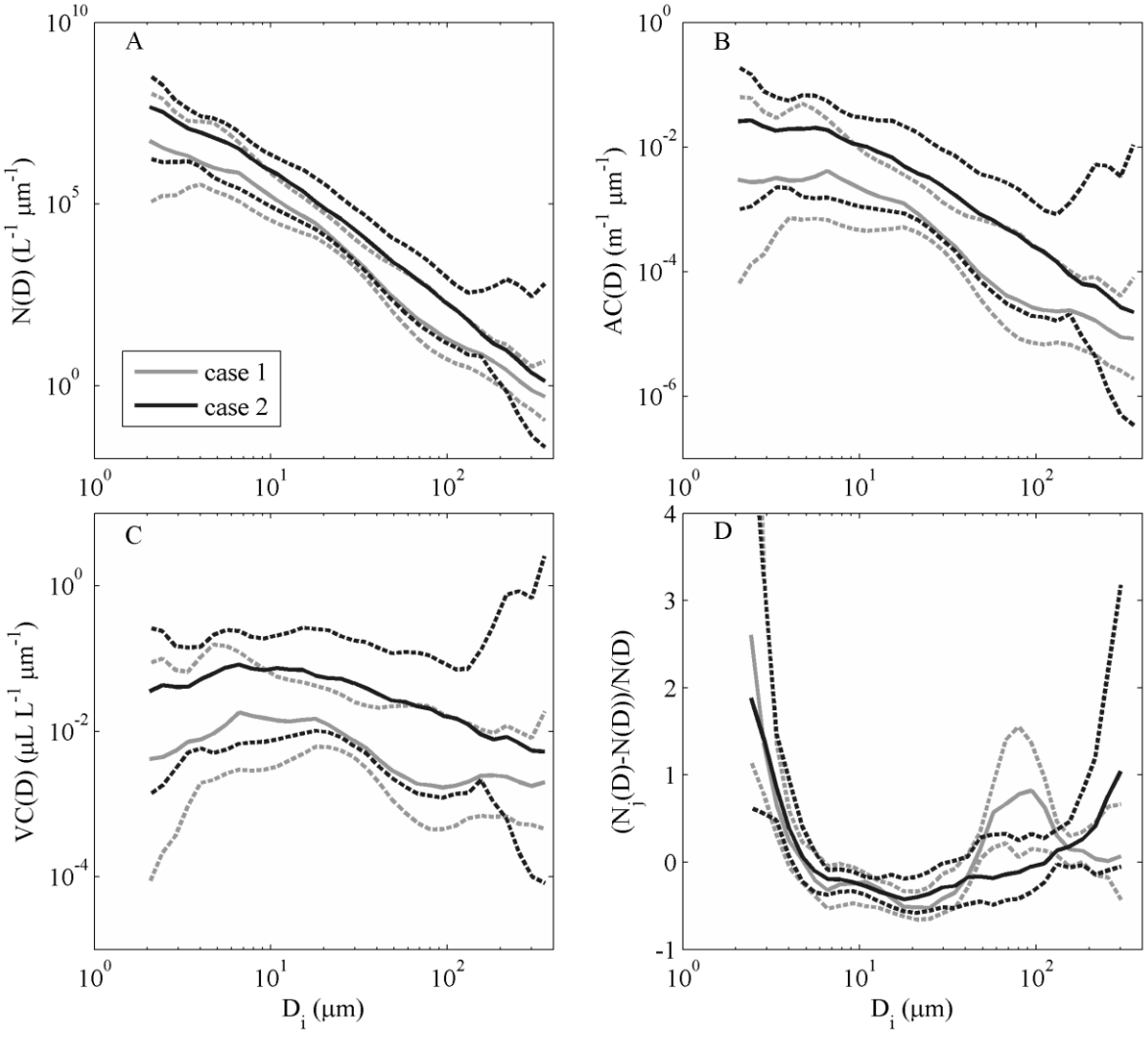

Figure 3.13. Particle size distributions derived from a LISST-C instrument for 105 case 1 waters and 149 case 2 waters by particle number concentration (A), particle area concentration (B), and particle volume concentration (C). For clarity the median, 5th, and 95th percentile values are shown by the solid and dashed lines, respectively. (D) Median, 5th, and 95th percentile values of the normalized bias from the Junge power law model $N_j(D)$ (see Eq. (3.4)) calculated as $\left(N_j(D) - N(D)\right)/N(D)$.

3.5.2.3 RELATIONSHIP BETWEEN JUNGE PSD SLOPE AND C_P SPECTRAL SLOPE FROM IN SITU MEASUREMENTS

Theoretical analysis for spherical, homogeneous, non-absorbing particles with constant index of refraction and with an infinite size distribution modeled by a Junge power law as in Eq. (3.4) demonstrate

that the spectral variations of the particulate attenuation coefficient, c_p, are described well by (Morel 1973):

$$c_p(\lambda) = A\lambda^{-\chi} \quad (3.23)$$

where χ is the hyperbolic c_p spectral slope. This power law model has been shown to be quite robust to perturbations of its assumptions (Boss et al. 2001). Furthermore, χ is linked to the Junge PSD slope γ by (Morel 1973):

$$\gamma = \chi + 3 \quad (3.24)$$

A correction to this model is proposed to account for the finite size of the largest particles in the ocean (Boss et al. 2001):

$$\gamma = \chi + 3 - 0.5e^{-6\chi} \quad (3.25)$$

and provides a significant correction to Eq. (3.24) when large particles are abundant. This inversion model is adequate also for non-spherical or absorbing particles (Boss et al. 2001).

Here, we investigate the relationship between in situ measured χ and γ, and more specifically the effect of departures of the particle number PSD from the assumed Junge power law. Departures from the Junge power law were quantified by the normalized bias in Eq. (3.22). To exclude uncertainties due to straylight or turbulent refractive index discontinuities on LISST PSDs described above, only size classes 5 to 29 with 4 μm<D_i<217 μm were considered. PSDs with $\sum_{i=5}^{29} \mathrm{NB(D_i)^2}$ below its 10$^{\mathrm{th}}$ percentile value were classified as Junge distributions, while PSDs with $\sum_{i=5}^{29} \mathrm{NB(D_i)^2}$ higher than its 90$^{\mathrm{th}}$ percentile value were classified as "non-Junge distributions". Spectral slopes were calculated using wavelengths with weak particulate absorption, i.e. between 490 and 650 nm, using a robust linear regression in log-log space (MATLAB robustfit.m routine with default parameters). Results are shown in Figure 3.14A. The model in Eq. (3.25) predicted well the PSD slope for the Jungian PSDs plotted in Figure 3.14B with relative uncertainties below 15% and an average of 6%. Conversely, the model overestimated γ by 0.8 on average for non-Jungian PSDs.

In six cases χ <0 was found, plotted in Figure 3.14C. Negative c_p spectral slopes have been observed previously (Sullivan et al. 2005; Snyder et al. 2008; Astoreca et al. 2012) and were associated with dominance of algal cells and breakdown of the Junge PSD. Based on Mie theory simulations for organic particles, negative c_p spectral slopes in offshore southern North Sea waters were attributed to blooms of *P. globosa* cells of size 7 μm causing a bump in the particle number PSDs (Astoreca et al. 2012). Here we find χ<0 for stations sampled in April 2010 close to the Scheldt mouth (250 and W04) and stations in French coastal waters near Brest (ZBLR stations) with particle number PSD shape shown

in Figure 3.15A and with bumps in the PSDs for various particle diameters (Figure 3.15B). An additional 9 stations with χ <0, but without PSD measurements, were identified with [Chl *a*] as low as 0.8 μg L^{-1} and organic particle content ranging from 55% to 94% in Belgian coastal and offshore waters and in French Guyana.

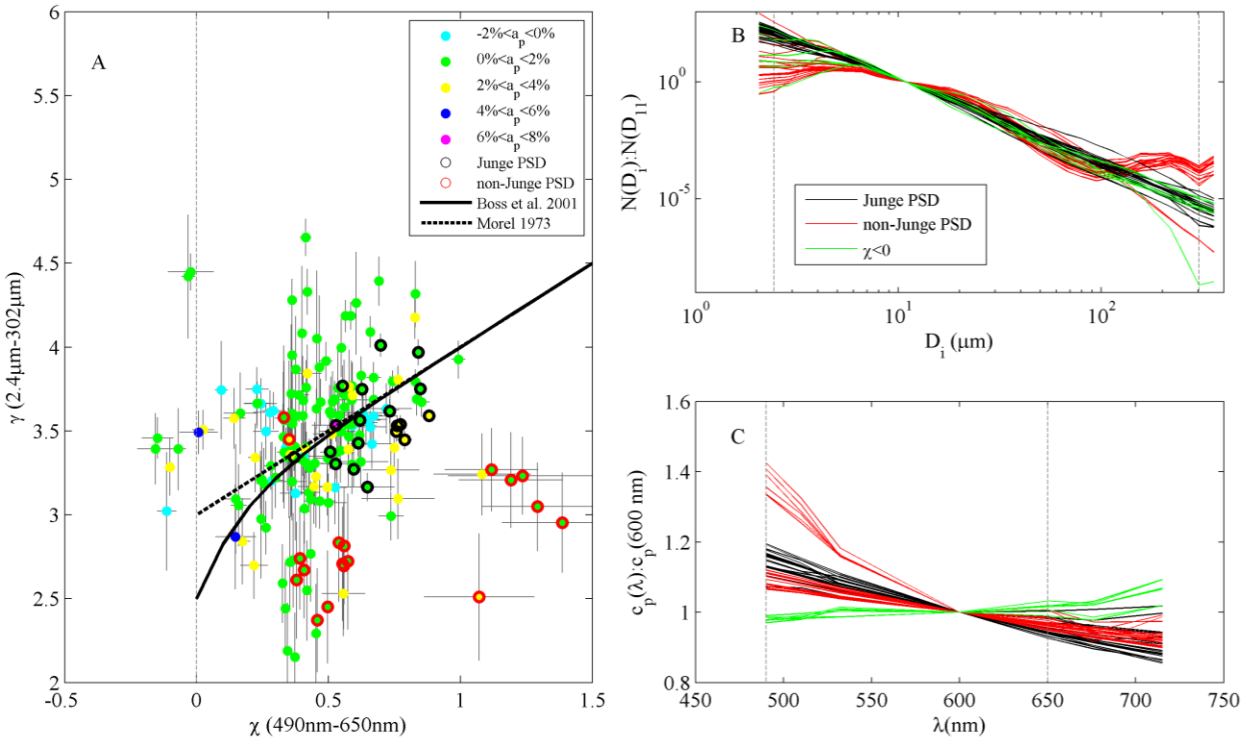

Figure 3.14. (A) Junge PSD slope vs. spectral slope of c_p according to particulate absorption at 650 nm. Jungian and non-Jungian PSDs are indicated by the black and red circles. Error bars denote standard errors on the retrieved slopes. The PSD slope models of Boss et al. 2001 and Morel 1973 are also shown, with model boundary represented by the dotted line. (B) Particle number PSDs normalized at 11 μm and (C) spectra of c_p normalized at 600 nm.

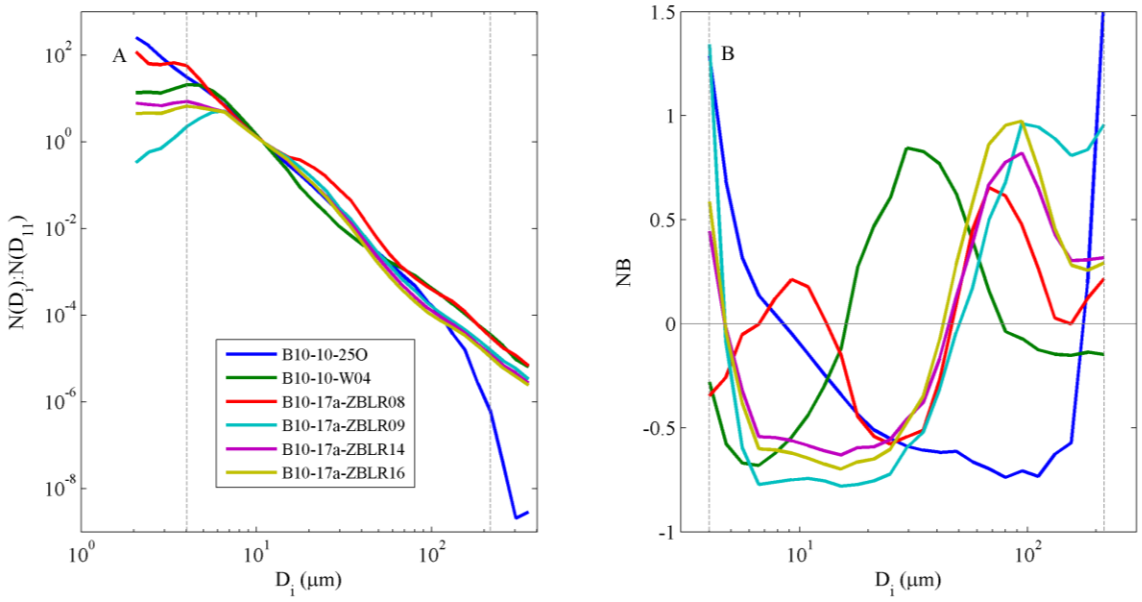

Figure 3.15. (A) Particle number PSDs normalized at 11 μm for observations with c_p spectral slope <0 and (B) normalized bias from the Junge PSD model.

Chapter 4 ATMOSPHERIC CORRECTION OF SEVIRI IMAGERY

A substantial part of this chapter was previously published in Neukermans et al. 2009, available in open-access from http://www.opticsinfobase.org/oe/viewmedia.cfm?URI=oe-17-16-14029&seq=0. Atmospheric correction of high spatial resolution has been accepted for publication in Remote Sensing of the Environment (Neukermans et al. accepted).

Abstract

Back in 2008, a couple of years before the first geostationary ocean colour sensor was launched into space by the Korean Space Agency (GOCI in June 2010), we investigated the feasibility for the mapping of [SPM] in the southern North Sea from the geostationary SEVIRI meteorological sensor (Neukermans et al. 2009). Despite SEVIRI having only two broad bands in the red and NIR and a low radiometric resolution, [SPM] mapping was achieved with sufficient accuracy in turbid waters. Based on a one month dataset of SEVIRI images, which are available every 15 minutes, it was shown that SEVIRI's [SPM] maps were highly correlated with [SPM] maps from the polar-orbiting MODIS Aqua ocean colour sensor and that high frequency dynamics of [SPM] could be detected on cloud-free days. Follow-up work (Neukermans et al. accepted) extended the work to a two year archive of SEVIRI North Sea imagery to investigate diurnal variability of suspended particles. The atmospheric correction, uncertainty estimation, and the spatial resolution of SEVIRI products were further improved.

This chapter combines the atmospheric correction work of both papers, while the diurnal variability of suspended particles is the subject of Chapter 5. More specifically, the objectives of this chapter are to (1) describe the SEVIRI radiometer and its characteristics, (2) introduce the necessary definitions and notation used in atmospheric correction, (3) estimate the uncertainty of marine reflectance products, including uncertainties due to atmospheric correction and sensor digitization, and (4) cross-validate SEVIRI's high and low resolution marine reflectance maps with MODIS Aqua. The limitations of the atmospheric correction are discussed in detail and the potential for extension to SEVIRI full disk imagery, which covers about one third of the globe, is considered.

4.1 Introduction

Polar-orbiting multispectral ocean colour sensors such as the Sea-viewing Wide Field-of-view Sensor (SeaWiFS), the Moderate Resolution Imaging Spectroradiometer (MODIS), and Medium Resolution Imaging Spectrometer (MERIS) provide two-day coverage of the global ocean and coastal zones since their respective launches in 1997 and 2002. These sensors have become well-established sources (McClain 2009) of concentration of chlorophyll *a*, Chl *a*, and suspended particulate matter, SPM, and there has been considerable progress towards many new products including particulate and dissolved organic and inorganic carbon (Stramski et al. 1999; Vantrepotte et al. 2011), particle size distribution (Loisel et al. 2006), phytoplankton species composition (Alvain et al. 2008), vertical light attenuation (Stumpf et al. 1999), turbidity (Stumpf et al. 1999; Woodruff et al. 1999; Nechad et al. 2009) etc. During the last decades the spectral and spatial resolution of space-borne ocean colour sensors has improved, from multispectral to hyperspectral (e.g., Hyperspectral Imager for the Coastal Ocean, launched in September 2009), and from 1 km nadir pixel resolution down to less than 100 m in coastal areas. The quality and quantity of atmospheric corrections (IOCCG 2010) and bio-optical algorithms (McClain 2009) has also significantly progressed.

Even though further progress can still be expected for polar-orbiting sensors in terms of sensor design and processing algorithms, their sampling frequency, typically once per day, is insufficient, especially in coastal waters, where physical and biogeochemical processes show variability at time scales shorter than the daily sampling frequency of polar-orbiting sensors. For example, in situ measurements have shown that [SPM] can vary by a factor two or more during the day due to horizontal advection and/or vertical resuspension forced by tides or wind events (Eisma and Irion 1988; Thompson et al. 2011). Hence, long term data series from polar-orbiting sensors are affected by aliasing that can only be treated indirectly (e.g., Stumpf et al. 1993). Furthermore, cloudiness and/or sun glint reduce data availability from typically once per day (e.g. mid-latitude MODIS imagery) to significantly less. Remote sensing applications, such as harmful algae bloom detection (Stumpf et al. 2003b; Tomlinson et al. 2004) have critical vulnerability to such data gaps.

Ocean colour remote sensing from geostationary sensors has the potential to overcome or mitigate these limitations: the availability of ocean colour data would significantly increase during periods of scattered clouds (Mazeran and Meskini 2008) and the much higher sampling frequency, typically 1 per hour or higher, allows to observe the diurnal or tidal cycles of optical and biogeochemical processes of the open ocean and coastal waters. Geostationary ocean colour data offer possibilities to study the coupling between physics and biogeochemistry, to quantify fluxes and study transport of carbon and sediment. Assimilation of geostationary ocean colour data into ecosystem models may improve modelling results and eutrophication studies. For example, the availability of light to marine organisms

may vary rapidly in coastal environments due to rapid changes in water turbidity. In light-limited ecosystems such as the Channel and Southern Bight of the North Sea, this unrepresented high frequency variability of underwater light may be a cause of discrepancy between the modelled and observed timing of the phytoplankton spring bloom (Lacroix et al. 2007).

The Geostationary Ocean Colour Imager (GOCI, Faure et al. 2008), launched by the Korean Space Agency (KORDI) in June 2010, is the first ocean colour sensor in geostationary orbit. It provides hourly multispectral imagery of waters surrounding the Korean peninsula at a spatial resolution of 500 m. More are likely to follow, as other national and international space agencies also have plans to launch geostationary ocean colour sensors. The European Space Agency (ESA), for example, has commissioned studies on user requirements and some concept design in the framework of Geo-Oculus. A proposal to host a GOCI-like sensor on a geostationary telecommunication satellite has been submitted to ESA (Antoine et al. 2011). The proposed Hosted Ocean Colour Imager, HOCI, would provide hourly multi-spectral imagery of the European seas and adjacent open ocean from late 2014. The American Space Agency, NASA, is preparing the Geostationary Coastal Ocean and Air Pollution Events (GEO-CAPE) mission, planned to be operational by 2020 (NRC 2007).

The first geostationary satellite, Syncom 2, was launched in 1963 for the purpose of telecommunication. Currently, over 300 geostationary satellites are orbiting the globe at an approximate altitude of 36000 km. These satellites have revolutionized global communications, television broadcasting, and weather forecasting. For optical oceanography, a similar revolution can be expected from geostationary ocean colour satellites. While we eagerly await the coming of geostationary ocean colour satellites covering the rest of the world's seas, the potential of geostationary meteorological sensors for marine applications can be tested.

The Spinning Enhanced Visible and Infrared Imager (SEVIRI) on board the METEOSAT Second Generation (MSG) weather satellite platform, for example, has a few broad spectral bands in the VIS and NIR, which may be all that is needed to detect the concentration of suspended particles in turbid waters, as shown by Stumpf and Pennock 1989 for the Advanced Very High Resolution Radiometer (AVHRR). [SPM] in the coastal waters of the southern North Sea is high and known to change rapidly due to tidal and wind-driven resuspension of sediment particles, and thus offers a good test area for mapping of [SPM] (and covarying parameters such as turbidity or light attenuation, *see* Chapter 5) with SEVIRI. The main concerns are the viewing geometry specific to geostationary imagery at high latitudes, which could increase uncertainties in atmospheric correction, and the sensor's low radiometric resolution. After all, the sea is a much darker target than the bright clouds it was designed to monitor.

This study allows to investigate some of the concerns (much higher viewing angles at latitudes or longitudes far from the sub-satellite point) and advantages (high temporal resolution, stable viewing geometry) specific to satellites in geostationary orbit.

4.2 Materials and methods

4.2.1 The SEVIRI radiometer

The Spinning Enhanced Visible and InfraRed Imager (SEVIRI) radiometer (Aminou et al. 1997) was primarily designed to support operational meteorology applications. It has 4 bands in the wavelength range 0.3-1.8 μm, termed "solar channels", and 8 thermal infrared bands. The spatial resolution at nadir of all bands is 3 km, except for the High Resolution Visual broadband channel (HRV) where the spatial resolution at nadir is 1 km. At 52°N the spatial resolution in the solar channels is 3 km (E-W direction) x 6.5 km (N-S direction) and 1 km (E-W direction) x 2km (N-S direction) for the HRV band. The nominal coverage is shown in Figure 4.1. Full-disk imagery is available in near real time every 15 minutes and operationally processed to level 1.5 (Muller 2010), *i.e.* corrected for radiometric and geometric non-linearity.

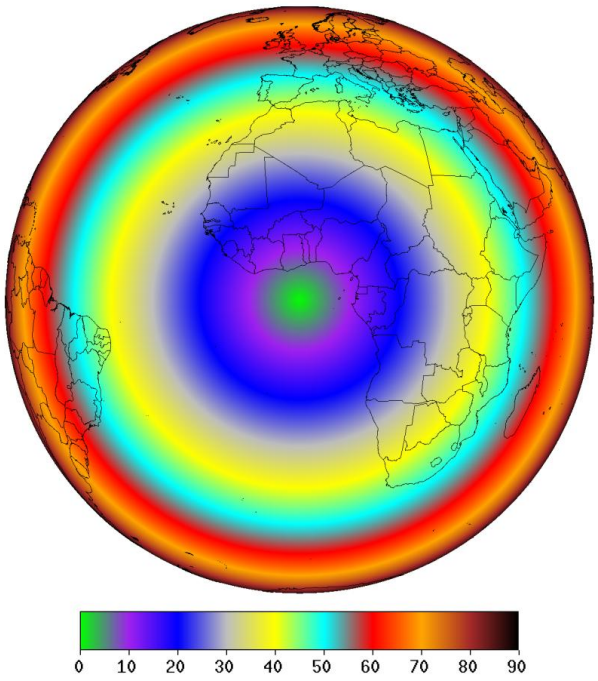

Figure 4.1. Spatial extent of SEVIRI full disk imagery and viewing angle in degrees of SEVIRI on the MSG2-Meteosat9 platform located at 0°W (image kindly provided by Nicholas Clerbaux).

The normalized spectral response functions, ω(λ), for the SEVIRI solar channels which are of interest here are shown in Figure 4.2. Two spectral bands were considered for aerosol correction of the VIS06 band (with central wavelength: $\lambda_0 = 0.635 \mu m$, range: 0.56-0.71μm): VIS08 ($\lambda_0 = 0.810 \mu m$, range: 0.74-0.88μm) and NIR16 ($\lambda_0 = 1.640 \mu m$, range: 1.50-1.78μm).

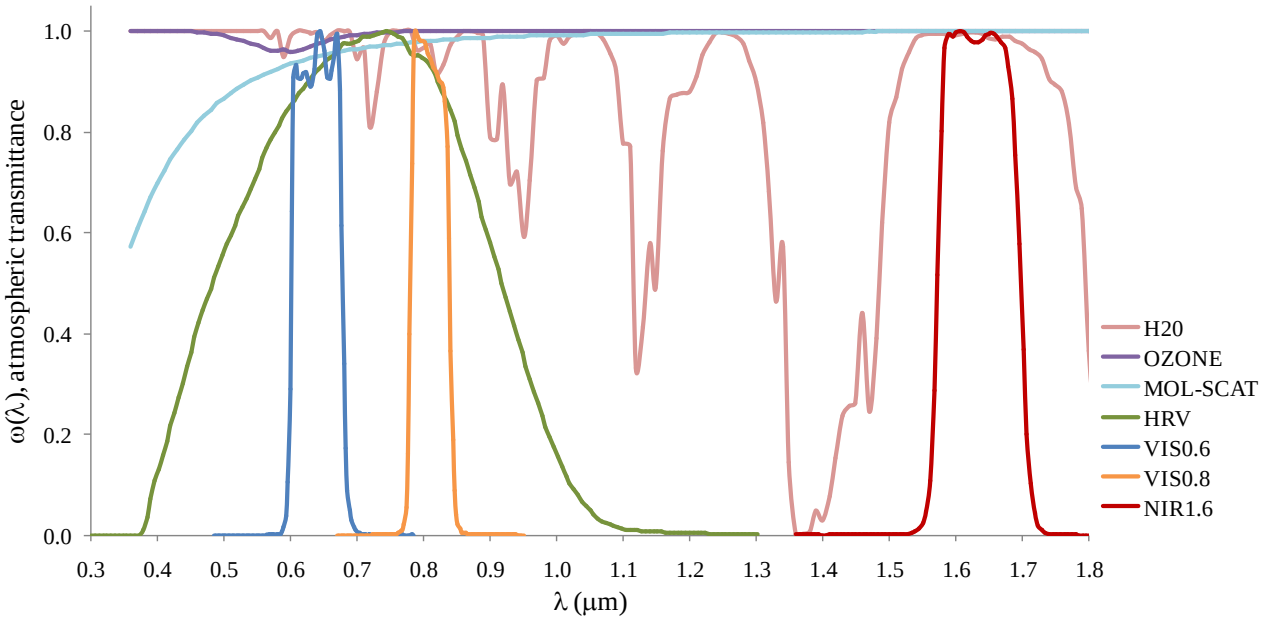

Figure 4.2. Normalized spectral response, ω(λ), of the SEVIRI solar channels (source: Govaerts and Clerici 2004) and one-way atmospheric transmittances for water vapor, ozone and molecular scattering for a vertical atmospheric path and the US standard atmosphere model simulated with LOWTRAN.

SEVIRI has been operational since 2004, giving full disk imagery images every 15 minutes from the Meteosat-8 platform at 3.5 °W. In May-June 2007, Meteosat-8 was replaced with Meteosat-9 and Meteosat-8 was re-orbited to 9.5° E to deliver reduced spatial coverage SEVIRI imagery over Europe at an even higher temporal resolution of 5 minutes, the so called "rapid-scan service" (RSS). An overview is given in Table 4.1. Examples of full disk imagery and RSS imagery is shown in Figure 4.3.

Table 4.1. Operational service of SEVIRI on Meteosat-8 and Meteosat-9 satellite platforms.

Service	Satellite platform	Operational period	Spatial coverage	Longitude	Repeat viewing frequency

full disk prime service	MSG, Meteosat-8	2004-May 2007	Europe-Africa-Atlantic Ocean	3.5° W	15 min
full disk prime service	MSG, Meteosat-9	May 2007-present	Europe-Africa-Atlantic Ocean	0° E	15 min
rapid scan service (RSS)	MSG, Meteosat-8	May 2007-present	Europe	9.5°E	5 min

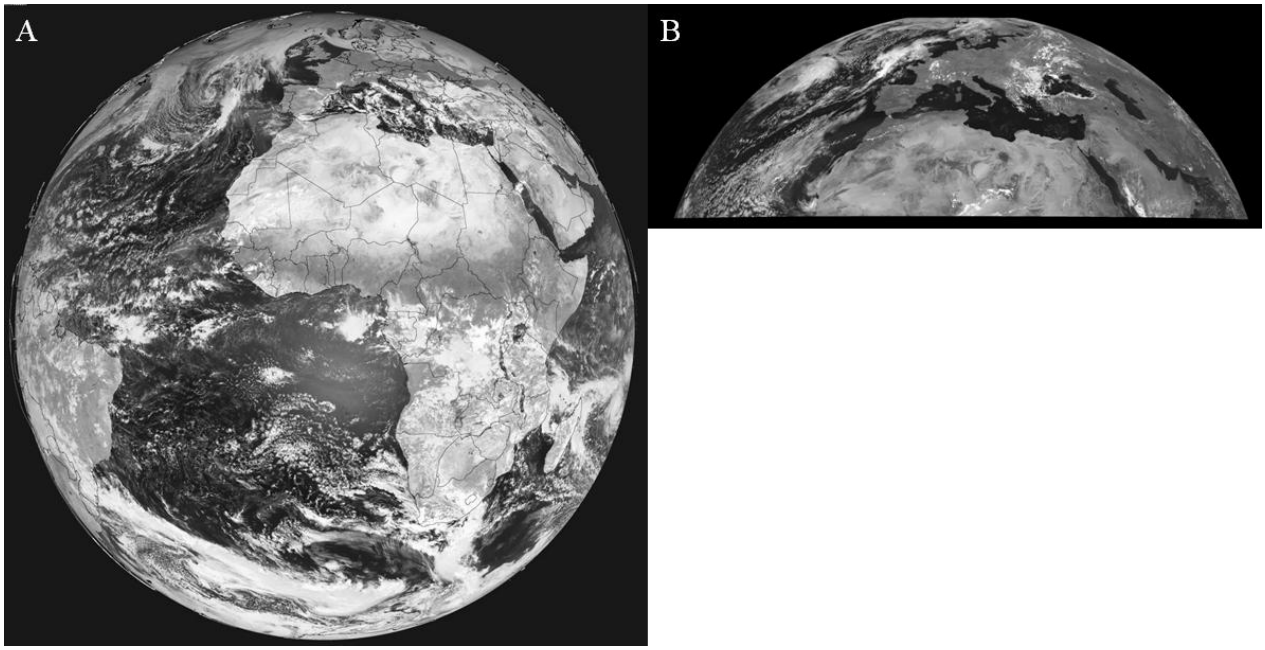

Figure 4.3. (A) SEVIRI Meteosat-9 full disk VIS06 image, (B) SEVIRI Meteosat-8 Rapid Scan Service (RSS) image.

4.2.2 Study area: SEVIRI subscene and viewing angles

The northern boundary of the study area corresponds to a maximum SEVIRI satellite viewing zenith angle of 64° and is shown in Figure 4.4. Two-way air mass, defined as:

$$m = \cos(\theta_v)^{-1} + \cos(\theta_0)^{-1} \quad (4.1)$$

where θ_v is the viewing zenith angle and θ_0 is the sun zenith angle, ranges between 3.4 and 5.5 during the day on June 15th 2008 for a location at the top of this subscene (see Figure 4.5A). In winter, minimum air mass at that location is 7.7 and 5.9 for a location in the middle of the scene (see Figure 4.5B), with

Rayleigh reflectances in the VIS06 band much larger than the marine signal, which is of the order 0.01-0.1.

The area of the southern North Sea and Western Channel chosen for this study is a relatively shallow sea region, mostly less than 50 m deep, and is subject to strong semi-diurnal tidal currents with typical amplitude of 1 m s^{-1}. Suspended particulate matter, SPM, originates from a variety of sources (Eisma 1987) including river discharges, inflow from the Atlantic Ocean (Fettweis et al. 2007), coastal and sea bottom erosion, atmospheric dust, primary production and dredging and mining operations. In the shallower near shore regions, tide and wind resuspension of bottom sediments is particularly important giving high (>100 mg L^{-1}) and highly fluctuating SPM concentrations. The dynamic coastal waters of the southern North Sea are thus an ideal test case for a 'crude' sensor such as SEVIRI in geostationary orbit. The deeper offshore waters have generally much lower concentrations (< 1 mg L^{-1}). Most of the region is vertically well-mixed except for some haline stratification along the Dutch coast and some thermal stratification in summer at the Northern limit of the domain (Otto et al. 1990). Optical remote sensing of SPM in this region has previously been achieved from a range of sensors including AVHRR (Van Raaphorst et al. 1998), CZCS (Doerffer and Fischer 1994), SeaWiFS (Eleveld et al. 2004), MODIS and MERIS (Nechad et al. 2010).

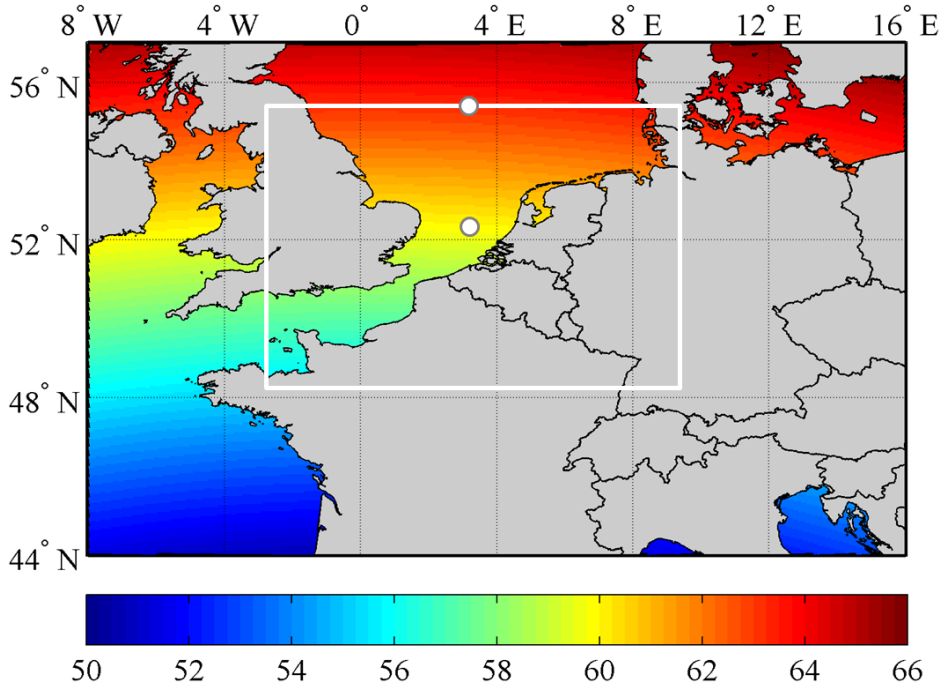

Figure 4.4. Viewing angle of SEVIRI (on MSG2-Meteosat9 platform located at 0°W) over Western-Europe. The white box delimits the study area, for which the northern limit corresponds to a 64° satellite viewing angle. The

white dots are the locations for which daily variability of airmass and Rayleigh scattering are presented in Figure 4.5.

The atmospheric correction approach was first tested on a one-month dataset of MSG1/Meteosat8 SEVIRI imagery obtained in June-July of 2006 (Neukermans et al. 2009). Following the successful outcome of that study, a two year MSG2/Meteosat9 SEVIRI archive obtained in 2008-2009 was processed.

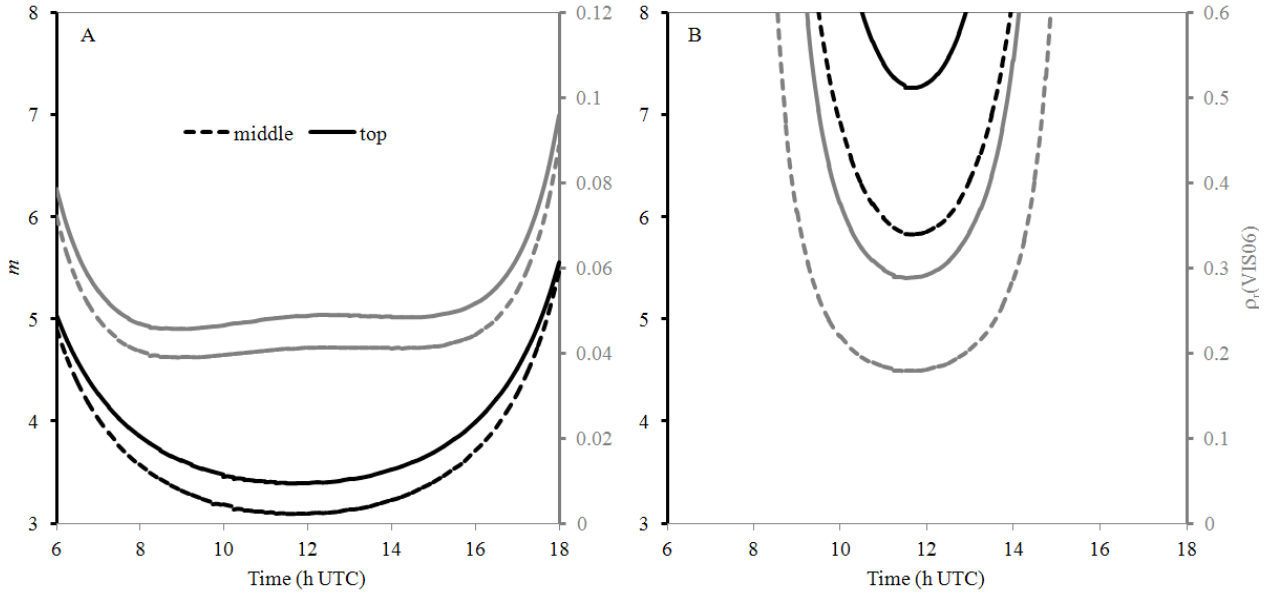

Figure 4.5. Variability of Rayleigh reflectance in the VIS06 band (grey lines) and total airmass (black lines) on (A) 15th June 2008 and (B) 15th December 2008 for the middle (dashed lines) and at the top (solid lines) of the SEVIRI subscene in Figure 4.4.

4.2.3 Definitions and general approach

At a wavelength λ, the total radiance at the top-of-atmosphere (TOA) sensed by a satellite sensor, $L_{tot}^{TOA}(\lambda)$, can be decomposed into radiances due to different processes occurring in the atmosphere, in the water, or at the air-water interface:

$$L_{tot}^{TOA}(\lambda) = L_r^{TOA}(\lambda) + L_a^{TOA}(\lambda) + L_{ra}^{TOA}(\lambda) + L_{wc}^{TOA}(\lambda) + L_g^{TOA}(\lambda) + L_w^{TOA}(\lambda) \qquad (4.2)$$

where $L_r^{TOA}(\lambda)$ and $L_a^{TOA}(\lambda)$ are the wavelength dependent radiances at TOA (units: Wm^{-2} sr^{-1} μm^{-1}) due to scattering by air molecules (Rayleigh scattering) and aerosols, respectively, $L_{ra}^{TOA}(\lambda)$ denotes Rayleigh-aerosol interactions, $L_{wc}^{TOA}(\lambda)$ for foam and white cap radiance, and $L_g^{TOA}(\lambda)$ denotes the sunglint radiance due to specular reflection of sunlight. We note that the $L_r^{TOA}(\lambda)$, $L_a^{TOA}(\lambda)$, and $L_{ra}^{TOA}(\lambda)$ terms also include reflected sky radiance. The marine radiance at TOA, denoted $L_w^{TOA}(\lambda)$, is related to the upwelling radiance just above the sea surface, $L_w^{0+}(\lambda)$, via the sea-sensor atmospheric transmittance $T_v(\lambda)$ (v for 'viewing'):

$$T_v(\lambda) = \frac{L_w^{TOA}(\lambda)}{L_w^{0+}(\lambda)} \tag{4.3}$$

It is assumed that the effects of atmospheric gases, aerosols, and air molecules on $T_v(\lambda)$ can be treated separately such that:

$$T_v(\lambda) = t_v^r(\lambda) t_v^a(\lambda) t_v^g(\lambda) \tag{4.4}$$

where $t_v^r(\lambda)$, $t_v^a(\lambda)$, and $t_v^g(\lambda)$ denote the transmittance due to air molecules, aerosols, and atmospheric gasses, respectively.

Normalization of detected by illuminating light yields reflectance, ρ. In this context radiances at TOA are normalized by the downwelling irradiance at TOA, $E_d^{TOA}(\lambda)$ (units: Wm^{-2} μm^{-1}) to give reflectance at TOA (dimensionless):

$$\rho_x^{TOA}(\lambda) = \pi \frac{L_x^{TOA}(\lambda)}{E_d^{TOA}(\lambda)} \quad \text{with } x \in \{tot, r, a, ra, wc, g, w\} \tag{4.5}$$

The marine reflectance, $\rho_w^{0+}(\lambda)$, also termed 'water-leaving reflectance' (e.g., by Doerffer and Schiller 2007), carries useful information on seawater constituents and is defined as:

$$\rho_w^{0+}(\lambda) = \pi \frac{L_w^{0+}(\lambda)}{E_d^{0+}(\lambda)} \tag{4.6}$$

where $E_d^{0+}(\lambda)$ is the above-water downwelling irradiance (units: Wm^{-2} μm^{-1}), which is related to $E_d^{TOA}(\lambda)$ via the total atmospheric transmittance from sun to sea:

$$T_0(\lambda) = \frac{E_d^{0+}(\lambda)}{E_d^{TOA}(\lambda)} \tag{4.7}$$

Like $T_0(\lambda)$ in Eq. (4.4), $T_v(\lambda)$ is decomposed into its Rayleigh, aerosol, and gas contributions, $t_0^r(\lambda)$, $t_0^a(\lambda)$, and $t_0^g(\lambda)$, respectively.

The radiance sensed by a sensor's spectral band *B* with spectral response function $\omega(\lambda)$ is the spectral integral of $L_{tot}^{TOA}(\lambda)$ over the band width:

$$\int \omega(\lambda) L_{tot}^{TOA}(\lambda) d\lambda \tag{4.8}$$

Application of spectral band-integration to all radiance terms in Eq. (4.2) and normalization of each term by the band-integrated $E_d^{TOA}(\lambda)$, $\int \omega(\lambda) E_d^{TOA}(\lambda) d\lambda$, gives the decomposition of total reflectance at TOA for band *B*:

$$\rho_{tot}^{TOA(B)} = \rho_r^{TOA(B)} + \rho_a^{TOA(B)} + \rho_{ra}^{TOA(B)} + \rho_{wc}^{TOA(B)} + \rho_g^{TOA(B)} + \rho_w^{TOA(B)} \tag{4.9}$$

where

$$\rho_x^{TOA(B)} = \pi \frac{\int \omega(\lambda) L_x^{TOA}(\lambda) d\lambda}{\int \omega(\lambda) E_d^{TOA}(\lambda) d\lambda} \quad \text{with } x \in \{tot, r, a, ra, wc, g, w\} \tag{4.10}$$

The band-integrated above-water marine reflectance is:

$$\rho_w^{0+(B)} = \pi \frac{\int \omega(\lambda) L_w^{0+}(\lambda) d\lambda}{\int \omega(\lambda) E_d^{0+}(\lambda) d\lambda} \tag{4.11}$$

which gives, after substitution of Eq. (4.6) and (4.7):

$$\rho_w^{0+(B)} = \frac{\int \omega(\lambda) T_0(\lambda) \rho_w^{0+}(\lambda) E_d^{TOA}(\lambda) d\lambda}{\int \omega(\lambda) T_0(\lambda) E_d^{TOA}(\lambda) d\lambda} \tag{4.12}$$

Now $\rho_w^{TOA(B)}$ can be re-written, using Eqs. (4.3), (4.6), and (4.7):

$$\rho_w^{TOA(B)} = \frac{\int \omega(\lambda) T_v(\lambda) T_0(\lambda) \rho_w^{0+}(\lambda) E_d^{TOA}(\lambda) d\lambda}{\int \omega(\lambda) E_d^{TOA}(\lambda) d\lambda} \tag{4.13}$$

For relatively narrow spectral bands away from strongly varying atmospheric absorption Eq. (4.13) simplifies to $\rho_w^{TOA(B)} = T_v^{(B)} T_o^{(B)} \rho_w^{0+(B)}$ so that Eq. (4.9) can be written:

$$\rho_{tot}^{TOA(B)} = \rho_r^{TOA(B)} + \rho_a^{TOA(B)} + \rho_{ra}^{TOA(B)} + \rho_{wc}^{TOA(B)} + \rho_g^{TOA(B)} + T_v^{(B)} T_o^{(B)} \rho_w^{0+(B)} \quad (4.14)$$

This simplification is valid for sufficiently narrow and appropriately chosen spectral bands such as those of ocean colour sensors (MERIS, MODIS, SeaWIFS etc.) and the SEVIRI VIS06 and VIS08 bands. However, for a very broad spectral band such as SEVIRI's HRV band, this simplification may no longer be valid since each component of the convolution in the spectral integral in Eq. (4.13) may show strong spectral variability as shown in Figure 4.6. The SEVIRI HRV band is therefore treated separately in section 4.2.6.

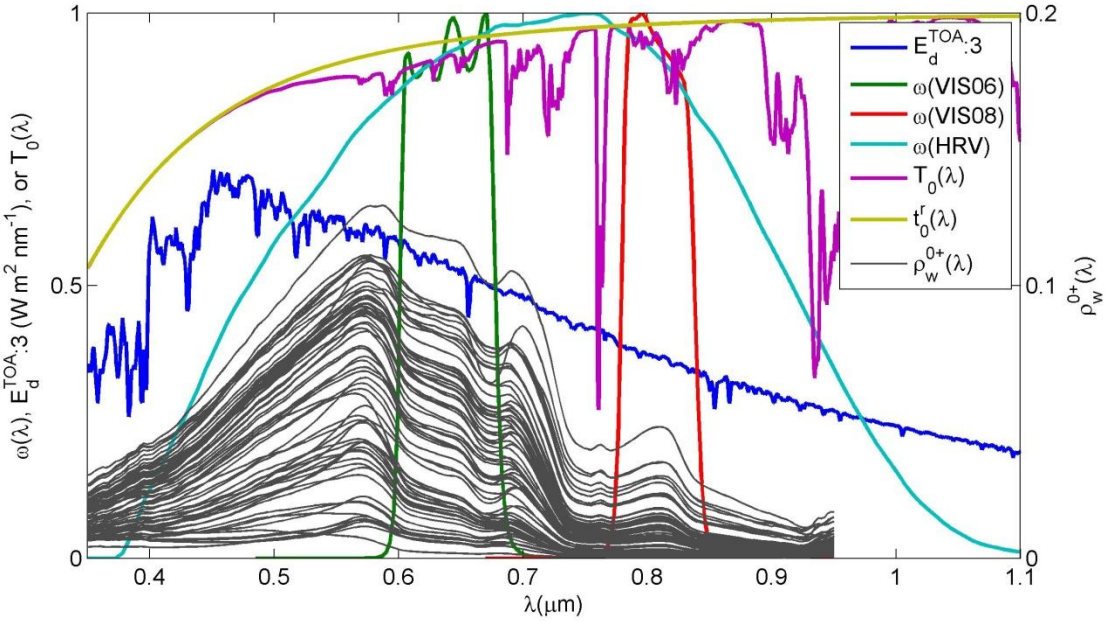

Figure 4.6. Normalized spectral response, ω(λ) of SEVIRI's VIS06, VIS08, and HRV bands, and one-way total (T_0) and Rayleigh transmittance, t_0^r, for a vertical atmospheric path and the US standard atmosphere model obtained from LOWTRAN simulations. Spectrum of solar irradiance at TOA from Thuillier et al. 2003. Thin lines represent above-water marine reflectance spectra, $\rho_w^{0+}(\lambda)$, recorded with above-water TriOS Ramses radiometers in the southern North Sea between 2001 and 2010. The reader is referred to Ruddick et al. 2006 for details on the seaborne measurement protocol.

4.2.4 SEVIRI solar channels calibration

Total reflectance at TOA for SEVIRI bands is obtained through calibration of the SEVIRI level 1.5 data. Count data (K) are transformed into total radiance at TOA, L_{tot}^{TOA} (units: W m^{-2} sr^{-1} μm^{-1}), by applying the appropriate calibration coefficients (c_f) and offset values (r_0) (Govaerts and Clerici 2004):

$$L_{tot}^{TOA(B)} = \frac{10(c_f^{(B)} K + r_0^{(B)})}{\left(\lambda_0^{(B)}\right)^2} \tag{4.15}$$

where $\lambda_0^{(B)}$ is band B's central wavelength. $L_{tot}^{TOA(B)}$ is then converted to total reflectance at TOA (Govaerts and Clerici 2004):

$$\rho_{tot}^{TOA(B)} = \frac{\pi\, d^2 L_{tot}^{TOA(B)}}{A_0^{(B)} E_0^{TOA(B)} \cos\theta_0} \tag{4.16}$$

where d is the Sun-Earth distance in astronomical units (AU), θ_0 is the sun zenith angle calculated from position, date and time, $E_0^{TOA(B)}$ is the extraterrestrial solar irradiance at TOA (units: Wm^{-2}μm^{-1}) for band B at 1AU. Calibration correction factors, $A_0^{(B)}$, for the Meteosat9 SEVIRI VIS06 and VIS08 channels of 0.92 and 0.94 are given by Ham and Sohn 2010 and Sohn (unpublished results), respectively. Correction factors for Meteosat8 VIS06, VIS08, and NIR16 bands can be found in Nicolas et al. 2006, as reported in Neukermans et al. 2009. An overview of these coefficients and signal-to-noise ratios (SNR) for SEVIRI's solar channels are given in Table 4.2. For comparison, ocean colour sensors such as MODIS and MERIS have SNRs of 1000-1500 in the 0.6-0.7 μm range, and of 500-1000 in the 0.7-0.9 μm range.

Table 4.2. Central wavelengths, $\lambda_0^{(B)}$, extraterrestrial solar irradiance, $E_0^{TOA(B)}$, Signal-to-Noise ratio (SNR), calibration coefficients (Govaerts and Clerici 2004) and correction factors, $A_0^{(B)}$ (Ham and Sohn 2010; Sohn unpublished results) for the SEVIRI Meteosat9 solar channels in 2008-2009.

Band	$\lambda_0^{(B)}$ (μm)	$c_f^{(B)}$ (mWm^{-2} sr^{-1} (cm^{-1})$^{-1}$)	$r_0^{(B)}$ (mWm^{-2} sr^{-1} (cm^{-1})$^{-1}$)	$E_0^{TOA(B)}$ (Wm^{-2}μm^{-1})	$A_0^{(B)}$	SNR
VIS06	0.635	0.020135	-1.026910	1618.0	0.92	610
		0.020419*	-1.041374*			
VIS08	0.810	0.025922	-1.32202	1113.0	0.94	70

		0.026168*	-1.334553*			
NIR16	1.640	0.022258	-1.135183	231.9	n.a.	11
		0.022322*	-1.138432*			
HRV	0.750	0.029499	-1.504429	1403.0	n.a.	2.5
		0.029934*	-1.526639*			

* from December 9 2008, 12:00 UTC onwards, n.a.: not available

4.2.5 Atmospheric correction of SEVIRI VIS06

In the case of SEVIRI, Eq. (4.14) can further be simplified. Sun glint reaches the sensor only for viewing zenith angles (θ_v) close to the sun zenith and for relative azimuth angles, $\Delta\phi$, between sun (ϕ_0) and sensor (ϕ_v) close to 180°. For the SEVIRI North Sea scene $\Delta\phi$ ranges between 3° and 100° during the day, clearly outside the directions contaminated by sun glint. Therefore, ρ_g^{TOA} can be dropped. ρ_{wc}^{TOA} is small for wind speeds lower than 10 m s^{-1} and largely corrected for in the aerosol correction for maritime aerosols (Gordon and Wang 1994). The difference between the spectral variation of white caps (Frouin et al. 1996) and aerosols gives an uncertainty on the marine reflectance of maximum 0.0009 for wind speeds of 10 m s^{-1}. The Rayleigh-aerosol interaction term, ρ_{ra}^{TOA} can be included in ρ_a^{TOA} so that Eq. (4.14) becomes:

$$\rho_{tot}^{TOA(B)} = \rho_r^{TOA(B)} + \rho_a^{TOA(B)} + T_{0,v}^{(B)}\rho_w^{0+(B)} \tag{4.17}$$

where $T_{0,v}^{(B)} = T_o^{(B)}T_v^{(B)}$ is the two-way sun-sea-sensor transmittance in spectral band *B*. The two-way transmittances for atmospheric gases, air molecules and aerosols are defined analogously.

4.2.5.1 RAYLEIGH AND GAS CORRECTIONS

The total reflectance received by the sensor is first corrected for two-way gas and Rayleigh transmittances, assuming that marine aerosols are generally low in the atmosphere. This gives, after Eq. (4.17):

$$\rho'^{TOA(B)}_{tot} = \rho'^{TOA(B)}_{r} + \rho'^{TOA(B)}_{a} + t_{0,v}^{a(B)}\rho_w^{0+(B)} \tag{4.18}$$

where $\rho' = \dfrac{\rho}{t_{0,v}^{g}t_{0,v}^{r}}$. For notational simplicity, the prime symbols, *B*, and TOA notation are dropped hereafter. The gaseous absorption correction is performed using the Msixs software package based on 6S

code (Vermote et al. 1997). This allows the computation of the transmittances of ozone (O_3) and water vapour (H_2O) in the VIS06 and VIS08 bands and for carbon dioxide (CO_2) and methane (CH_4) gases in the NIR16 band.

The correction for absorption by H_2O, which is strong in the VIS08 band (*see* Figure 4.6) and varies over the day, is done using the precipitable water content (PWC) obtained at 6:00, 12:00, and 18:00 UTC from the National Weather Service's National Centers for Environmental Prediction (NCEP) meteorological data. Data are linearly interpolated to give PWC (units: kg m^{-2}) every 15 minutes. Ozone column content is obtained from AIRS (1.0° x 1.0° daily Level-3 product) through NASA's Giovanni application, and daily averaged over the study area. CO_2 and CH_4 concentrations are obtained from climatological values for these gas vertical profiles (mid-latitude summer atmospheric model, McClatchey et al. 1972). Then, the 6S software is used to simulate the transmittances of these two gases for different airmasses. Finally a second order polynomial interpolation of the transmittances as a function of airmass is applied to derive the CO_2 and CH_4 transmittances for SEVIRI.

The Rayleigh scattering component, ρ_r, and two-way Rayleigh transmittances, $t_{0,v}^r$ are calculated from viewing and illumination geometry ($\theta_v, \theta_0, \phi_v, \phi_0$), atmospheric pressure, and wind speed using lookup tables (LUTs) constructed the Msixs software package based on 6S code (Vermote et al. 1997). Atmospheric pressure and wind speed are spatially averaged over the study area from 6-hourly NCEP atmospheric pressure data. A daily mean pressure is computed, while a temporal nearest neighbour is taken for wind speeds. The Rayleigh and gas corrected reflectance is defined as:

$$\rho_c = \rho_{tot} - \rho_r = \rho_a + t_{0,v}^a \rho_w^{0+} \tag{4.19}$$

4.2.5.2 AEROSOL CORRECTION

To obtain ρ_w^{0+} in the VIS06 band, denoted $\rho_w^{0+(0.6)}$, from Eq. (4.19), the aerosol reflectance and two-way aerosol transmittance, $\rho_a^{(0.6)}$ and $t_{0,v}^{a(0.6)}$, remain to be computed. In the clearest waters, the water reflectance is negligible, and ρ_a can be computed. For more turbid waters, further knowledge or assumptions are required regarding the spectral behaviour of ρ_a, which varies with aerosol size and refractive index. Two approaches are considered using either the VIS08 or NIR16 band to correct for aerosol scattering. It is shown (*see* Appendix, section 4.5.1) that the VIS08 band gives the lowest atmospheric correction uncertainties on the desired $\rho_w^{0+(0.6)}$. Therefore, the atmospheric correction of VIS06 using VIS08 for aerosol correction is described hereafter.

The relations and unknown quantities for the VIS06 and VIS08 bands are, after Eq. (4.19)

$$\rho_c^{(0.6)} = \rho_{tot}^{(0.6)} - \rho_r^{(0.6)} = \rho_a^{(0.6)} + t_{0,v}^{a(0.6)} \rho_w^{0+(0.6)} \quad (4.20)$$

$$\rho_c^{(0.8)} = \rho_{tot}^{(0.8)} - \rho_r^{(0.8)} = \rho_a^{(0.8)} + t_{0,v}^{a(0.8)} \rho_w^{0+(0.8)} \quad (4.21)$$

where $\rho_c^{(0.6)}$ and $\rho_c^{(0.8)}$ are known for each image pixel and the other six parameters ($\rho_a^{(0.6)}$, $\rho_a^{(0.8)}$, $\rho_w^{(0.6)}$, $\rho_w^{(0.8)}$, $t_{0,v}^{a(0.6)}$, and $t_{0,v}^{a(0.8)}$) are unknown.

LUTs for maritime aerosols were created using 6S software (Vermote et al. 1997): (1) LUT(ρ_a) giving ρ_a as a function of viewing and illumination geometry, spectral band, and aerosol optical thickness, τ_a. (2) LUT(t_a) giving aerosol transmittances as a function of zenith angle, spectral band, and τ_a. The two-way aerosol transmittances, $t_{0,v}^{a(0.6)}$ and $t_{0,v}^{a(0.8)}$, can thus be obtained from viewing and illumination geometry and τ_a via LUT(t_a), where τ_a in turn can be obtained from "inversion" of LUT(ρ_a) as follows:

(1) compute ρ_a corresponding to τ_a of 0.01, 0.5, and 1 from LUT(ρ_a)

(2) linearly interpolate the observed ρ_a over the aerosol reflectance range obtained in the previous step to obtain the corresponding τ_a. Values outside this range are considered clouds and masked.

4.2.5.3 ATMOSPHERIC CORRECTION ASSUMPTIONS

There are 6 unknowns with 4 equations: Eqs. (4.20) and (4.21), $t_{0,v}^{a(0.6)} = \mathrm{LUT}(t_a) \circ \mathrm{LUT}(\rho_a)^{-1}\left(\rho_a^{(0.6)}\right)$, and $t_{0,v}^{a(0.8)} = \mathrm{LUT}(t_a) \circ \mathrm{LUT}(\rho_a)^{-1}\left(\rho_a^{(0.8)}\right)$. To solve these, further assumptions regarding the spectral shape of aerosols and marine reflectances are needed, in analogy to the assumptions made previously for the SeaWiFS 765nm and 865nm bands (Ruddick et al. 2000):

(1) The VIS06:VIS08 band ratio of marine reflectances is constant in space and time:

$$\sigma = \frac{\rho_w^{0+(0.6)}}{\rho_w^{0+(0.8)}} \quad (4.22)$$

(2) The VIS06:VIS08 band ratio of aerosol reflectances at TOA is spatially homogeneous over the SEVIRI scene:

$$\varepsilon = \frac{\rho_a^{(0.6)}}{\rho_a^{(0.8)}} \quad (4.23)$$

The marine reflectance ratio, σ, is calibrated from an extensive archive of hyperspectral in situ above-water radiance and irradiance measurements collected between 2001 and 2010 with a set of TriOS

Ramses radiometers. From a total of 840 measurements, 67 measurements were selected with clear skies, low wind speeds, and small deviation from the time-averaged mean reflectance at 780 nm (for details *see* Ruddick et al. 2006). The 67 remaining measurements of $L_w^{0+}(\lambda)$ and $E_d^{0+}(\lambda)$ were band-integrated according to Eq. (4.11) to give $\rho_w^{0+(0.8)}$ and $\rho_w^{0+(0.6)}$, shown in Figure 4.7. The parameter σ is calibrated via least-squares regression through the origin of 47 reflectance measurements for which $\rho_w^{0+(0.8)}$ <0.011.

The least squares estimator of the slope of a line of the form $y=ax$ through a cloud of points (x_i,y_i) is:

$$\hat{a} = \frac{\sum x_i y_i}{\sum x_i^2} \tag{4.24}$$

with standard deviation:

$$S_a = \sqrt{\frac{1}{(n-1)\sum x_i^2}\left(\sum y_i^2 - \frac{\left(\sum x_i y_i\right)^2}{\sum x_i^2}\right)} \tag{4.25}$$

Application of Eqs. (4.24) and (4.25) to the ($\rho_w^{0+(0.8)}$, $\rho_w^{0+(0.6)}$) reflectance measurements gives:

$$\sigma = 6.09 \pm 0.16 \tag{4.26}$$

The relationship between $\rho_w^{0+(0.8)}$ and $\rho_w^{0+(0.6)}$ becomes non-linear for higher reflectances, as shown in Figure 4.7. The very turbid water points represented by the grey dots in Figure 4.7 generally correspond to near-shore waters less than 3 km from the Belgian coast, which are not mapped by SEVIRI due to its coarse spatial resolution. The limitations of the model for $\rho_w^{0+(0.8)}$ exceeding 0.011 are discussed in section 4.4.1.

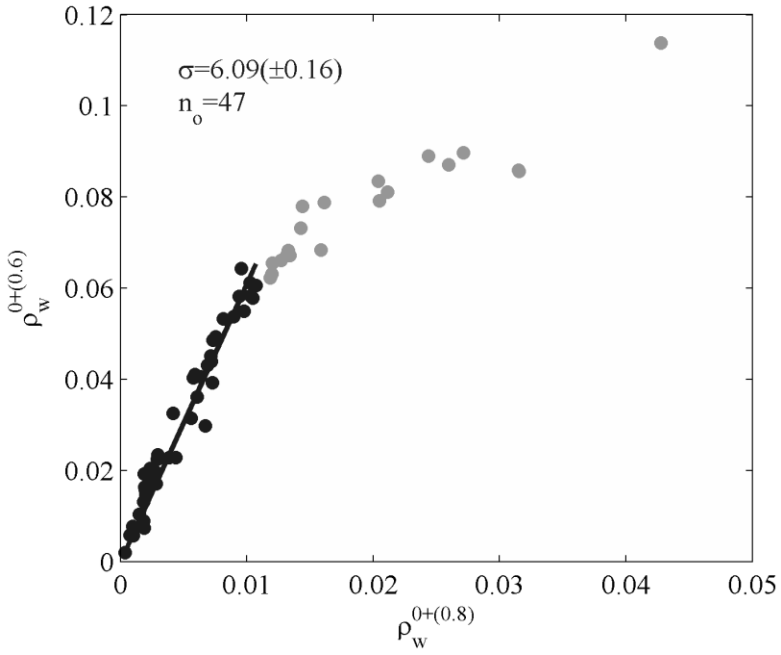

Figure 4.7. Marine reflectances in the VIS06 and VIS08 bands obtained from optimal in situ above-water marine reflectance measurements collected between 2001 and 2010 in the southern North Sea waters. The parameter σ is calibrated through linear regression (black line) of 47 reflectance measurements for which $\rho_w^{0+(0.8)}$ <0.011.

An estimate of ε is obtained on an image-by-image basis from the VIS06:VIS08 band ratio of Rayleigh and gas corrected reflectances, $\rho_c^{(B)}$, over clear waters pixels where $\rho_w^{0+(B)} \approx 0$. The two year SEVIRI archive was first processed using the clear water pixel areas described in Neukermans et al. 2009 and shown as black rectangles in Figure 4.8. Afterwards, clear water pixels were redefined as those pixels having SPM below 3 mg L^{-1} for 95% of the observations in 2008-2009 and are outlined by the red polygons in Figure 4.8. The newly defined clear water areas exclude the turbid water plume that can be seen in Figure 4.8 and are more evenly distributed throughout the study area.

Neukermans et al. 2009 estimate ε and its uncertainty, $\Delta\varepsilon$, from the mean and standard deviation of $\rho_c^{(0.6)}$: $\rho_c^{(0.8)}$ for these pixels, assuming that these ratios are normally distributed. An example histogram of $\rho_c^{(0.6)}$: $\rho_c^{(0.8)}$ values is shown in Figure 4.9(a). Besides the need for the $\rho_c^{(0.6)}$: $\rho_c^{(0.8)}$ to be approximately normally distributed, this assessment of ε is sensitive to data outliers and noise. Especially the noise of the ratios may be large for SEVIRI due to digitization effects (quantified in section 4.2.7.2). Alternatively, as implemented in Neukermans et al. accepted, ε can be assessed from the

slope of the $\rho_c^{(0.6)}$ *vs.* $\rho_c^{(0.8)}$ regression line as shown in Figure 4.9(b). An iteratively reweighted least squares technique using the MATLAB robustfit.m routine is applied, where $\Delta\varepsilon$ is estimated from the standard error of the slope estimate. This approach minimizes effects of outliers and data noise and is independent of the normality of the reflectance ratio distribution. Moreover, the offset of the regression line reflects small uncertainties in the calibration of the SEVIRI sensor and the Rayleigh and gas corrections, and allows to correct for these uncertainties through subtraction of the offset from $\rho_c^{(0.6)}$. Values of this offset typically lie between -0.0051 and 0.0126 (5 and 95th percentiles) with a median of 0.0028 for 15384 observations. This procedure is effectively a vicarious calibration of the VIS06 band performed on an image-by-image basis without the need to assume a temporally constant aerosol type. The effectiveness of this procedure to correct for uncertainties in the calibration of VIS06 and VIS08 bands is investigated in the Appendix, section 4.5.2.

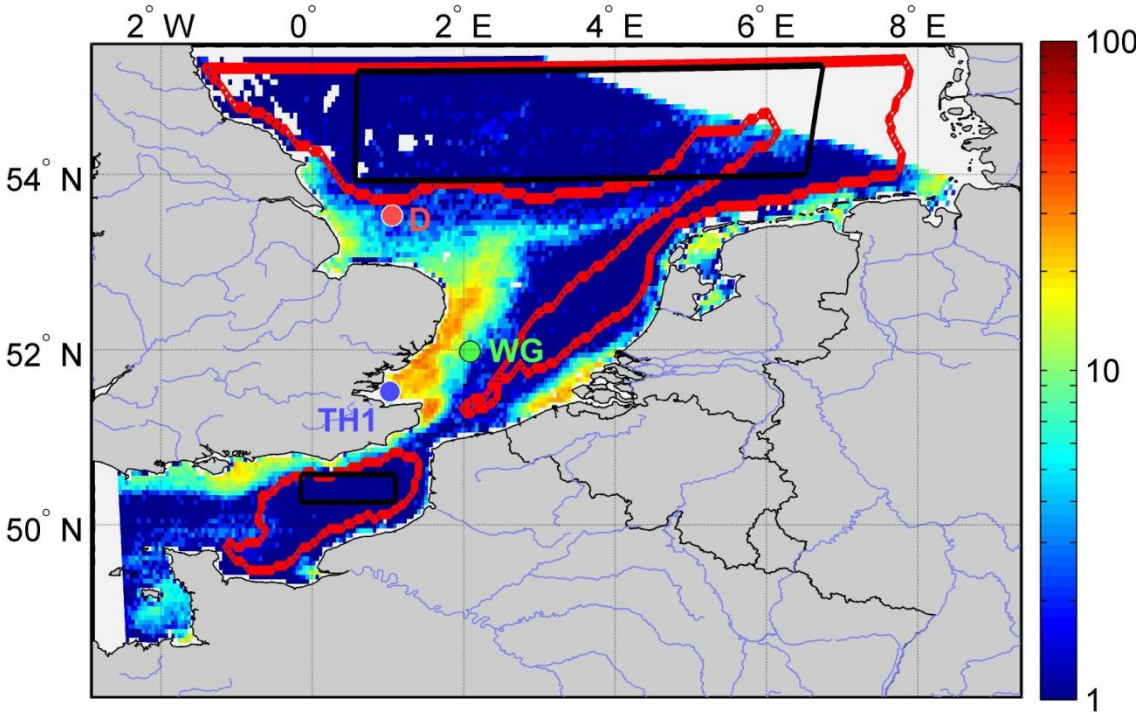

Figure 4.8. Identification of clear water pixels from which the VIS06:VIS08 band ratio of aerosol reflectance, ε, is obtained. The black rectangles delineate the clear water pixels identified by Neukermans et al. 2009, while the red polygons delineate the revised clear water pixels. Background: SPM (in mg L^{-1}) map from SEVIRI on February 11, 2008 at 10:45 UTC. The location of the Cefas SmartBuoys at Warp Anchorage (TH1), West Gabbard (WG), and Dowsing (D), used in Chapter 5 is also indicated.

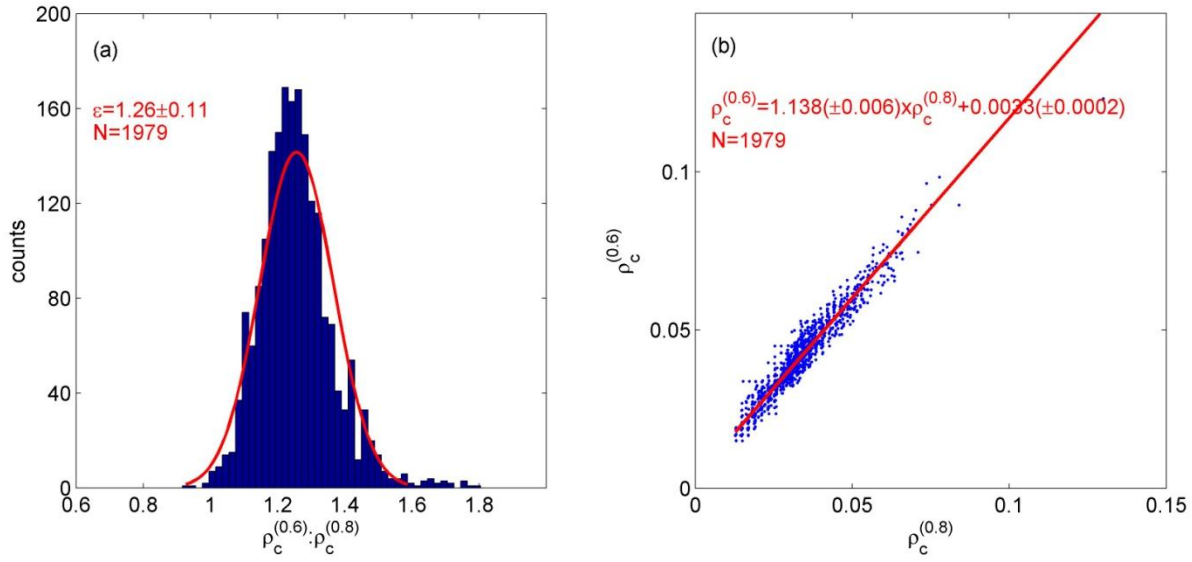

Figure 4.9. Example of the estimation of the VIS06:VIS08 band ratio of aerosol reflectances, ε, on April 9, 2008 at 09:45 UTC from the Rayleigh and gas corrected reflectances, ρ_c, in the VIS06 and VIS08 bands of clear water pixels via (a) the mean and standard error of $\rho_c^{(0.6)}:\rho_c^{(0.8)}$ values, shown as the normal fit to the histogram, or (b) via linear regression of $\rho_c^{(0.6)}$ vs. $\rho_c^{(0.8)}$, with uncertainties on regression coefficients given by their standard error. N is the number of pixels.

4.2.5.4 SOLVING FOR MARINE AND AEROSOL REFLECTANCES

Using Eq. (4.22), we rewrite:

$$t_{0,v}^{a(0.6)}\rho_w^{0+(0.6)} = \frac{t_{0,v}^{a(0.6)}}{t_{0,v}^{a(0.8)}} t_{0,v}^{a(0.8)}\varepsilon\rho_w^{0+(0.8)} = \gamma\varepsilon t_{0,v}^{a(0.8)}\rho_w^{0+(0.8)} \tag{4.27}$$

defining γ as the VIS06:VIS08 ratio of two-way aerosol transmittances:

$$\gamma = \frac{t_{0,v}^{a(0.6)}}{t_{0,v}^{a(0.8)}} \tag{4.28}$$

Substitution of Eqs. (4.27), (4.28), and (4.23) into Eqs.(4.20)-(4.21) gives:

$$\varepsilon\rho_a^{(0.8)} + \gamma\varepsilon t_{0,v}^{a(0.8)}\rho_w^{0+(0.8)} = \rho_c^{(0.6)} \tag{4.29}$$

$$\rho_a^{(0.8)} + t_{0,v}^{a(0.8)}\rho_w^{0+(0.8)} = \rho_c^{(0.8)} \tag{4.30}$$

which can be solved by substitution to give:

$$\rho_a^{(0.8)} = \frac{\gamma\sigma\rho_c^{(0.8)} - \rho_c^{(0.6)}}{\gamma\sigma - \varepsilon} \tag{4.31}$$

$$\rho_w^{0+(0.8)} = \frac{\rho_c^{(0.6)} - \varepsilon\rho_c^{(0.8)}}{t_{0,v}^{a(0.8)}(\gamma\sigma - \varepsilon)} \tag{4.32}$$

$$\rho_a^{(0.6)} = \varepsilon\frac{\gamma\sigma\rho_c^{(0.8)} - \rho_c^{(0.6)}}{\gamma\sigma - \varepsilon} \tag{4.33}$$

$$\rho_w^{0+(0.6)} = \sigma\frac{\rho_c^{(0.6)} - \varepsilon\rho_c^{(0.8)}}{t_{0,v}^{a(0.8)}(\gamma\sigma - \varepsilon)} \tag{4.34}$$

The parameter γ remains unknown until after computation of the aerosol reflectances from Eqs. (4.31) and (4.33). Therefore, a two-pass algorithm was used: first setting $\gamma = 1$ and solving Eqs. (4.31) and (4.33), yielding a second approximation of γ which is then used to solve Eqs. (4.31)-(4.34).

4.2.5.5 ATMOSPHERIC CORRECTION PROCESSING STEPS

The atmospheric correction is schematically depicted in Figure 4.10 and can be summarized as follows:

1. Calibrate SEVIRI level 1.5 VIS06 and VIS08 data to obtain ρ_{tot}^{TOA} in VIS06 and VIS08 SEVIRI channels from Eq. (4.16)
2. Correct for gaseous absorption, Rayleigh transmittance, and Rayleigh scattering using Eqs. (4.18)-(4.19).
3. Compute the calibration parameter ε (Eq. (4.23)) from the regression slope of Rayleigh and gas corrected reflectances in the VIS06 and VIS08 bands over clear waters pixels in every scene, and estimate $\Delta\varepsilon$ as the standard error of the slope estimate.
4. Compute $\rho_a^{(0.8)}$ and $\rho_a^{(0.6)}$ from Eqs. (4.31) and (4.33), first setting $\gamma = 1$
5. Get $\tau_a^{(0.8)}$ and $\tau_a^{(0.6)}$ from $\rho_a^{(0.6)}$ and $\rho_a^{(0.8)}$, respectively, through linear interpolation of ρ_a on [0.001, 0.05, 0.5] as described in section 4.2.5.2.
6. Get $t_{0,v}^{a(0.8)}$ and $t_{0,v}^{a(0.6)}$ from LUT(t_a)
7. Repeat steps (5)-(7) with $\gamma = \frac{t_{0,v}^{a(0.6)}}{t_{0,v}^{a(0.8)}}$
8. Compute $\rho_w^{0+(0.8)}$ and $\rho_w^{0+(0.6)}$ from Eqs. (4.32) and (4.34)

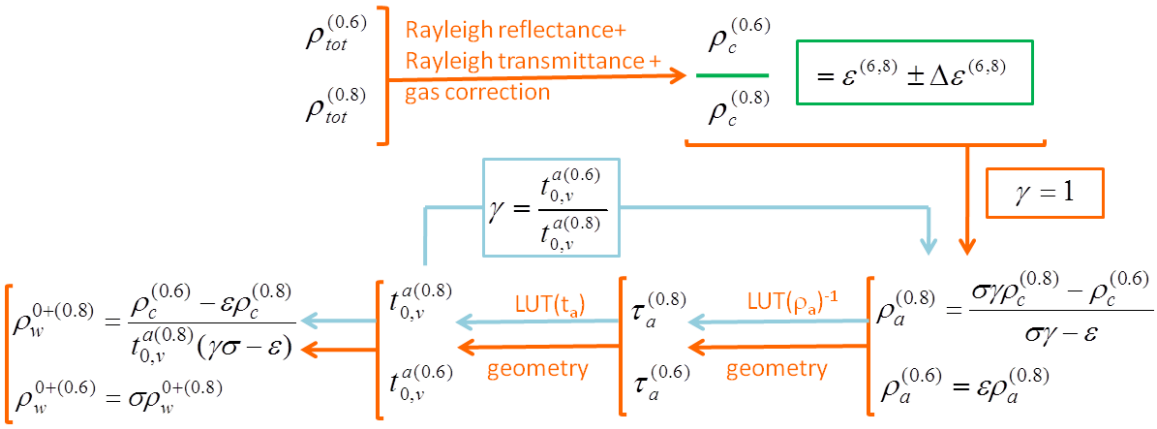

Figure 4.10. Schematical depiction of the processing steps in the atmospheric correction of the SEVIRI VIS06 and VIS08 channels. The second pass in the two-pass algorithm is represented by the blue lines (in the first pass, shown by the orange lines, $\gamma = 1$).

4.2.6 Atmospheric correction using the HRV band

To minimize uncertainties of atmospheric correction of the HRV band, the spatial variability of HRV marine reflectance within each VIS06 pixel is used as a small perturbation to the VIS06 derived marine reflectance. To use the higher spatial resolution information of the HRV band, first a relationship is established between the marine reflectances in the HRV and VIS06 bands taking account of the different sensor response functions and the different effective atmospheric transmittances. Then this relationship is used to estimate the spatial variability of $\rho_w^{0+(0.6)}$ on the fine HRV grid using the spatial anomaly of TOA HRV reflectance.

4.2.6.1 RELATING MARINE REFLECTANCES IN THE HRV AND VIS06 BANDS

Re-examining Figure 4.6, it can be seen that in the case of the HRV band the dominant contributions of T_0 and T_v to the spectral integral in Eq. (4.13) are limited: in the spectral range 0.75-0.90μm, the strong atmospheric absorption, dominated by water vapour, is compensated by a low $\rho_w^{0+}(\lambda)$ and important Rayleigh effects on transmittance in the range 0.35-0.45μm are compensated by a low $\omega(\lambda)$. Hence, atmospheric transmittances in the range 0.45-0.75μm contribute most strongly to the spectral integral in Eq. (4.13). In this range the atmospheric transmittances are reasonably smooth and high. A good linear correlation between $\rho_w^{0+(0.6)}$ and $\rho_w^{0+(HRV)}$ is observed as shown in Figure 4.11(a). Combination of these observations suggests that $\rho_w^{TOA(HRV)}$ can be approximated by

$$\rho_w^{TOA(HRV)} \approx \left(A\rho_w^{0+(0.6)} + B\right)T_{o,v}^{(0.6)}\alpha^{m/2} \tag{4.35}$$

where $T_{0,v}^{(0.6)}$ is the two-way (sun-sea and sea-sensor) atmospheric transmittance for a given two-way airmass *m* in the VIS06 band:

$$T_{o,v}^{(0.6)} = \frac{\int \omega(\lambda)T_v(\lambda)T_0(\lambda)E_d^{TOA}(\lambda)d\lambda}{\int \omega(\lambda)E_d^{TOA}(\lambda)d\lambda} \tag{4.36}$$

The values of A and α have been obtained by spectral convolution of 67 measured hyperspectral seaborne spectra with: (a) $\rho_w^{0+(0.6)}$ and $\rho_w^{0+(HRV)}$ computed according to Eq. (4.11) and (b) with $\rho_w^{TOA(HRV)}$ and $T_{0,v}^{(0.6)}$ according to Eqs. (4.13) and (4.36), respectively. The atmospheric transmittances, $T_{0,v}(\lambda)$, are obtained from LOWTRAN simulations for *m*=2 and the US standard atmosphere model, shown in Figure 4.6. These include Rayleigh transmittances, aerosol transmittances, and gas transmittances for ozone, carbon dioxide, and water vapor. The results of these calculations are shown in Figure 4.11 and give (a) *A*=0.71(±0.01) and (b) $A\alpha$=0.68(±0.01) and hence α=0.96(±0.02).

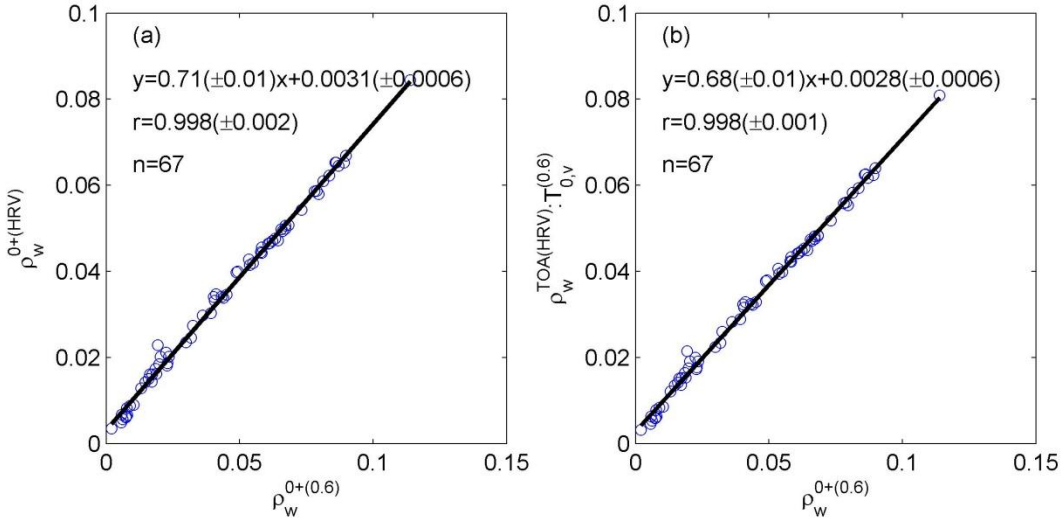

Figure 4.11. (a) Linear regression of above-water marine reflectance in the HRV and the VIS06 bands and (b) linear regression of marine reflectance of the HRV band at TOA, normalized by two-way atmospheric transmittance in the VIS06 band vs. above-water marine reflectance in the VIS06 band.

4.2.6.2 ESTIMATING SPATIAL VARIABILITY OF $\rho_w^{0+(0.6)}$ ON THE HRV GRID FROM HRV SPATIAL ANOMALY

Each pixel in the VIS06 grid corresponds to 3x3 pixels in the HRV grid. The spatial variability of $\rho_w^{TOA(HRV)}$ within each VIS06 pixel is used to represent a small perturbation to the marine reflectance retrieved from the VIS06 band. Let the bar superscript denote the mean value of 9 HRV pixels corresponding to one pixel in the VIS06 grid. The spatial anomaly of the HRV signal within the VIS06 grid is:

$$\hat{\rho}_{tot}^{TOA(HRV)} = \rho_{tot}^{TOA(HRV)} - \overline{\rho}_{tot}^{TOA(HRV)} \tag{4.37}$$

The spatial average of Eq. (4.17) is given by:

$$\overline{\rho}_{tot}^{TOA(HRV)} = \overline{\rho}_{r}^{TOA(HRV)} + \overline{\rho}_{a}^{TOA(HRV)} + \overline{\rho}_{w}^{TOA(HRV)} \tag{4.38}$$

Subtraction of Eq. (4.38) from Eq. (4.17) gives the spatial anomaly of $\rho_{tot}^{TOA(HRV)}$ within the VIS06 grid pixels as:

$$\hat{\rho}_{tot}^{TOA(HRV)} = \hat{\rho}_{a}^{TOA(HRV)} + \hat{\rho}_{r}^{TOA(HRV)} + \hat{\rho}_{w}^{TOA(HRV)} \tag{4.39}$$

It is assumed that the Rayleigh and aerosol reflectances are spatially constant within each 3 km x 6 km VIS06 pixel:

$$\hat{\rho}_{a}^{TOA(HRV)} = 0 \text{ and } \hat{\rho}_{r}^{TOA(HRV)} = 0 \tag{4.40}$$

Eq. (4.39) then simplifies to:

$$\hat{\rho}_{tot}^{TOA(HRV)} = \hat{\rho}_{w}^{TOA(HRV)} \tag{4.41}$$

Now, let $\rho_{w,\otimes}^{0+(0.6)}$ and $T_{o,v,\otimes}^{(0.6)}$ denote the above-water marine reflectance and the two-way total transmittance in the VIS06 band on the HRV grid, respectively and $m_\otimes$ denote the airmass on the HRV grid. From Eq. (4.35) and subject to the underlying approximation we have:

$$\rho_{w}^{TOA(HRV)} = \left(A\rho_{w,\otimes}^{0+(0.6)} + B\right)T_{o,v,\otimes}^{(0.6)}\alpha^{m_\otimes/2} \tag{4.42}$$

and

$$\overline{\rho}_{w}^{TOA(HRV)} = \left(A\overline{\rho}_{w,\otimes}^{0+(0.6)} + B\right)\overline{T}_{o,v,\otimes}^{(0.6)}\alpha^{\overline{m}_\otimes/2} \tag{4.43}$$

where $\overline{\rho}_{w,\otimes}^{0+(0.6)} = \rho_w^{0+(0.6)}$, $\overline{T}_{o,v,\otimes}^{(0.6)} = T_{o,v}^{(0.6)}$, and $\overline{m}_\otimes = m$. Within each VIS06 grid pixel it is reasonable to assume that $T_{o,v,\otimes}^{(0.6)} \approx T_{o,v}^{(0.6)}$ and $m_\otimes \approx m$. Substitution of Eqs. (4.42) and (4.43) in (4.41) then gives:

$$\hat{\rho}_{tot}^{TOA(HRV)} = A\left(\rho_{w,\otimes}^{0+(0.6)} - \rho_{w}^{0+(0.6)}\right)T_{o,v}^{(0.6)}\alpha^{m/2} \tag{4.44}$$

and so

$$\rho_{w,\otimes}^{0+(0.6)} = \rho_{w}^{0+(0.6)} + \frac{\hat{\rho}_{tot}^{TOA(HRV)}}{AT_{o,v}^{(0.6)}\alpha^{m/2}} \tag{4.45}$$

The first term in Eq. (4.45) is known for each VIS06 grid pixel. The second term represents the spatial variation of $\rho_{w}^{0+(0.6)}$ on the HRV grid within each VIS06 grid pixel. It is computed from the spatial anomaly of the HRV total reflectance at TOA (= spatial anomaly of HRV marine reflectance at TOA) after modification to account for differences in atmospheric transmittances and spectral convolution with marine reflectances between the VIS06 and HRV bands. An uncertainty estimate on $\rho_{w,\otimes}^{0+(0.6)}$ is derived in section 4.2.7.4.

4.2.7 Estimate of uncertainty on marine reflectance

Uncertainties on marine reflectances arise from different sources. Here, we estimate uncertainties associated with the atmospheric correction assumptions given by Eqs. (4.22) and (4.23). Digitization effects are investigated next. Other uncertainties, such as aerosol model, whitecap correction etc. are not included here.

4.2.7.1 UNCERTAINTIES ASSOCIATED WITH THE ATMOSPHERIC CORRECTION ASSUMPTIONS

Uncertainties on the assumptions of the atmospheric correction in Eqs. (4.22) and (4.23) introduce an uncertainty on the marine reflectance $\rho_{w}^{0+(0.6)}$, which can be estimated from first order error propagation (ISO 1995):

$$\Delta\rho_{w}^{0+(0.6)} = \left[\left(\frac{\partial\rho_{w}^{0+(0.6)}}{\partial\varepsilon^{(6,8)}}\Delta\varepsilon\right)^{2} + \left(\frac{\partial\rho_{w}^{0+(0.6)}}{\partial\sigma}\Delta\sigma\right)^{2}\right]^{1/2} \tag{4.46}$$

where $\Delta\varepsilon$ and $\Delta\sigma$ are the uncertainties in the estimation of the calibration parameters σ and ε respectively. Partial derivation of $\rho_{w}^{0+(0.6)}$ in expression (4.34) to σ and ε gives:

$$\Delta\rho_{w}^{(0.6)} = \left[\left(\frac{\rho_{a}^{(0.8)}\sigma}{t_{0,v}^{a(0.8)}(\gamma\sigma-\varepsilon)}\Delta\varepsilon\right)^{2} + \left(\frac{\rho_{w}^{0+(0.8)}\varepsilon}{\gamma\sigma-\varepsilon}\Delta\sigma\right)^{2}\right]^{1/2} \tag{4.47}$$

The first component ($\Delta_a \rho_w^{0+(0.6)}$), is related to the aerosol turbidity, while the second component ($\Delta_w \rho_w^{0+(0.6)}$) is related to the water turbidity. The contribution of each component can be understood by simplifying with $t_{o,v}^{a(0.8)} = 1 = \gamma$ and taking a typical value of $\varepsilon = 1.02 \pm 0.01$. Then $\Delta_a \rho_w^{0+(0.6)} = 0.012 \rho_a^{(0.8)}$ and $\Delta_w \rho_w^{0+(0.6)} = 0.032 \rho_w^{0+(0.8)}$.

4.2.7.2 DIGITIZATION UNCERTAINTIES

The uncertainty on the TOA reflectances due to digitization can be derived from Eqs. (4.15) and (4.16), giving:

$$\Delta \rho_{tot}^{TOA(B)} = \frac{10 c_f^{(B)} \pi d^2}{\left(\lambda_0^{(B)}\right)^2 E_0^{TOA(B)} A_0^{(B)} \cos\theta_0} \tag{4.48}$$

Digitization uncertainty increases with increasing sun zenith angle, $0° \le \theta_0 \le 80°$, between 0.001 and 0.006 for the VIS06 band and between 0.001 and 0.007 for the VIS08 band, as shown in Table 4.3. The uncertainty on $\rho_w^{0+(0.6)}$ due to digitization in VIS06 and VIS08 at TOA, $\Delta_d \rho_w^{0+(0.6)}$, is also obtained from first order error propagation (ISO 1995):

$$\Delta_d \rho_w^{0+(0.6)} = \left[\left(\frac{\partial \rho_w^{0+(0.6)}}{\partial \rho_{tot}^{TOA(0.6)}} \Delta \rho_{tot}^{TOA(0.6)} \right)^2 + \left(\frac{\partial \rho_w^{0+(0.6)}}{\partial \rho_{tot}^{TOA(0.8)}} \Delta \rho_{tot}^{TOA(0.8)} \right)^2 \right]^{1/2} \tag{4.49}$$

Partial derivation of Eq. (4.34) to $\rho_{tot}^{TOA(0.6)}$ and to $\rho_{tot}^{TOA(0.8)}$ using Eq. (4.19) gives:

$$\Delta_d \rho_w^{0+(0.6)} = \frac{\sigma}{t_{0,v}^{a(0.8)} (\gamma\sigma - \varepsilon)} \left[\left(\frac{\Delta \rho_{tot}^{(0.6)}}{t_{o,v}^{r,g(0.6)}} \right)^2 + \left(\frac{\varepsilon \Delta \rho_{tot}^{(0.8)}}{t_{o,v}^{r,g(0.8)}} \right)^2 \right]^{1/2} \tag{4.50}$$

This digitization uncertainty is evaluated in Table 4.3 for a typical $\theta_v = 60°$ (corresponding to the middle of the SEVIRI North Sea scene in Figure 4.4), $\varepsilon = 1.02 \pm 0.01$, $\gamma = 1$, typical gas concentrations (320 Dobson units for ozone and 29.3 kg m^{-2} for PWC) and for clear (CA) and turbid (TA) atmospheres with aerosol optical thicknesses, $\tau_a(550\text{nm})$, of 0.01 and 0.5, respectively. In the clearest waters where $\rho_w^{0+(0.6)}$ is about 0.002-0.006 and for moderate air masses, the magnitude of the digitization uncertainty is comparable to $\rho_w^{0+(0.6)}$. Digitization uncertainty increases rapidly for air masses above 4, reaching 0.03 for turbid atmospheres and an air mass of 7.8.

4.2.7.3 COMBINED ATMOSPHERIC-DIGITIZATION UNCERTAINTY

The uncertainty due to digitization is added to the uncertainty associated with the atmospheric correction to give:

$$\Delta\rho_w^{0+(0.6)} = \left[\left(\Delta_d \rho_w^{0+(0.6)}\right)^2 + \left(\Delta_a \rho_w^{0+(0.6)}\right)^2 + \left(\Delta_w \rho_w^{0+(0.6)}\right)^2 \right]^{1/2} \quad (4.51)$$

The contribution of each component in Eq. (4.51) to $\Delta\rho_w^{0+(0.6)}$ is further evaluated in Table 4.3 for a relative azimuth angle of 40° and for clear (CW) and turbid water (TW) with $\rho_w^{0+(0.6)}$ of 0.004 and 0.07, respectively. Even for turbid water and a turbid atmosphere the digitization uncertainty is the dominant contributor to the total uncertainty on marine reflectance.

Table 4.3. Contribution of each component in Eq. (4.51) to $\Delta\rho_w^{0+(0.6)}$ for varying sun zenith angles (θ_0), clear (CA, $\tau_a(550\text{nm}) = 0.01$) and turbid (TA, $\tau_a(550\text{nm}) = 0.5$) atmospheres, and clear (CW, $\rho_w^{0+(0.6)} = 0.004$) and turbid (TW, $\rho_w^{0+(0.6)} = 0.07$) waters. Viewing geometry values typical for the SEVIRI North Sea area were taken: $\theta_v = 60°$ and $\Delta\phi = 40°$, typical gas concentrations and $\varepsilon = 1.02 \pm 0.01$, $\gamma = 1$, and $\sigma = 6.09 \pm 0.16$. Airmass and digitization uncertainty for total TOA reflectance in the VIS06 ($\Delta\rho_{tot}^{TOA(0.6)}$) and VIS08 bands ($\Delta\rho_{tot}^{TOA(0.8)}$) computed using Eq. (4.48) are also shown.

				$\Delta_d\rho_w^{0+(0.6)}$		$\Delta_a\rho_w^{0+(0.6)}$		$\Delta_w\rho_w^{0+(0.6)}$		$\Delta\rho_w^{0+(0.6)}$	
θ_0	m	$\Delta\rho_{tot}^{TOA(0.6)}$	$\Delta\rho_{tot}^{TOA(0.8)}$	CA	TA	CA	TA	CW	TW	CA, CW	TA, TW
0	3.00	0.0011	0.0012	0.002300	0.002841	0.000006	0.000562	0.000021	0.000370	0.002300	0.002920
10	3.02	0.0011	0.0012	0.002337	0.002889	0.000007	0.000558	0.000021	0.000370	0.002337	0.002965
20	3.06	0.0011	0.0013	0.002455	0.003055	0.000008	0.000645	0.000021	0.000370	0.002455	0.003144
30	3.15	0.0012	0.0014	0.002674	0.003352	0.000010	0.000775	0.000021	0.000370	0.002674	0.003460
40	3.31	0.0014	0.0015	0.003043	0.003858	0.000013	0.000973	0.000021	0.000370	0.003043	0.003996
50	3.56	0.0016	0.0018	0.003667	0.004734	0.000017	0.001245	0.000021	0.000370	0.003667	0.004909
60	4.00	0.0021	0.0024	0.004804	0.006393	0.000022	0.001600	0.000021	0.000370	0.004804	0.006601
70	4.92	0.0031	0.0035	0.007311	0.010986	0.000033	0.002672	0.000021	0.000370	0.007311	0.011312
80	7.76	0.0061	0.0068	0.016202	0.031027	0.000053	0.004607	0.000021	0.000370	0.016202	0.031369

4.2.7.4 UNCERTAINTY ESTIMATE OF MARINE REFLECTANCE IN THE VIS06 BAND ON THE HRV GRID

Using the formula for first order error propagation (ISO 1995), the uncertainty on $\rho_{w,\otimes}^{0+(0.6)}$ introduced by uncertainties in $\rho_w^{0+(0.6)}$, *A*, and α can be estimated from an expression analogous to Eq. (4.49). Partial derivation of the expression in Eq. (4.45) to each parameter then gives:

$$\Delta\rho_{w,\otimes}^{0+(0.6)} = \left[\left(\Delta\rho_w^{0+(0.6)}\right)^2 + \left(\frac{\hat{\rho}_{tot}^{TOA(HRV)}}{AT_{o,v}^{(0.6)}\alpha^{m/2}} \right)^2 \left(\left(\frac{\Delta A}{A}\right)^2 + \left(\frac{m\Delta\alpha}{2\alpha}\right)^2 \right) \right]^{1/2} \qquad (4.52)$$

with A=0.71, ΔA=0.01, α=0.96, $\Delta\alpha$=0.02, and $\Delta\rho_w^{0+(0.6)}$ from Eq. (4.51).

4.2.8 Cross-validation with MODIS reflectance data

SEVIRI VIS06 marine reflectance products were cross-validated with simultaneously acquired reflectances of the spectrally similar MODIS Aqua 645 nm band, $\rho_w^{0+(M645)}$ (*see* Figure 4.12 for MODIS spectral response curves). MODIS imagery is atmospherically corrected by the Stumpf et al. 2003a algorithm, updated by Bailey et al. 2010. Scenes with at least 300 SEVIRI cloud free pixels and covering a representative range of water turbidity were selected. MODIS images were resampled to the larger SEVIRI VIS06 or HRV grids using a nearest neighbour approach. Pixels with negative reflectance values were omitted, as well as pixels where $\rho_w^{0+(0.6)}$ was below the SEVIRI digitization uncertainty of 0.004, typical for North Sea illumination geometry (*see* Table 4.3, corresponding to $\theta_0 = 40°$).

To clarify the effect of different wavelengths and bandwidths, the relationship between SEVIRI and MODIS reflectances is first investigated using in situ reflectance measurements. Least-squares regression through the origin of $\rho_w^{0+(0.6)}$ and $\rho_w^{0+(M645)}$ is shown in Figure 4.13 and gives:

$$\rho_w^{0+(0.6)} = 1.02(\pm 0.02)\rho_w^{0+(M645)} \qquad (4.53)$$

Ordinary least squares regression analysis of satellite-derived $\rho_w^{0+(0.6)}$ vs. $1.02\,\rho_w^{0+(M645)}$ was carried out. To quantify the agreement between marine reflectances derived from SEVIRI and MODIS Aqua, after accounting for slight differences in their spectral response given by Eq. (4.53), the 5th, 50th, and 95th percentiles of the normalized absolute error, NAE:

$$\mathrm{NAE} = \frac{\left|\rho_w^{0+(0.6)} - 1.02\rho_w^{0+(M645)}\right|}{1.02\rho_w^{0+(M645)}} \qquad (4.54)$$

and the normalized bias:

$$\mathrm{NB} = \frac{\rho_w^{0+(0.6)} - 1.02\rho_w^{0+(\mathrm{M645})}}{1.02\rho_w^{0+(\mathrm{M645})}} \tag{4.55}$$

are computed.

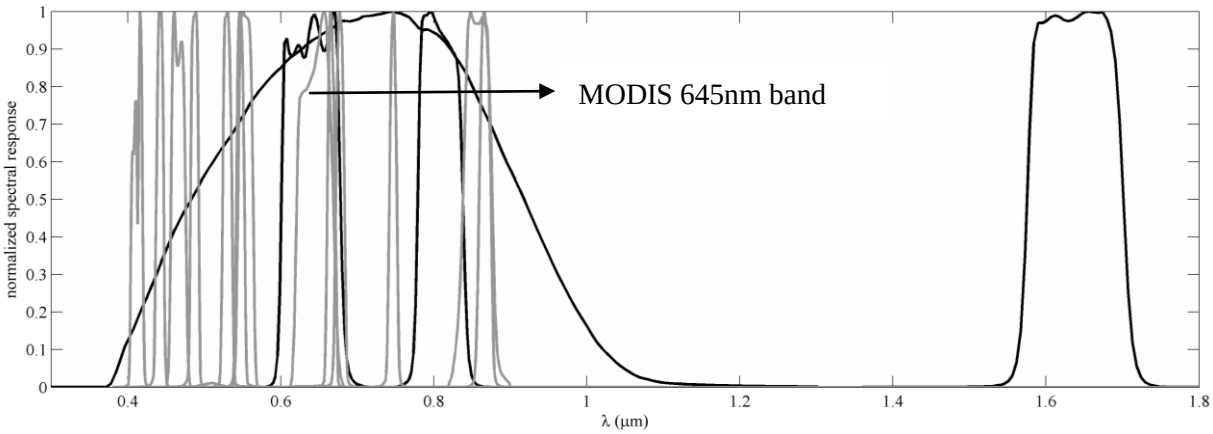

Figure 4.12. Normalized spectral response of the SEVIRI meteorological satellite (black) and the MODIS-Aqua ocean colour satellite (grey).

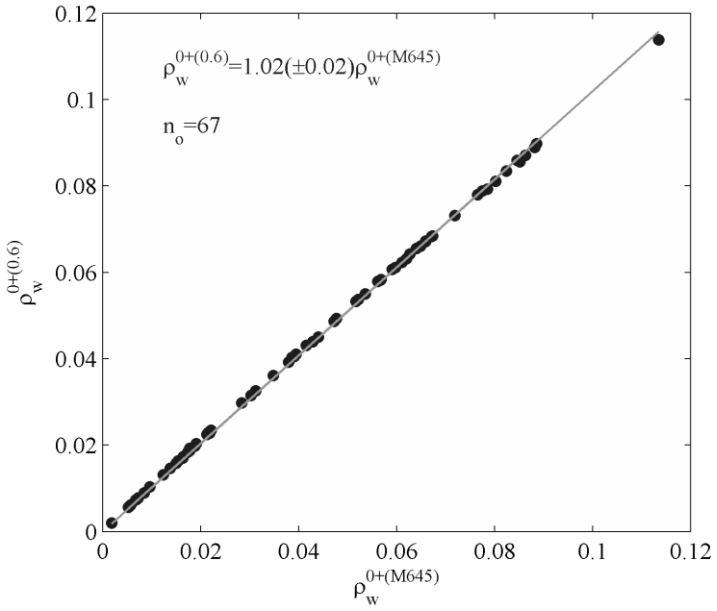

Figure 4.13. Marine reflectances in the SEVIRI VIS06 band and the MODIS Aqua 645 nm band obtained from optimal in situ above-water marine reflectance measurements collected between 2001 and 2010 in the southern North Sea waters. The least-squares linear regression through the origin is shown with equation and 95% confidence interval on the slope estimate.

4.3 Results

4.3.1 Mapping marine reflectance and its uncertainties

A map of marine reflectance in the VIS06 band on 16 February 2008 at 13:00 h UTC is shown in Figure 4.14A, with $\rho_w^{0+(0.6)}$ varying between 0 and 0.08. The spatial distribution of reflectances matches the spatial distribution of SPM as reported in many previous remote sensing studies from CZCS (Holligan et al. 1989), AVHRR (Van Raaphorst et al. 1998), SeaWiFS (Eleveld et al. 2004), MODIS or MERIS (Nechad et al. 2010). Moderate and high reflectances (>0.05) are found in some areas close to the coast and near river estuaries and especially East of the Thames Estuary, e.g. (51.5°N, 1.5°E). Reflectances are lower (<0.02) further offshore, in the Central North Sea and in the English Channel. Figure 4.14B shows the relative uncertainty on the derived reflectance associated with uncertainties in the atmospheric correction and digitization as obtained from Eq. (4.51). Uncertainties far exceeding 100% are seen in the clearest waters, while uncertainties between 10% and 20% are observed in the more turbid waters.

A decomposition of this uncertainty (shown in Figure 4.15A), into its digitisation, aerosol, and water components is shown in Figure 4.15B, C, and D, respectively. The digitization uncertainty is the dominant component, exceeding water and aerosol contributions by an order of magnitude. The solar angle dependence of digitization uncertainty is also clearly visible in Figure 4.15B. High aerosol uncertainties are found near clouds and near the coast due to strong aerosol turbidity, as shown in Figure 4.15C. The spatial distribution of marine reflectance is reflected in the uncertainty associated with water turbidity, shown in Figure 4.15D.

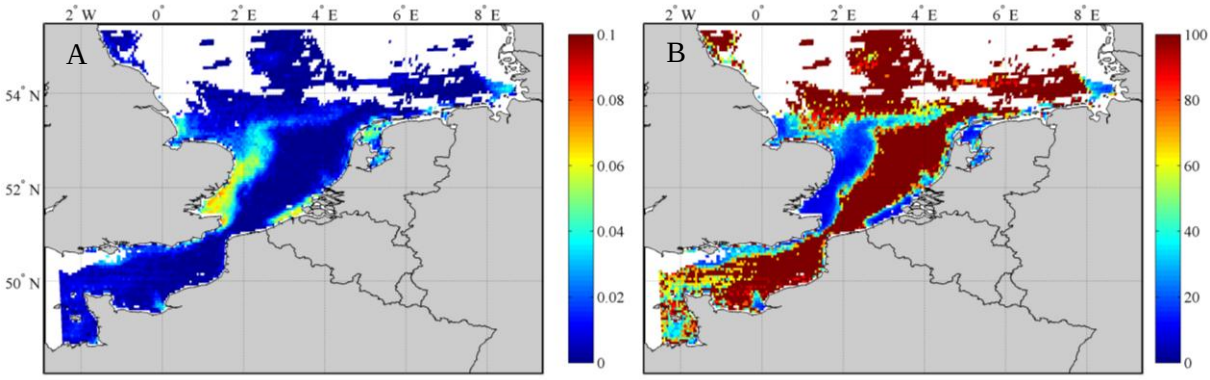

Figure 4.14. (A) Marine reflectance from SEVIRI VIS06 on 16-02-08 at 13:00 h UTC and (B) associated relative uncertainty in %, obtained from Eq. (4.51).

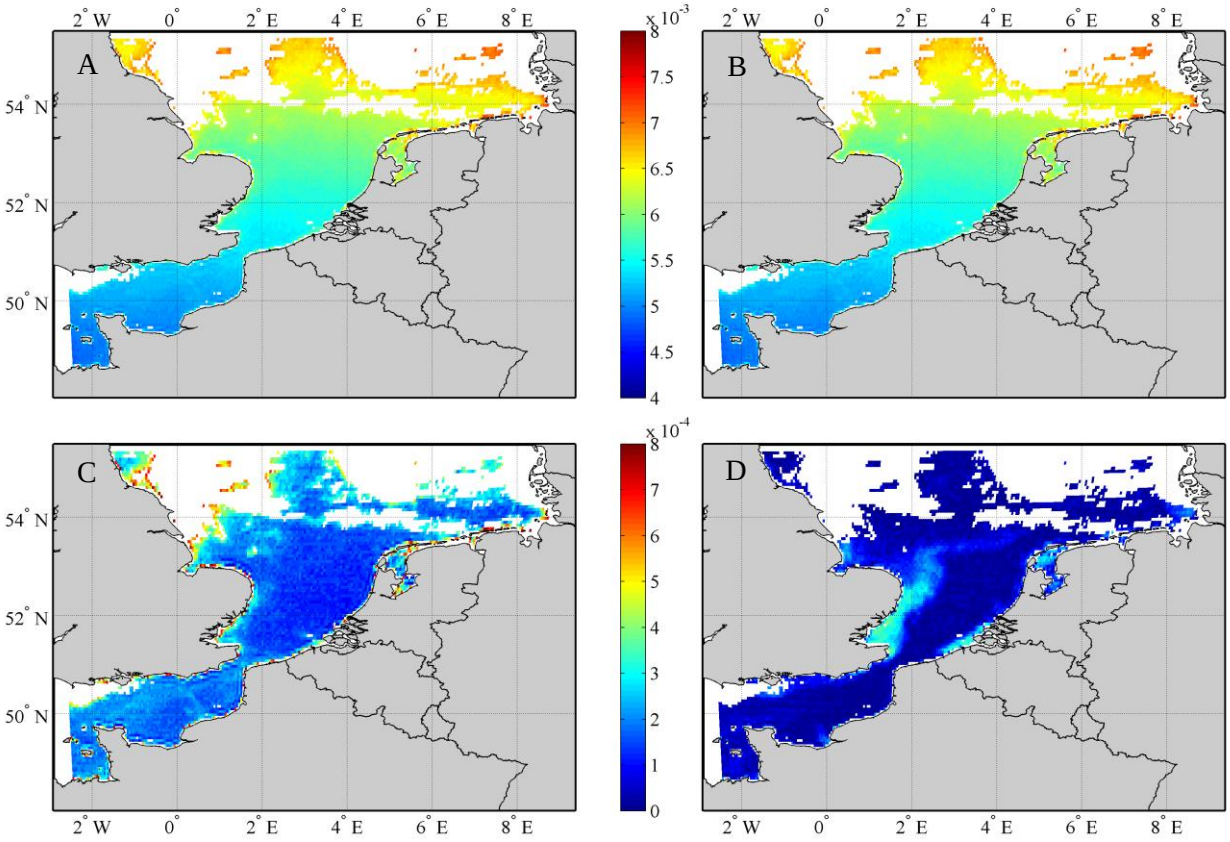

Figure 4.15. Uncertainty components of SEVIRI VIS06 marine reflectance on 16-02-2008 at 13:00 h UTC. (A) total uncertainty as in Eq. (4.51), (B) digitization uncertainty as in Eq. (4.50), (C) uncertainty due to aerosol turbidity as in the first term of Eq. (4.47), and (D) uncertainty due to water turbidity as in the second term of Eq. (4.47).

4.3.2 Marine reflectance on the HRV grid

An example of the improvement in spatial resolution achieved by the use of the HRV band is shown in Figure 4.16. In the clearest waters, atmospheric correction of the VIS06 band may give negative marine reflectances, which were set equal to zero. On the HRV grid, negative reflectances may be found where $\rho_w^{0+(0.6)}$ is zero because only the spatial anomaly term in Eq. (4.45) remains.

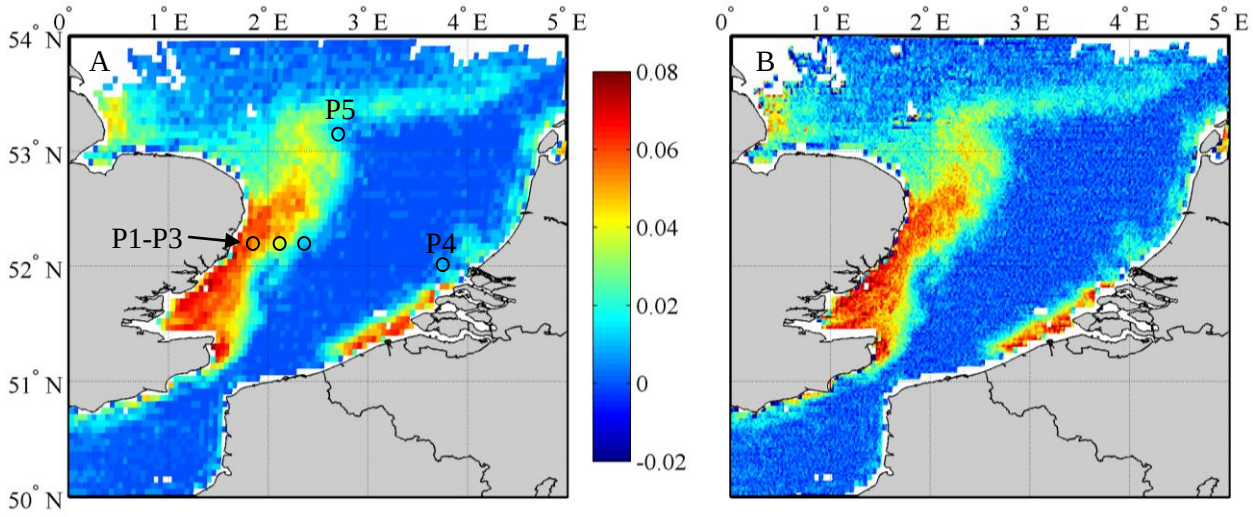

Figure 4.16. Marine reflectance on 16-02-2008 at 13:00 h UTC for a subset of the SEVIRI southern North Sea scene on (A) the SEVIRI VIS06 grid with a spatial resolution of 3 km x 6.5 km and (B) on the HRV grid with a spatial resolution of 1 km x 2 km. Circles represent five selected stations for which diurnal variability of marine reflectances is shown in Figure 4.20.

4.3.3 SEVIRI – MODIS cross validation

4.3.3.1 VIS06 REFLECTANCE

Figure 4.17 shows a spatial comparison for 4 out of 42 SEVIRI-MODIS match-ups in 2008-2009. Both sensors show comparable spatial patterns and marine reflectance ranges, but SEVIRI is clearly strongly affected by noise. The finer spatial structures seen in the MODIS images are not picked up by SEVIRI due to the coarse spatial resolution of the VIS06 band. Corresponding scatter plots and regressions of $\rho_w^{0+(0.6)}$ vs. $1.02\,\rho_w^{0+(M645)}$ are shown in Figure 4.18, while Table 4.4 lists the results of regression analysis for all match-ups. SEVIRI VIS06 and MODIS reflectances are overall well correlated with correlation coefficients ranging between 0.68 and 0.97, with a median of 0.91. The regression slopes of $\rho_w^{0+(0.6)}$ vs. $1.02\,\rho_w^{0+(M645)}$ range between 0.61 and 1.14 with a median value of 0.85. The largest relative differences between MODIS and SEVIRI are found in the clearest scenes, as seen from the increase in the 95th percentile value of NAE with decreasing median $\rho_w^{0+(0.6)}$ shown in Figure 4.19A. Underestimation of reflectance by SEVIRI are most pronounced in the most turbid waters, as can been seen in the scatter plots in Figure 4.18A, D and for the most turbid scenes (*see* Figure 4.19B).

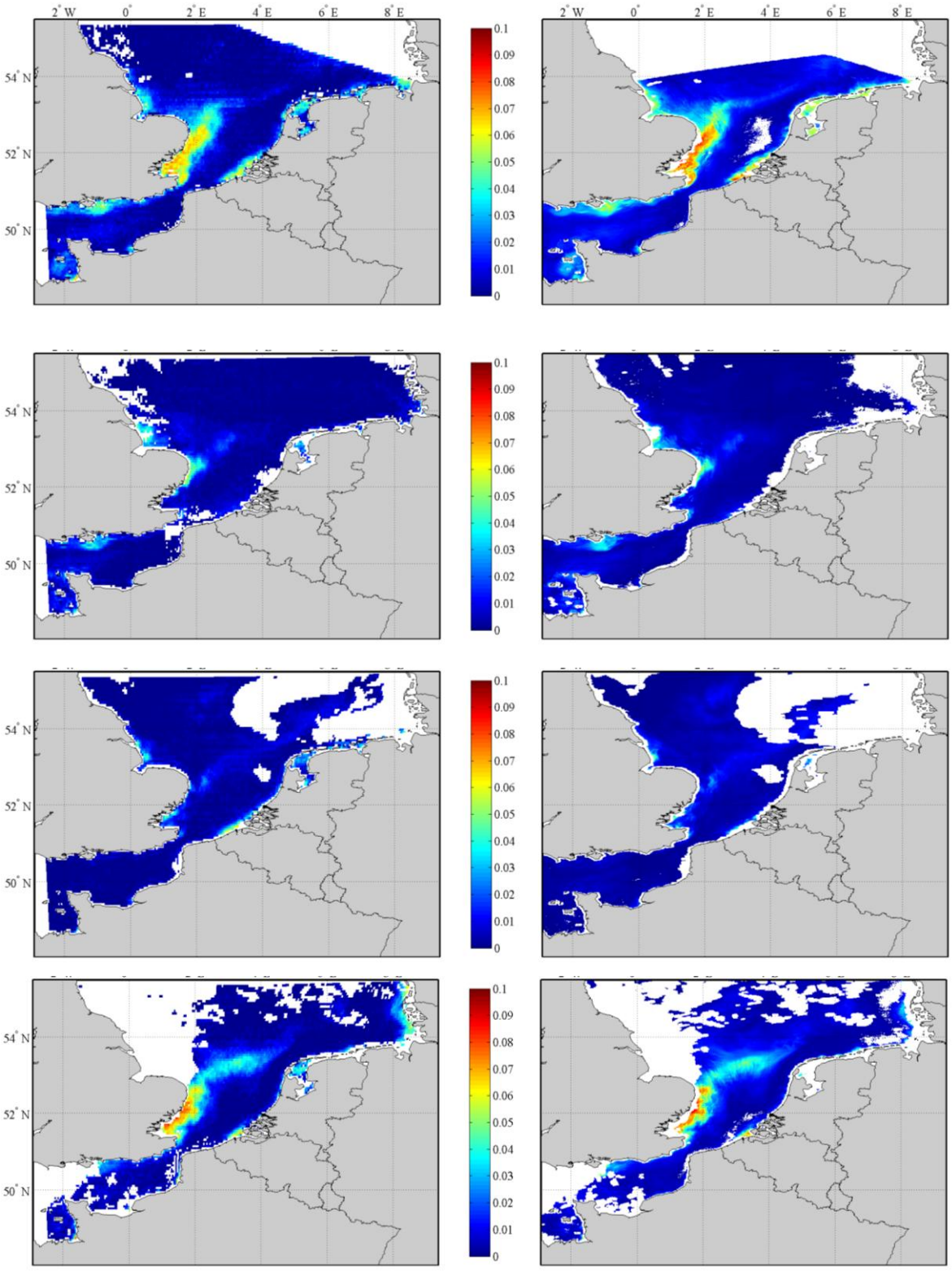

Figure 4.17. Maps of marine reflectances from the SEVIRI VIS06 band (left) and MODIS Aqua 645nm band (right), acquired on (from top to bottom): 11 Feb. 2008 at 12:45 h UTC, 6 May 2008 at 13:00 h UTC, 23 July 2008 at 13:15 h UTC, and on 8 March 2009 at 13:00 h UTC. Corresponding scatter plots are shown in Figure 4.18.

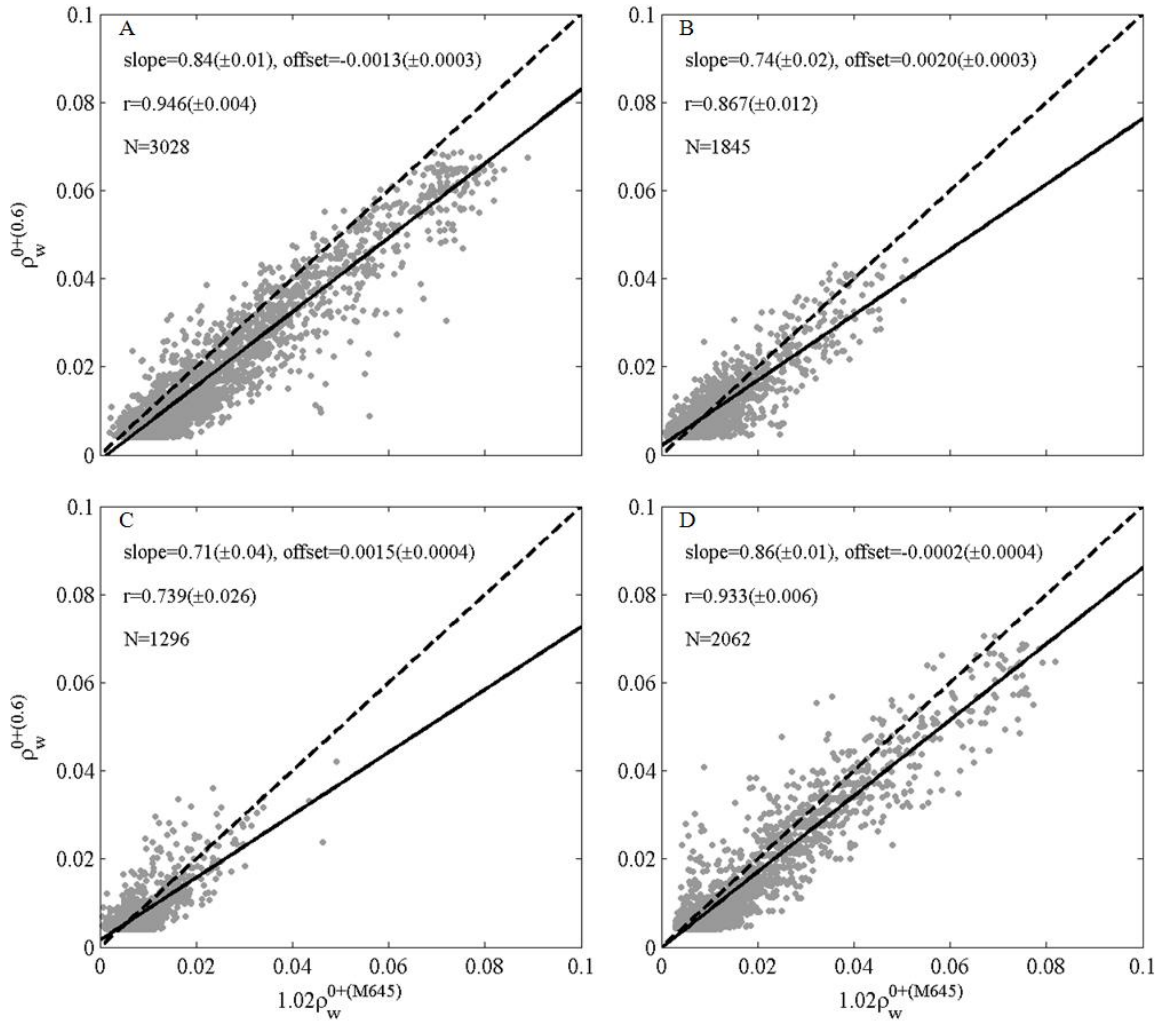

Figure 4.18. Scatter plots of SEVIRI VIS06 marine reflectance vs. MODIS Aqua 645nm reflectances, acquired on (A) 11 Feb. 2008 at 12:45 h UTC, (B) 6 May 2008 at 13:00 h UTC, (C) 23 July 2008 at 13:15 h UTC, and on (D) 8 March 2009 at 13:00 h UTC, corresponding to the scenes shown in Figure 4.17. The least-squares regression and statistics are shown, as well as the 1:1 line (dashed).

The observed underestimation of SEVIRI marine reflectance compared to MODIS Aqua marine reflectance may be due to differences in design of the atmospheric corrections. A recent inter-comparison study (Jamet et al. 2011) of the atmospheric correction algorithms of Stumpf et al. 2003a (MODIS) and Ruddick et al. 2000 (SEVIRI) applied to SeaWiFS imagery showed a systematic underestimation of water-leaving radiances by the Ruddick et al. 2000 algorithm of a factor 0.68 at 670 nm (see Table 3 in Jamet et al. 2011).

Table 4.4. Regression equation and statistics of reflectances obtained from SEVIRI VIS06 and MODIS 645 nm for 42 match-ups in 2008-2009. Uncertainties on regression parameters and correlation coefficients represent a 95% confidence interval.

					$\rho_w^{0+(0.6)}$ vs. $1.02\rho_w^{0+(M645)}$				NAE (%)			NB (%)		
Date	h UTC	N	r	Δr	slope	Δslope	offset	Δoffset	5	50	95	5	50	95
12-01-08	12:30	697	0.95	0.01	0.90	0.02	-0.0020	0.0009	2	21	63	-59	-17	26
09-02-08	13:00	1443	0.93	0.01	0.82	0.02	-0.0015	0.0005	3	29	65	-64	-26	23
11-02-08	12:45	3028	0.95	0.00	0.84	0.01	-0.0013	0.0003	3	26	62	-61	-24	20
12-02-08	11:45	1098	0.89	0.01	0.87	0.03	-0.0010	0.0005	3	26	60	-57	-23	29
12-02-08	13:30	2241	0.93	0.01	0.89	0.02	-0.0003	0.0003	2	22	63	-54	-14	50
16-02-08	13:00	2405	0.93	0.01	0.86	0.01	0.0016	0.0003	2	24	136	-46	-2	136
17-02-08	12:15	1523	0.92	0.01	0.86	0.02	0.0013	0.0003	2	21	84	-46	-3	84
17-02-08	13:45	656	0.90	0.01	0.79	0.03	0.0033	0.0005	2	31	260	-41	14	260
08-04-08	12:45	1121	0.92	0.01	0.71	0.02	0.0013	0.0005	4	26	66	-58	-23	50
09-04-08	11:45	652	0.91	0.01	0.81	0.03	-0.0001	0.0005	2	26	56	-52	-22	35
09-04-08	13:30	1107	0.92	0.01	0.86	0.02	-0.0009	0.0005	3	24	56	-54	-21	26
15-04-08	12:45	1016	0.91	0.01	0.79	0.02	0.0017	0.0004	2	20	67	-42	-11	64
06-05-08	13:00	1845	0.87	0.01	0.74	0.02	0.0020	0.0003	2	25	107	-50	-2	107
07-05-08	12:15	1996	0.86	0.01	0.72	0.02	0.0020	0.0002	3	21	83	-47	-5	80
07-05-08	13:45	1041	0.81	0.02	0.82	0.04	0.0024	0.0003	2	26	175	-37	16	175
08-05-08	13:00	1487	0.87	0.01	0.71	0.02	0.0024	0.0003	2	23	157	-48	-3	157
09-06-08	13:00	1047	0.86	0.02	0.66	0.02	0.0034	0.0003	4	42	317	-44	31	317
23-07-08	11:45	1124	0.70	0.03	0.65	0.04	0.0014	0.0004	3	33	76	-55	-25	76
23-07-08	13:15	1296	0.74	0.03	0.71	0.04	0.0015	0.0004	4	28	93	-50	-18	93
24-07-08	12:30	826	0.77	0.03	0.62	0.04	0.0021	0.0004	4	28	86	-50	-20	86
30-08-08	12:45	1043	0.79	0.02	0.79	0.04	0.0029	0.0004	3	34	216	-40	21	216
18-09-08	13:15	1284	0.89	0.01	0.80	0.02	0.0014	0.0004	3	28	150	-52	-11	150
19-09-08	12:15	924	0.88	0.02	0.81	0.03	0.0014	0.0004	2	25	105	-50	-9	105
27-09-08	13:00	724	0.84	0.02	0.69	0.03	0.0042	0.0005	3	36	161	-48	20	161
27-09-08	13:15	400	0.90	0.02	0.95	0.05	0.0023	0.0005	4	37	260	-32	32	260
12-10-08	12:30	300	0.89	0.03	0.85	0.05	0.0038	0.0009	2	34	175	-37	26	175
18-10-08	13:30	580	0.95	0.01	0.92	0.02	0.0001	0.0005	2	20	72	-49	-9	69
26-12-08	12:15	765	0.68	0.04	0.61	0.05	0.0023	0.0010	4	33	71	-68	-29	39
06-01-09	11:45	492	0.88	0.02	0.93	0.04	-0.0010	0.0011	2	22	63	-58	-14	46
02-03-09	12:00	723	0.92	0.01	0.97	0.03	-0.0010	0.0006	1	22	71	-52	-14	70
02-03-09	12:00	783	0.97	0.00	1.14	0.02	-0.0027	0.0004	2	16	51	-49	-8	31
02-03-09	13:30	1864	0.94	0.01	0.99	0.02	-0.0017	0.0003	2	20	53	-51	-15	24
06-03-09	13:15	1039	0.94	0.01	0.90	0.02	0.0013	0.0004	2	15	74	-42	-4	74
08-03-09	13:00	2062	0.93	0.01	0.86	0.01	-0.0002	0.0004	2	24	62	-55	-18	45
18-03-09	13:30	613	0.92	0.01	0.90	0.03	0.0045	0.0005	2	39	351	-21	36	351
01-04-09	12:15	1494	0.94	0.01	0.91	0.02	0.0006	0.0003	2	17	77	-43	-4	77
08-04-09	12:15	1056	0.95	0.01	0.87	0.02	0.0004	0.0004	2	19	76	-49	-11	75
08-04-09	14:00	550	0.89	0.02	0.90	0.04	0.0008	0.0006	2	21	85	-45	0	85
24-04-09	12:15	531	0.84	0.03	0.64	0.04	0.0030	0.0003	4	39	295	-45	27	295
29-04-09	12:30	839	0.95	0.01	0.77	0.02	0.0022	0.0003	3	26	156	-43	2	156
30-04-09	11:45	448	0.95	0.01	0.97	0.03	0.0017	0.0004	1	24	138	-28	16	138
30-04-09	13:15	880	0.94	0.01	0.79	0.02	0.0027	0.0003	3	31	162	-37	20	162

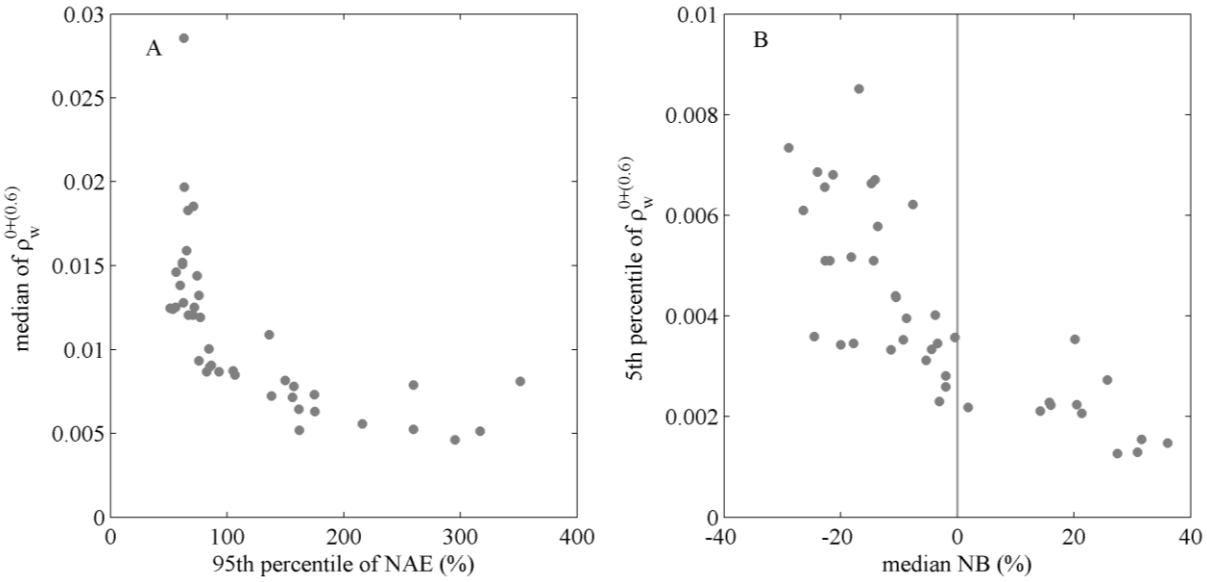

Figure 4.19. Trends in SEVIRI-MODIS reflectance match-ups statistics. Scatter plots of (A) median VIS06 reflectance vs. the 95th percentile value of the normalized absolute error, NAE and (B) the 5th percentile of VIS06 reflectance vs. the median normalized bias, NB.

4.3.3.2 VIS06 REFLECTANCES ON THE HRV GRID

Results of the regression analysis of $\rho_{w,\otimes}^{0+(0.6)}$ vs. $1.02\,\rho_w^{0+(M645)}$ for all match-ups are given in Table 4.5. Correlation coefficients range between 0.55 and 0.93 with a median of 0.86, giving overall lower correlations than for the marine reflectances on the low spatial resolution grid. Regression slopes of $\rho_{w,\otimes}^{0+(0.6)}$ vs. $1.02\,\rho_w^{0+(M645)}$ were also lower with a median value of 0.80 (range: 0.57-1.01) and a wider scatter along the regression line as seen by the much higher 95th percentile values of NAE compared to the same values in Table 4.4. The improvement of the spatial resolution of SEVIRI imagery did not result in better correlation with MODIS data.

Table 4.5. Regression equation and statistics of reflectances obtained from SEVIRI HRV and MODIS 645 nm for 42 match-ups in 2008-2009. Uncertainties on regression parameters represent a 95% confidence interval.

					$\rho_{w,\otimes}^{0+(0.6)}$ vs. $1.02\,\rho_w^{0+(M645)}$				NAE (%)			NB (%)		
Date	h UTC	N	r	Δr	slope	Δslope	offset	Δoffset	5	50	95	5	50	95
12-01-08	12:30	7321	0.86	0.01	0.80	0.01	0.0047	0.0005	2	25	205	-59	-8	205
09-02-08	13:00	14526	0.87	0.00	0.75	0.01	0.0022	0.0002	3	29	110	-64	-16	110
11-02-08	12:45	27107	0.91	0.00	0.78	0.00	0.0015	0.0001	3	26	83	-59	-14	81
12-02-08	11:45	9304	0.82	0.01	0.80	0.01	0.0019	0.0002	3	27	88	-58	-10	88
12-02-08	13:30	20021	0.88	0.00	0.83	0.01	0.0027	0.0001	2	27	166	-52	0	166
16-02-08	13:00	22195	0.90	0.00	0.81	0.01	0.0040	0.0001	3	33	321	-49	11	321
17-02-08	12:15	14685	0.89	0.00	0.80	0.01	0.0036	0.0001	3	32	273	-48	12	273
17-02-08	13:45	6625	0.87	0.01	0.80	0.01	0.0048	0.0002	3	43	560	-40	35	560
08-04-08	12:45	12032	0.86	0.00	0.67	0.01	0.0036	0.0002	3	29	131	-58	-17	131
09-04-08	11:45	6693	0.88	0.01	0.80	0.01	0.0011	0.0002	2	25	73	-53	-15	72
09-04-08	13:30	10527	0.89	0.00	0.80	0.01	0.0010	0.0002	2	24	68	-55	-16	61
15-04-08	12:45	10330	0.90	0.00	0.76	0.01	0.0027	0.0001	2	23	124	-46	-5	124
06-05-08	13:00	19346	0.85	0.00	0.69	0.01	0.0035	0.0001	3	35	343	-46	15	343
07-05-08	12:15	19420	0.84	0.00	0.68	0.01	0.0031	0.0001	3	30	287	-47	6	287
07-05-08	13:45	9857	0.78	0.01	0.80	0.01	0.0036	0.0001	4	42	371	-37	35	371
08-05-08	13:00	14851	0.86	0.00	0.67	0.01	0.0036	0.0001	3	35	322	-46	17	322
09-06-08	13:00	11566	0.81	0.01	0.64	0.01	0.0045	0.0001	5	80	534	-41	80	534
23-07-08	11:45	10698	0.65	0.01	0.70	0.02	0.0024	0.0002	3	31	144	-53	-6	144
23-07-08	13:15	13624	0.72	0.01	0.70	0.01	0.0028	0.0001	3	31	224	-49	1	224
24-07-08	12:30	8137	0.65	0.01	0.58	0.01	0.0036	0.0002	3	31	190	-53	-5	190
30-08-08	12:45	10541	0.75	0.01	0.76	0.01	0.0043	0.0001	4	54	397	-35	51	397
18-09-08	13:15	13349	0.88	0.00	0.80	0.01	0.0032	0.0001	3	34	336	-46	13	336
19-09-08	12:15	8974	0.83	0.01	0.74	0.01	0.0034	0.0002	3	31	366	-48	7	366
27-09-08	13:00	7508	0.82	0.01	0.69	0.01	0.0055	0.0002	4	52	322	-46	44	322
27-09-08	13:15	5780	0.63	0.02	0.79	0.02	0.0060	0.0002	8	129	666	-19	129	666
12-10-08	12:30	2896	0.73	0.02	0.75	0.03	0.0062	0.0005	4	43	359	-46	31	359
18-10-08	13:30	5169	0.82	0.01	0.83	0.02	0.0043	0.0004	3	30	428	-51	7	428
26-12-08	12:15	7179	0.55	0.02	0.57	0.02	0.0067	0.0004	4	38	139	-67	-6	139
06-01-09	11:45	5539	0.80	0.01	0.86	0.02	0.0035	0.0004	3	31	146	-58	2	146
02-03-09	12:00	6936	0.88	0.01	0.91	0.01	0.0014	0.0002	2	24	141	-51	-2	141
02-03-09	12:00	7652	0.89	0.00	1.01	0.01	0.0009	0.0002	2	24	138	-45	6	138
02-03-09	13:30	16945	0.90	0.00	0.89	0.01	0.0015	0.0001	2	24	138	-50	-2	138
06-03-09	13:15	11589	0.86	0.00	0.82	0.01	0.0039	0.0002	2	26	314	-43	8	314
08-03-09	13:00	20499	0.90	0.00	0.80	0.01	0.0025	0.0001	2	26	139	-53	-6	139
18-03-09	13:30	5851	0.89	0.01	0.88	0.01	0.0057	0.0002	3	50	461	-28	48	461
01-04-09	12:15	16015	0.92	0.00	0.88	0.01	0.0022	0.0001	2	26	241	-43	7	241
08-04-09	12:15	11036	0.92	0.00	0.85	0.01	0.0021	0.0002	2	22	188	-47	-2	188
08-04-09	14:00	5205	0.85	0.01	0.85	0.01	0.0030	0.0002	3	28	227	-42	14	227
24-04-09	12:15	8233	0.82	0.01	0.64	0.01	0.0044	0.0001	8	106	585	-29	106	585
29-04-09	12:30	8391	0.90	0.00	0.73	0.01	0.0039	0.0001	3	35	445	-41	16	445
30-04-09	11:45	5262	0.93	0.00	0.90	0.01	0.0031	0.0001	3	40	467	-25	37	467
30-04-09	13:15	8347	0.93	0.00	0.77	0.01	0.0039	0.0001	3	44	450	-35	38	450

4.3.4 Diurnal variability of marine reflectances and aerosols

Time series of marine reflectance and the aerosol calibration parameter, ε, defined in Eq. (4.23), were extracted on three relatively cloud free days at five different stations (shown in Figure 4.16A) in clear, moderately turbid, and turbid waters. Diurnal variability of the extracted parameters is shown in

Figure 4.20. The variability of marine reflectances at P1, P2, and P3 suggests a periodicity related to the tidal cycle, such as could be expected from resuspension and/or advection of sediment particles. This diurnal variability is further investigated in Chapter 5. In clearer waters (P4), potential diurnal variability is masked by the high noise level.

Figure 4.20 also shows diurnal variability of the ratio $\varepsilon = \rho_a^{(0.6)} : \rho_a^{(0.8)}$, which can be related to the spectral variability and size distribution of aerosols described by the aerosol Angstrom coefficient (α) via:

$$\alpha = -\frac{\log\left(\frac{\rho_a^{TOA(0.6)}}{\rho_a^{TOA(0.8)}}\right)}{\log\left(\frac{0.635\mu\text{m}}{0.810\mu\text{m}}\right)} = 0.24\log\left(\varepsilon\gamma_\varepsilon\right) \tag{4.56}$$

where $\gamma_\varepsilon = t_{r,g}^{(0.8)} : t_{r,g}^{(0.6)}$. This transmittance ratio takes a value of γ_ε=1.05 for an air mass of 2 and of 1.22 for an air mass of 7 for a standard atmosphere simulated with LOWTRAN. α is known to vary seasonally in the southern North Sea (Behnert et al. 2007), and diurnal variations in α have been observed previously from AERONET and SEVIRI (De Paepe et al. 2008).

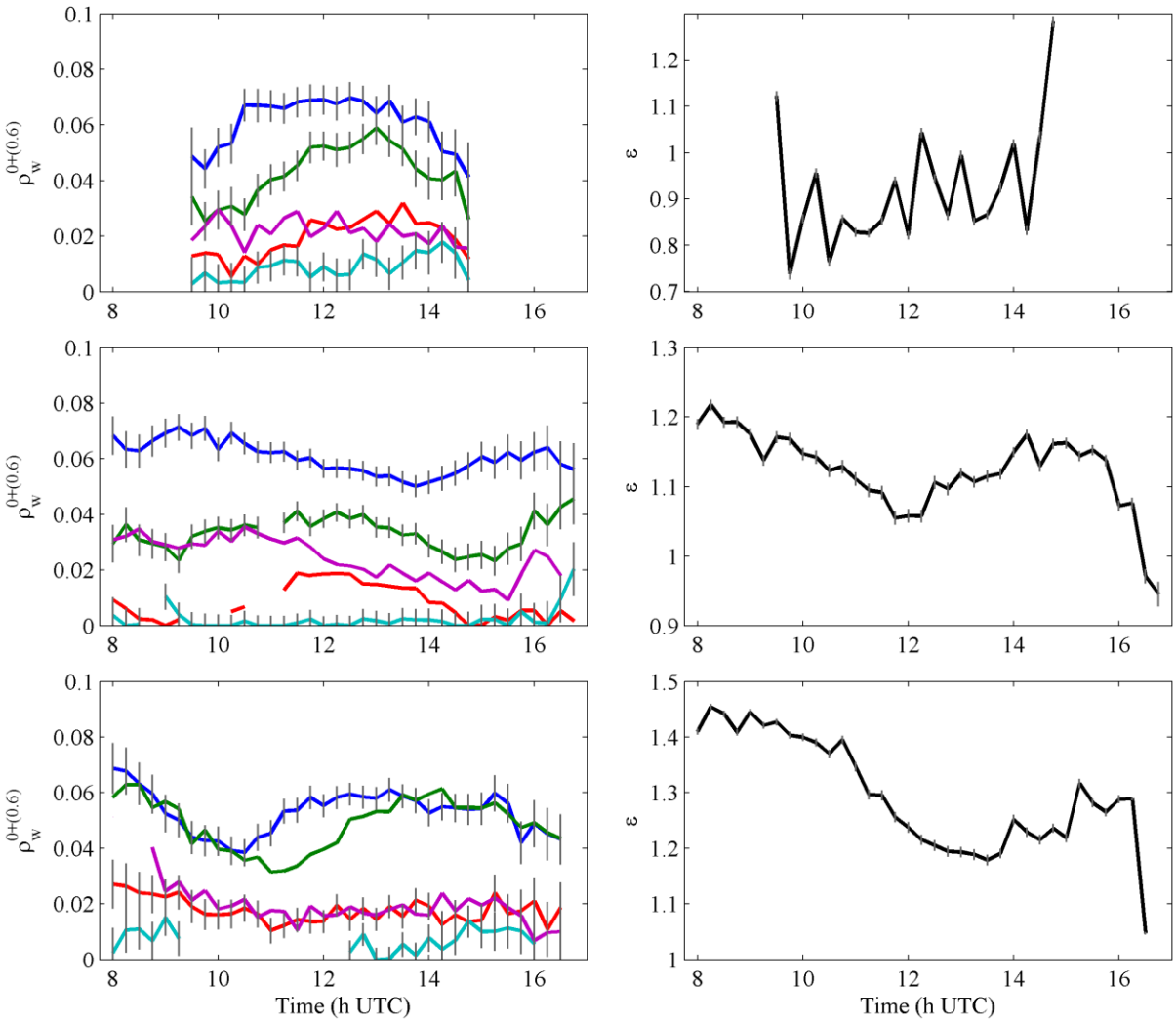

Figure 4.20. Diurnal variability of SEVIRI VIS06 marine reflectance (left) and the VIS06:VIS08 band ratio of aerosol reflectance (right) on three cloud free days: 11 February 2008 (top), 8 April 2008 (middle), and 1 April 2009 (bottom). Time series of marine reflectance are plotted at P1 (blue), P2 (green), P3 (red), P4 (cyan), and P5 (purple), with location shown in Figure 4.16. Errorbars denote uncertainties on marine reflectance derived from Eq. (4.51) or on ε from the standard error of slope estimate.

4.4 Discussion and conclusion

4.4.1 Optimal reflectance range for atmospheric correction

Though the geostationary meteorological SEVIRI sensor, with its few and broad spectral bands, high radiometric noise level and medium ground resolution, is not designed for ocean colour remote sensing, we have shown that SEVIRI reflectances in the red band are highly correlated with similar data from MODIS Aqua. However, retrieval of marine reflectance is highly uncertain in clear waters,

mainly due to digitization uncertainties, which are of the order 0.004 for typical North Sea illumination geometry (*see* Table 4.3 for $\theta_0 = 40°$). While the retrieval of SEVIRI marine reflectance in clear waters is limited by sensor digitization, the atmospheric correction is expected to fail in very turbid waters, due to the limitation of assumption (4.22) to cases where $\rho_w^{0+(0.8)} < 0.011$ and thus where $\rho_w^{0+(0.6)} < 0.067$. For higher reflectances, assumption (4.22) no longer holds, as can be seen in Figure 4.7. Above this threshold, atmospheric correction underestimates $\rho_w^{0+(0.6)}$ with increasing marine reflectance. Figure 4.21 shows the relationship between the normalized bias of the marine reflectance retrieved from Eq. (4.34), with simplifications $\gamma = 1 = t_{o,v}^{a(0.8)}$, from the in situ measured marine reflectance $\rho_{w,m}^{0+(0.6)}$:

$$\mathrm{NB} = \frac{\rho_w^{0+(0.6)} - \rho_{w,m}^{0+(0.6)}}{\rho_{w,m}^{0+(0.6)}} \tag{4.57}$$

For a typical value of ε=1.02, $\rho_w^{0+(0.6)}$ is underestimated by about 10% for $\rho_w^{0+(0.6)}$=0.08, and by over 25% for larger reflectances. The degree of underestimation increases to 15% and 35%, respectively, for ε=1.30. This may explain why observations with $\rho_w^{0+(0.6)} > 0.067$ deviate more from the 1:1 lines in Figure 4.18A, D than lower reflectance observations.

Taking account of sensor digitization and the limitations due to assumption (4.22), SEVIRI's atmospheric correction is expected to perform optimally for $0.004 < \rho_w^{0+(0.6)} < 0.080$. It might be possible to push this upper limit further by refining the algorithm to have a non-constant σ via an extra iterative loop with σ calculated as a function of $\rho_w^{0+(0.8)}$. This possibility is further discussed in section 5.4.1.

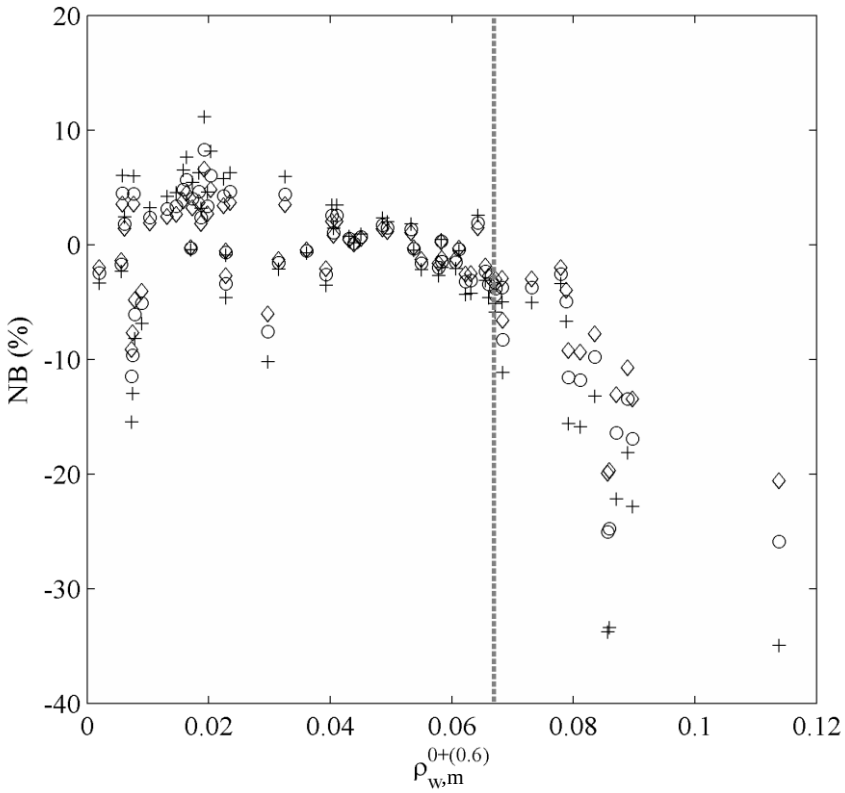

Figure 4.21. Effect of the atmospheric correction assumption (4.22) on the retrieval of $\rho_w^{0+(0.6)}$: normalized bias of $\rho_w^{0+(0.6)}$ obtained from Eq. (4.34) from the true marine reflectance for $\varepsilon = 0.84$ (diamonds), $\varepsilon = 1.02$ (circles), and $\varepsilon = 1.30$ (crosses), with simplifications $\gamma = 1 = t_{o,v}^{a(0.8)}$. The dashed line corresponds to the reflectance region where σ was calibrated (see Figure 4.7).

4.4.2 Spatial resolution

Unfortunately, improvement of the spatial resolution of SEVIRI reflectance products did not result in better correlation with MODIS. In fact, the opposite is observed. This could be caused by (1) uncertainties in the resampling of MODIS imagery to the SEVIRI HRV grid, (2) geolocation uncertainties of the HRV (Seiz et al. 2007), and hence imperfect alignment with the VIS06 spatial grid, (3) spatial heterogeneity of aerosols within the larger grid pixels, (4) digitization effects of the HRV band (similar to VIS08 digitization at TOA), or (5) the low signal-to-noise ratio of 2.5.

The geolocation of the HRV is known to be accurate within 1-2 HRV pixels (Seiz et al. 2007), which is within the EUMETSAT mission requirements of 3 km absolute geometric accuracy. Based on a few selected HRV images and an accurately geolocated coastline shapefile, the geolocation accuracy of the HRV was found to be off by 2 HRV pixels. A fine-correction was applied to the entire two-year dataset, but geolocation errors might still be present as it is uncertain whether this offset is systematic.

Validation of SEVIRI's low and high spatial resolution products with in-situ data (instead of MODIS imagery) excludes uncertainties due to the resampling of MODIS imagery to the SEVIRI spatial grids. This is done in Chapter 5.

4.4.3 Exploiting high temporal resolution imagery

The striking advantage of SEVIRI is its superior temporal resolution: every 15 minutes compared to once/twice per day for MODIS. Up to 40 usable images per day can be recorded by SEVIRI, giving a twenty- to thirtyfold increase in the number of available images per day, compared to MODIS. On cloudfree days, diurnal variability of reflectance is detected in turbid waters, but remains to be validated. This is ideally achieved with continuous radiometry measurements, below or above-water, at fixed locations. The AERONET-Ocean Color network (Zibordi et al. 2009), for example, operates autonomous radiometers on fixed platforms in coastal waters around the world. Unfortunately, none are currently operational in the North Sea. Alternatively, validation can be done using the more widely available continuous in-water measurements of optical parameters such as turbidity and light attenuation recorded from moored buoys. This is investigated in Chapter 5.

When cloud patterns change during the day, a cloud-cleared composite image may be created. An example for 15 April 2008 is given as an animation on ftp://ftp.mumm.ac.be/griet/SEVIRIanimation. The daily composite (derived from the mean day value) covered 95% of the southern North Sea area, compared to 50% for the MODIS Aqua image acquired on that day. Moreover, for SEVIRI, daily compositing significantly reduced the noise in clear waters (*see* also ftp://ftp.mumm.ac.be/griet/SEVIRIanimation). This example demonstrates that daily compositing of imagery from geostationary platforms increases data availability for monitoring applications requiring imagery on a daily basis (IOCCG 2012).

4.4.4 Expanding to SEVIRI full disk imagery

The atmospheric correction procedure developed here could be expanded to the entire SEVIRI disk shown in Figure 4.1 and to the entire operational period (2004-present). Some considerations:

- The spatial resolution gets down to 1 km for the HRV and 3 km for the other channels when moving closer to the SEVIRI nadir point, which is at 0° N, 3.5° E or 0° E, depending on the satellite platform.
- The geostationary geometry limits sunglint problems to equatorial areas (generally between 10° S and 10° N), with the sunglint spot moving from East to West along with the sun's position (Mazeran and Meskini 2008).
- The temporal window of usable imagery increases with decreasing distance to the sub-satellite point, except at sunglint impacted areas, giving the largest windows at 20° E-20° W and 10°-20° N or S.

- SEVIRI full disk imagery is scanned from South to North with a repeat cycle of 15 minutes of which 12.5 minutes are used for image acquisition and 2.5 minutes for retrace and stabilization (Seiz et al. 2007). Scanning at 52°N, for example, occurs about 700 seconds after the start of image acquisition (N. Clerbaux, personal communication).
- The TOA digitization effect on marine reflectance also decreases with decreasing distance to the sub-satellite point, due to higher atmospheric transmittances and lower solar zenith angles.
- The σ parameter in assumption (4.22), is calibrated here with North Sea data, but can possibly be applied elsewhere, since no differences were observed between North Sea, Guyana, and Mediterranean σ parameter calibrations.
- The marine reflectance in SEVIRI's red waveband is proportional to the particulate backscattering coefficient in the red, b_{bp}. As shown in Chapter 3, b_{bp} is closely related to the concentration of particles in suspension and to turbidity. If the marine reflectance is sufficiently large (turbid waters), its temporal variability (associated with temporal variability of [SPM]) is likely to be picked up by SEVIRI. Diurnal variability of [SPM] can be expected from tidal or storm induced sediment resuspension processes in large estuaries like the Amazon and the Congo river deltas. Sufficiently turbid water areas where SEVIRI may be used to reliably detect the marine reflectance are indicated in Figure 4.22.
- AERONET-OC radiometry measurements could be used for validation of diurnal variability of SEVIRI reflectance if stations are located sufficiently far from the coast (accounting for SEVIRI's low spatial resolution) and in sufficiently turbid waters (accounting for SEVIRI's low radiometric resolution). The Aqua Alta Oceanographic Tower (AAOT) in the northern Adriatic Sea (Zibordi et al. 2009) could be a good candidate.

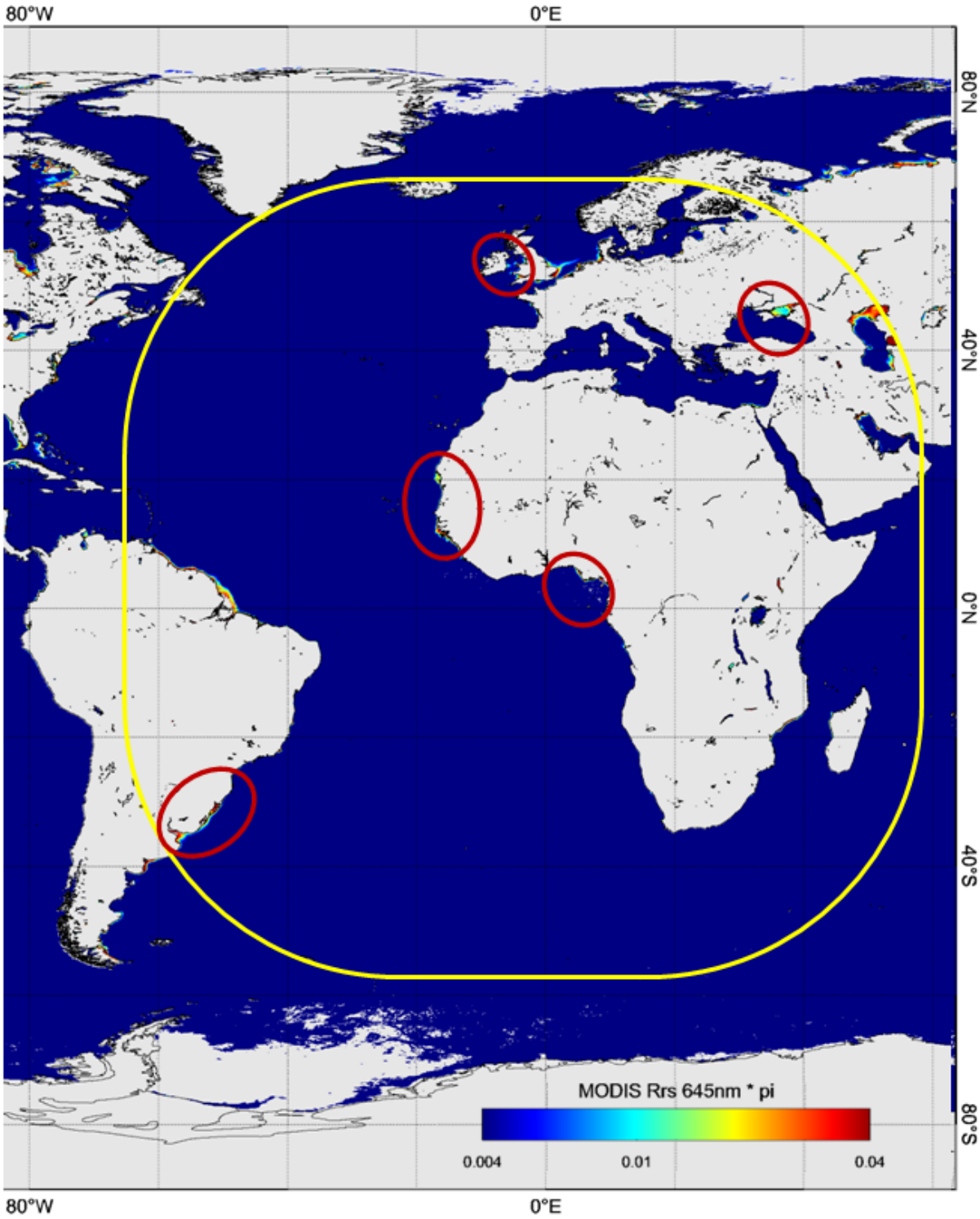

Figure 4.22. MODIS 2009 climatology of marine reflectance at 645 nm. The yellow polygon delineates the SEVIRI full disk coverage and the red polygons indicate waters that are sufficiently turbid to be reliably detected by SEVIRI.

4.5 Appendices

4.5.1 Comparison of bands VIS08 and NIR16 for aerosol correction of VIS06

4.5.1.1 ESTIMATION OF UNCERTAINTY ON $\rho_w^{0+(0.6)}$ USING BAND COMBINATION (VIS06, NIR16)

If the NIR16 band is used as correction band we assume zero marine reflectance in NIR16 and spatial homogeneity of aerosol scattering:

$$\rho_a^{(1.6)} = \rho_c^{(1.6)} \tag{4.58}$$

$$\varepsilon^{(6,16)} = \frac{\rho_a^{(0.6)}}{\rho_a^{(1.6)}} \tag{4.59}$$

In analogy with the derivation of $\Delta\rho_w^{0+(0.6)}$ using the (VIS06, VIS08) band pair, we estimate the uncertainty on the marine reflectance $\rho_w^{0+(0.6)}$, resulting from an uncertainty on the estimation of the calibration parameter $\varepsilon^{(6,16)}$:

$$\Delta\rho_w^{(0.6)} = \left|\frac{\partial\rho_w^{(0.6)}}{\partial\varepsilon^{(6,16)}}\Delta\varepsilon^{(6,16)}\right| = \frac{1}{t_{0,v}^{a(0.6)}}\left|\frac{\partial\rho_a^{(0.6)}}{\partial\varepsilon^{(6,16)}}\Delta\varepsilon^{(6,16)}\right| = \frac{\rho_a^{(1.6)}}{t_{0,v}^{a(0.6)}}\Delta\varepsilon^{(6,16)} \tag{4.60}$$

The ratio of aerosol reflectance $\varepsilon^{(6,16)}$ is obtained on an image-by-image basis from the ratio of Rayleigh and gas corrected reflectances for SEVIRI bands VIS06 and NIR16 over clear waters pixels in the black boxes in Figure 4.8. The distribution of these reflectance ratios is approximately normal (see example in Figure 4.23). $\varepsilon^{(6,16)}$ is estimated from the mean and the uncertainty on $\varepsilon^{(6,16)}$ is quantified from two times the standard deviation. Figure 4.23 shows discretisation effects coming from digitisation of the top of atmosphere signal and is of the order 0.0013 for the VIS06 channel and 0.0014 for the NIR16 channel. Typical values for $\varepsilon^{(6,16)}$ are 3.4±2.4. For comparison, the scatterplot of Rayleigh corrected reflectances for bands VIS06 vs. VIS08 and the corresponding histogram of reflectance ratios obtained on June 29th 2006 at 11:30UTC is shown in Figure 4.24.

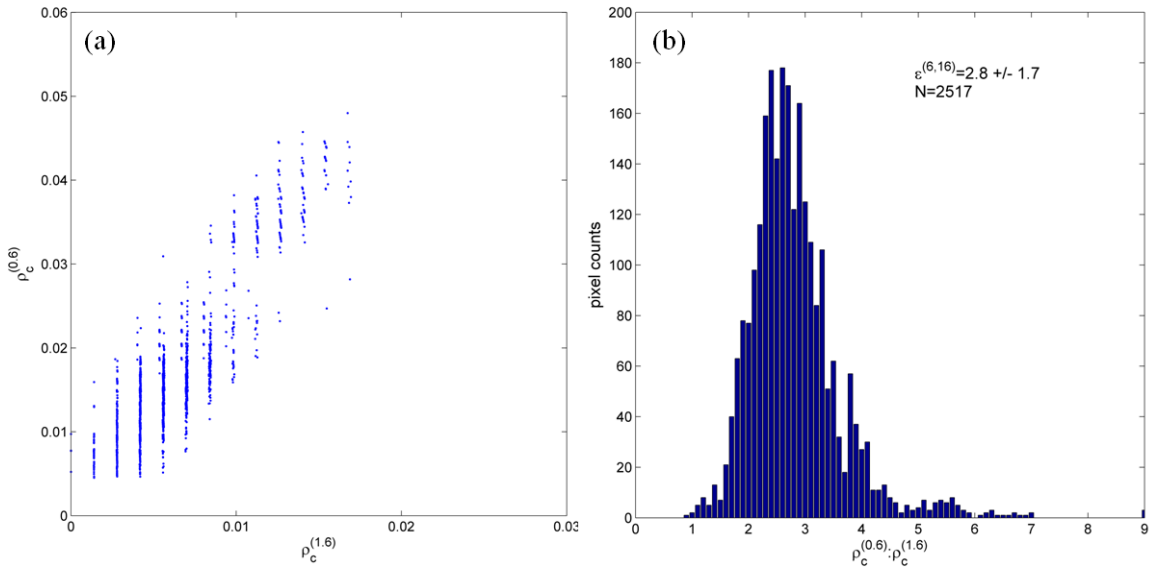

Figure 4.23. Estimation of VIS06:NIR16 ratio of aerosol reflectances. (a) Rayleigh corrected reflectances for a set of clear water pixels in VIS06 and NIR16 bands on June 29th 2006 at 11:30UTC. (b) The corresponding histogram of the VIS06:NIR16 Rayleigh corrected reflectance ratios (N is the number of pixels).

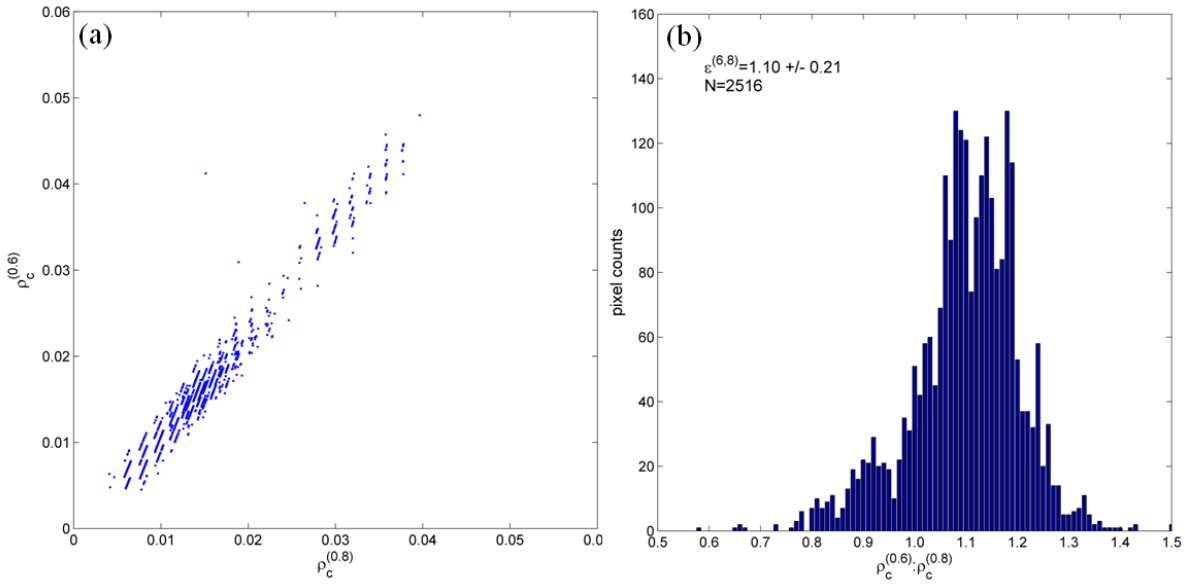

Figure 4.24. Estimation of VIS06:VIS08 ratio of aerosol reflectances. (a) Rayleigh corrected reflectances for a set of clear water pixels in VIS06 and VIS08 bands on June 29th 2006 at 11:30UTC. (b) The corresponding histogram of the VIS06:VIS08 Rayleigh corrected reflectance ratios (N is the number of pixels).

4.5.1.2 BAND PAIR SELECTION BASED ON MINIMIZATION OF $\Delta\rho_w^{0+(0.6)}$

The purpose is to find the band pair that minimizes $\Delta\rho_w^{0+(0.6)}$, obtained from Eqs. (4.47) and (4.60) for the (VIS06,VIS08) and (VIS06, NIR16) band pairs, respectively. We evaluate $\Delta\rho_w^{0+(0.6)}$ in Table 4.6 using values typical of the southern North Sea: $t_{0,v}^{a,r,(0.6)} = 1$, $\varepsilon^{(6,8)} = 1.1 \pm 0.3$, $\varepsilon^{(6,16)} = 3.1 \pm 2.1$, $\sigma = 6.1 \pm 0.3$, with an aerosol optical thickness $\tau_a^{(0.8)}$ between 0.05 (clear atmosphere) and 0.50 (turbid atmosphere) and $\rho_w^{0+(0.8)}$ varying from 0.001 (clear water) to 0.010 (turbid water). The $\rho_a^{(0.8)}$ values corresponding to different values of $\tau_a^{(0.8)}$ are obtained from the T90-aerosol look-up table for sun-sea-satellite geometry values typical for SEVIRI: $\theta_v = 60°, \phi = 60°$ and the sun at zenith. $\rho_a^{(1.6)}$ is then obtained from:

$$\rho_a^{(1.6)} = \rho_a^{(0.8)} \frac{\rho_a^{(0.6)}}{\rho_a^{(0.8)}} \frac{\rho_a^{(1.6)}}{\rho_a^{(0.6)}} = \rho_a^{(0.8)} \frac{\varepsilon^{(6,8)}}{\varepsilon^{(6,16)}} \tag{4.61}$$

Table 4.6 shows that the estimated uncertainties on $\rho_w^{0+(0.6)}$ when derived from the (VIS06, NIR16) band pair are in all cases of atmosphere and water turbidities approximately a factor 2 larger than the uncertainties on $\rho_w^{0+(0.6)}$ when derived from the (VIS06, VIS08) band pair. We note that, for the (VIS06, NIR16) band pair, the estimated uncertainty on $\rho_w^{0+(0.6)}$ is independent of water turbidity. Clearly, the (VIS06, VIS08) band pair is the preferred band combination, resulting in much smaller uncertainties on the derived $\rho_w^{0+(0.6)}$.

Table 4.6. Evaluation of uncertainty on $\rho_w^{0+(0.6)}$, $\Delta\rho_w^{0+(0.6)}$, associated with the atmospheric correction assumptions using the VIS08 or NIR16 band for aerosol correction. For the (VIS06, VIS08) band pair, $\Delta\rho_w^{0+(0.6)}$ is given by Eq. (4.47), based on assumptions in Eqs. (4.22) and (4.23), and for the (VIS06, NIR16) band pair $\Delta\rho_w^{0+(0.6)}$ is given by Eq. (4.60) with assumptions in Eqs. (4.58) and (4.59). Values typical of the southern North Sea were used: $\varepsilon^{(6,8)} = 1.1 \pm 0.3$, $\varepsilon^{(6,16)} = 3.1 \pm 2.1, \sigma = 6.1 \pm 0.3$, $\tau_a^{(0.8)}$ between 0.05 and 0.5 and $\rho_w^{0+(0.8)}$ between 0.001 and 0.010. Some simplifications: $t_{0,v}^{a,r,(0.6)} = 1$, $\gamma = 1$. [SPM] is obtained from the single band retrieval algorithm of Nechad et al. 2010, calibrated for SEVIRI VIS06.

			$\rho_w^{0+(0.8)}$	$\rho_w^{0+(0.6)}$	[SPM] (mg L^{-1})
	Water	clear	0.001	0.006	1.488
		mod. turbid	0.005	0.031	8.818
		turbid	0.010	0.061	22.963
			$\tau_a^{(0.8)}$	$\rho_a^{(0.8)}$	$\rho_a^{(1.6)}$
	Atmosphere	very clear	0.05	0.004	0.002
		clear	0.10	0.008	0.003
		turbid	0.20	0.017	0.006
		very turbid	0.50	0.047	0.017
			Water		
			clear	mod. turbid	turbid
$\Delta\rho_w^{0+(0.6)}$ **(VIS06,VIS08)**	Atmosphere	very clear	0.0015	0.0015	0.0016
		clear	0.0031	0.0031	0.0031
		turbid	0.0063	0.0063	0.0063
		very turbid	0.0171	0.0171	0.0171
			All water types		
$\Delta\rho_w^{0+(0.6)}$ **(VIS06,NIR16)**	Atmosphere	very clear	0.0031		
		clear	0.0063		
		turbid	0.0129		
		very turbid	0.0348		

4.5.2 Inter-calibration of VIS06 and VIS08 bands using Rayleigh and gas-corrected reflectances

The $\rho_c^{(0.6)}$ *vs.* $\rho_c^{(0.8)}$ regression for clear water pixels presented in section 4.2.5.3, not only offers an estimate of ε (from its slope), but also a way to correct for uncertainties in the calibration of the

VIS06 and VIS08 bands and the Rayleigh and gas corrections through subtraction of the offset from $\rho_c^{(0.6)}$. Calibration correction factors $A_0^{(0.6)}$ for the Meteosat9 VIS06 band range between 0.91 and 0.94 (Ham and Sohn 2010), depending on the method and data used. Similar values were found for the VIS08 band, but uncertainties are even larger due to strong water vapour absorption in this band (Sohn, personal communication).

Here, we simulate the effect of SEVIRI sensor calibration uncertainties on the retrieval of ε, marine and aerosol reflectances, and we test the effectiveness of the offset method to correct for these uncertainties. First, assume a perfectly calibrated VIS06 band and an uncertainty $\delta A_0^{(0.8)}$ on the calibration factor $A_0^{(0.8)}$ of the VIS08 band between -0.05 and 0.05. The offset and slope of the $\rho_c^{(0.6)}$ *vs.* $\rho_c^{(0.8)}$ regression increase as $\rho_c^{(0.8)}$ decreases with increasing $\delta A_0^{(0.8)}$ (*see* Figure 4.25A, C). Aerosol reflectance $\rho_a^{(0.8)}$ decreases along with $\rho_c^{(0.8)}$ after Eq. (4.31), while $\rho_w^{0+(0.6)}$ increases after Eq. (4.34). Removal of the offset from $\rho_c^{(0.6)}$ limits these effects (dashed vs. solid lines in Figure 4.25A), so that the retrieved $\rho_w^{0+(0.6)}$ varies by less than 2% over the $\delta A_0^{(0.8)}$ range.

Next, assume a perfectly calibrated VIS08 band and an uncertainty $\delta A_0^{(0.6)}$ on the calibration factor $A_0^{(0.6)}$ of the VIS06 band between -0.05 and 0.05. Now, the offset and slope of the regression decrease as $\rho_c^{(0.6)}$ decreases with increasing $\delta A_0^{(0.6)}$ as shown in Figure 4.25B, D. Marine reflectance decreases along with $\rho_c^{(0.6)}$. The impact of VIS06 calibration on $\rho_a^{(0.8)}$ is much smaller, compared to VIS08 calibration, while the opposite is true for $\rho_w^{0+(0.6)}$. Again, removal of the offset from $\rho_c^{(0.6)}$ limits these effects, with $\rho_w^{0+(0.6)}$ varying less than 10% over the $\delta A_0^{(0.6)}$ range.

We note that the offset of the $\rho_c^{(0.6)}$ *vs.* $\rho_c^{(0.8)}$ regression reflects combined uncertainties due to sensor calibration, Rayleigh and gas corrections, assuming that ε is spatially homogeneous and clear water pixels have near-zero marine reflectance.

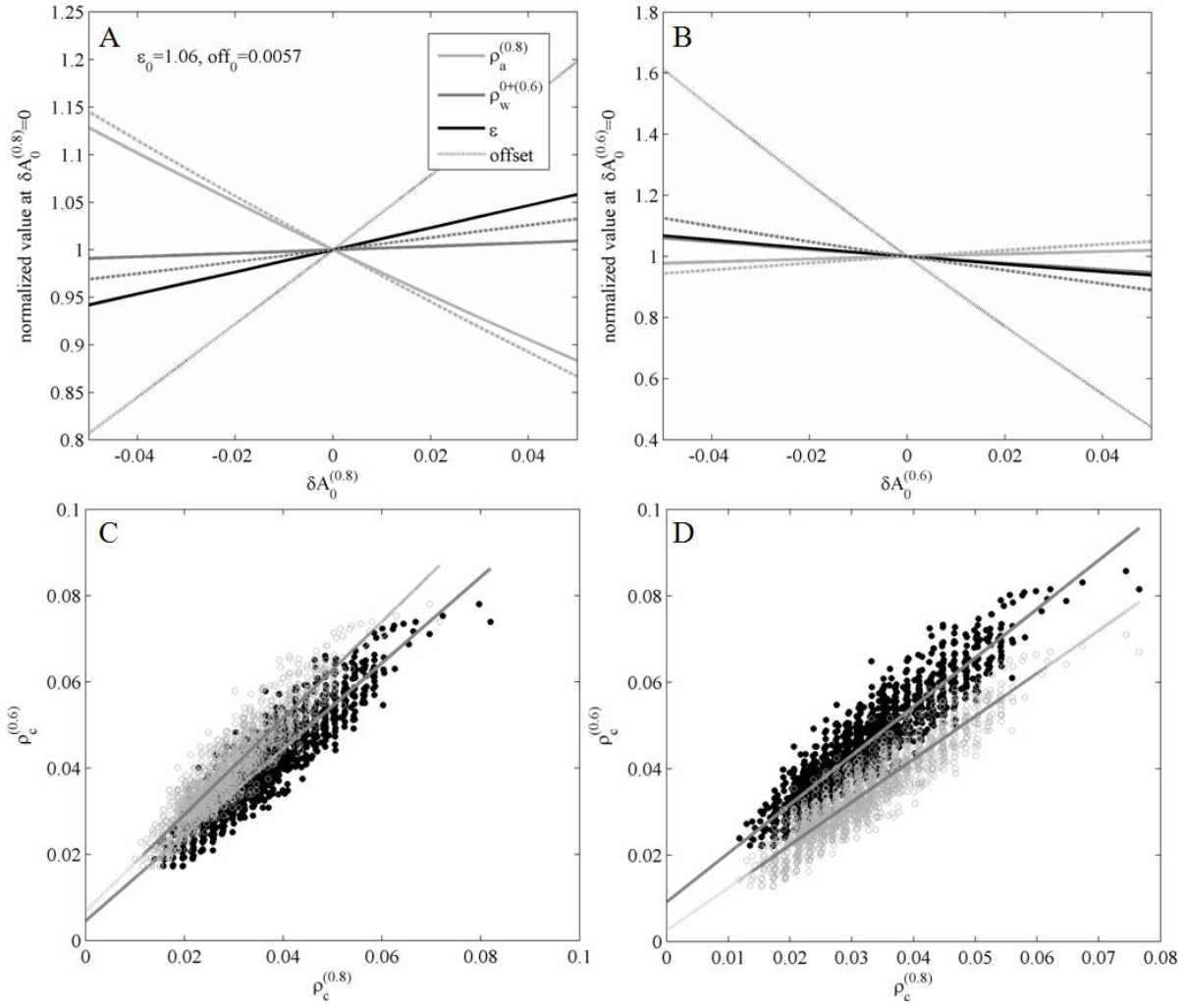

Figure 4.25. Effectiveness of SEVIRI VIS06-VIS08 inter-calibration method using the offset of the regression of their Rayleigh and gas corrected reflectances, $\rho_c^{(0.6)}$ and $\rho_c^{(0.8)}$. Variation of ε, $\rho_a^{(0.8)}$, and $\rho_w^{0+(0.6)}$ with uncertainty $\delta A_0^{(0.8)}$ on the VIS08 calibration factor (A) or with uncertainty $\delta A_0^{(0.6)}$ on the VIS06 calibration factor (B). (C) Scatter plot of $\rho_c^{(0.6)}$ vs. $\rho_c^{(0.8)}$ for $\delta A_0^{(0.8)}$ = -0.05 (black dots) and $\delta A_0^{(0.8)}$ = 0.05 (grey circles) with fitted regression lines. (D) same as (C) but for $\delta A_0^{(0.6)}$ = -0.05 and $\delta A_0^{(0.6)}$ = 0.05. (data for 8 April 2008 at 12:00UTC were used).

Chapter 5 DIURNAL VARIABILITY OF TURBIDITY AND LIGHT ATTENUATION IN TURBID SOUTHERN NORTH SEA WATERS FROM THE SEVIRI GEOSTATIONARY SENSOR

This chapter has been accepted for publication in Remote Sensing of the Environment (Neukermans et al. accepted).

Abstract

With the atmospheric correction of SEVIRI imagery now being fully described and validated in the previous chapter, we can focus here on some of SEVIRI's potential for marine applications. Single-band retrieval algorithms for turbidity (T) and vertical attenuation of photosynthetically active radiation (K_{PAR}) are applied to the two-year archive of marine reflectance in SEVIRI's red waveband. The diurnal variability of T and K_{PAR} is investigated during cloud free periods and validated using half-hourly T and K_{PAR} data obtained from a system of moored buoys (SmartBuoys) in the turbid waters of the southern North Sea. Based on numerous match-ups, 80% of SEVIRI derived T and K_{PAR} are within 53% and 39% of SmartBuoy T and K_d, respectively. Results further show that on cloudfree days, the SEVIRI T and K_{PAR} signals are in phase with the SmartBuoy data, with an average difference in the timing of the maximum T and K_{PAR} of 11 minutes and 23 minutes, respectively. Diurnal variability of T and K_{PAR} in turbid waters can now be mapped by remote sensing offering new opportunities for improving ecosystem models and monitoring of turbidity.

5.1 Introduction

Remote sensing of [SPM] and T in turbid waters is of interest in various fields of marine science, including monitoring of water quality, the underwater light field and visibility. Imagery of [SPM] from ocean colour polar-orbiting satellites has been assimilated in modelling studies of sediment transport (Van Raaphorst et al. 1998; Fettweis and Van den Eynde 2003; Fettweis et al. 2006; Vos et al. 2000), coastal erosion, and ecosystems (Lacroix et al. 2007). The reduction of sunlight available for photosynthesis by phytoplankton has been primarily attributed to suspended particles in turbid coastal waters (Devlin et al. 2008; Xu et al. 2005) and in lagoons and estuaries (Christian and Sheng 2003; Lawson et al. 2007; Painting et al. 2007). In shallow temperate seas, such as the southern North Sea, light availability is an important factor controlling phytoplankton carbon fixation and growth (Peeters et al. 1991, Nedwell et al. 1999) and is thought to affect the timing of the spring bloom (Legendre 1990), which, in turn, affects the survival of larvae of fish and crustaceans (Platt et al. 2003; Fuentes-Yaco et al. 2007).

In shallow coastal environments, [SPM] and covarying parameters such as T and the vertical light attenuation coefficient (K_{PAR}), may show strong diurnal variability due to tidal resuspension and/or horizontal advection of suspended particles.

In this chapter, we investigate the potential of SEVIRI to detect the diurnal variability of T and K_{PAR}. Single-band retrieval algorithms for T and K_{PAR} are applied to the two-year archive of marine reflectance in SEVIRI's red waveband. Single waveband [SPM] (or T) retrieval algorithms have been used intensively in coastal waters, and have been established either empirically (Chen et al. 1991; Ouillon et al. 1997; Hu et al. 2004) or semi-empirically (Stumpf and Pennock 1989; Van Der Woerd and Pasterkamp 2004; Nechad et al. 2009; Nechad et al. 2010). The latter are based on simplified optical reflectance models, calibrated with in-situ data and their limitations are relatively well documented (Nechad et al. 2010; Neil et al. 2011). Even a broad waveband of low radiometric resolution, such as the AVHRR red band (similar to SEVIRI's VIS06 band), has provided reliable data on [SPM] in turbid waters (Stumpf and Pennock 1989). The diurnal variability of T and K_{PAR} is investigated during cloud free periods and validated using half-hourly T and K_{PAR} data obtained from a system of moored buoys (SmartBuoys) in the southern North Sea.

5.2 Materials and methods

5.2.1 Retrieval of turbidity and suspended matter from SEVIRI

5.2.1.1 RETRIEVAL ALGORITHMS

The single band turbidity and [SPM] retrieval algorithms of Nechad et al. 2009 and Nechad et al. 2010, respectively, are:

$$T = \frac{A_T \rho_w^{0+(0.6)}}{C - \rho_w^{0+(0.6)}} + B_T \quad \text{and} \quad S = \frac{A_S \rho_w^{0+(0.6)}}{C - \rho_w^{0+(0.6)}} + B_S \tag{5.1}$$

where C is band specific, giving C=0.1639 for the SEVIRI VIS06 band. The coefficients (A_T , B_T) of the turbidity algorithm and (A_S , B_S) of the [SPM] algorithm are derived from non-linear regression of 68 in situ observations of marine reflectance and T or [SPM] obtained in the southern North Sea in 2007-2010 (see Nechad et al. 2010 for details on curve fitting). Selection criteria for reflectance and T or [SPM] measurements are described in more detail in this Chapter's Appendix, section 5.6.1. Regression gives coefficients with standard error A_T=35.8±3.8 FNU and B_T=-0.1±0.9 FNU for the T algorithm and A_S= 37.1±5.7 mg L^{-1} and B_S= -0.17±1.4 mg L^{-1} for the [SPM] algorithm. Measurements and fitted curves are shown in Figure 5.1. The offsets B_T and B_S are not significantly different from zero, and the T and [SPM] algorithms are applied without it.

Turbidity and [SPM] products on the HRV grid, denoted $T_{\otimes}$ and $S_{\otimes}$, are derived simply by replacing $\rho_w^{0+(0.6)}$ by $\rho_{w,\otimes}^{0+(0.6)}$ in Eqs. (5.1), where $\rho_{w,\otimes}^{0+(0.6)}$ is given in Eq. (4.45).

5.2.1.2 UNCERTAINTY ON SEVIRI TURBIDITY AND SUSPENDED MATTER PRODUCTS

The uncertainty on the retrieval of *T* or [SPM] using algorithms of the form (5.1) resulting from uncertainties on $\rho_w^{0+(0.6)}$ and their respective calibration parameters, A_T or A_S , and is estimated from first order error propagation (ISO 1995) to give:

$$\Delta T = \frac{1}{C - \rho_w^{0+(0.6)}} \left[\left(\frac{A_T C \Delta \rho_w^{0+(0.6)}}{C - \rho_w^{0+(0.6)}} \right)^2 + \left(\rho_w^{0+(0.6)} \Delta A_T \right)^2 \right]^{1/2} \quad (5.2)$$

This expression can be written analogously for the uncertainty on [SPM], denoted ΔS, by replacing A_T with A_S. The relative uncertainty on turbidity can be expressed as follows:

$$\frac{\Delta T}{T} = \left[\left(\frac{C}{C - \rho_w^{0+(0.6)}} \frac{\Delta \rho_w^{0+(0.6)}}{\rho_w^{0+(0.6)}} \right)^2 + \left(\frac{\Delta A_T}{A_T} \right)^2 \right]^{1/2} \quad (5.3)$$

where $\frac{\Delta A_T}{A_T} = 0.11$. Analogously for [SPM] with $\frac{\Delta A_S}{A_S} = 0.15$. The two components in Eq. (5.3) are of very different nature. The first component is related to the uncertainty on marine reflectance due to atmospheric correction and digitization, where the latter is the dominant source of uncertainty for SEVIRI (*see* sections 4.2.7.1 to 4.2.7.3). The second component is the uncertainty arising from the calibration of the retrieval algorithms for *T* and [SPM] and is equal to 11% and 15%, respectively, everywhere in the scene. Uncertainties in the [SPM] and *T* algorithm calibration are caused by various factors such as in-situ measurement uncertainties for reflectances, *T*, and [SPM] and uncertainties in the optical model underlying Eq. (5.1). As discussed in Nechad et al. 2010, the main source of uncertainty in the *T* and [SPM] algorithms is the natural variability of the turbidity- and mass-specific backscattering ratios, respectively. This is further investigated in this Chapter's Appendix, section 5.6.2.

The uncertainty on *T* and [SPM] products on the HRV grid, denoted $\Delta T_{\otimes}$ and $\Delta S_{\otimes}$, are expressed by replacing $\rho_w^{0+(0.6)}$ by $\rho_{w,\otimes}^{0+(0.6)}$ and $\Delta\rho_w^{0+(0.6)}$ by $\Delta\rho_{w,\otimes}^{0+(0.6)}$ in Eq. (5.2).

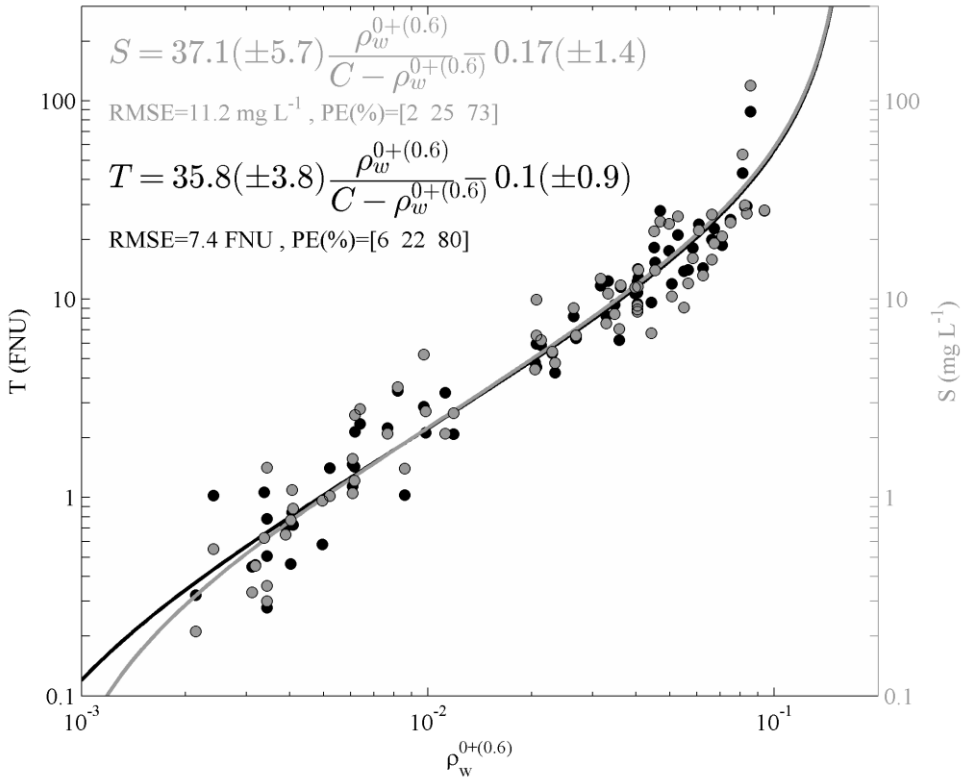

Figure 5.1. Scatterplot of 68 seaborne measurements of marine reflectance in the VIS06 band, and turbidity (*T*) and SPM concentration (*S*). The black and grey lines represent the SEVIRI VIS06 retrieval algorithms for *T* (Nechad et al. 2009) and *S* (Nechad et al. 2009; Nechad et al. 2010) with C=0.1639. The RMSE and the [5 50 95]th percentiles of the relative model prediction errors are also shown.

5.2.2 Retrieval of PAR attenuation

5.2.2.1 PAR ATTENUATION ALGORITHM

Many studies have illustrated that the variability in light attenuation is primarily driven by [SPM] in turbid coastal waters (Devlin et al. 2008; Xu et al. 2005) and in lagoons and estuaries (Christian and Sheng 2003; Lawson et al. 2007; Painting et al. 2007). From a spatially extensive survey of vertical profiles of PAR and [SPM] in coastal and offshore UK waters a strong linear relationship (R^2=0.98) between the water column mean [SPM], $\overline{S}$, and the water column mean attenuation coefficient of PAR, $\overline{K}_{PAR}$, was found (Devlin et al. 2008):

$$\overline{K}_{PAR} = 0.325(\pm 0.06) + 0.066(\pm 0.002) \times \overline{S} \quad (5.4)$$

where $\overline{S}$ varied between 0.1 mg L^{-1} and 250 mg L^{-1}, with most values below 50 mg L^{-1} and $\overline{K}_{PAR}$ varied between 0.3 m^{-1} and 15 m^{-1} with most values below 3 m^{-1}. This model has been shown to work well in turbid waters dominated by suspended sediments (Devlin et al. 2008).

Replacing $\overline{S}$ in Eq. (5.4) by the SEVIRI [SPM] retrieval algorithm in Eq. (5.1) gives the SEVIRI K_{PAR} on the VIS06 and HRV grids, denoted K_{PAR} and $K_{PAR,\otimes}$, respectively.

5.2.2.2 UNCERTAINTY ON PAR ATTENUATION RETRIEVAL

The uncertainty on the SEVIRI K_{PAR} product, introduced by uncertainties on S and the slope and offset of the model in Eq. (5.4) is:

$$\Delta K_{PAR} = \left[(0.066 \Delta S)^2 + (0.002 S)^2 + 0.06^2 \right]^{1/2} \quad (5.5)$$

with ΔS given by Eq. (5.2) and S from Eq. (5.1). Replacing S by $S_{\otimes}$ and ΔS by $\Delta S_{\otimes}$ gives ΔK_{PAR} on the HRV grid, denoted $\Delta K_{PAR,\otimes}$.

5.2.3 Validation of SEVIRI turbidity and PAR attenuation products

5.2.3.1 SMARTBUOY MEASUREMENTS OF TURBIDITY AND PAR ATTENUATION

Half-hourly measurements of physical, chemical, optical, and biological variables are made in UK shelf seas from moored platforms, SmartBuoys (Mills et al. 2003), operated by the Centre for Environment, Fisheries and Aquaculture Sciences (Cefas) on a regular basis since 2001. Several SmartBuoys were operational in the southern North sea in 2008-2009: Warp Anchorage (TH1) (51.5235°N, 1.0240°E) and West Gabbard (WG) (51.9802°N, 2.0828°E), and since 2009 also Dowsing (D) (53.5313°N, 1.0532°E). Their location is shown in Figure 4.8. Cefas SmartBuoys measure water turbidity, denoted T^{SB}, using a Seapoint turbidity meter, which records light scattered by suspended particles between 15° to 150° from a light source emitted at 880 nm. Turbidity is measured 1-2 m below the surface and expressed in Formazine Turbidity Units (FTU). PAR is recorded using LI-COR (LI-192SB) underwater quantum sensors just above the surface and at 1 m and 2 m depths (units: μE m^{-2} s^{-1}). SmartBuoy turbidity and PAR measurements are recorded during 10 minute bursts, every half hour. Every burst gives 600 scans, which were mean-averaged.

The vertical light attenuation coefficient can be derived from PAR measurements at 1 m and 2 m depth using the Lambert-Beer equation:

$$K_{PAR}^{SB} = \ln\left(\frac{\mathrm{PAR(1m)}}{\mathrm{PAR(2m)}} \right) \quad (5.6)$$

with uncertainty:

$$\Delta K_{PAR}^{SB} = \left[\left(\frac{\Delta \mathrm{PAR(1m)}}{\mathrm{PAR(1m)}} \right)^2 + \left(\frac{\Delta \mathrm{PAR(2m)}}{\mathrm{PAR(2m)}} \right)^2 - 2 \frac{\Delta \mathrm{PAR(1m)} \Delta \mathrm{PAR(2m)}}{\mathrm{PAR(1m)PAR(2m)}} \right]^{1/2} \quad (5.7)$$

where Δ represents the measurement standard deviation during each burst and the third term accounts for the dependence between PAR(1m) and PAR(2m) (r>0.95 for each SmartBuoy. The above water PAR measurements, PAR(0m), were used for data quality control based on following criterion:

$$\ln\left(\frac{\mathrm{PAR(0m)}}{\mathrm{PAR(1m)}}\right)-\ln\left(\frac{\mathrm{PAR(1m)}}{\mathrm{PAR(2m)}}\right)\le 0.5\ln\left(\frac{\mathrm{PAR(0m)}}{\mathrm{PAR(1m)}}\right) \tag{5.8}$$

thus rejecting observations where PAR attenuation between 1 m and 2 m depth differs more than 50% from the PAR attenuation between the surface and 1 m depth. The 0.5 threshold value corresponds to the 75th percentile so that 25% of the PAR data were rejected. Unfortunately no surface PAR measurements are available at WG, so the validation of SEVIRI K_{PAR} is limited to TH1 and D.

5.2.3.2 COMPARISON OF INSTANTANEOUS SEVIRI-SMARTBUOY OBSERVATIONS

All cloudfree SEVIRI T and K_{PAR} products, P, were regressed against corresponding Smartbuoy data, P^{SB}. Correlation analysis and 'least squares cubic' regressions (York 1966), which take into account measurement uncertainties in the data, are used. The least squares cubic regression is applied after removal of outliers, identified by the MATLAB robustfit.m routine. Correlation coefficients are given with their 95% confidence intervals, obtained from bootstrapping. Details of these statistical procedures are described in the Web appendix of Neukermans et al. 2012.

Several statistics are used to quantify agreement between SEVIRI and SmartBuoys products. The Root-Mean-Square-Error (RMSE), computed after removal of outliers:

$$\mathrm{RMSE}=\sqrt{\frac{1}{n-2}\sum_{k=1}^{n}(P^{SB}-P)^2} \tag{5.9}$$

and the 5th, 50th, and 95th percentiles of the normalized absolute prediction error, PE (computed from all observations):

$$PE=\frac{\left|P-P^{SB}\right|}{P^{SB}} \tag{5.10}$$

and the normalized bias:

$$\mathrm{bias}=\frac{P-P^{SB}}{P^{SB}} \tag{5.11}$$

5.2.3.3 VALIDATION OF SEVIRI PRODUCT TIME SERIES

Continuous and cloudfree SEVIRI T and K_{PAR} time series longer than 4.5 hours were compared against corresponding Smartbuoy time series. A moving average filter with a span of 5 observations was applied twice to the SEVIRI and Cefas time series and local maxima were identified using the findextrema.m MATLAB script of Deng 2009. In the case of multiple local maxima for SEVIRI time series, only the global maximum was retained. The timing of the global maximum of the SEVIRI

product, $t(P_{\max})$, was then compared against the timing of the nearest maximum of the corresponding SmartBuoy product, $t(P_{\max}^{SB})$. Smoothed time series where the amplitude of diurnal variability of *P* detected by SEVIRI (P_{max}-P_{min}) was smaller than the daily mean standard error on *P* were not considered. This removes the noisiest time series. We further rejected time series with small in-situ diurnal variability, i.e. time series with SmartBuoy amplitude smaller than a certain fraction of the maximum SmartBuoy data for a given day. This fraction was arbitrarily set to 0.4 for *T* and 0.2 for K_{PAR}.

The agreement in timing of the maximum between SEVIRI and SmartBuoy timeseries of a product *P* is quantified by the mean and standard deviation and the 5th, 50th, and 95th percentiles of the timing bias, $\text{bias}_t = t(P_{\max}) - t(P_{\max}^{SB})$, and the timing prediction error, $PE_t = \left| t(P_{\max}) - t(P_{\max}^{SB}) \right|$.

5.3 Results

5.3.1 Comparison of instantaneous SEVIRI-SmartBuoy observations

5.3.1.1 TURBIDITY OBSERVATIONS

A total of 3068 SEVIRI-SmartBuoy T match-ups were observed at TH1, WG, and D. Scatterplots of T vs. T^{SB} are shown in Figure 5.2 (a). Observations with over 100% uncertainty on $\rho_w^{0+(0.6)}$ (see grey dots in Figure 5.2 (a)) were removed, giving 2598 (=n_v) remaining observations. Least squares cubic regression was applied to this dataset after removal of 51 (=n_x) outliers. Equation and statistics of the regression are shown in Table 5.1. A good correlation is observed between T and T^{SB} with correlation coefficient r=0.933±0.006. On average, T is underestimated by SEVIRI by 14%, with a median prediction error of 29% and an RMSE of 5.8 FNU. In 80% of the cases T is within 53% of T^{SB} and in 95% of the cases within 80% (see Table 5.1). For validation of the high spatial resolution *T* product, $T_{\otimes}$, observations neighboring cloud or low aerosol transmittance (where $t_{o,v}^{a(0.6)} < 0.85$) pixels were further removed (shown by grey dots in Figure 5.2 (b)), giving 1412 remaining match-ups. The correlation coefficient, regression equation, and RMSE found for $T_{\otimes}$ vs. T^{SB} were similar to the values found for the low spatial resolution T vs. T^{SB} comparison. However, the scatter in the $T_{\otimes}$ vs. T^{SB} plots is higher with higher spread in the 5-95th percentiles of *PE* and bias and higher median underestimation by SEVIRI of 20% (see Table 5.1).

5.3.1.2 PAR ATTENUATION OBSERVATIONS

A total of 1492 SEVIRI-SmartBuoy K_{PAR} match-ups were observed at TH1 and D. Scatterplots of K_{PAR} vs. K_{PAR}^{SB} are shown in Figure 5.2 (c). Observations with over 100% uncertainty on $\rho_w^{0+(0.6)}$ or

quality flagged PAR data (after Eq. (5.8)) are shown as grey dots in Figure 5.2 (c). These observations were removed from the dataset, giving 988 remaining match-ups. Equation and statistics of the regression are shown in Table 5.1. A good correlation is observed between K_{PAR} and K_{PAR}^{SB} with correlation coefficient r=0.926±0.008. Overall, SEVIRI overestimates K_{PAR} by 9% on average, with a median prediction error of 18% and an RMSE of 0.34 m^{-1}. In 80% of the cases K_{PAR} is within 39% of K_{PAR}^{SB} and in 95% of the cases within 81% (see Table 5.1). Analogously to the validation of $T_{\otimes}$, observations neighboring cloud or low aerosol transmittance pixels were further removed (shown by grey dots in Figure 5.2 (d)), giving 424 remaining match-ups for $K_{PAR,\otimes}$. The correlation coefficient, regression line, and prediction errors of $K_{PAR,\otimes}$ vs. K_{PAR}^{SB} are comparable to the values found the low spatial resolution product. The overestimation of K_{PAR} by SEVIRI for the high resolution product decreased by 4% on average compared to the low resolution product.

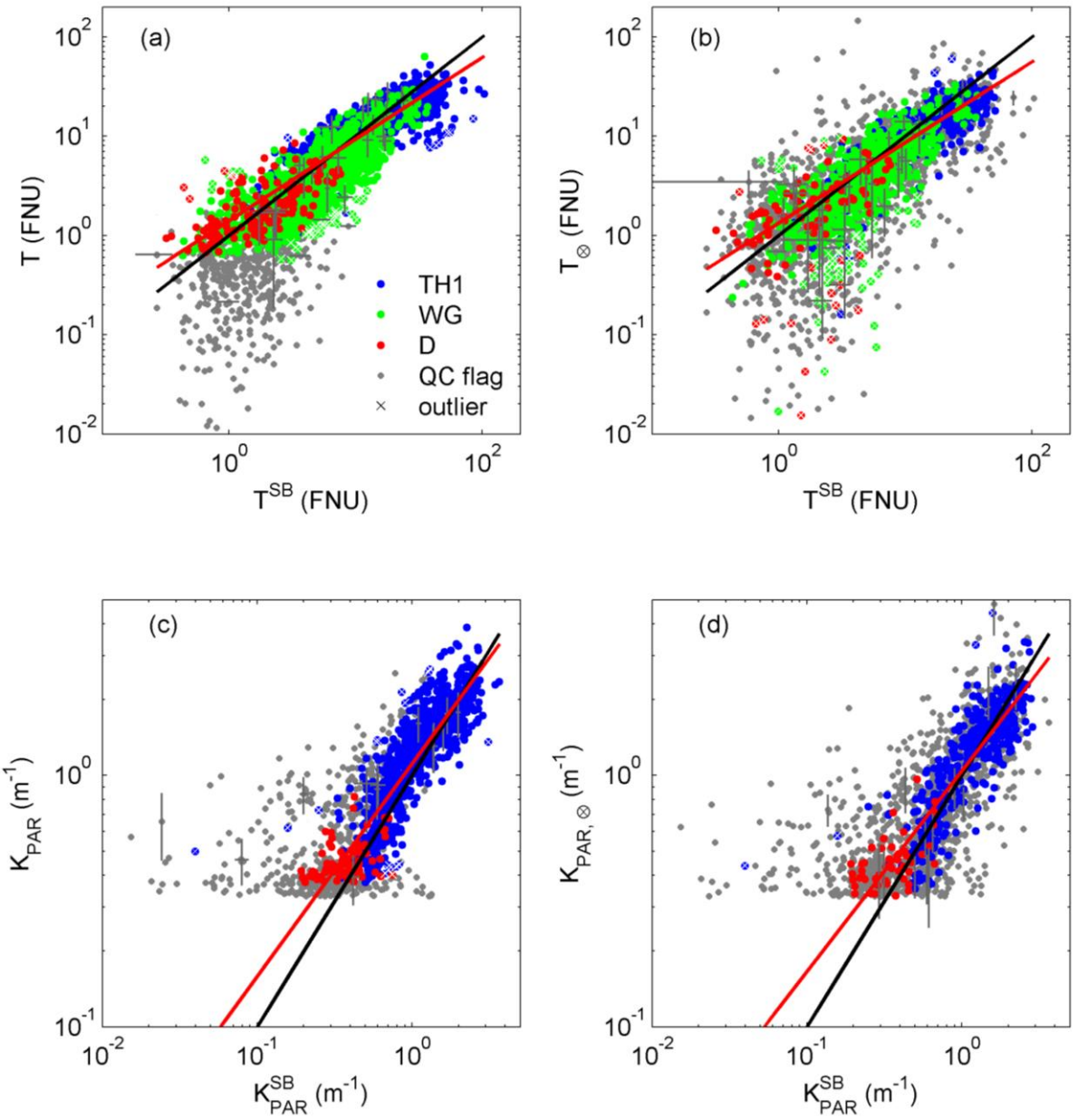

Figure 5.2. Scatter plots of SEVIRI vs. SmartBuoy turbidity (T) and light attenuation (K_{PAR}) at TH1, WG, and D for the period 2008-9 on the low (a, c) and the high (b, d) spatial resolution SEVIRI grids. Regression and 1:1 lines are shown in red and black, respectively, with equations and statistics in Table 3. Quality flagged observations are shown in grey and correspond to pixels where either the SEVIRI marine reflectances have over 100% uncertainty (a,b,c,d), or are in the proximity of cloud or low aerosol transmittance pixels (c, d), or low quality PAR measurements (c, d). Errorbars are plotted for 1% random observations and denote uncertainties on SmartBuoy (Eq. (5.7)) and SEVIRI (Eqs. (5.2) and (5.5)) products. Regression outliers are labelled by white crosses.

Table 5.1. Equation and statistics of the least-squares-cubic log-log regressions between SmartBuoy and SEVIRI *T* and K_{PAR} products obtained on the SEVIRI low and high ($\otimes$ subscript) spatial resolution grids. The total number of match-ups is given by n_{tot}, of which n_v passed the quality control criteria (see sections 5.3.1.1 and 5.3.1.2 for details), and from which n_x were removed as regression outliers. The correlation coefficient, *r* , with 95% confidence interval ($r\pm\Delta r$), slope (a) and offset (b) of the regression line are given with their standard errors. The RMSE (expressed in units of *P*), and the 5th, 50th, and 95th percentiles of the prediction error (*PE*) and the bias are given.

						$\log_{10} P = a(\pm\Delta a)\log_{10} P^{SB} + b(\pm\Delta b)$					*PE* (%)			bias (%)		
P	n_{tot}	n_v	n_x	*r*	Δr	*a*	Δa	*b*	Δb	RMSE	5	50	95	5	50	95
T	3068	2598	51	0.933	0.006	0.822	0.009	0.148	0.010	5.795	3	29	80	-65	-14	77
$T_{\otimes}$	3068	1412	72	0.922	0.009	0.812	0.012	0.126	0.013	5.340	3	32	93	-73	-20	82
K_{PAR}	1492	988	16	0.926	0.008	0.846	0.014	0.047	0.003	0.342	2	18	81	-27	9	81
$K_{PAR,\otimes}$	1492	424	4	0.917	0.015	0.798	0.022	0.018	0.005	0.341	2	19	79	-35	5	79

5.3.2 Validation of SEVIRI product time series

5.3.2.1 TIME SERIES OF TURBIDITY

A random selection of 12 out of 49 available time series of *T* derived from SEVIRI and the SmartBuoys are shown in Figure 5.3 and Figure 5.4 . The in situ data shows strong variability with a period of about 6 hours, typical of resuspension dynamics induced by a semi-diurnal tide, but strong wind and wave action also affect advection and resuspension of sediments from the bottom. Overall, the diurnal variability of *T* detected by the SmartBuoys is picked up well by SEVIRI, albeit with some exceptions (e.g., Figure 5.3 C, Figure 5.4 G). In general, the high spatial resolution time series of SEVIRI are noisier than the low resolution time series. In some occasions the high spatial resolution time series picks up small scale variability that is not detected on the low resolution grid (Figure 5.3 B, Figure 5.4 L). For comparison, data availability from MODIS Aqua is also indicated on Figure 5.3 and Figure 5.4, clearly showing the tremendous increase in data availability that can be gained from a sensor in geostationary orbit, even in winter and at high latitudes (see Figure 5.3A, E, F).

Figure 5.5 shows the comparison of the timing of maximum *T* derived from the smoothed SEVIRI VIS06 time series (see big red dots in Figure 5.3 and Figure 5.4) against the timing of maximum *T* obtained from the SmartBuoys for all available cloudfree periods (n=49). In 75% of the cases, the phase difference is less than one hour. On average, the maximum SEVIRI *T* is reached 11 minutes before the maximum SmartBuoy *T*, with a standard error of 1.46h.

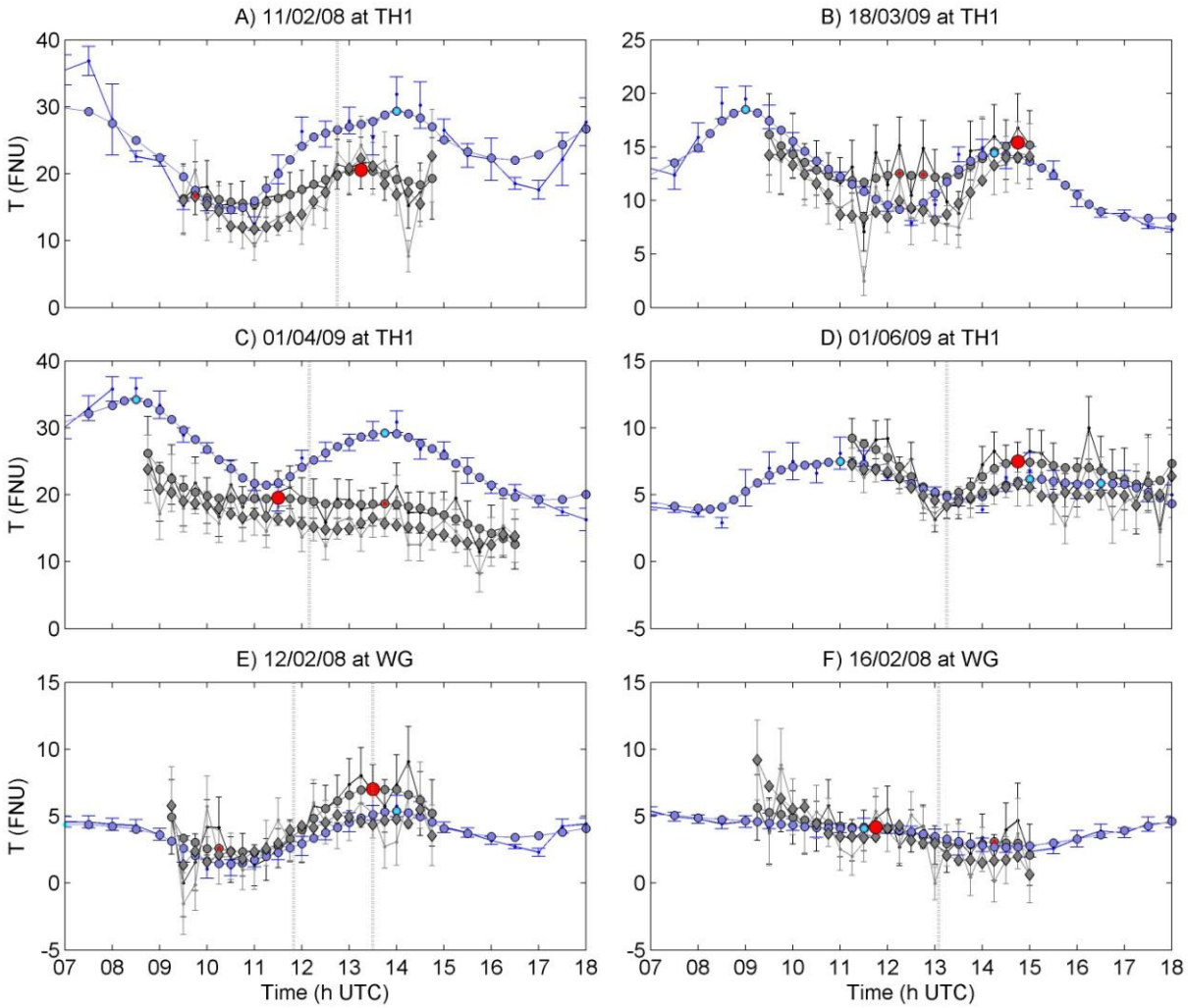

Figure 5.3. Randomly selected original and smoothed time series of *T* obtained from SEVIRI and SmartBuoys. SEVIRI *T* data from the VIS06 and HRV bands with uncertainty from Eq. (5.2) are shown by the black and grey errorbars, respectively. Temporally smoothed data series for VIS06 and HRV T products are shown by grey circles and diamonds, respectively, with global (big red dot) and local (small red dots) maxima. SmartBuoy *T* and its uncertainty is shown by the blue errorbars, while the temporally smoothed data series is shown by blue circles with local maxima highlighted in cyan. Grey vertical dotted lines represent data availability from MODIS Aqua.

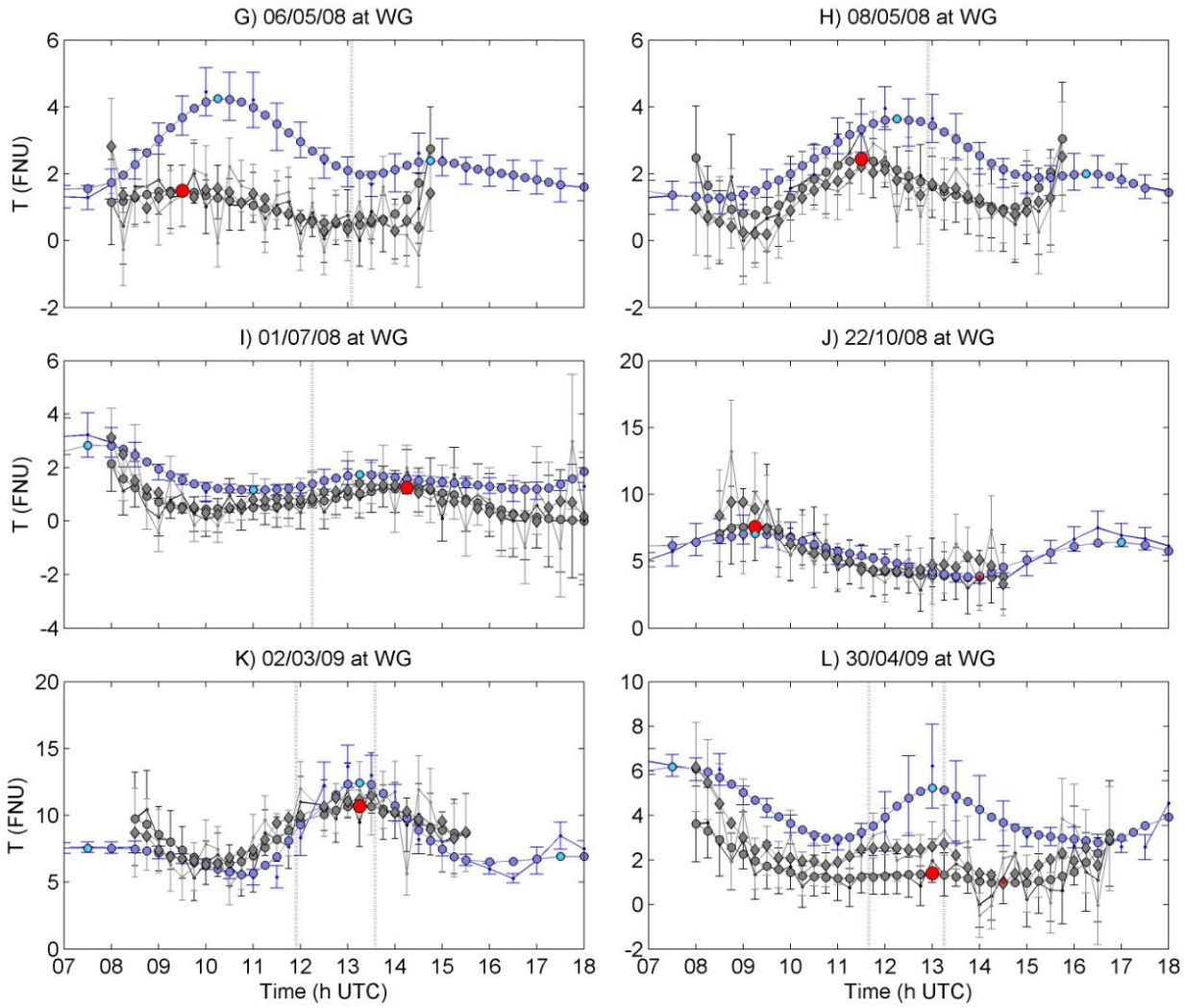

Figure 5.4. Continuation of Figure 5.3.

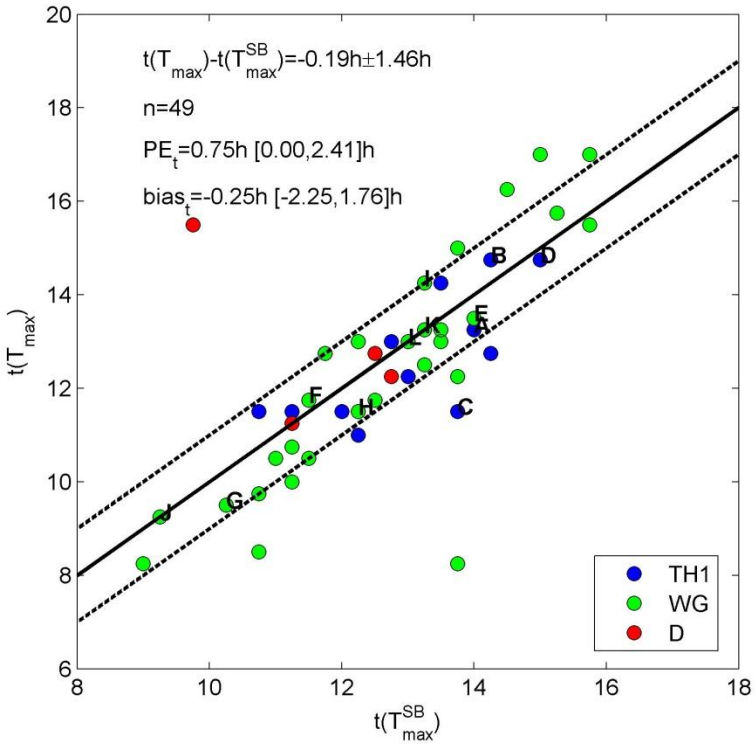

Figure 5.5. Scatterplot of the timing of maximum turbidity derived from the SmartBuoys (TH1, WG, and D) and SEVIRI on 49 cloudfree periods. The 1:1 line (solid) and 1 hour offset lines (dashed) are shown in black. Labels refer to the time series shown in Figure 5.3 and Figure 5.4. The mean and standard deviation of the phase difference, median and 5th-95th percentile interval for prediction error and bias are also given in black.

5.3.2.2 TIMES SERIES OF PAR ATTENUATION

From a total of 27 available time series of PAR attenuation from SEVIRI and the SmartBuoys at TH1 and D, six randomly selected time series are shown in Figure 5.6. Approximately 6-hourly variability is apparent for some time series, although other temporal variability is also apparent. For comparison, data availability from MODIS Aqua is also indicated in Figure 5.6. Figure 5.7 shows the comparison of the timing of maximum K_{PAR} derived from the smoothed SEVIRI VIS06 time series (see big red dots in Figure 5.6) against the timing of maximum K_{PAR} obtained from the SmartBuoys for all available cloudfree periods. In 80% of the cases, the phase difference is less than one hour. On average, the maximum SEVIRI K_{PAR} is reached 23 minutes before the maximum SmartBuoy K_{PAR}, with a standard error of 1.27h. Also shown in Figure 5.7 are the statistics corresponding to a random timing of K_{PAR}^{SB}. Again, the

standard error of the phase difference is much larger for a random timing, as are the 5-95th percentile intervals of PE_t and bias_t.

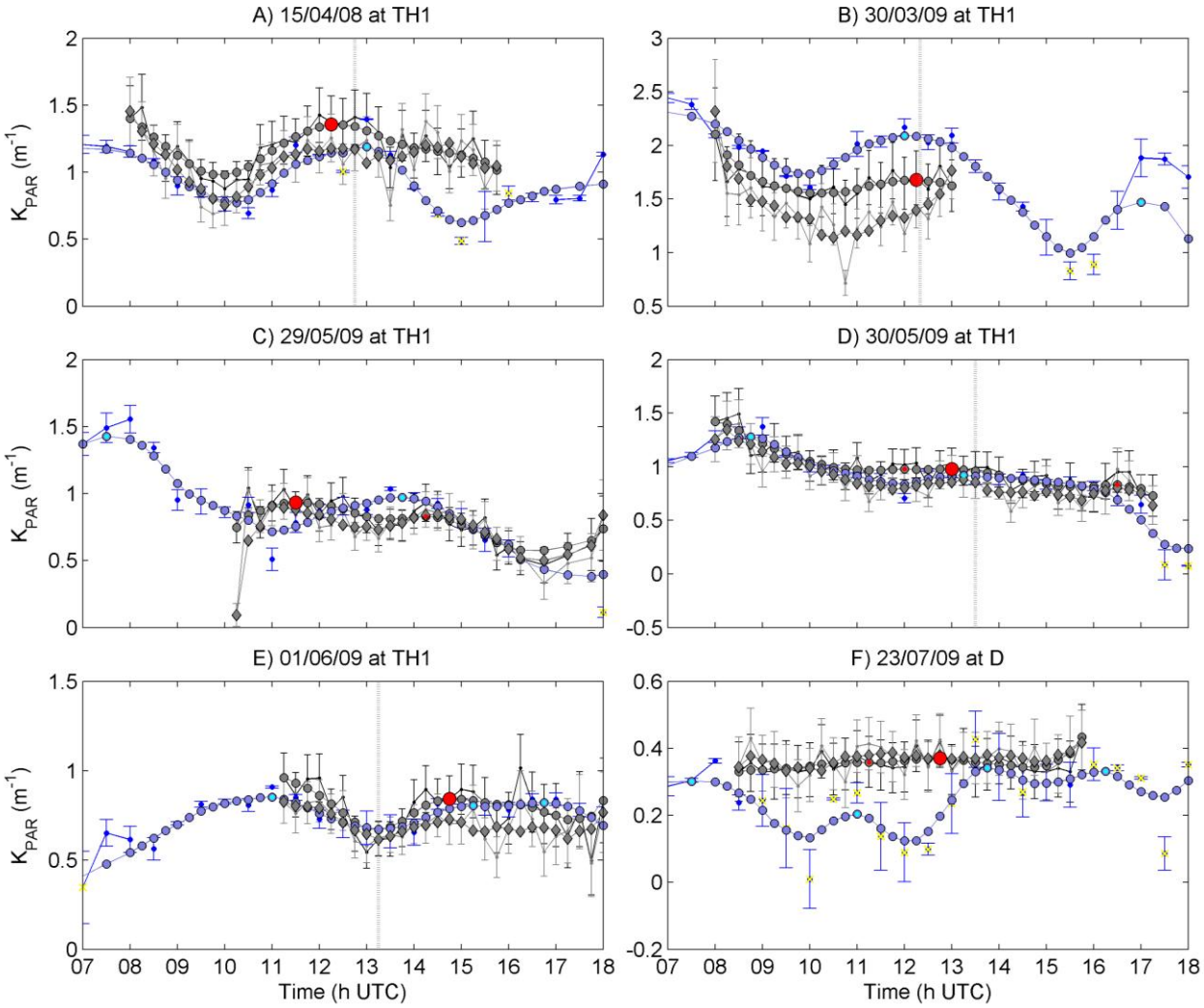

Figure 5.6. Six randomly selected original and smoothed time series of K_d obtained from SEVIRI and SmartBuoys. SEVIRI K_{PAR} data from the VIS06 and HRV bands with uncertainty expressed by Eq.(5.5) are shown by the dark and light grey errorbars, respectively. Temporally smoothed data series for VIS06 and HRV K_{PAR} products are shown by grey circles and diamonds, respectively, with global (big red dot) and local (small red dots) maxima. SmartBuoy K_{PAR} and uncertainty (after Eq. (5.7)) are shown by the blue errorbars, while the temporally smoothed data series are shown by blue circles with local maxima highlighted in cyan. Grey vertical dotted lines represent data availability from MODIS Aqua. The yellow crosses indicate quality flagged K_{PAR} SmartBuoy data (from Eq. (5.8)).

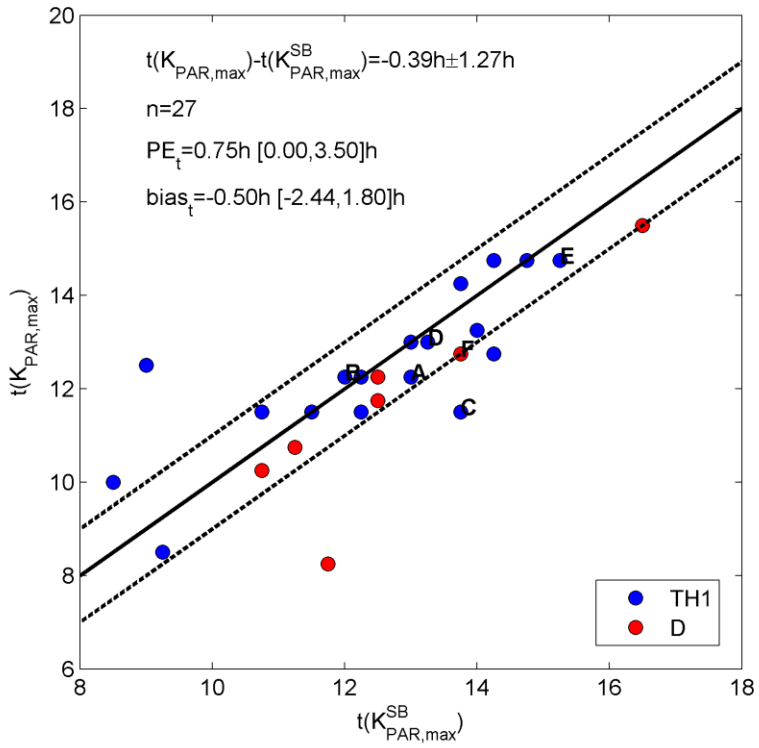

Figure 5.7. Scatterplot of the timing of maximum PAR attenuation derived from the SmartBuoys (TH1 and D) and SEVIRI during 27 cloudfree periods. The 1:1 line (solid) and 1 hour offset lines (dashed) are shown in black. Labels refer to the time series shown in Figure 5.6. The mean and standard deviation of the phase difference, median and 5th-95th percentile interval for prediction error and bias are also given in black.

5.4 Discussion

Overall, good correspondence is found between the SEVIRI and SmartBuoy products for both T and K_{PAR}, but with considerable scatter along the 1:1 line as shown in Figure 5.2. Possible causes for differences between SEVIRI and SmartBuoy data include small spatial scale variability (point vs. pixel comparison), SEVIRI atmospheric correction and digitization uncertainties, design of the SEVIRI retrieval algorithms for T and K_{PAR}, and incommensurability between in-situ and remotely sensed products. These are discussed below.

5.4.1 SEVIRI atmospheric correction and digitization uncertainties

The uncertainty on $\rho_w^{0+(0.6)}$ due to the atmospheric correction assumptions and digitization, expressed by Eq. (4.51), is of the order 0.004 for typical North Sea viewing and illumination geometry (*see* Table 4.3,

θ_0=40°). This value defines the SEVIRI detection limit in clear waters: 1 FNU for *T* or 1 mg L^{-1} for [SPM]. The *T* detection limit explains the location of the majority of the grey dots in Figure 5.2(a), where comparison with T^{SB} is clearly problematic.

Whereas the SEVIRI atmospheric correction in clear waters is limited by the SEVIRI digitization uncertainty, the atmospheric correction is expected to fail in very turbid waters, due to the non-linearity of the VIS06:VIS08 marine reflectance ratio (assumption (4.22)) for $\rho_w^{0+(0.6)} > 0.062$, which corresponds to *T*>23 FNU. Above this threshold, SEVIRI underestimates *T* with increasing *T*, up to 60% for *T*=80 FNU, as shown in Figure 5.8 (cfr. Figure 4.21). This underestimation by SEVIRI for high turbidity is also observed in the scatter plot in Figure 5.2(a). With the current atmospheric correction, the optimal range of SEVIRI *T* retrieval is 1-35 FNU. It might be possible to push this upper limit further by refining the algorithm to have a non-constant σ via an extra iterative loop with σ calculated as a function of $\rho_w^{0+(0.8)}$. The issue of non-constant σ in the atmospheric correction is mirrored by limitations of the reflectance model underlying Eq. (5.1) near its high reflectance asymptote. This "saturation" phenomenon (Bowers et al. 1998) is ideally avoided for ocean colour sensors such as MERIS by using longer wavelengths where pure water absorption is higher. For SEVIRI, the only option is the VIS08 band, but this band has much lower SNR than the VIS06 band (*see* Table 4.2).

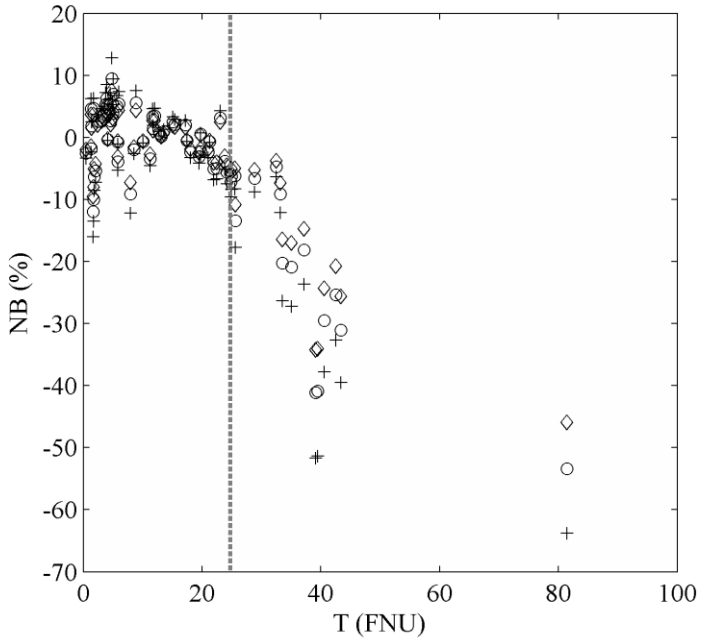

Figure 5.8. Effect of the atmospheric correction assumption of constant σ, as in Eq. (4.22), on the retrieval of T from $\rho_w^{0+(0.6)}$: normalized bias of T retrieved by SEVIRI (after Eq. (4.34)) from the true T (=T algorithm applied to the in situ marine reflectance) for $\varepsilon = 0.84$ (diamonds), $\varepsilon = 1.02$ (circles), and $\varepsilon = 1.30$ (crosses), with simplifications $\gamma = 1 = t_{o,v}^{a(0.8)}$. The dashed line demarcates the reflectance region where σ was calibrated (see Figure 4.7).

5.4.2 Limitations of SEVIRI spatial resolution

5.4.2.1 SUB-PIXEL SCALE VARIABILITY

MODIS Aqua imagery with a spatial resolution of 1 x 1 km² was used to investigate SEVIRI VIS06 sub-pixel scale variability at TH1 and WG for the period 2002-2010. SmartBuoy turbidity from the MODIS 645nm band on a 1 x 1 km² pixel centred at TH1 and WG were compared to their a 5 x 5 km² spatial mean value. The spatially averaged to center pixel *T* ratios are typically between 0.8 and 1.2, with a mean of 1. Differences due to spatial averaging are generally below 30%, with a RMSE of of 0.74 FNU, as shown in Figure 5.9A. Cross validations of MODIS *T* vs. in-situ *T* for 1 x 1 km² and 5 x 5 km² pixels are shown in Figure 5.9B, C, respectively, and illustrate that spatial averaging increases the scatter along the 1:1 line. We further note that MODIS *T* corresponds much better to SmartBuoy *T* than SEVIRI *T* (even

when spatially averaged) with an RMSE of 3.6 FNU compared to 5.8 FNU for SEVIRI, and a median PE of 18%, compared to 29% for SEVIRI.

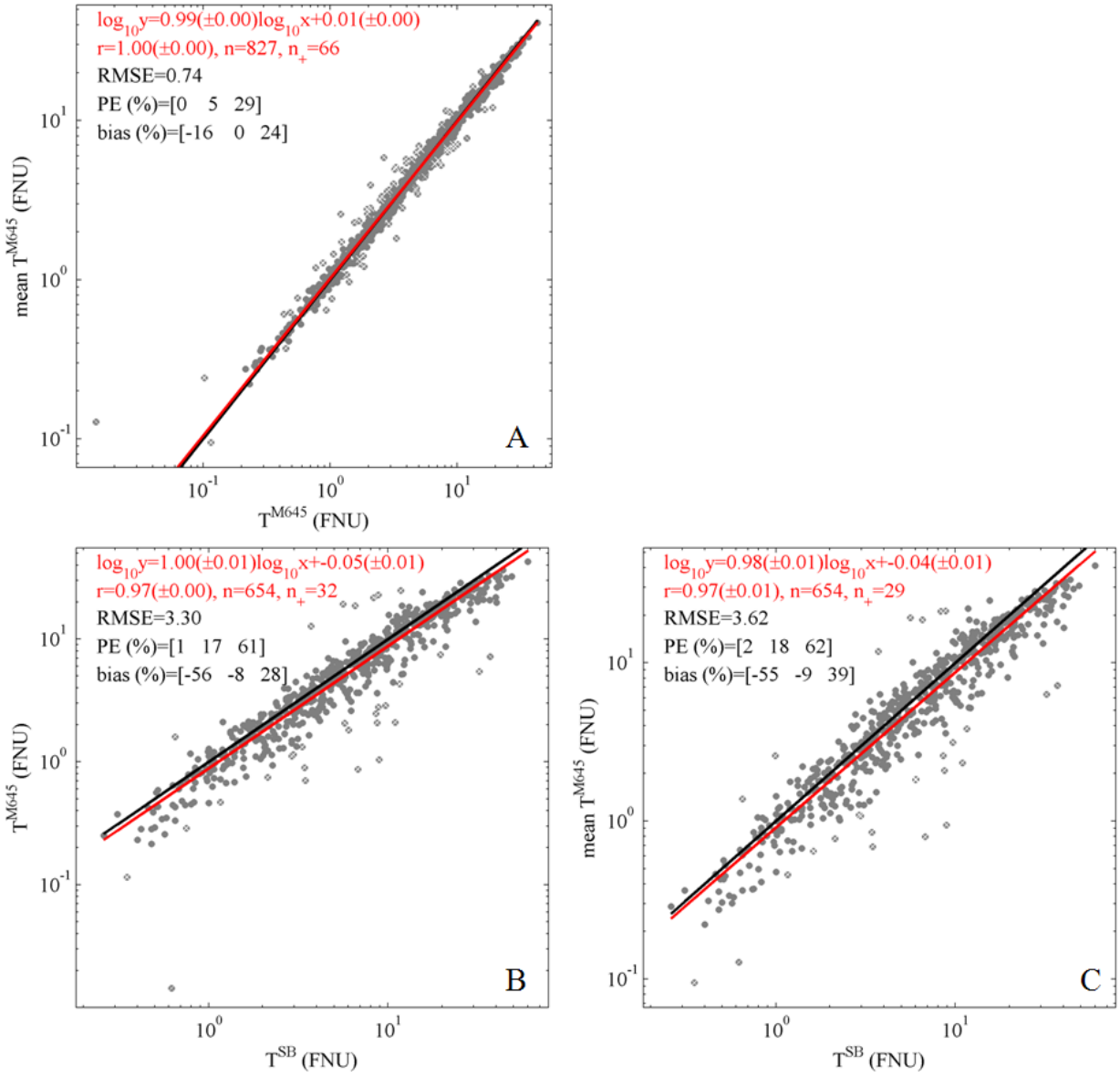

Figure 5.9. Investigation of SEVIRI VIS06 sub-pixel scale variability using MODIS Aqua imagery. (A) Scatter plot of 5 x 5 km² spatial mean turbidity from MODIS 645nm at WG and TH1 for the period 2002-2010 vs. the 1 x 1 km² center pixel turbidity, (B) Scatter plot of MODIS 645nm turbidity vs. SmartBuoy turbidity (T^{SB}) at TH1 and WG. (C) same as (B) but using the 5 x 5 km² spatial mean value. Regression and 1:1 lines are shown in red and black respectively. Regression outliers are marked by white crosses. The turbidity algorithm of Nechad et al. 2009 was used.

5.4.2.2 USE OF THE HRV BAND

Improvement of the spatial resolution of SEVIRI products using the HRV band adversely affected correspondence with SmartBuoy data: an increased scatter along the 1:1 lines for both T and K_{PAR} was observed (Figure 5.2b,d). A similar effect was observed for cross-validation of SEVIRI reflectance with MODIS reflectance (*see* section 4.3.3.2). We therefore conclude that the use of SEVIRI's HRV band is limited due to its poor geolocation and low SNR. It is expected that the methodology developed in section 4.2.6 can be more successfully applied to a sensor with an HRV band that is better geolocated and has a higher SNR (e.g., MODIS, MERIS).

5.4.3 Limitations of the T and K_d retrieval algorithms

5.4.3.1 TURBIDITY RETRIEVAL ALGORITHM

Analogous to the assumption of constant SPM-specific particulate backscattering (=b_{bp}:SPM) in the single band SPM retrieval algorithm of Nechad et al. 2010, the T retrieval algorithm (Nechad et al. 2009in Eq. (5.1)) is based on the assumption that the T-specific backscattering coefficient (=b_{bp}:T) is constant. Like b_{bp}:SPM, b_{bp}:T is relatively well constrained with variability of a factor 3, mainly related to variations in particle composition (see Appendix, section 5.6.2), but particle size and density were also found to affect b_{bp}:T. This implies that for a water mass of fixed turbidity, changes in particle composition from mainly organic to mainly inorganic will lead to a higher remotely sensed T. Particle composition may vary on time scales of a few hours for example due to tidal resuspension of inorganic bottom sediments (Thompson et al. 2011).

5.4.3.2 K_{PAR} RETRIEVAL ALGORITHM

The K_{PAR} retrieval algorithm is based on the optical model of Devlin et al. 2008, identifying suspended particles as the main source of light attenuation (K_{PAR} is proportional to SPM, see Eq. (5.4)). This one parameter model was found by Devlin et al. 2008 to represent most of the variability in K_{PAR} that was measured at a variety of North Sea stations and gives good performance here for the more turbid waters. It is ideally suited to the limited spectral resolution of the SEVIRI sensor which is essentially limited to the retrieval of SPM concentration (and covarying parameters) only. See also Stumpf et al. 1999 for a study with the spectrally similar polar-orbiting AVHRR sensor.

Expressing K_{PAR} as a linear function of SPM is clearly a gross simplification because K_{PAR} can be affected by variability of many factors including: concentration of coloured dissolved organic matter (CDOM), phytoplankton (expressed via Chl *a* concentration), size, shape, and composition of suspended particles, the average cosine of downwelling irradiance (or sun zenith angle), the spectral composition of incident irradiance, and the invalidity of the Lambert-Beer "law" (Gordon 1989). Any of the first three

factors could explain the apparent difference in performance of the SEVIRI K_{PAR} product during clear water periods at TH1 (SEVIRI underestimates) and D (SEVIRI overestimates). The single parameter K_{PAR} model is expected to perform poorly in clearer waters with varying concentrations of CDOM and Chl *a*, because their contribution is represented by a constant offset (see Eq. (5.4)). Unfortunately, no measurements of CDOM are available from the SmartBuoys, but salinity can be used as a proxy, since in the North Sea CDOM has a mainly terrestrial origin (Foden et al. 2008) and decreases with salinity. Salinity data recorded by the SmartBuoys in 2008-9 give average values of 34.14±0.68 PSU and 34.54±0.17 PSU at TH1 and D, respectively, which corresponds to observations in Figure 5.2(c,d) of higher K_{PAR} at TH1 than at D in clear waters. It is, however, beyond the scope of the SEVIRI sensor to resolve the question of CDOM impact on K_{PAR}, although improvement of the SEVIRI K_{PAR} model might be achievable by integrating lower frequency information on CDOM and phytoplankton (or euphotic depth) from suitably designed polar-orbiting ocean colour sensors such as MODIS or MERIS.

5.4.4 Incommensurability between in-situ and remotely sensed products

5.4.4.1 REMOTELY SENSED VS. IN-SITU *T*

In the linear regime of the SEVIRI *T* algorithm of Nechad et al. 2009 (i.e. $\rho_w^{0+(0.6)} << C$ in Eq. (5.1)), *T* is proportional to the particulate backscattering coefficient, b_{bp} , in the red waveband. The SmartBuoy *T* is measured with a Seapoint turbidity meter, which represents a relative measurement of the particulate VSF integrated between 15° and 150° scattering angles at a wavelength of 880 nm. While the shape of the VSF is known to vary little in the backward direction (Sullivan and Twardowski 2009), the wide solid angle of the Seapoint turbidity meter also includes forward scattering angles so that large relative differences between Seapoint *T* and b_{bp} are expected due to changes in particle size, shape, and composition.

In-situ measurements of the particulate VSF of Sullivan and Twardowski 2009; Twardowski et al. 2012) recorded with the WET Labs MASCOT instrument (λ=658 nm) in a wide range of coastal and offshore waters are used here to investigate the variability between SEVIRI *T* (i.e. b_{bp}) and SmartBuoy/Seapoint *T*. Figure 5.10 shows the relationship and regression between 15°-150° angular integration[1] of the VSF and b_{bp}. This variability of about a factor 2 is caused by changes in particle size, shape, and composition, which are known to occur on time scales of a few hours (Verney et al. 2011).

It is expected that the dispersion between SEVIRI *T* and SmartBuoy *T* will decrease when a turbidity meter with a narrower solid angle in the back direction, such as for example the D&A Tech optical backscatter instruments (OBS-3, FOBS-7), is used for validation (see Downing 2006 for a comprehensive overview of instrument characteristics). In fact, skipping all go-betweens, one could

[1] No angular response function of the Seapoint turbidity instrument is available, so it was set to 1 for 15-150° and 0 elsewhere.

validate SEVIRI backscattering products with in-situ measurements of the backscattering coefficient at red wavelengths, with *a posteriori* conversion to [SPM], turbidity, or light attenuation.

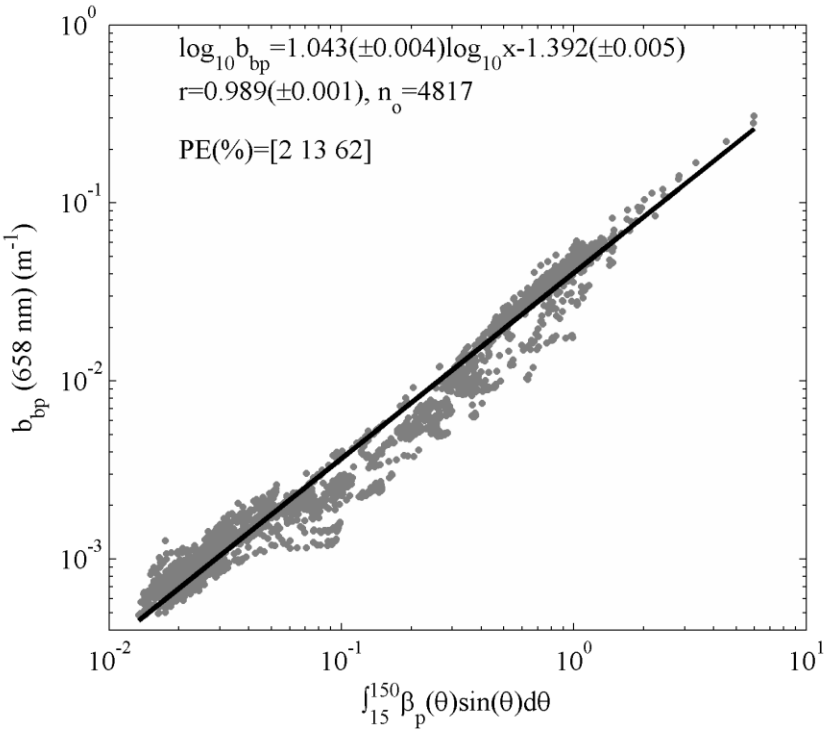

Figure 5.10. Scatter plot and regression analysis of the particulate backscattering coefficient vs. simulated SmartBuoy turbidity (scattering between 15° and 150°) obtained from in-situ measurements with the WET Labs MASCOT instrument (λ=658 nm, Sullivan and Twardowski 2009) collected in a wide diversity of coastal and offshore waters.

5.4.4.2 REMOTELY SENSED VS. IN-SITU K_{PAR}

Differences between remotely sensed K_{PAR} and in situ K_{PAR} can be caused by differences in the thickness and depth of the water layer considered for deriving K_{PAR}. The SmartBuoy K_{PAR} is obtained from PAR measurements at 1 m and 2 m depth, while the thickness of the remotely sensed layer varies with water clarity and with the wavelength of the light considered. For a vertically homogenous water column, approximately 90% of the marine reflectance at a given wavelength is derived from a layer between the surface and depth K_{PAR}^{-1} (Gordon and McCluney 1975). From inversion of SmartBuoy K_{PAR}, this results in K_{PAR} remote sensing contributions of a layer of water of 3m±1m deep at D and of 1.1m±1.0m at TH1, on average. Although K_{PAR} may be depth dependent (Lee 2009), an average PAR attenuation coefficient, $\overline{K}_{PAR}$, is usually derived from a water layer extending from the surface down to the euphotic depth,

where PAR has dropped to 1% of its surface value (Morel 1988; Kirk 1996; Kirk 2003). Therefore, the SEVIRI derived K_{PAR} represents the mean PAR attenuation in the euphotic zone.

5.4.5 Perspectives for the design of future geostationary sensors and synergy with polar-orbiting sensors

It is shown here that the SEVIRI sensor can be used to estimate T and K_{PAR} in the turbid waters of the southern North Sea and their tidal variability for the first time from space. However, this meteorological sensor was not designed for ocean remote sensing and hence its ocean application has a number of limitations, as shown in this study. Future geostationary ocean colour sensors should have (i) better spectral resolution, e.g over 16 bands in the visible and NIR spectral domain instead of two for SEVIRI (VIS06 and VIS08), (ii) finer digitization and better SNR for observation of dark targets like the ocean, and (iii) higher spatial resolution, possibly by the use of mixed resolution broad/narrow bands (mimicked here by the VIS06/HRV combination).

For Chl *a* estimation, the atmospheric correction for blue bands will be particularly difficult, especially for the high air masses encountered at high latitudes by geostationary remote sensing. The use of a geosynchronous orbit (IOCCG 2012) may mitigate this slightly but at the cost of a varying viewing geometry.

While the current paper demonstrates remote sensing of tidal variability associated with SPM, many other high frequency processes become potentially amenable to remote sensing by a geostationary ocean colour sensor, including diurnal variability of photosynthetic processes, bidirectionality of aerosol or hydrosol particulate scattering (via sun variation in day, for stable conditions), diurnal migration of certain algal species, etc (IOCCG 2012). These new processes add to the obvious practical advantage of better coverage from high temporal frequency data in regions or periods of scattered clouds. Finally, it is probable that entirely new ways will be found to process high frequency ocean colour data, where the current pixel-by-pixel approach may be supplemented by consideration of temporal coherency of data in analogy to approaches already explored in atmospheric remote sensing (Kaufman et al. 1997).

The synergy between polar-orbiting and geostationary sensors still needs to be investigated with the aim of exploiting the advantages of each orbit: the higher spatial resolution and better atmospheric correction of polar-orbiters, especially for high latitudes and the higher frequency of geostationary-orbiters. In the context of the current paper, a potential synergy would be to use background information on CDOM and Chl *a* concentration and higher spatial resolution information on SPM from polar-orbiters, modulated by the high frequency variability of SPM observed here by SEVIRI. This could further be combined with a geostatistical cloud-filling and outlier detection approach, similar to that of Sirjacobs et

al. 2011, to give unprecedented details of spatio-temporal variability of PAR attenuation for the forcing of ecosystem models.

5.5 Conclusion

This study illustrates the potential of the geostationary SEVIRI weather satellite sensor for mapping of turbidity, *T*, and vertical attenuationof photosynthetically active radiation, K_{PAR}. Based on numerous match-ups from a two year archive of SEVIRI imagery and half-hourly *T* and K_{PAR} data from a system of moored buoys (SmartBuoys), good correspondence was found, with 80% of SEVIRI derived *T* and K_{PAR} being within 53% and 39% of SmartBuoy *T* and K_{PAR}, respectively. Uncertainties on marine reflectance due to digitization and atmospheric correction were considered. For SEVIRI, the former was identified as the main source of uncertainty. A methodology was developed to improve the spatial resolution using the finer spatial information from a panchromatic band, but applicability to SEVIRI's HRV is limited by its poor geolocation and low SNR. During cloudfree periods diurnal variability of *T* and K_{PAR} is detected by SEVIRI and comparison with SmartBuoy time series shows that the signals are in phase with an average difference in the timing of the maximum *T* and K_{PAR} of 11 minutes and 23 minutes, respectively. This diurnal variability of *T* and K_{PAR} is now detected from remote sensing for the first time, offering new opportunities for improving ecosystem models and monitoring of turbidity.

The limitations of this study have also been clearly identified and include: the limited spectral and spatial resolution of SEVIRI, poor digitization of SEVIRI, limitations in usage of the HRV band, limitations of the remote sensing retrieval algorithms for *T* and K_{PAR}, as well as incommensurability between in-situ and remotely sensed *T* and K_{PAR}. In fact, when considering all these difficulties it is perhaps surprising that any useful marine information at all can be retrieved from a meteorological sensor designed to look at clouds, a much brighter target. However, the information on tidal variability of *T* and K_{PAR} presented here is clearly a significant improvement on the aliased information that is provided by MODIS and MERIS and that is already being used in both monitoring and modeling applications. The present study provides a glimpse of what will become possible when dedicated geostationary ocean colour sensors become operational and provides some first hints on the methodological challenges and opportunities that they will raise.

5.6 Appendices

5.6.1 Calibration dataset for turbidity and [SPM] retrieval algorithms

Simultaneous in-situ measurements of [SPM] and marine reflectance have been recorded by MUMM since 2001, mainly in the southern North Sea. Since 2007 measurements of *T* with a portable Hach

turbidity meter (described in section 2.2.2) are also recorded. Marine reflectance is derived from hyperspectral above-water radiance and irradiance measurements recorded with a set of TriOS Ramses radiometers as described in Ruddick et al. 2006. The entire database contains 846 records and has been used for algorithm validation and calibration (Ruddick et al. 2008; Nechad et al. 2009; Nechad et al. 2010; Dogliotti et al. 2011; Vantrepotte et al. in press). Here we discuss details on the calibration of *T* and [SPM] retrieval algorithms from the SEVIRI VIS06 band given in Eq. (5.1).

5.6.1.1 DATA COLLECTION, TREATMENT, AND SELECTION

A subset of the in-situ measurements database was used for the simultaneous calibration of T and [SPM] algorithms. This subset comprised 383 concomitant measurements of marine reflectance, *T*, and [SPM] collected between 2007 and 2010 in the southern North Sea. In June 2008, the sample mixing method for [SPM] measurement was changed from mixing by hand to mixing by tumbling (see Chapter 2 for details). This resulted in higher quality measurements of [SPM], especially in clear waters as shown in the scatter plot of *T* vs. [SPM] in Figure 2.5(b) and reproduced for this data subset in Figure 5.11. Note the slope near 1 and zero offset of the regression line between *T* and [SPM] for the tumble mix data, compared to their values for the hand mix dataset. The use of *T* to quality control [SPM] is also exploited here: measurements outside the 90% prediction bounds of the tumble mix dataset were rejected (see Figure 5.11), as well as measurements where the difference between turbidity recorded before and after filtration was over 50%. From the remaining 325 [SPM]-*T* quality controlled measurements, marine reflectances collected in homogeneous skies (either sunny or completely overcast) and low wind speed (*W*) conditions, and with small deviation from the time-averaged mean reflectances were retained. More specifically, the following marine reflectance criteria were implemented:

$$\begin{cases} \dfrac{L_{sky}^{0+}(750)}{E_d^{0+}(750)} < 0.05 \text{ or } \dfrac{L_{sky}^{0+}(750)}{E_d^{0+}(750)} > 0.3 \\ W < 10 \text{ m s}^{-1} \\ \dfrac{d\rho_w^{0+}(780)}{\rho_w^{0+}(780)} < 0.25 \\ \dfrac{d\rho_w^{0+}(\lambda)}{\rho_w^{0+}(\lambda)} < 0.50 \;\; \forall \lambda \in [400,900] \text{nm} \end{cases} \tag{5.12}$$

Note that these criteria are less stringent than those for optimal reflectance measurements set-up by Ruddick et al. 2006 in order to remain with a sufficiently large dataset: completely overcast sky measurements are also included here and deviations from the time-averaged mean reflectances at 780nm

up to 25% were allowed instead of 10%. The 68 remaining hyperspectral measurements of $L_w^{0+}(\lambda)$ and $E_d^{0+}(\lambda)$ were then band-integrated according to Eq. (4.11) to give $\rho_w^{0+(0.6)}$.

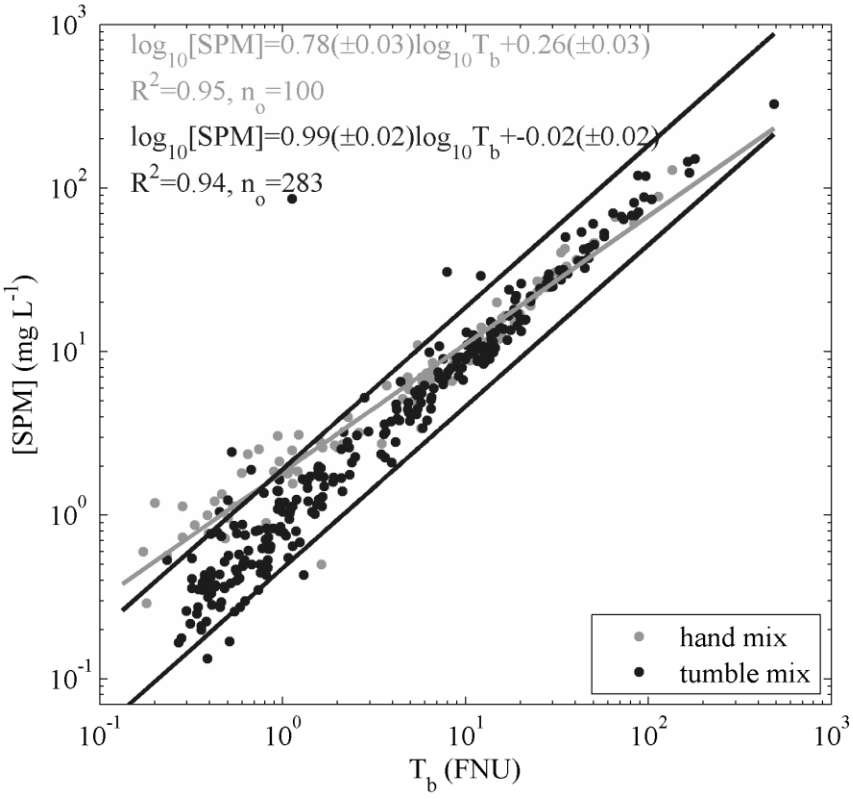

Figure 5.11. Relationship between [SPM] and turbidity recorded before filtration (T_b) for the hand mix and tumble mix dataset. Black lines denote the 90% prediction bounds of the [SPM] vs. T_b relationship for the tumble mix dataset, outside which data were rejected. The regression line equations and statistics are also shown, with n_0 denoting the number of observations and R^2 the coefficient of determination.

5.6.1.2 IMPACT OF [SPM] MEASUREMENT IMPROVEMENT ON THE [SPM] RETRIEVAL ALGORITHM

The [SPM] retrieval algorithm of Nechad et al. 2010 of the form (5.1) was fitted to quality controlled in-situ measurements collected in 2007-2010 (68 observations selected as described above) to give A_S= 37.1±5.7 mg L^{-1} and B_S= -0.17±1.4 mg L^{-1}. The algorithm was previously fitted (Neukermans et al. 2009) to in-situ measurements collected between 2001 and 2006 giving a similar asymptote, A_{S01}= 38.02±3.1 mg L^{-1}, but a much larger offset, B_{S01}= 2.32±1.6 mg L^{-1}. Both algorithms and in-situ data are shown in Figure 5.12. In theory, particle-free waters with [SPM]=0 mg L^{-1} would have a non-zero reflectance due to the backscattering of pure water and bubbles. Radiative transfer simulation for pure sea water with

Hydrolight gives $\rho_w^{0+(0.6)}$ =0.00029, implying a theoretical offset of B_S =-0.07 mg L^{-1}. This illustrates the much better closure between theory and in-situ measurement in the 2007-2010 dataset due to a simple change in the [SPM] measurement protocol, which resulted in higher quality [SPM] measurements.

Because both algorithms are applied without the offset, the actual differences between them are very small, with the 2007-2010 algorithm giving [SPM] values that are lower by 4% to 7% over the [SPM] range 0 to 100 mg L^{-1}.

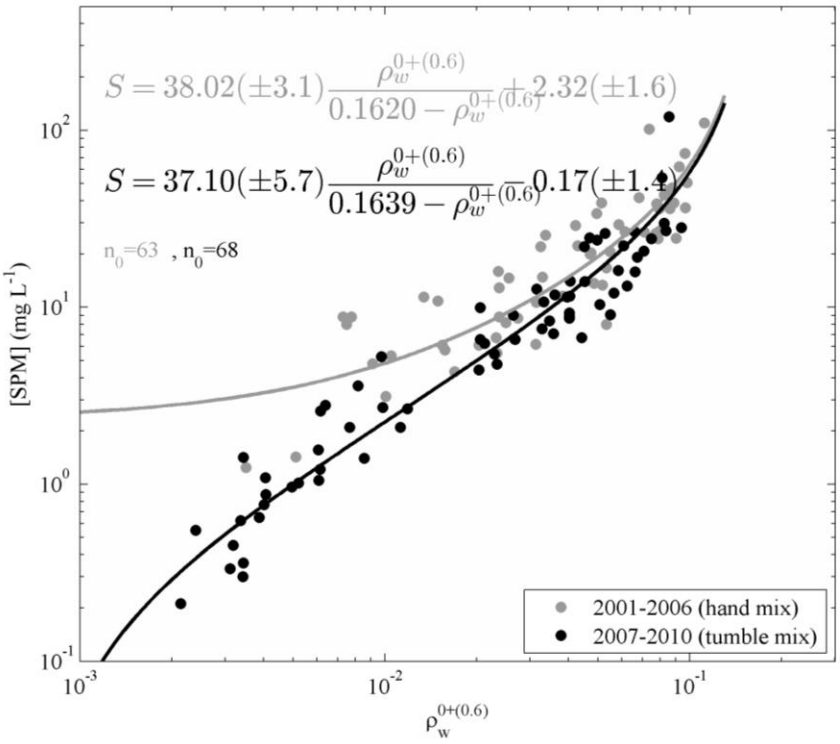

Figure 5.12. SEVIRI VIS06 single band [SPM] retrieval algorithm calibrated with datasets collected in the southern North Sea during the periods 2001-2006 and 2007-2010.

5.6.2 Variability of turbidity-specific backscattering

The single band retrieval algorithms for *T* (Nechad et al. 2009) and [SPM] (Nechad et al. 2010) are based on the assumption that *T*- and [SPM]-specific particulate backscattering coefficients (b_{bp}), respectively, are constant. In analogy with the study of natural variability of [SPM]-specific backscattering in Chapter 3, the variability of *T*-specific particulate backscattering (=b_{bp}:*T*) is investigated using the same dataset and methodology. Figure 5.13 (a) shows a scatter plot of all available in situ *T* and b_{bp} data (n=251). *T* and b_{bp} are well correlated with a correlation coefficient of 0.987±0.004 and the fitted log-log regression has a median prediction error (MPE) of 16%. Results of the correlation and regression analysis of b_{bp}:*T* vs.

mean particle diameter (D_A), mean apparent density (ρ_a), and particle composition on the same data subset as described in Chapter 3 are shown in Table 5.2. The median b_{bp} to T ratio is 0.0089, with 90% of the ratios between 0.0045 and 0.0135 m^{-1} FNU^{-1}, giving a factor 3 variability in b_{bp}:T. A similarly small range of variability in b_{bp}:[SPM] was found (a factor 3-4). For pooled clear (case 1) and turbid (case 2) waters b_{bp}:T is statistically significantly correlated with ρ_a, D_A , and particle composition (expressed as the ratio of particulate organic carbon concentration, POC, to total carbon concentration, POC+PIC). The highest amount of variability (32%) is explained by the latter, with inorganic particles having b_{bp}:T coefficients that are about 2 times higher than for organic particles (see Figure 5.13 (b)).

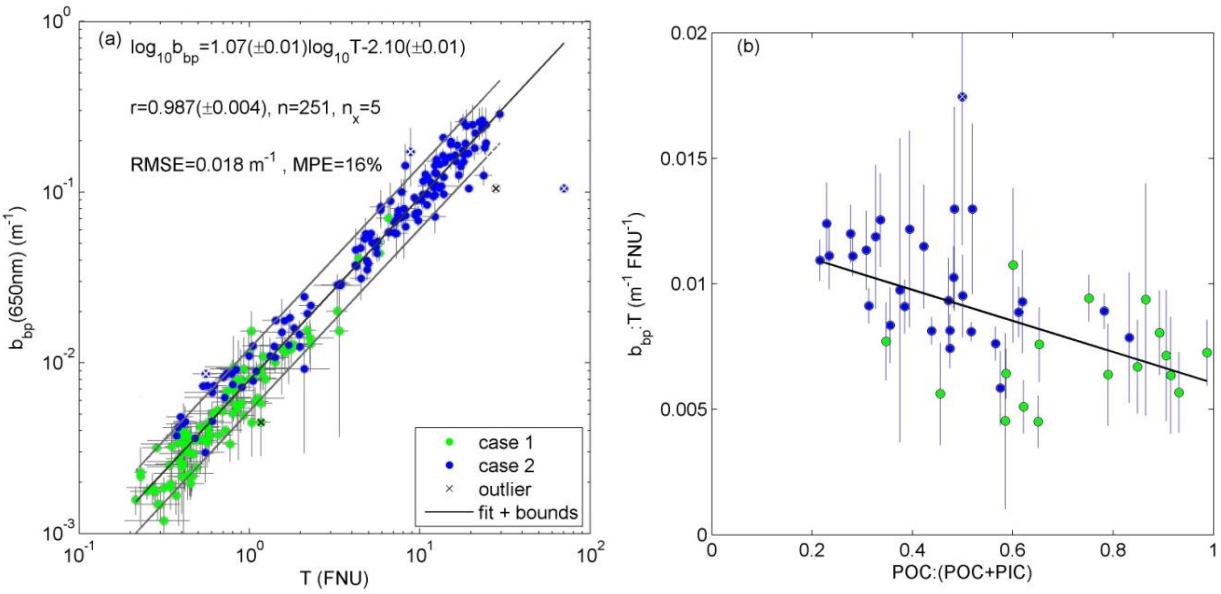

Figure 5.13. (a) Relationship between the particulate backscattering coefficient, b_{bp} (λ=650nm), and turbidity in clear (case 1) and turbid (case 2) waters. The regression line with its 90% confidence bounds in log-log scale and statistics are shown (MPE= median *PE*). (b) Variability of *T*-specific b_{bp} as a function of particle composition. The fitted regression and statistics can be found in. See also Chapter 3 for details on in situ measurement and data treatment.

Table 5.2. Correlations and regression analysis of turbidity-specific backscattering vs. mean particle diameter (D_A), mean apparent density (ρ_a), and particle composition. ns: not significant (i.e., p>0.05), *: p<0.001, n_o is the number of observations, n_x is the number of outliers removed as described in section 3.5.1.3

x	case	n_o	n_x	r	equation (units: m^{-1} FNU^{-1}), RMSE, MPE(%)
ρ_a	1	35	0	0.43±0.34	-
(kg L^{-1})	2	72	2	ns	-
	1+2	107	3	0.27±0.17*	0.013(±0.002) x +0.0052 (±0.0005),0.0029,19
D_A	1	35	0	ns	-
(μm)	2	72	3	0.59±0.17*	0.00006(±0.00002) x +0.0075(±0.0004),0.0019,11
	1+2	107	4	0.32±0.17*	0.00004(±0.00002) x +0.0077(±0.0004),0.0023,15
[POC]:	1	17	0	ns	-
([POC]+[PIC])	2	30	1	-0.52±0.22*	-0.007(±0.002) x +0.013(±0.001),0.0017,12
	1+2	47	1	-0.57±0.17*	-0.006(±0.001) x +0.012(±0.001),0.0019,14
[POM]:	1	5	0	-0.70±0.28*	-0.0014(±0.0023) x +0.003(±0.001),0.0087,73
SPM	2	17	0	ns	-
	1+2	22	1	ns	-

The factor 3-4 variability in b_{bp}:b_s obtained with the WET Labs BB-9 and the Hach turbidity instrument observed here may seem surprisingly high at first sight. Indeed, from in-situ VSF measurements with the WET Labs MASCOT instrument (Sullivan and Twardowski 2009) collected in a wide range of water types, β_p(120°,658 nm): β_p (90°,658 nm) is expected to vary by a factor 1.7 at the very most (a factor 1.20 being more typical). The much higher variability of b_{bp}:b_s obtained with the in-water BB-9 and the portable Hach turbidity instruments suggests that subsampling uncertainties may be high, that sampling volume may be important, that the spectral shape of side scattering varies considerably between 658 nm and 880 nm, or that the variability of β_p(120°,658 nm): β_p (90°,658 nm) is underestimated by the MASCOT instrument.

5.6.3 Uncertainties of the *T* and [SPM] retrieval algorithms

5.6.3.1 VARIABILITY OF THE MASS- AND TURBIDITY-SPECIFIC BACKSCATTERING COEFFICIENT

Nechad et al. 2010 suggested that the main source of error in the retrieval algorithms for [SPM] and *T* is the variability of the mass- and *T*-specific backscattering coefficients, respectively. For the [SPM]

algorithm, a constant mass-specific coefficient, denoted b_{bp}^{m}, of 0.01 m^2g^{-1} was assumed at 488 nm with "average" spectral variations as of $b_p(\lambda)$ in Babin et al. 2003. For 41 out of 68 observations used to calibrate the algorithm, b_{bp} data are also available giving $b_{bp}^{m}(488nm)$[2] between 0.004 and 0.017 m^2g^{-1} with a mean value of 0.011 m^2g^{-1}. Figure 5.12 (left) shows the [SPM] algorithm with measurement uncertainties of in-situ [SPM] (derived from triplicates) and marine reflectance (derived from variability during a 10 minute record), colour coded according to $b_{bp}^{m}(488nm)$. The uncertainties on the measurements themselves are quite small, due to careful selection of reflectance data and increased quality of [SPM] measurements, even in clear waters. Figure 5.12 further shows that much (r=0.72±0.19) of the scatter in the [SPM] algorithm can be attributed to variations in b_{bp}^{m}, with model overestimates for b_{bp}^{m} higher than the assumed value and model underestimates for b_{bp}^{m} lower than the assumed value. It was shown in Chapter 3 that b_{bp}^{m} is driven by changes in particle composition, with lower values for organic particles. This indicates that [SPM] retrieval algorithms can significantly be improved if the composition of the suspended particles is known.

For very turbid waters such as most of the Guyana coastal waters, the SEVIRI VIS06 [SPM] algorithm is pushed to its non-linear regime, where it is less reliable. It is therefore recommended to apply an [SPM] or *T* algorithm calibrated for the VIS08 band, and implement an iterative loop so that also the σ atmospheric correction calibration parameter can be taken out of its linear range.

[2] A wavelength of 488nm was chosen here to maximize the number of valid b_{bp} data. At 650 nm for example, the backscatter instrument saturated at 4 stations, reducing the number of available data points to 37.

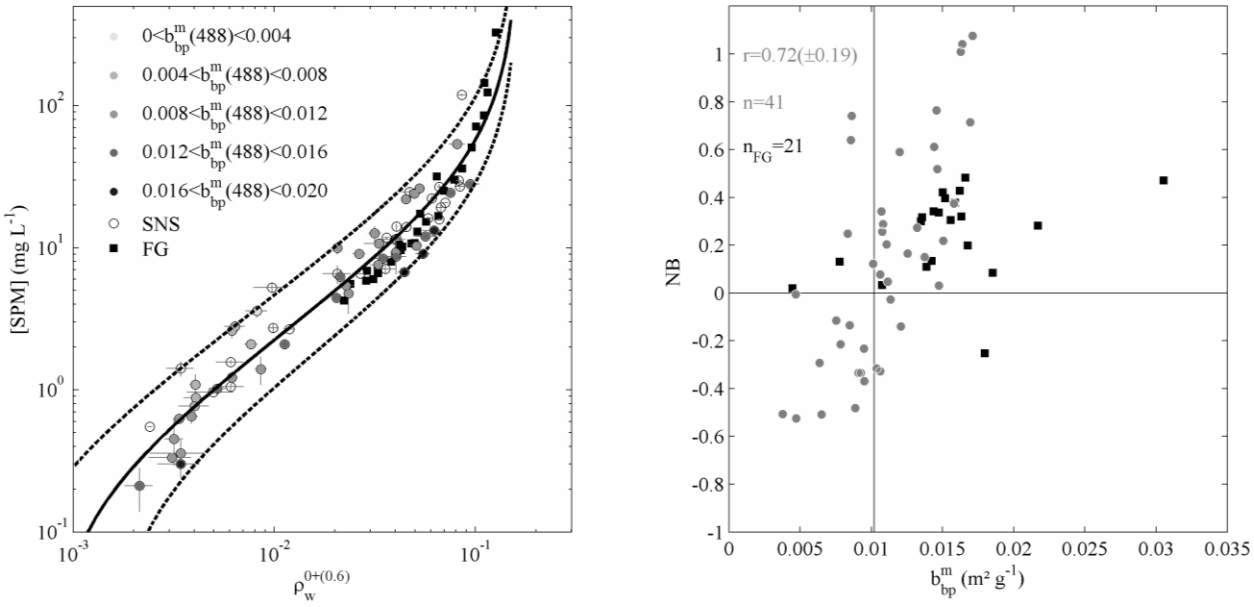

Figure 5.14. Influence of the variability of the mass-specific backscattering coefficient, b_{bp}^{m}, on the suspended matter retrieval algorithm of Nechad et al. 2010 for the SEVIRI VIS06 band, calibrated with southern North Sea (SNS) in-situ data (solid black line). (left) Dashed lines represent the [SPM] algorithm corresponding to a factor 4 variability in A_s. Error bars indicate measurement uncertainties. French Guyana (FG) data are also shown. (right) relationship between b_{bp}^{m} and the normalized bias of the [SPM] algorithm for SNS (grey dots) and FG data (black squares).

5.6.3.2 REGIONAL CALIBRATION

The natural variability of b_{bp}^{m} (and a_{p}^{m}) is accounted for through calibration of the A coefficient by non-linear regression and depends on the in situ dataset. It can be questioned whether this algorithm, calibrated with North Sea data, can be applied elsewhere. We therefore tested its applicability in French Guyana waters using in-situ measurements collected in October 2009 following the same measurement protocols. For all 16 observations in the linear regime, i.e., $\rho_w^{0+(0.6)}$ <0.06, where this algorithm is optimally applied, the North Sea algorithm overestimates [SPM] by 2% to 50% (median of 32%), due to the much higher b_{bp}^{m}(488nm) in French Guyana waters. We therefore recommend that the [SPM] algorithm of Nechad et al. 2010 be calibrated regionally. Likewise for the *T* algorithm.

5.6.4 Coupling between turbidity and hydrodynamics

An attempt was made to investigate the coupling between hydrodynamic parameters and the temporal dynamics of turbidity. At 18 selected stations, time series of hydrodynamic parameters such as bottom stress, current velocity, and tidal amplitude were extracted from the COHERENS 3D hydrodynamical

model of Lacroix et al. 2007. Modeled hydrodynamic data are available every 15 minutes in 5 km x 5 km grid cells.

SEVIRI *T* time series were selected as described in section 5.2.3.3 on page 150. Some example time series for bottom stress at P2 (see Figure 4.16 for location) are shown in Figure 5.15. Next, the timing of maximum *T* from SEVIRI was compared to the timing of maximum bottom stress during cloudfree periods. Some examples for bottom stress at P1 and P2 are shown in Figure 5.16. The observed mean and standard deviation of the phase difference, median and 5^{th}-95^{th} percentile interval for bias were computed and compared against values obtained for a random timing of maximum bottom stress. Results show that the observed phase differences of 3.4 h ±1.5 h at P1 and 3.1 h ±1.8 h at P2 are not different than one would expect from random chance. Similar results were obtained for all other stations and other hydrodynamic parameters, suggesting that temporal turbidity dynamics may not be governed by currents and tides alone.

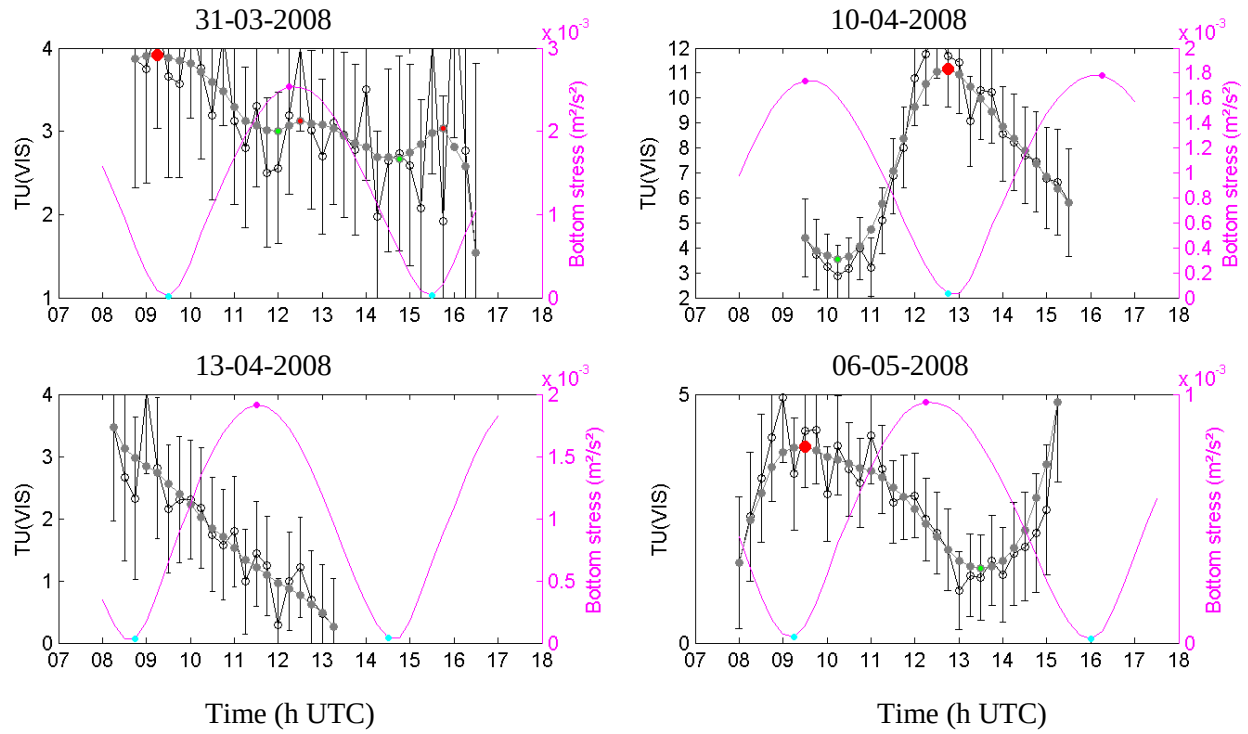

Figure 5.15. Some selected time series of *T* from SEVIRI on the VIS06 grid and modelled bottom stress at P2 (see Figure 4.16 for location). Global maxima are indicated by the large red dots, small dots indicate local maxima (red) and minima (green). Errorbars denote uncertainties on *T* after Eq. (5.2).

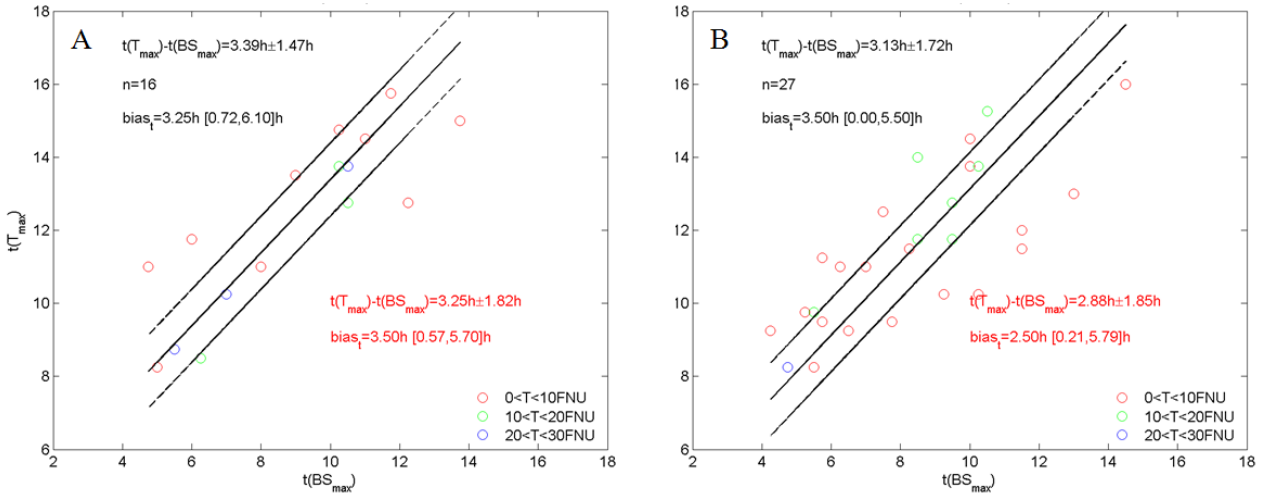

Figure 5.16. Scatterplot of the timing of maximum *T* from SEVIRI vs. timing of maximum bottom stress during cloudfree periods at P1 (A) and P2 (B) with location given in Figure 4.16. The 1:1 line (solid) and 1 hour offset lines (dashed) are shown in black. The observed mean and standard deviation of the phase difference, median and 5th-95th percentile interval for bias are shown in black. The red numbers refer to the same statistics obtained for a random timing of maximum bottom stress.

Chapter 6 GENERAL CONCLUSIONS AND PERSPECTIVES

This work contributes to the study of suspended particles in coastal waters by offering unprecedented remote sensing of their diurnal variability and by characterizing the in-situ variability of the particulate beam attenuation and backscattering coefficient. Below, are the main findings, perspectives, and limitations of each study and some reflections on the way forward.

6.1 In-situ variability of scattering properties and suspended matter concentration

Summary: We analyzed relationships between concentration of suspended particles represented by dry mass, [SPM], or area, [AC], and optical properties including particulate beam attenuation (c_p), side scattering (b_s), and backscattering (b_{bp}). An extensive dataset combining optical properties, measurements of particle concentration, size distribution, apparent density, and composition was acquired in coastal and offshore waters around Europe and French Guyana. We showed that, first order variability of optical properties is driven by particle concentration with best predictions of [SPM] by b_{bp} and b_s, and of [AC] by c_p. Second order variability of b_{bp} to [SPM] is relatively small, with variability of a factor 3-4, influenced by particle composition. Second order variability of c_p to [SPM], on the other hand, spans over one order of magnitude and is strongly driven by particle apparent density. In this dataset no effect of particle size on mass-specific optical properties was found, despite size variations over one order of magnitude. We further investigated uncertainties in the gravimetric measurement procedure of [SPM] and suggested the use of simple, fast, and low-cost measurements of turbidity (b_s) to optimize and quality control [SPM].

Limitations: A significant fraction of the variability in mass-specific b_{bp} remains unexplained. Possible causes are the limitation of the measured size distributions to the 2-302 μm range and effects of particle shape and internal structure which affect b_{bp} more than c_p and were not accounted for.

Relevance: This study offers new insights into the sources of optical variability in natural waters and contributes to the in-situ monitoring of suspended particles and the development of remote sensing algorithms for suspended matter concentration and turbidity.

Perspectives: To advance our understanding of optical variability in the natural environment, new experimental as well as theoretical developments are needed. For instance, the acquisition of particle size distributions covering the full optically significant size range will increase our understanding of the role of particle size. First results on the counting and sizing of colloidal particles smaller than 1 μm in the natural environment based on Brownian motion are promising (Tatarkiewicz et al. 2012). In-water digital holographic particle imaging sensors, such as Sequoia's LISST-HOLO operating over the 25-2500 μm size range, have become available recently (Graham and Smith 2010; Davies et al. 2011) and research is

ongoing for extension of these systems into the sub-micron range. The majority of theoretical investigations on the IOPs of marine particles are based on Mie theory, which assumes that particles are homogeneous spheres. There is strong evidence that application of this model is inappropriate for computations of backscattering for natural particles (Bohren and Singham 1991;Kitchen and Zaneveld 1992; Clavano et al. 2007; Hedley 2011), presenting new challenges (need for new models), and opportunities (extract information on particle shape from polarimetry).

6.2 Remote sensing of diurnal variability of suspended particles from the geostationary SEVIRI meteorological sensor

Summary: While we eagerly await the launch of the first European geostationary ocean colour sensor into space, we investigated the potential for the mapping of suspended matter concentration and related parameters in the southern North Sea with the geostationary SEVIRI meteorological sensor. First, an atmospheric correction of SEVIRI's red waveband was developed and applied to a two-year image archive. Cross-validation with MODIS Aqua marine reflectance imagery showed good spatial and quantitative correspondence. Next, single-band retrieval algorithms for turbidity (T) and vertical attenuation of photosynthetically active radiation (K_{PAR}) were applied. Half-hourly in-situ data of T and K_{PAR} recorded by a system of moored buoys were used for validation of corresponding SEVIRI products. We showed that SEVIRI T and K_{PAR} products are in good agreement with buoy data, and that on cloudfree days, the SEVIRI T and K_{PAR} signals are in phase with in-situ time series. Uncertainties on SEVIRI products due to digitization, atmospheric correction, and retrieval algorithms were assessed, which effectively confine marine remote sensing by SEVIRI to waters with turbidity ranging between 1 and 35 FNU (same range for [SPM]).

Limitations: Because SEVIRI is a meteorological sensor with visible bands designed to monitor clouds and ice, much brighter targets than the sea, the limitations of SEVIRI for marine applications are numerous: poor digitization, low signal-to-noise ratio and limited spectral and spatial resolution. Attempts to improve the spatial resolution from 3 x 6 km² to 1 x 2 km² using the finer spatial information from SEVIRI's panchromatic band failed, mainly due to its poor geolocation and low signal-to-noise ratio. Further uncertainties arise from the remote sensing retrieval algorithms for T and K_{PAR}, as well as incommensurability between in-situ and remotely sensed T and K_{PAR}.

Relevance: In cloudfree conditions, the tidal variability of suspended matter concentration and covarying parameters (T and K_{PAR}) in the southern North Sea can now be mapped by remote sensing for the first time, offering new opportunities for improving ecosystem models and monitoring of turbidity. This is clearly a significant improvement on the aliased information that is provided by polar-orbiting ocean colour satellites that are already being used in monitoring and modeling applications. Data availability

significantly increased during periods of scattered clouds. This work provides a glimpse of what will become possible when dedicated geostationary ocean colour sensors become operational over Europe and provides some first hints on the methodological challenges and opportunities that they will raise.

Perspectives: The first geostationary ocean colour sensor, GOCI, was launched by the Korean space agency in June 2010. First results seem very promising (Figure 6.1) and it seems to be only a matter of time before the American and European space agencies launch geostationary ocean colour satellites covering other oceans and seas. Meanwhile, it may be worth testing the application of the methodology developed for SEVIRI in the southern North Sea to other sufficiently turbid waters on the SEVIRI full disk (identified in Figure 4.22) and to other geostationary meteorological satellites with spectral characteristics similar to SEVIRI (*see* Table 6.1 for an overview), such as the Multichannel Scanning Unit (MSU) on the Russian Electro-L1 satellite platform[3]. Figure 6.2 shows areas where MSU might be suitable for marine application following an approach similar to the one developed in this work for SEVIRI. Besides mapping [SPM] in turbid waters, these geostationary meteorological satellites may also successfully map coccolithophore blooms (Holligan et al. 1983; Balch et al. 1991), such as previously demonstrated with AVHRR (Ackleson and Holligan 1989), a polar-orbiter with similar spectral resolution.

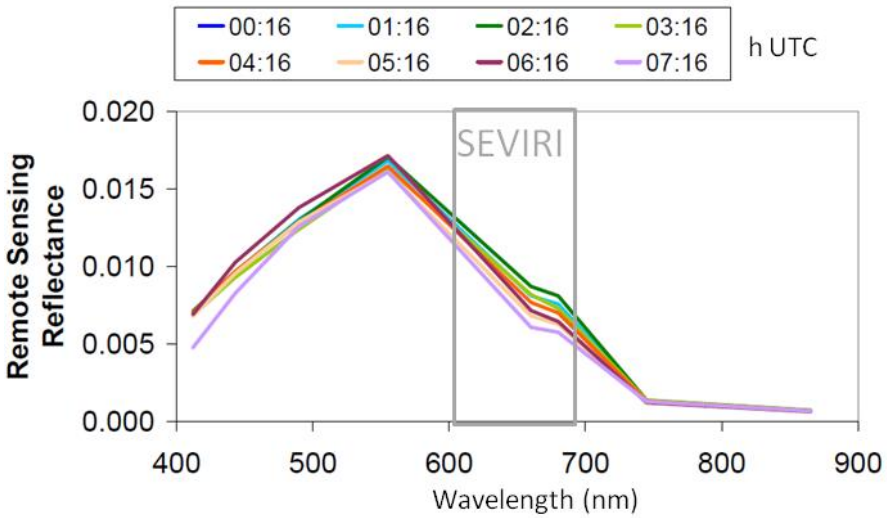

Figure 6.1. Diurnal variability of remote sensing reflectance (R_{rs}) in the VIS and NIR as recorded by GOCI on 13 June 2011 at a station in the Bohai Sea (source: Ruddick et al. submitted). SEVIRI's red band approximate spectral coverage is also shown.

[3] Most meteorological sensors have only one band in the red or NIR, followed by bands in the SWIR or thermal infra-red, making atmospheric correction difficult, but perhaps not impossible.

Table 6.1. Overview of spatial, spectral, and temporal resolutions of geostationary meteorological satellites currently operational and planned in the near-future with spectral characteristics similar to or better than SEVIRI (summarized from http://goes.gsfc.nasa.gov/text/geonews.html#GOMS)

Sensor	SEVIRI (prime service)	FCI	MSU	AGRI
Satellite	MSG, Meteosat-8/9	MTG-I	Elektro-L1	Feng-Yun-4
Agency	EUMETSAT (Europe)	EUMETSAT (Europe)	(Russia)	(China)
Operational period	2004-May 2007/ May 2007-present	>2017	Feb 2011-present	>2014
Spatial resolution	1 km/ 3 km	0.5 km/1 km	1 km	0.5 km/ 1km
Spatial coverage	Europe-Africa *See* Figure 6.2	Europe-Africa	Indian Ocean *See* Figure 6.2	Indian-Pacific Ocean
Longitude	3.5° W/0° E	around 0°	76° E	86.5° E - 123.5°E
VIS-NIR-SWIR bands (μm)	0.6-0.7, 0.76-0.82, 1.57-1.72	0.4, 0.5, 0.6, 0.8, 0.9, 1.3, 1.6	0.50-0.65, 0.65-0.80, 0.80-0.90,	0.45-0.49, 0.55-0.75, 0.75-0.90
Repeat viewing frequency	15 min	10 min (2.5 min for Europe)	30 min	

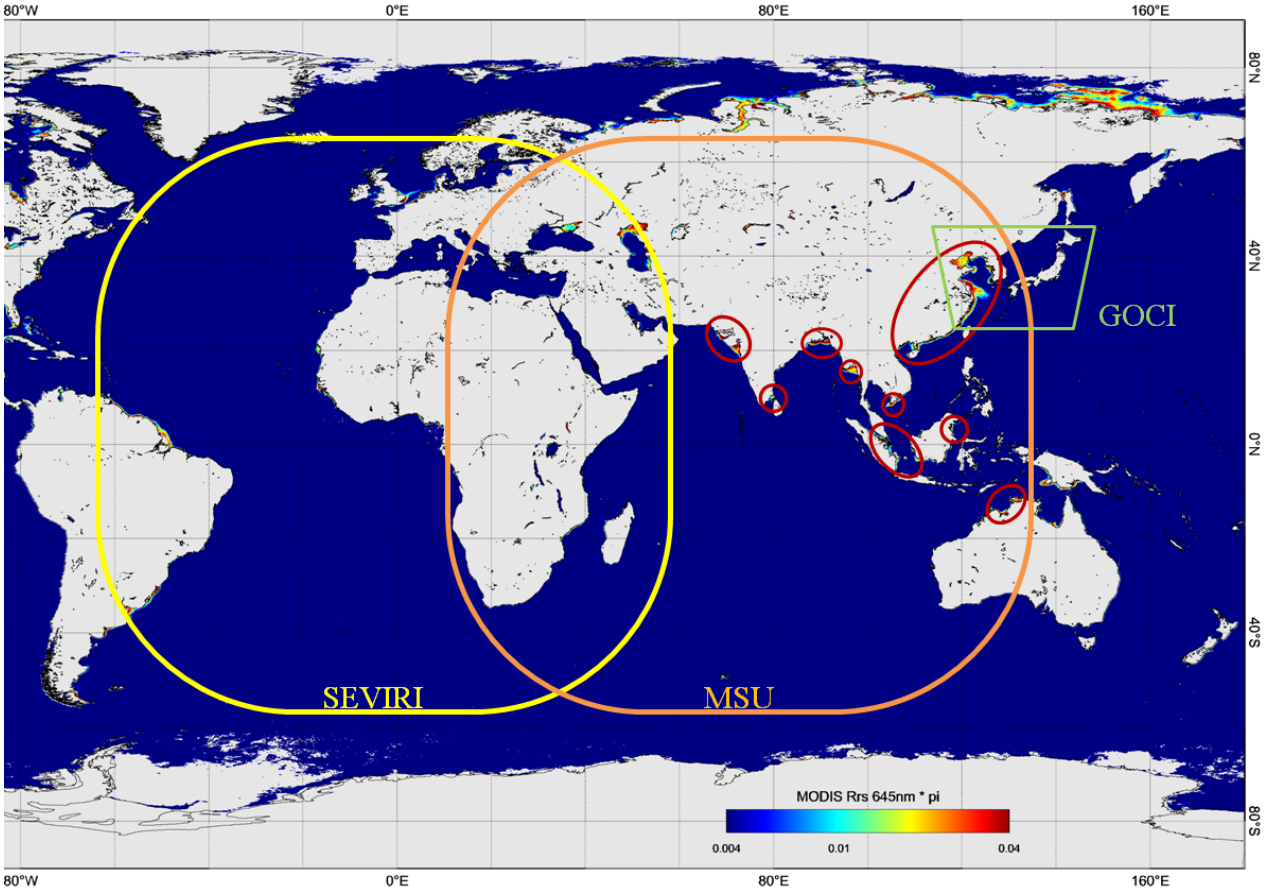

Figure 6.2. MODIS 2009 climatology of marine reflectance at 645 nm. Spatial coverage of MSG-SEVIRI, Electro-MSU, and COMS-GOCI are shown by the yellow, orange, and green polygons, respectively. Red polygons indicate waters that are expected to be detectable by MSU.

REFERENCES

Aas, E. 1996. Refractive index of phytoplankton derived from its metabolite composition. J. Plankton Res. **18:** 2223-2249.

Ackleson, S. G., and P. M. Holligan. 1989. AVHRR observations of a Gulf of Maine coccolithophore bloom. Photogramm. Eng. Remote Sens. **55:** 473-474.

Agrawal, Y. C., and H. C. Pottsmith. 2000. Instruments for particle size and settling velocity observations in sediment transport. Mar. Geol. **168:** 89-114.

Agrawal, Y. C., A. Whitmire, O. A. Mikkelsen, and H. C. Pottsmith. 2008. Light scattering by random shaped particles and consequences on measuring suspended sediments by laser diffraction. J. Geophys. Res. Oceans **113:** C04023, doi: 04010.01029/02007JC004403.

Ahn, Y. H., A. Bricaud, and A. Morel. 1992. Light Backscattering Efficiency And Related Properties Of Some Phytoplankters. Deep-Sea Res. **39:** 1835-1855.

Alvain, S., C. Moulin, Y. Dandonneau, and H. Loisel. 2008. Seasonal distribution and succession of dominant phytoplaknton groups in the global ocean: a satellite view. Global Biogeochemical Cycles **22**. doi: 10.1029/2007GB003154

Aminou, D. M. A., B. Jacquet, and F. Pasternak. 1997. Characteristics of the Meteosat second generation (MSG) radiometer/imager: SEVIRI. Proc. SPIE - Int. Soc. Opt. Eng. (USA). Sensors, systems, and next-generation satellites. Sep. 22-25, 1997, London, United Kingdom. doi: 10.1117/12.298084

Andrews, S., D. Nover, and S. G. Schladow. 2010. Using laser diffraction data to obtain accurate particle size distributions: the role of particle composition. Limnol. Oceanogr. Meth. **8:** 507-526.

Andrews, S. W., D. M. Nover, K. E. Reardon, J. E. Reuter, and S. G. Schladow. 2011a. The influence of ambient light intensity on in situ laser diffractometers. Water Resour. Res. **47**.

Andrews, S. W., D. M. Nover, J. E. Reuter, and S. G. Schladow. 2011b. Limitations of laser diffraction for measuring fine particles in oligotrophic systems: Pitfalls and potential solutions. Water Resour. Res. **47**.

Antoine, D., colleagues from Astrium, LOV, and ACRI. 2011. HOCI: A hosted ocean colour imager on board EDRS-C. Proposal in answer to ESA call for interest on in-orbit validation of payloads hosted on-board telecommunication satellites. Ref: EB.LT.TB.11.00002.

APHA. 1998. Standard Methods for the Examination of Water and Wastewater (20th edition). American Public Health Association. L. S. Clescerl, A. E. Greenberg and A. D. Eaton. Washington, DC, USA.

Astoreca, R., D. Doxaran, K. Ruddick, V. Rousseau, and C. Lancelot. 2012. Influence of suspended particle concentration, composition, and size on the variability of inherent optical properties in the southern North Sea. Cont. Shelf Res. **35:** 117-128. doi: 10.1016/j.csr.2012.01.007

Astoreca, R., V. Rousseau, and C. Lancelot. 2009. Coloured dissolved organic matter (CDOM) in Southern North Sea waters: Optical characterization and possible origin. Estuar. Coast. Shelf Sci. **85:** 633-640.

Babin, M., A. Morel, V. Fournier-Sicre, F. Fell, and D. Stramski. 2003. Light scattering properties of marine particles in coastal and open ocean waters as related to the particle mass concentration. Limnol. Oceanogr. **48:** 843-859.

Babin, M., C. Roesler, and J. Cullen. 2008. Real-time coastal observing systems for ecosystem dynamics and harmful algal blooms. UNESCO Publishing, Paris, France,

Bailey, S. W., B. A. Franz, and P. J. Werdell. 2010. Estimation of near-infrared water-leaving reflectance for satellite ocean color data processing. Opt. Express **18:** 7251-7527.

Baker, E. T., and J. W. Lavelle. 1984. The effect of particle-size on the light attenuation coefficient of natural suspensions. J. Geophys. Res. **89:** 8197-8203.

Balch, W. M., P. M. Holligan, S. G. Ackleson, and K. J. Voss. 1991. Biological and optical properties of mesoscale coccolithophore blooms in the Gulf of Maine. Limnol. Oceanogr. **36:** 629-643.

Behnert, I., V. Matthias, and R. Doerffer. 2007. Aerosol climatology from ground-based measurements for the southern North Sea. Atmos. Res. **84:** 201-220.

Behrenfeld, M. J., and E. Boss. 2006. Beam attenuation and chlorophyll concentration as alternative optical indices of phytoplankton biomass. J. Mar. Res. **64:** 431-451.

Behrenfeld, M. J., and P. G. Falkowski. 1997. Photosynthetic rates derived from satellite-based chlorophyll concentration. Limnol. Oceanogr. **42:** 1-20.

Bohren, C. F., and S. B. Singham. 1991. Backscattering by nonspherical particles - a review of methods and suggested new approaches. J. Geophys. Res. **96:** 5269-5277.

Boss, E., and W. S. Pegau. 2001. Relationship of light scattering at an angle in the backward direction to the backscattering coefficient. Appl. Opt. **40:** 5503-5507.

Boss, E., W. S. Pegau, M. Lee, M. Twardowski, E. Shybanov, G. Korotaev, and F. Baratange. 2004. Particulate backscattering ratio at LEO 15 and its use to study particle composition and distribution. J. Geophys. Res.-Oceans **109**.

Boss, E., W. Slade, and P. Hill. 2009a. Effect of particulate aggregation in aquatic environments on the beam attenuation and its utility as a proxy for particulate mass. Opt. Express **17:** 9408-9420.

Boss, E., W. H. Slade, M. Behrenfeld, and G. Dall'Olmo. 2009b. Acceptance angle effects on the beam attenuation in the ocean. Opt. Express **17:** 1535-1550.

Boss, E. and others. 2009c. Comparison of inherent optical properties as a surrogate for particulate matter concentration in coastal waters. Limnol. Oceanogr. Meth. **7:** 803-810.

Boss, E., M. S. Twardowski, and S. Herring. 2001. Shape of the particulate beam attenuation spectrum and its inversion to obtain the shape of the particulate size distribution. Appl. Opt. **40:** 4885-4893.

Bowers, D. G., S. Boudjelas, and G. E. L. Harker. 1998. The distribution of fine suspended sediments in the surface waters of the Irish Sea and its relation to tidal stirring. Int. J. Remote Sens. **19:** 2789-2805.

Bowers, D. G., K. M. Braithwaite, W. A. M. Nimmo-Smith, and G. W. Graham. 2009. Light scattering by particles suspended in the sea: The role of particle size and density. Cont. Shelf Res. **29:** 1748-1755.

Bricaud, A., A. Morel, M. Babin, K. Allali, and H. Claustre. 1998. Variations of light absorption by suspended particles with chlorophyll a concentration in oceanic (case 1) waters: Analysis and implications for bio-optical models. J. Geophys. Res. **103:** 31033-31044, doi:31010.31029/31098JC02712.

Briggs, N., M. J. Perry, I. Cetinic, C. Lee, E. D'Asaro, A. M. Gray, and E. Rehm. 2011. High-resolution observations of aggregate flux during a sub-polar North Atlantic spring bloom. Deep-Sea Res. **58:** 1031-1039, doi: 1010.1016/j.dsr.2011.1007.1007.

Brown, C. A., Y. Huot, P. J. Werdell, B. Gentili, and H. Claustre. 2008. The origin and global distribution of second order variability in satellite ocean color and its potential applications to algorithm development. Remote Sens. Environ. **112:** 4186-4203.

Bunt, J. A. C., P. Larcombe, and C. F. Jago. 1999. Quantifying the response of optical backscatter devices and transmissometers to variations in suspended particulate matter. Cont. Shelf Res. **19:** 1199-1220.

Buonassissi, C. J., and H. M. Dierssen. 2010. A regional comparison of particle size distributions and the power law approximation in oceanic and estuarine surface waters. J. Geophys. Res. **115:** C10028.

Carder, K. L., J. Beardsley, F. George, and H. Pak. 1975. Physical, chemical and optical measures of suspended-particle concentrations: their intercomparison and application to the West African Shelf, p. 173-193. *In* R. J. Gibbs [ed.], Suspended solids in waters. Plenum.

Chen, Z., J. D. Hanson, and P. J. Curran. 1991. The form of the relationship between suspended sediment concentration and spectral reflectance: Its implications for the use of Daedalus 1268 data. Int. J. Remote Sens. **12:** 215-222.

Christian, D., and Y. P. Sheng. 2003. Relative influence of various water quality parameters on light attenuation in Indian River Lagoon. Estuar. Coast. Shelf Sci. **57:** 961-971.

Clavano, W. R., E. Boss, and L. Karp-Boss. 2007. Inherent optical properties of non-spherical marine-like particles - From theory to observation. Oceanogr. Mar. Biol. **45:** 1-38.

Costello, D. K., K. L. Carder, and W. L. Hou. 1995a. Aggregation Of Diatom Bloom In A Mesocosm - Bulk And Individual Particle Optical Measurements. Deep-Sea Research Part Ii-Topical Studies In Oceanography **42:** 29-45.

---. 1995b. Aggregation of diatom bloom in a mesocosm - bulk and individual particle optical measurements. Deep-Sea Res. **42:** 29-45.

Curran, K. J., P. S. Hill, T. G. Milligan, O. A. Mikkelsen, B. A. Law, X. Durrieu de Madron, and F. Bourrin. 2007. Settling velocity, effective density, and mass composition of suspended sediment in a coastal bottom boundary layer, Gulf of Lions, France. Cont. Shelf Res. **27:** 1408-1421.

Dall'Olmo, G., T. K. Westberry, M. J. Behrenfeld, E. Boss, and W. H. Slade. 2009. Significant contribution of large particles to optical backscattering in the open ocean. Biogeosciences **6:** 947-967.

Davies, E. J., W. A. M. Nimmo-Smith, Y. C. Agrawal, and A. J. Souza. 2011. Scattering signatures of suspended particles: an integrated system for combining digital holography and laser diffraction. Opt. Express **19:** 25488-25499.

De Paepe, B., A. Ignatov, S. Dewitte, and A. Ipe. 2008. Aerosol retrieval over ocean from SEVIRI for the use in GERB Earth's radiation budget analyses. Remote Sens. Environ. **112:** 2455-2468. doi: 10.1016/j.rse.2007.11.005

Deng, S. 2009. Findextrema.m. MATLAB script to find indices of local extrema (minina, maxima) and zero-crossings. Source: http://www.mathworks.com/matlabcentral/fileexchange/24306-findextrema

Devlin, M. J., J. Barry, D. K. Mills, R. J. Gowen, J. Foden, D. Sivyer, and P. Tett. 2008. Relationships between suspended particulate material, light attenuation and Secchi depth in UK marine waters. Estuar. Coast. Shelf Sci. **79:** 429-439.

Deyong, S., L. Yunmei, W. Qiao, J. Gao, L. Heng, L. Chengfeng, and H. Changchun. 2009. Light scattering properties and their relation to the biogeochemical composition of turbid productive waters: a case study of Lake Taihu. Appl. Opt. **48:** 1979-1989.

Doerffer, R., and J. Fischer. 1994. Concentrations of chlorophyll, suspended matter, gelbstoff in case II waters derived from satellite coastal zone color scanner data with inverse modeling methods. J. Geophys. Res. **99:** 7457-7466.

Doerffer, R., and H. Schiller. 2007. The MERIS case 2 water algorithm. Int. J. Remote Sens. **28:** 517-535. doi: 10.1080/01431160600821127

Dogliotti, A. I. and others. 2011. Calibration and validation of an algorithm for remote sensing of turbidity over La Plata River estuary, Argentina. EARSeL eProceedings (10):119–130.

Downing, J. 2006. Twenty-five years with OBS sensors: the good, the bad and the ugly. Cont. Shelf Res. **26:** 2299-2318.

Eisma, D. 1987. The North Sea: an overview. Phil. Trans. R. Soc. Lond. B **316:** 461-485.

Eisma, D., and G. Irion. 1988. Suspended matter and sediment transport, p. 20–33. *In* W. Salomons, B. B.L., D. E.K. and U. Förstner [eds.], Pollution of the North Sea: An assessment. Springer, Berlin.

Eleveld, M. A., R. Pasterkamp, and H. J. Van der woerd. 2004. A survey of total suspended matter in the Southern North Sea based on 2001 SeaWiFS data, p. 166-178. EARSeL eProceedings.

EPA. 1993. Method 180.1: Determination of turbidity by nephelometry. Environmental Protection Agency. Environmental Monitoring Systems Laboratory. J. W. O'Dell. Cincinnati, Ohio, USA. http://water.epa.gov/scitech/methods/cwa/bioindicators/upload/2007_07_10_methods_method_180_1.pdf

Faure, F., P. Coste, and G. Kang. 2008. The GOCI instrument on COMS mission - The first geostationary ocean color imager. Proceedings of the International Conference on Space Optics (ICSO). 14-17 October 2008, Toulouse, France. http://www.ioccg.org/sensors/GOCI-Faure.pdf

Feely, R. A., J. H. Trefry, and B. Monger. 1991. Particle sampling and preservation, p. 5–22. *In* D. C. Heard and D. W. Spencer [eds.], Marine Particles: Analysis and Characterization. American Geophysical Union. Washington, DC, USA

Fettweis, M., F. Francken, V. Pison, and D. Van den Eynde. 2006. Suspended particulate matter dynamics and aggregate sizes in a high turbidity area. Mar. Geol. **235:** 63-74.

Fettweis, M., B. Nechad, and D. Van den Eynde. 2007. An estimate of the suspended particulate matter (SPM) transport in the southern North Sea using SeaWiFS images, in situ measurements and numerical model results. Cont. Shelf Res. **27:** 1568-1583.

Fettweis, M., and D. Van den Eynde. 2003. The mud deposits and the high turbidity in the Belgian-Dutch coastal zone, Southern bight of the North Sea. Continental Shelf Research **23:** 669-691.

Flory, E. N., P. S. Hill, T. G. Milligan, and J. Grant. 2004. The relationship between floc area and backscatter during a spring phytoplankton bloom. Deep-Sea Res. **51:** 213-223.

Foden, J., D. Sivyer, D. Mills, and M. J. Devlin. 2008. Spatial and temporal distribution of chromophoric dissolved organic matter (CDOM) fluorescence and its contribution to light attenuation in UK waterbodies. Estuar. Coast. Shelf Sci. **79:** 707-717.

Froidefond, J. M., L. Gardel, D. Guiral, M. Parra, and J. F. Ternon. 2002. Spectral remote sensing reflectances of coastal waters in French Guiana under the Amazon influence. Remote Sens. Environ. **80:** 225-232.

Froidefond, J. M., F. Lahet, C. Hu, D. Doxaran, D. Guiral, M. T. Prost, and J. F. Ternon. 2004. Mudflats and mud suspension observed from satellite data in French Guiana. Mar. Geol. **208:** 153-168.

Frouin, R., M. Schwindling, and P. Y. Deschamps. 1996. Spectral reflectance of sea foam in the visible and near-infrared: In situ measurements and remote sensing implications. J. Geophys. Res. C Oceans **101:** 14361-14371.

Fuentes-Yaco, C., P. A. Koeller, S. Sathyendranath, and T. Platt. 2007. Shrimp (Pandalus borealis) growth and timing of the spring phytoplankton bloom on the Newfoundland-Labrador Shelf. Fish. Oceanogr. **16:** 116-129. doi: 10.1111/j.1365-2419.2006.00402.x

Ganju, N. K., D. H. Schoellhamer, M. C. Murrell, J. W. Gartner, and S. A. Wright. 2006. Constancy of the relation between floc size and density in San Francisco Bay, p. 75-91. *In* J. P. Maa, L. H. Sanford and D. H. Schoellhamer [eds.], Estuarine and coastal fine sediment dynamics. INTERCOH 2003. Elsevier.

Gardner, W. D. and others. 2001. Optics, particles, stratification, and storms on the New England continental shelf. J. Geophys. Res. **106:** 9473-9497.

Gibbs, R. J. 1974. Sediment transport model for Amazon river Atlantic Ocean. Trans. Am. Geophys. Union **55:** 279-279.

Gordon, H. R. 1989. Can the Lambert-Beer law be applied to the diffuse attenuation coefficient of ocean water? Limnol. Oceanogr. **34:** 1389-1409.

Gordon, H. R., O. B. Brown, R. H. Evans, J. W. Brown, R. C. Smith, K. S. Baker, and D. K. Clark. 1988. A semianalytical radiance model of ocean color. Journal of Geophysical Research **93:** 10909-10924.

Gordon, H. R., and T. Du. 2001. Light scattering by nonspherical particles: Application to coccoliths detached from Emiliania huxleyi. Limnol. Oceanogr. **46:** 1438-1454.

Gordon, H. R., and W. R. McCluney. 1975. Estimation of depth of sunlight penetration in sea for remote sensing. Appl. Opt. **14:** 413-416.

Gordon, H. R., and M. Wang. 1994. Influence of oceanic whitecaps on atmospheric correction of ocean-color sensors. Appl. Opt. **33:** 7754-7763.

Govaerts, Y., and M. Clerici. 2004. MSG-1/SEVIRI solar channels calibration commissioning activity report. EUMETSAT, European Organisation for the Exploitation of Meteorological Satellites. EUM/MSG/TEN/04/0024. http://www.eumetsat.int/groups/ops/documents/document/pdf_ten_040024_seviri-solcalib.pdf

Graham, G. W., and W. A. M. N. Smith. 2010. The application of holography to the analysis of size and settling velocity of suspended cohesive sediments. Limnol. Oceanogr. Meth. **8:** 1-15.

Ham, S. H., and B. J. Sohn. 2010. Assessment of the calibration performance of satellite visible channels using cloud targets: application to Meteosat-8/9 and MTSAT-1R. Atmos. Chem. Phys. **10:** 11131-11149.

Hatcher, A., P. Hill, and J. Grant. 2001. Optical backscatter of marine flocs. J. Sea Res. **46:** 1-12.

Hedley, J. 2011. Modelling the optical properties of suspended particulate matter of coral reef environments using the finite difference time domain (FDTD) method. Geo-Mar. Lett. doi: 10.1007/s00367-011-0265-8

Hill, P. S., E. Boss, J. P. Newgard, B. A. Law, and T. G. Milligan. 2011. Observations of the sensitivity of beam attenuation to particle size in a coastal bottom boundary layer. J. Geophys. Res. **116:** C02023, doi: 02010.01029/02010JC006539.

Hill, P. S., C. R. Sherwood, R. W. Sternberg, and A. R. M. Nowell. 1994. In-Situ measurements of particle settling velocity on the northern California continental shelf. Cont. Shelf Res. **14:** 1123-1137.

Holligan, P. M., T. Aarup, and S. B. Groom. 1989. The North Sea satellite colour atlas. Cont. Shelf Res. **9:** 665-765.

Holligan, P. M., M. Viollier, D. S. Harbour, P. Camus, and M. Champagnephilippe. 1983. Satellite and ship studies of coccolithophore production along a continental-shelf edge. Nature **304:** 339-342.

Hooker, S. B., C. R. McClain, and A. Holmes. 1993. Ocean Color Imaging: CZCS to SeaWiFS. Marine Technology Society **27:** 3-15.

Hooker, S. B., and A. Morel. 2003. Platform and environmental effects on above-water determinations of water-leaving radiances. Journal of Atmospheric and Oceanic Technology **20:** 187-205.

Hovis, W. A. and others. 1980. Nimbus-7 Coastal Zone Color Scanner - system description and initial imagery. Science **210:** 60-63. doi: 10.1126/science.210.4465.60

Hu, C., Z. Chen, T. D. Clayton, P. Swarzenski, J. C. Brock, and F. E. Muller-Karger. 2004. Assessment of estuarine water-quality indicators using MODIS medium-resolution bands: initial results from Tampa Bay, FL. Remote Sens. Environ. **93:** 423-441.

ICES. 2004. Chemical measurements in the Baltic Sea: Guidelines on quality assurance. International Council for the Exploration of the Sea. ICES Techniques in Marine Environmental Sciences 35. E. Lysiak-Pastuszak and M. Krysell. Copenhagen, Denmark. http://www.ices.dk/pubs/times/times35/TIMES35.pdf

IOCCG. 2010. Atmospheric correction for remotely-sensed ocean colour products. M. Wang. Reports of the International Ocean-Colour Coordinating Group, No. 10, IOCCG, Dartmouth, Canada.

---. 2012. Ocean colour observations from a geostationary orbit. D. Antoine. Reports of the International Ocean-Colour Coordinating Group, No. 12, IOCCG, Dartmouth, Canada.

ISO. 1995. Guide to the expression of uncertainty in measurement. International Standard Organisation. ISO 1995:101.

---. 1997. Water quality - determination of suspended solids by filtration through glass-fibre filters. International Standard Organisation. ISO 11923.

---. 1999. Water quality — determination of turbidity. International Standard Organisation. ISO 7027:1999(E).

Jamet, C., H. Loisel, C. P. Kuchinke, K. Ruddick, G. Zibordi, and H. Feng. 2011. Comparison of three SeaWiFS atmospheric correction algorithms for turbid waters using AERONET-OC measurements. Remote Sens. Environ. **115:** 1955-1965. doi: 10.1016/j.rse.2011.03.018

Jonasz, M. 1983. Particle size distributions in the Baltic. Tellus B **35:** 346-358.

Jonasz, M., and G. R. Fournier. 2007. Light scattering by particles in water - theoretical and experimental foundations. Elsevier, Amsterdam,

Jouon, A., S. Ouillon, P. Douillet, J. P. Lefebvre, J. M. Fernandez, X. Mari, and J. M. Froidefond. 2008. Spatio-temporal variability in suspended particulate matter concentration and the role of aggregation on size distribution in a coral reef lagoon. Mar. Geol. **256:** 36-48.

Kaufman, Y. J. and others. 1997. Passive remote sensing of tropospheric aerosol and atmospheric correction for the aerosol effect. J. Geophys. Res. **102:** 16815-16830.

Kirk, J. T. O. 1996. Light and photosynthesis in aquatic ecosystems. Cambridge University Press,

---. 2003. The vertical attenuation of irradiance as a function of the optical properties of the water. Limnol. Oceanogr. **48:** 9-17.

Kitchen, J. C., and J. R. V. Zaneveld. 1992. A 3-layered sphere model of the optical properties of phytoplankton. Limnol. Oceanogr. **37:** 1680-1690.

Kitchen, J. C., J. R. V. Zaneveld, and H. Pak. 1982. Effect of particle size distribution and chlorophyll content on beam attenuation spectra. Appl. Opt. **21:** 3913-3918.

Kostadinov, T. S., D. A. Siegel, and S. Maritorena. 2009. Retrieval of the particle size distribution from satellite ocean color observations. J. Geophys. Res.-Oceans **114**. doi: 10.1029/2009JC005303

Lacroix, G., Y. Park, K. Ruddick, and C. Lancelot. 2007. Spatial and interannual variability of the spring phytoplankton bloom in the North Sea investigated by modelling and remote sensing. Proceedings of the 6th European Conference on Ecological Modelling (ECEM'07). 27-30 November 2007, Trieste, Italy.

Latimer, P. 1985. Experimental tests of a theoretical method for predicting light scattering by aggregates. Appl. Opt. **24:** 3231-3239.

Lawson, S. E., P. L. Wiberg, K. J. McGlathery, and D. C. Fugate. 2007. Wind-driven sediment suspension controls light availability in a shallow coastal lagoon. Estuar. Coast. **30:** 102-112.

Lee, M. E., and M. R. Lewis. 2003. A new method for the measurement of the optical volume scattering function in the upper ocean. Journal Of Atmospheric And Oceanic Technology **20:** 563-571.

Lee, Z. 2009. KPAR: An optical property associated with ambiguous values. J. Lake Sci. **21:** 159-164.

Lee, Z., K. Du, and R. Arnone. 2005. A model for the diffuse attenuation coefficient of downwelling irradiance. J. Geophys. Res. **110**. doi:10.1029/2004JC002275

Legendre, L. 1990. The significance of microalgal blooms for fisheries and for the export of particulate organic carbon in oceans. J. Plankton Res. **12:** 681-699. doi: 10.1093/plankt/12.4.681

Leymarie, E., D. Doxaran, and M. Babin. 2010. Uncertainties associated to measurements of inherent optical properties in natural waters. Appl. Opt. **49:** 5415-5436.

Loisel, H., B. Lubac, D. Dessailly, L. Duforet-Gaurier, and V. Vantrepotte. 2010. Effect of inherent optical properties variability on the chlorophyll retrieval from ocean color remote sensing: an in situ approach. Opt. Express **18:** 20949-20959, doi: 20910.21364/OE.20918.020949.

Loisel, H., X. Meriaux, J. F. Berthon, and A. Poteau. 2007. Investigation of the optical backscattering to scattering ratio of marine particles in relation to their biogeochemical composition in the eastern English Channel and southern North Sea. Limnol. Oceanogr. **52:** 739-752.

Loisel, H. and others. 2009. Analyze of the inherent optical properties of French Guiana coastal waters for remote sensing applications. J. Coast. Res.**:** 1532-1536.

Loisel, H., and A. Morel. 1998. Light scattering and chlorophyll concentration in case 1 waters: A reexamination. Limnol. Oceanogr. **43:** 847-858.

---. 2001. Non-isotropy of the upward radiance field in typical coastal (Case 2) waters. Int. J. Remote Sens. **22:** 275-295.

Loisel, H., J. M. Nicolas, A. Sciandra, D. Stramski, and A. Poteau. 2006. Spectral dependency of optical backscattering by marine particles from satellite remote sensing of the global ocean. J. Geophys. Res. **111:** C09024, doi: 09010.01029/02005JC003367.

Maffione, R. A., and D. R. Dana. 1997. Instruments and methods for measuring the backward-scattering coefficient of ocean waters. Appl. Opt. **36:** 6057-6067.

Martinez-Vicente, V., P. E. Land, G. H. Tilstone, C. Widdicombe, and J. R. Fishwick. 2010. Particulate scattering and backscattering related to water constituents and seasonal changes in the Western English Channel. J. Plankton Res. **32:** 603-619.

Mazeran, C., and N. Meskini. 2008. Mission couleur de l'océan géostationnaire: Charactérisation de la géométrie, gain en couverture, impact d'instabilites instrumentals. CNES-044-R650-RF-v1.

McClain, C. R. 2009. A decade of satellite ocean color observations. Annu. Rev. Marine. Sci. **1:** 19-42. doi: 10.1146/annurev.marine.010908.163650

McClatchey, R. A., R. W. Fenn, J. E. A. Selby, F. E. Volz, and J. S. Garing. 1972. Optical Properties of the Atmosphere (Third Edition). Air force Cambridge research laboratories, Optical Physcis Laboratory. Environmental research papers 411. http://www.dtic.mil/cgi-bin/GetTRDoc?Location=U2&doc=GetTRDoc.pdf&AD=AD0753075

McKee, D., M. Chami, I. Brown, V. S. Calzado, D. Doxaran, and A. Cunningham. 2009. Role of measurement uncertainties in observed variability in the spectral backscattering ratio: a case study in mineral-rich coastal waters. Appl. Opt. **48:** 4663-4675.

McKee, D., and A. Cunningham. 2006. Identification and characterisation of two optical water types in the Irish Sea from in situ inherent optical properties and seawater constituents. Estuar. Coast. Shelf Sci. **68:** 305-316.

Mikkelsen, O. A., and M. Pejrup. 2000. In situ particle size spectra and density of particle aggregates in a dredging plume. Mar. Geol. **170:** 443-459.

Mills, D. K. and others. 2003. Smartbuoy: A marine environmental monitoring buoy with a difference., p. 311-316. *In* H. Dahlin, N. C. Flemming, K. Nittis and S. E. Peterson [eds.], Building the European Capacity in Operational Oceanography, Proc. Third International Conference on EuroGOOS. Elsevier Oceanography Series Publication series 19.

Mobley, C. D. 1994. Light and water: radiative transfer in natural waters. Academic Press, London, UK,

---. 1999. Estimation of the remote-sensing reflectance from above-surface measurements. Appl. Opt. **38:** 7442-7455.

Moore, G. F., J. Aiken, and S. J. Lavender. 1999. The atmospheric correction of water colour and the quantitative retrieval of suspended particulate matter in Case II waters: application to MERIS. Int. J. Remote Sens. **20:** 1713-1734.

Morel, A. 1973. Diffusion de la lumière par les eaux de mer; résultats expérimentaux et approche théorique. [The scattering of light by sea water: Experimental results and theoretical approach]. AGARD Lecture Series No. 61,

---. 1974. Optical properties of pure water and sea water, p. 1-24. *In* N. G. Jerlov and E. Steeman-Nielsen [eds.], Optical aspects of Oceanography. Academic Press.

---. 1988. Optical modelling of the upper ocean in relation to its biogenous matter content (Case I waters). J. Geophys. Res. **93:** 10749-10768.

---. 2008. Introduction to optical properties in the sea: theoretical aspects. *In* M. Babin, C. Roesler and J. Cullen [eds.], Real-time coastal observing systems for ecosystem dynamics and harmful algal blooms. UNESCO Publishing. Paris, France

Morel, A., and Y. H. Ahn. 1991. Optics of heterotrophic nanoflagellates and ciliates - a tentative assessment of their scattering role in oceanic waters compared to those of bacterial and algal cells. J. Mar. Res. **49:** 177-202.

Morel, A., and A. Bricaud. 1981. Theoretical results concerning light absorption in a discrete medium, and application to specific absorption of phytoplankton. Deep-Sea Res. **28:** 1375-1393.

---. 1986. Inherent optical properties of algal cells, including picoplankton. Theoretical and experimental results. Can. B. Fish. Aquat. Sci. **214:** 521-559.

Morel, A., and B. Gentili. 1991. Diffuse reflectance of oceanic waters: its dependence on sun angle as influenced by the molecular scattering contribution. Appl. Opt. **30:** 4427-4438.

---. 1996. Diffuse reflectance of oceanic waters. III. Implications of bidirectionality for the remote sensing problem. Appl. Opt. **35:** 4850-4862.

Morel, A., and H. Loisel. 1998. Apparent optical properties of oceanic water: dependence on the molecular scattering contribution. Appl. Opt. **37:** 4765-4776.

Mueller, J. L. and others. 2003. Ocean optics protocols for satellite ocean color sensor validation. National Aeronautical and Space administration (NASA). J. L. Mueller, G. S. Fargion and C. R. McClain. Technical Memorandum TM-2003-21621/Revision 5, Volume 5, Greenbelt, Maryland.

---. 2000. Above-water radiance and remote sensing reflectance measurements and analysis protocols, p. 98-107. Ocean Optics protocols for satellite ocean color sensor validation Revision 2. National Aeronautical and Space Administration. Greenbelt, Maryland

Muller, J. 2010. MSG Level 1.5 Image Data Format Description. EUMETSAT, European Organisation for the Exploitation of Meteorological Satellites. Technical document EUM/MSG/ICD/105. http://www.eumetsat.int/groups/ops/documents/document/pdf_ten_05105_msg_img_data.pdf

Nechad, B., K. G. Ruddick, and G. Neukermans. 2009. Calibration and validation of a generic multisensor algorithm for mapping of turbidity in coastal waters. Proc. SPIE - Int. Soc. Opt. Eng. (USA). 31 Aug. 2009, Berlin, Germany. doi: 10.1117/12.830700

Nechad, B., K. G. Ruddick, and Y. Park. 2010. Calibration and validation of a generic multisensor algorithm for mapping of total suspended matter in turbid waters. Remote Sens. Environ. **114:** 854-866.

Nedwell, D. B., T. D. Jickells, M. Trimmer, and R. Sanders. 1999. Nutrients in estuaries, p. 43-92. *In* D. B. Nedwell and D. G. Raffaelli [eds.], Advances In Ecological Research, Vol 29: Estuaries. Advances in Ecological Research.

Neil, C., A. Cunningham, and D. McKee. 2011. Relationships between suspended mineral concentrations and red-waveband reflectances in moderately turbid shelf seas. Remote Sens. Environ. **115:** 3719-3730. doi: 10.1016/j.rse.2011.09.010

Neukermans, G., H. Loisel, X. Meriaux, R. Astoreca, and D. McKee. 2012. In situ variability of mass-specific beam attenuation and backscattering of marine particles with respect to particle size, density, and composition. Limnol. Oceanogr. **57:** 124–144, doi:110.4319/lo.2011.4357.4311.0124.

Neukermans, G., K. Ruddick, E. Bernard, D. Ramon, B. Nechad, and P.-Y. Deschamps. 2009. Mapping total suspended matter from geostationary satellites: a feasibility study with SEVIRI in the Southern North Sea. Opt. Express **17:** 14029-14052.

Neukermans, G., K. Ruddick, and N. Greenwood. accepted. Diurnal variability of turbidity and light attenuation in the southern North Sea from the SEVIRI geostationary sensor. Remote Sens. Environ.

Nicolas, J.-M., P. Y. Deschamps, and O. Hagolle. 2006. Radiometric calibration of the visible and near-infrared bands of SEVIRI using Rayleigh scattering and sun-glint over oceans. Proceedings of the 3rd MSG RAO Workshop (ESA SP-619). 15 June 2006, Helsinki, Finland. http://articles.adsabs.harvard.edu/cgi-bin/nph-iarticle_query?2006ESASP.619.19N&data_type=PDF_HIGH&whole_paper=YES&type=PRINTER&filetype=.pdf

NRC. 2007. Earth science and applications from space: national imperatives for the next decade and beyond. National Research Council. 978-0-309-10387-9. National Academy of Sciences,

Oishi, T. 1990. Significant relationship between the backward scattering coefficient of seawater and the xcatterance at 120 degrees. Appl. Opt. **29:** 4658-4665.

Otto, L., J. T. F. Zimmerman, G. K. Furnes, M. Mork, R. Saetre, and G. Becker. 1990. Review of the Physical Oceanography of the North Sea. Netherlands Journal of Sea Research **26:** 161-238.

Oubelkheir, K. J., H. Claustre, A. Sciandra, and M. Babin. 2005. Bio-optical and biogeochemical properties of different trophic regimes in oceanic waters. Limnol. Oceanogr. **50:** 1795-1809.

Ouillon, S., P. Forget, J. M. Froidefond, and J. J. Naudin. 1997. Estimating suspended matter concentrations from SPOT data and from field measurements in the Rhone River plume. Mar. Technol. Soc. J. **31:** 15-20.

Painting, S. J. and others. 2007. Assessing the impact of nutrient enrichment in estuaries: Susceptibility to eutrophication. Mar. Pollut. Bull. **55:** 74-90.

Pak, H., Beardsle.Gf, G. R. Heath, and H. Curl. 1970. Light scattering vectors of some marine particles. Limnol. Oceanogr. **15:** 683-&.

Pak, H., and J. R. V. Zaneveld. 1977. Bottom nepheloid layers and bottom mixed layers observed on continental shelf off Oregon. J. Geophys. Res. **82:** 3921-3931.

Pearlman, S. R., H. S. Costa, R. A. Jung, J. J. McKeown, and H. E. Pearson. 1995. Solids (section 2540), p. 2-53–52-64. *In* A. D. Eaton, L. S. Clesceri and A. E. Greenberg [eds.], Standard Methods for the Examination of Water and Wastewater. American Public Health Association. Washington, USA.

Peeters, J. C. H., H. Haas, L. Peperzak, and L. Wetsteyn. 1991. Limiting Factors For Phytoplankton In The North-Sea. Water Sci. Technol. **24:** 261-267.

Pegau, S., J. R. V. Zaneveld, and M. J.L. 2003. Beam transmission and attenuation coefficients: instruments, characterization, field measurements and data analysis protocols. National Aeronautical and Space administration (NASA). J. L. Mueller, G. S. Fargion and C. R. McClain. Ocean optics protocols for satellite ocean color sensor validation. Technical Memorandum TM-2003-21621/Revision 4, Volume IV, Greenbelt, Maryland.

Pegau, W. S., D. Gray, and J. R. V. Zaneveld. 1997. Absorption and attenuation of visible and near-infrared light in water: dependence on temperature and salinity. Appl. Opt. **36:** 6035-6046.

Peng, F., and S. W. Effler. 2007. Suspended minerogenic particles in a reservoir: Light-scattering features from individual particle analysis. Limnol. Oceanogr. **52:** 204-216.

---. 2010. Characterizations of individual suspended mineral particles in western Lake Erie: Implications for light scattering and water clarity. J. Gt. Lakes Res. **36:** 686-698.

Petzold, T. J. 1972. Volume scattering function for selected oceanic waters. Scripps Institute of Oceanography, La Jolla, USA. Techical Report 72-78.

Platt, T., C. Fuentes-Yaco, and K. T. Frank. 2003. Spring algal bloom and larval fish survival. Nature **423:** 398-399. doi: 10.1038/423398b

PML, and ICES. 2004. ECASA (Ecosystem Approach for Sustainable Aquaculture) book of protocols: Particulate matter in seawater. Plymouth Marine Laboratory and International Council for the Exploration of the Sea. http://www.ecasatoolbox.org.uk/the-toolbox/eia-country/book-of-protocols/particulate-matter-in-seawater

Pope, R. M., and E. S. Fry. 1997. Absorption spectrum (380-700nm) of pure water. II. Integrating cavity measurements. Appl. Opt. **36:** 8710-8723.

Preisendorfer, R. W. 1961. Application of radiative transfer theory to light measurements in the sea, p. 11-30. Radiant Energy in the sea. International Union for Geodesy and Geophysics. Paris, France

Rast, M., J. L. Bézy, and S. Bruzzi. 1999. The ESA Medium Resolution Imaging Spectrometer, MERIS - a review of the instrument and its mission. Int. J. Remote Sens. **20:** 1681-1702.

Reynolds, R. A., D. Stramski, V. M. Wright, and S. B. Wozniak. 2010. Measurements and characterization of particle size distributions in coastal waters. J. Geophys. Res. Oceans **115:** C08024, doi: 08010.01029/02009JC005930.

Roesler, C., and E. Boss. 2008. In situ measurement of the inherent optical properties (IOPs) and potential for harmful algal bloom detection and coastal ecosystem observations. *In* M. Babin, C. Roesler and J. Cullen [eds.], Real-time coastal observing systems for ecosystem dynamics and harmful algal blooms. UNESCO Publishing. Paris, France

Ruddick, K., Y. Park, R. Astoreca, G. Neukermans, and B. Van Mol. 2008. Validation of MERIS water products in the Southern North Sea: 2002-2008. 2nd MERIS-(A)ASTR workshop. Frascati.

Ruddick, K., Q. Vanhellemont, J. Yan, G. Neukermans, G. Wei, and S. Shang. submitted. Variability of suspended particulate matter in the Bohai Sea from the Geostationary Ocean Color Imager (GOCI). (Korean) Ocean Science Journal, Special Issue on Proceedings of the 2nd GOCI PI workshop.

Ruddick, K. G., V. De Cauwer, Y. Park, and G. Moore. 2006. Seaborne measurements of near infrared water-leaving reflectance - the similarity spectrum for turbid waters. Limnol. Oceanogr. **51:** 1167-1179.

Ruddick, K. G., F. Ovidio, and M. Rijkeboer. 2000. Atmospheric correction of SeaWiFS imagery for turbid coastal and inland waters. Appl. Opt. **39:** 897-912.

Salomonson, V. V., W. Barnes, H. Montgomery, and H. Ostrow. 1987. MODIS: advanced facility instrument for studies of the Earth as a system. IGARSS '87. Remote Sensing: Understanding the Earth as a System (Cat. No.87CH2434-9).

Seiz, G., S. Tjemkes, and P. Watts. 2007. Multiview cloud-top height and wind retrieval with photogrammetric methods: Application to Meteosat-8 HRV observations. Journal Of Applied Meteorology And Climatology **46:** 1182-1195. doi: 10.1175/JAM2532.1

Sheldon, R. W. 1972. Size Separation Of Marine Seston By Membrane And Glass-Fiber Filters. Limnol. Oceanogr. **17:** 494-498.

Sheldon, R. W., and W. H. J. Sutcliffe. 1969. Retention of marine particles by screens and filters. Limnol. Oceanogr. **14:** 441-444.

Sirjacobs, D. and others. 2011. Cloud filling of ocean color and sea surface temperature remote sensing products over the southern North Sea by the data interpolating empirical orthogonal functions methodology. J. Sea Res. **65:** 114-130.

Slade, W. H., E. Boss, and C. Russo. 2011. Effects of particle aggregation and disaggregation on their inherent optical properties. Opt. Express **19:** 7945-7959.

Snyder, W. A. and others. 2008. Optical scattering and backscattering by organic and inorganic particulates in US coastal waters. Appl. Opt. **47:** 666-677.

Spinrad, R. W., J. R. V. Zaneveld, and J. C. Kitchen. 1983. A study of the optical characteristics of the suspended particles in the benthic nepheloid layer of the Scotian rise. J. Geophys. Res. Oceans **88:** 7641-7645.

Stavn, R. H., H. J. Rick, and A. V. Falster. 2009. Correcting the errors from variable sea salt retention and water of hydration in loss on ignition analysis: Implications for studies of estuarine and coastal waters. Estuar. Coast. Shelf Sci. **81:** 575-582. doi: 10.1016/j.ecss.2008.12.017

Stramski, D., M. Babin, and S. B. Woźniak. 2007. Variations in the optical properties of terrigenous mineral-rich particulate matter suspended in seawater. Limnol. Oceanogr. **52:** 2418-2433.

Stramski, D., E. Boss, D. Bogucki, and K. J. Voss. 2004. The role of seawater constituents in light backscattering in the ocean. Prog. Oceanogr. **61:** 27-56.

Stramski, D., and D. A. Kiefer. 1991. Light scattering by microorganisms in the open ocean. Prog. Oceanogr. **28:** 343-383.

Stramski, D., and A. Morel. 1990. Optical properties of photosynthetic picoplankton in different physiological states as affected by growth irradiance. Deep-Sea Res. **37:** 245-266.

Stramski, D. and others. 2008. Relationships between the surface concentration of particulate organic carbon and optical properties in the eastern South Pacific and eastern Atlantic Oceans. Biogeosciences **5:** 171-201.

Stramski, D., R. A. Reynolds, M. Kahru, and B. G. Mitchell. 1999. Estimation of particulate organic carbon in the ocean from satellite remote sensing. Science **285:** 239-242.

Stramski, D., A. Sciandra, and H. Claustre. 2002. Effects of temperature, nitrogen, and light limitation on the optical properties of the marine diatom Thalassiosira pseudonana. Limnol. Oceanogr. **47:** 392-403.

Strickland, J. D. H., and T. R. Parsons. 1968. A Practical Handbook of Seawater Analysis. Bulletin 167. Fisheries Research Board of Canada, Ottawa (Canada), pp. 181–184

Stumpf, R. P., R. A. Arnone, R. W. Gould, and V. Ransibrahmanakul. 2003a. A partially coupled ocean-atmosphere model for retrieval of water-leaving radiance from SeaWiFS in coastal waters. NASA technical memorandum (pp. 51-59) 2003-206892. S. B. Hooker. Volume 22: Algorithm updates for the fourth SeaWiFS data reprocessing, Greenbelt, NASA Goddard Space Flight Center. http://oceancolor.gsfc.nasa.gov/SeaWiFS/TECH_REPORTS/PLVol22.pdf

Stumpf, R. P. and others. 2003b. Monitoring Karenia brevis blooms in the Gulf of Mexico using satellite ocean color imagery and other data. Harmful Algae **2:** 147-160.

Stumpf, R. P., M. L. Frayer, M. J. Durako, and J. C. Brock. 1999. Variations in water clarity and bottom albedo in Florida Bay from 1985 to 1997. Estuaries **22:** 431-444.

Stumpf, R. P., G. Gelfenbaum, and J. R. Pennock. 1993. Wind and tidal forcing of a buoyant plume, Mobile Bay, Alabama. Cont. Shelf Res. **13:** 1281-1301.

Stumpf, R. P., and J. R. Pennock. 1989. Calibration of a general optical equation for remote sensing of suspended sediments in a moderately turbid estuary. J. Geophys. Res. **94:** 14363-14371.

Sullivan, J. M., and M. S. Twardowski. 2009. Angular shape of the oceanic particulate volume scattering function in the backward direction. Appl. Opt. **48:** 6811-6819.

Sullivan, J. M., M. S. Twardowski, P. L. Donaghay, and S. A. Freeman. 2005. Use of optical scattering to discriminate particle types in coastal waters. Appl. Opt. **44:** 1667-1680.

Sullivan, J. M., M. S. Twardowski, J. R. Zaneveld, and C. C. Moore. submitted. Measuring optical backscattering in water.

Sullivan, J. M., M. S. Twardowski, J. R. V. Zaneveld, C. M. Moore, A. H. Barnard, P. L. Donaghay, and B. Rhoades. 2006. Hyperspectral temperature and salt dependencies of absorption by water and heavy water in the 400-750 nm spectral range. Appl. Opt. **45:** 5294-5309.

Tatarkiewicz, J. J., R. A. Reynolds, and D. Stramski. 2012. Counting and sizing of colloidal particles in the Arctic Ocean. Ocean Sciences Meeting 2012. 20-24 February 2012, Salt Lake City, USA. http://www.sgmeet.com/osm2012/viewabstract2.asp?AbstractID=9632

Thompson, C. E. L. and others. 2011. In situ flume measurements of resuspension in the North Sea. Estuar. Coast. Shelf Sci. **94:** 77-88.

Thuillier, G. and others. 2003. The solar spectral irradiance from 200 to 2400 nm as measured by the SOLSPEC spectrometer from the ATLAS and EURECA missions. Sol. Phys. **214:** 1-22.

Tilstone, G. and others. 2003. REVAMP Regional Validation of MERIS Chlorophyll products in North Sea coastal waters: Protocols document. MERIS and AATSR Calibration and Geophysical Validation (MAVT-2003). Frascati.

Tomlinson, M. C. and others. 2004. Evaluation of the use of SeaWiFS imagery for detecting Karenia brevis harmful algal blooms in the eastern Gulf of Mexico. Remote Sens. Environ. **91:** 293-303.

Townsend, D. W., M. D. Keller, M. E. Sieracki, and S. G. Ackleson. 1992. Spring Phytoplankton Blooms In The Absence Of Vertical Water Column Stratification. Nature **360:** 59-62.

Traykovski, P., R. J. Latter, and J. D. Irish. 1999. A laboratory evaluation of the laser in situ scattering and transmissometery instrument using natural sediments. Mar. Geol. **159:** 355-367.

Trees, C. C. 1978. Analytical analysis of effect of dissolved solids on suspended solids determination. J. Water Poll. Control Fed. **50:** 2370-2373.

Twardowski, M. and others. 2012. The optical volume scattering function in a surf zone inverted to derive sediment and bubble particle subpopulations. J. Geophys. Res. **117**. doi:10.1029/2011JC007347

Twardowski, M. S., E. Boss, J. B. Macdonald, W. S. Pegau, A. H. Barnard, and J. R. V. Zaneveld. 2001. A model for estimating bulk refractive index from the optical backscattering ratio and the implications for understanding particle composition in case I and case II waters. J. Geophys. Res. **106:** 14129-14142.

Ulloa, O., S. Sathyendranath, and T. Platt. 1994. Effect of the particle size distribution on the backscattering ratio in seawater. Appl. Opt. **33:** 7070-7077.

Vaillancourt, R. D., C. W. Brown, R. R. L. Guillard, and W. M. Balch. 2004. Light backscattering properties of marine phytoplankton: relationships to cell size, chemical composition and taxonomy. J. Plankton Res. **26:** 191-212.

Van De Hulst, H. C. 1957. Light scattering by small particles. John Wiley,

van der Linde, D. W. 1998. Protocol for the determination of total suspended matter in oceans and coastal zones. Joint Research Centre, Ispra. Technical note I.98.182.

Van Der Woerd, H., and R. Pasterkamp. 2004. Mapping of the North Sea turbid coastal waters using SeaWiFS data. Can. J. Remote. Sens. **30:** 44-53.

Van Raaphorst, W., C. J. M. Philippart, J. P. C. Smit, F. J. Dijkstra, and J. F. P. Malschaert. 1998. Distribution of suspended particulate matter in the North Sea as inferred from NOAA/AVHRR reflectance images and in situ observations. J. Sea Res. **39:** 197-215.

Vantrepotte, V., H. Loisel, F. Melin, D. Desailly, and L. Duforet-Gaurier. 2011. Global particulate matter pool temporal variability over the SeaWiFS period (1997-2007). Geophysical Research Letters **38:** L02605. doi: 10.1029/2010GL046167

Vantrepotte, V. and others. in press. Seasonal and inter-annual (2002-2010) variability of the suspended particulate matter as retrieved from satellite ocean color sensor over the French Guiana coastal waters. J. Coast. Res.

Vermote, E. F., D. Tanre, J. L. Deuze, M. Herman, and J. J. Morcrette. 1997. Second Simulation of the Satellite Signal in the Solar Spectrum, 6S: An overview. IEEE Trans. Geosci. Remote Sensing **35:** 675-686.

Verney, R., R. Lafite, J. C. Brun-Cottan, and P. Le Hir. 2011. Behaviour of a floc population during a tidal cycle: Laboratory experiments and numerical modelling. Cont. Shelf Res. **31:** S64-S83. doi: 10.1016/j.csr.2010.02.005

Volten, H. and others. 1998. Laboratory measurements of angular distributions of light scattered by phytoplankton and silt. Limnol. Oceanogr. **43:** 1180-1197.

Vos, R. J., P. G. J. ten Brummelhuis, and H. Gerritsen. 2000. Integrated data-modelling approach for suspended sediment transport on a regional scale. Coastal Engineering **41:** 177-200. doi: 10.1016/S0378-3839(00)00032-6

Wells, J. T., and S. Y. Kim. 1991. The relationship between beam transmission and concentration of suspended particulate material in the Neuse river estuary, North-Carolina. Estuaries **14:** 395-403.

Wells, M. L., and E. D. Goldberg. 1994. The distribution of colloids in the North-Atlantic and Southern Oceans. Limnol. Oceanogr. **39:** 286-302.

Woodruff, D. L., R. P. Stumpf, J. A. Scope, and H. W. Paerl. 1999. Remote estimation of water clarity in optically complex estuarine waters. Remote Sens. Environ. **68:** 41-52.

Woźniak, S. B., and D. Stramski. 2004. Modeling the optical properties of mineral particles suspended in seawater and their influence on ocean reflectance and chlorophyll estimation from remote sensing algorithms. Appl. Opt. **43:** 3489-3503.

Woźniak, S. B. and others. 2010. Optical variability of seawater in relation to particle concentration, composition, and size distribution in the nearshore marine environment at Imperial Beach, California. J. Geophys. Res. **115:** C08027, doi: 08010.01029/02009JC005554.

Xu, J., R. R. Hood, and S.-Y. Chao. 2005. A simple empirical optical model for simulating light attenuation variability in a partially mixed estuary. Estuaries **28:** 572-580.

York, D. 1966. Least-squares fitting of a straight line. Can. J. Phys. **44:** 1079-1086.

Zhang, X., L. Hu, and M. He. 2009. Scattering by pure seawater: effect of salinity. Opt. Express **17:** 5698-57105710, doi: 57105710.57101364/OE.57105717.57005698.

Zibordi, G., J. F. Berthon, F. Melin, D. D'Alimonte, and S. Kaitala. 2009. Validation of satellite ocean color primary products at optically complex coastal sites: Northern Adriatic Sea, Northern Baltic Proper and Gulf of Finland. Remote Sens. Environ. **113:** 2574-2591. doi: 10.1016/j.rse.2009.07.013

CURRICULUM VITAE OF THE AUTHOR

Personalia

Surname	Neukermans
First name	Griet
Date of birth	9 December 1979
Place of birth	Gent, Belgium
Nationality	Belgian
e-mail	grietneukermans@yahoo.com

Educational background

University

Timeframe	University and diploma	Degree	Major Subjects
2002-2004	MSc. in Ecological Marine Management (ECOMAMA), Vrije Universiteit Brussel, Brussels, Belgium	With great distinction	Physical & Chemical oceanography, Marine Ecology, GIS, Ecosystem Modeling
1997-2002	MSc. in Applied Mathematics Vrije Universiteit Brussel, Brussels, Belgium	With satisfaction	Astronomy & astrophysics, numerical analysis, statistics

Additional education and training

PADI Open Water and Advanced Open Water Scuba Diving Licence, Sharm-el-Sheikh, Egypt, September 2000, 31 certified dives to date.

Development cooperation training course of the Belgian Development Cooperation Agency (Belgian Technical Cooperation), November 2004.

Postgraduate Teacher training course in Mathematics, Vrije Universiteit Brussel (VUB), 2004-2005. Graduated with satisfaction.

ArcGIS Advanced GIS training courses (Geodatabase, Editing, Visualization, Querying, Geoprocessing), Geographic Information Management (GIM), Heverlee, Belgium, May 2006 (5 days).

Short course "Observational Approaches in Ocean Optics" by Michael Twardowski, October 5th 2008, Ocean Optics XIX Conference, Barga, Italy (1 day).

MSc. Biology course on Marine Optics by Hubert Loisel, 26-28 November 2008, Université du Littoral Côte d'Opale, Wimereux, France (3 days).

MATLAB training courses "Programming techniques" (1d), "Statistical Methods" (1d), "Building Graphical User Interfaces" (1d). July, September 2009.

SPIE course "Multispectral and hyperspectral remote sensing", San Diego, USA (1d).

Short course "Hydrolight" by Curtis Mobley, September 26th 2010, Ocean Optics XX Conference, Anchorage, USA (1 d).

Employment history

Timeframe	Employment	Main tasks
December 2007-May 2012	Marine researcher at the Royal Belgian Institute for Natural Sciences – Management Unit of the North Sea Mathematical Models (RBINS-MUMM) Ph.D. student at the Université du Littoral, Côte d'Opale, Wimereux, France	Research on scattering properties and remote sensing of suspended matter in coastal waters within the BELCOLOUR-2 and GEOCOLOUR projects. Work at sea (±120 days to date, see Field Work for details), data processing and archiving. Calibration of optical instruments. Cruise planning, organisation and reporting. BELCOLOUR project website content delivery and updates.
August-November 2007	Research assistant at NATO's Undersea Research Centre (NURC), La Spezia, Italy	Development of a visualization tool for high resolution sonar images and bathymetry data in NASA World Wind
February– July 2007	Coordinator of International Master Programme in Ecological Marine Management, VUB, Brussels, Belgium	Screen and select candidates for admission to the study program, identify and contact international coastal managers and marine experts, plan and coordinate workshops, seminars, field excursions and management training, and supervise students during field excursions. Set up and coordinate promotional activities, financial management of the program and set up and strengthen collaboration between governmental/private institutions and universities
February 2005-	Researcher at the Vrije	Investigating spatio-temporal dynamics of mangroves

January 2007	Universiteit Brussels (VUB), Brussels, Belgium	in East-Africa using very high resolution multispectral satellite imagery and historic aerial photography in the framework of an EU FP6 - INCO project. Project progress reporting to the European Commission.

Field work

2008-2012: Collection of sea-borne measurements (±120 days to date):

- Above-water marine reflectance (TriOS RAMSES)
- Particle size distribution (LISST)
- On-board filtrations for suspended matter and phytoplankton pigment concentration
- Inherent Optical Properties: total, side and backscattering (ac-s, BB-9, ECO-VSF, Turbidimeter)

2003-2007: Collection of remote sensing ground truth data in the mangrove forests of:

- Gazi Bay (Kenya), July-August 2003
- Mombasa (Kenya) and Dar-es-Salaam (Tanzania), August-December 2005
- Maputo (Mozambique), February 2006
- Gazi Bay (Kenya), February 2007

Teaching assignments

- "Scientific writing" course at M.Sc. ECOMAMA (VUB) (20 h in 2007)
- Coordinate excursions at sea for M.Sc. ECOMAMA (VUB) and supervise students during field excursions (150 h in 2007)

Student mentoring

Undergraduate students

From 2001 to 2006 I thought mathematics to about fifteen undergraduate students.

Master students

- Maniatis, D., 2005. Retrospective study of the mangroves of the Tanbi Wetland Complex, The Gambia. MSc. Environmental Science and Technology thesis, Vrije Universiteit Brussel, Brussels, Belgium. Thesis adviser.
- Msafiri, M., 2006. Spatial and temporal change of mangrove of Mtoni-Kijichi in Dar es Salaam, Tanzania. MSc Ecological Marine Management thesis. Vrije Universiteit Brussel, Brussels, Belgium. Thesis adviser.
- Vaes, T., 2011. Improving the spatial resolution of total suspended matter maps using the HRV band of the SEVIRI geostationary satellite in the North Sea. MSc Ecological Marine Management thesis. Vrije Universiteit Brussel, Brussels, Belgium. Thesis co-promoter.

Interns

Vanhellemont, Q., 2008. Professional Internship at MUMM for MSc. Marine and lacustrine sciences, Ghent University. Research adviser.

Publications

Peer review

Ruddick, K., Q. Vanhellemont, J. Yan, G. Neukermans, G. Wei, and S. Shang. Variability of suspended particulate matter in the Bohai Sea from the Geostationary Ocean Color Imager (GOCI). Submitted to the *(Korean) Ocean Science Journal*, Special Issue on Proceedings of the 2nd GOCI PI workshop on April 3, 2012.

Neukermans, G. and N. Koedam (in press). Mapping mangrove mosaics using high-resolution satellite imagery at Inhaca Island. *In:* S. Bandeira & J. Paula (eds), The Maputo Bay Ecosystem, WIOMSA.

Neukermans, G., K. Ruddick and N. Greenwood. Diurnal variability of turbidity and light attenuation in the southern North Sea from the SEVIRI geostationary sensor. (accepted for publication in *Remote sensing of the Environment*).

Neukermans G., Loisel H., Mériaux X., Astoreca R. & McKee D., 2012. In situ variability of mass-specific beam attenuation and backscattering of marine particles with respect to particle size, density, and composition. *Limnology and Oceanography* (57): 124–144. doi: doi:10.4319/lo.2011.57.1.0124.

Vantrepotte, V., H. Loisel , X. Mériaux, G. Neukermans, D. Dessailly, C. Jamet, E. Gensac, and A. Gardel, 2011. Seasonal and inter-annual (2002-2010) variability of the suspended particulate matter as retrieved from satellite ocean color sensor over the French Guiana coastal waters. *Journal of Coastal Research* SI 64, ISSN 0749-0208, 1750-1754.

Nechad, B., Ruddick, K.G. and G. Neukermans, 2009. Calibration and validation of a generic multisensor algorithm for mapping of turbidity in coastal waters. Proceedings of SPIE "Remote Sensing of the Ocean, Sea Ice, and Large Water Regions" Conference held in Berlin (Germany), 31 August 2009. *Proc. SPIE* Vol. 7473, 74730H.

Neukermans, G., K. Ruddick, E. Bernard, D. Ramon, B. Nechad & P.Y. Deschamps, 2009. Mapping Total Suspended Matter from geostationary satellites: a feasibility study with SEVIRI in the Southern North Sea. *Optics Express*, 17(16):14029-14052.

Obade, P., N. Koedam, K. Soetaert, G. Neukermans, J. Bogaert, E. Nyssen, F. Van Nedervelde, U. Berger & F. Dahdouh-Guebas, 2009. Impact of anthropogenic disturbance on a mangrove forest assessed by a 1D-cellular automaton model using Lotka-Volterra type competition. *International Journal of Design & Nature and Ecodynamics* 3(4).

Neukermans, G., F. Dahdouh-Guebas, J.G. Kairo & N. Koedam, 2008. Mangrove species and stand mapping in Gazi Bay (Kenya) using Quickbird satellite imagery. *Journal of Spatial Science* 53(1): 75-86.

Mohamed, M.O.S., G. Neukermans, J.G. Kairo, F. Dahdouh-Guebas & N. Koedam, 2008. Mangrove forests in a peri-urban setting: the case of Mombasa (Kenya). *Wetlands Ecology and Management, 17(3):* 243-255, doi:10.1007/s11273-008-9104-8.

Publications and abstracts for oral and poster presentations on international conferences and workshops

Neukermans, G., K. Ruddick, Q. Vanhellemont and Greenwood, N. 2012. Diurnal variability of turbidity and light attenuation from the SEVIRI geostationary sensor. Oceans Sciences meeting, 20-34 February 2012, Salt Lake City, USA. *Oral presentation.*

Neukermans, G., Loisel, H., Mériaux, X., McKee, D. , and R. Astoreca, 2011. Variability of mass specific beam attenuation and backscattering of marine particles: the role of particle size, density, and composition. Optical Processes Symposium workshop, NATO Undersea Research Center (NURC), 29-31 March 2011, La Spezia, Italy. *Invited talk.*

Neukermans, G., Loisel, H., Mériaux, X., McKee, D. , Astoreca, R. and D. Doxaran, 2010. Variability of mass specific (back)scattering of marine particles. Particles in Europe (PiE) workshop, 15-17 November 2010, Villefranche-sur-Mer, France. *Oral presentation.*

Neukermans, G., Loisel, H., Mériaux, X., McKee, D. , Astoreca, R. and D. Doxaran, 2010. Variability of total, back and side scattering to mass concentration ratio of marine particles. Ocean Optics XX Conference, 26 September – 1 October 2010, Anchorage, USA. *Poster presentation.*

Neukermans, G., Forster, R., Greenwood, N. and K. Ruddick, 2010. Diurnal variability of suspended matter from the SEVIRI geostationary sensor. Oceans From Space conference, 26-30 April 2010, Venice, Italy. *Poster presentation.*

Neukermans, G., K. Ruddick, E. Bernard, D. Ramon, B. Nechad & P.Y. Deschamps, 2009. Mapping Total Suspended Matter from geostationary satellites: a feasibility study with SEVIRI in the Southern North Sea. SPIE Ocean Remote Sensing conference, 2-6 August 2009, San Diego, USA. *Oral presentation.*

Neukermans, G., Loisel, H., and X. Mériaux, 2009. Vertical variability of IOPs and their influence on Rrs in coastal waters. Ocean Colour Research Team (OCRT) meeting, 4-6 May 2009, New-York, USA. *Poster presentation.*

Neukermans, G., Loisel, H., Mériaux, X. and Ruddick, K., 2009. Vertical Variability of suspended matter and its influence on remote sensing reflectance. Young Researcher's Day of Flanders Marine Institute (VLIZ), March 6th, Bruges, Belgium. *Poster presentation.*

Neukermans, G., Nechad, B. and K. Ruddick, 2008. Optical remote sensing of coastal waters from geostationary platforms: a feasibility study – Mapping suspended matter with SEVIRI. Ocean Optics XIX Extended abstract, 6-10 October 2008, Barga, Italy. *Poster presentation.*

Neukermans, G., Nechad, B. and K. Ruddick, 2008. High temporal resolution mapping of total suspended matter in Belgian coastal waters with SEVIRI data: a feasibility study, *in*: Mees, J.; Seys, J. (Ed.) (2008). *VLIZ Young Scientists' Day, Brugge, Belgium, 29 February 2008: book of abstracts. VLIZ Special Publication,* 40: pp. 59. *Poster presentation.*

Neukermans, G., Dahdouh-Guebas, F., Kairo, J.G. and N. Koedam, 2007. Mangrove species and stand mapping in Gazi Bay (Kenya) using QuickBird satellite imagery, *in*: Mees, J.; Seys, J. (Ed.) (2007). *VLIZ Young Scientists' Day, Brugge, Belgium 2 March 2007: book of abstracts. VLIZ Special Publication*, 39: pp. 45. *Poster presentation.*

Neukermans, G., Dadouh-Guebas, F., Kairo, J.G. and N. Koedam, 2006. Mangrove species and stand mapping in Gazi Bay (Kenya) using QuickBird satellite imagery. The 13th Australasian Remote Sensing and Photogrammetry Conference, 20-24 November 2006, Canberra, Australia. *Poster presentation.*

Neukermans, G., Dahoudh-Guebas, F., Kairo, J.G. and N. Koedam, 2006. Automated mangrove stand recognition and species mapping with QuickBird satellite imagery. In: J.A. Sobrino (Ed.), *Proceedings of the 2nd International Symposium on Recent Advances in Quantitative Remote Sensing: RAQRS'II*, 25-29 September 2006, Torrent (Valencia), Spain., pp. 174-181. *Poster presentation.*

Neukermans, G., Koedam, N., Kairo, J.G. and F. Dahdouh-Guebas, 2006. Mapping Kenyan mangroves with very high resolution QuickBird satellite imagery. Workshop on 3D Remote Sensing in Forestry, 14-15 February 2006, Vienna, Austria. *Poster presentation.*

Di Nitto, D., Neukermans, G., Defever, H., Decleir, H., Koedam, N., Kairo, J.G. and F. Dahdouh-Guebas, 2006. Effects of sea level rise on mangroves using GIS and Remote Sensing: A case study in Gazi Bay (Kenya). International Symposium on Aquatic Vascular Plants: 25 years later, 11-13 January, Brussels, Belgium. *Oral presentation (co-presented with D. Di Nitto).*

Neukermans, G., Koedam, N., Kairo, J.G. and F. Dahdouh-Guebas. Mapping Kenyan mangroves with very high resolution QuickBird satellite imagery. VLIZ Young Scientist's Day, 25 February 2005, Brugge, Belgium. *Poster presentation.*

Neukermans, G., 2005. Remote sensing of mangroves in Gazi Bay (Kenya) with very high resolution QuickBird Satellite imagery: automated methods for species and assemblage identification, *in*: Mees, J.; Seys, J. (Ed.) (2005). *VLIZ Young Scientists' Day, Brugge, Belgium 25 February 2005: book of abstracts. VLIZ Special Publication*, 20: pp. 2-3. *Oral presentation.*

Theses

Neukermans G., 2012. *Optical in situ and geostationary satellite-borne observations of suspended particles in coastal waters*. Ph.D. dissertation, Université du Littoral – Côte d'Opale, Wimereux, France. Academic and Scientific Publishers, Ravensteingalerij 28, 1000 Brussels, Belgium. ISBN 978 90 7028 949 2.

Neukermans G., 2004. *Remote sensing of mangroves in Gazi Bay (Kenya) with very high resolution QuickBird satellite imagery: automated methods for species and assemblage identification.* MSc. Ecological Marine Management, Vrije Universiteit Brussel, Brussels, Belgium, pp. 193, with greatest distinction.

Neukermans G., 2002. *Delta Scuti variability of GSC223-1761 (GP Cnc).* MSc. Mathematics thesis, Vrije Universiteit Brussel, Brussels, Belgium, pp. 121.

Scientific awards

European Commission distinguished poster award for the poster entitled "Diurnal variability of suspended matter from the SEVIRI geostationary sensor", (Neukermans, G., Forster, R., Greenwood, N. and Ruddick, K.), presented at Oceans From Space 2010, 26-30 April 2010, Venice, Italy.

VLIZ (Flanders Marine Institute) Professional Jury's award for the best poster entitled "Vertical Variability of suspended matter and its influence on remote sensing reflectance" (Neukermans, G., Loisel, H., Mériaux, X. and Ruddick, K.), Young Researcher's Day of Flanders Marine Institute (VLIZ), 6 March 2009, Bruges, Belgium.

The Oceanography Society Honorable Mention Student Paper (1st runner up) for the extended abstract entitled "Optical remote sensing of coastal waters from geostationary platforms: a feasibility study" (Neukermans, G., Ruddick K. And Nechad, B.), submitted for the Ocean Optics XIX Conference, 6-10 October 2008, Barga, Italy.

VLIZ (Flanders Marine Institute) Young Researcher's Thesis Award 2004 for the thesis "Remote sensing of mangroves in Gazi Bay (Kenya) with very high resolution QuickBird satellite imagery: automated methods for species and assemblage identification", VLIZ Young Scientist's Day, 25 February 2005, Bruges, Belgium.

Languages

Language	Speaking	Writing	Reading
Dutch	Mother tongue	Mother tongue	Mother tongue
English	Very good	Very good	Very good
French	Good	Good	Good
Kiswahili	Elementary	Elementary	Elementary

Computer literacy

Programming skills	MATLAB, IDL
Operating systems	MS Windows, Linux
Radiative transfer	Hydrolight/Ecolight
Text editors	MS Word, LateX
Image analysis software	Erdas Imagine 9.0, Definiens 5.0, ENVI, IDRISI
GIS software	ArcGIS ArcInfo 9.0
Presentation software	MS Powerpoint, Adobe Illustrator

Extracurricular activities

Hobbies	Sports (trekking, scuba diving, cycling, hiking, running) Travel Photography
Voluntary work	Action Group for Sustainable Development, Vrije Universiteit Brussel, Brussels, Belgium (February 2005-August 2007) Working group on sustainable development, Royal Belgian Institute for Natural Sciences, Brussels, Belgium (since April 2008)


SPIRAL UP, NOT DOWN.
HIDE THE REMOTE CONTROL.
SHAKE WELL BEFORE USE.
NEVER STOP EXPLORING.
JUST DO IT!
LIVE AND LET LIVE.
DO WHAT YOU LOVE,
AND DO IT OFTEN.
ENJOY LIFE,
EVERY SINGLE BITE OF IT.
Griet